

Patterns in natural systems

PROEFSCHRIFT

TER VERKRIJGING VAN DE GRAAD VAN
DOCTOR AAN DE UNIVERSITEIT LEIDEN, OP
GEZAG VAN RECTOR MAGNIFICUS
PROF. MR. C.J.J.M. STOLKER, VOLGENS
BESLUIT VAN HET COLLEGE VOOR PROMOTIES
TE VEREDEDIGEN OP DONDERDAG 8
SEPTEMBER 2016
KLOKKE 13.45 UUR

DOOR

Lotte Sewalt

GEBOREN TE ALPHEN AAN DEN RIJN
OP 16 JUNI 1990

Promotor:	prof. dr. A. Doelman	Universiteit Leiden
Co-promotores:	dr. P. J. A. van Heijster dr. A. Zagaris	Queensland University of Technology Wageningen University & Research centre
Promotiecommissie:	prof. dr. ir. G. Derk prof. dr. R. M. H. Merks dr. V. Rottschäfer dr. H. M. Schuttelaars prof. dr. A. W. van der Vaart	University of Surrey Universiteit Leiden, Centrum Wiskunde & Informatica Universiteit Leiden Technische Universiteit Delft Universiteit Leiden

Copyright © 2016 Lotte Sewalt

Printed by Uitgeverij BOXPress || Proefschriftmaken.nl

This research was funded by NWO through the NDNS+-cluster project ‘Phytoplankton dynamics, spatio-temporal chaos and destabilization mechanisms’ awarded to prof. dr. Arjen Doelman and dr. Antonios Zagaris.

We can be heroes.

– David Bowie

Table of Contents

Preface	v
1 Introduction	9
1.1 Laplace's method	11
1.2 Center manifold reduction	13
1.3 WKB-method	15
1.4 Geometric singular perturbation theory	17
1.4.1 Fenichel's theorems	18
1.4.2 Canard theory	21
1.4.3 Example: The forced Van der Pol equations	23
1.5 Outline of this thesis	27
1.5.1 Blooming phytoplankton	27
1.5.2 Spreading of malignant tumor	30
1.5.3 Traveling vegetation stripes	31
2 Extended center manifold reduction	33
2.1 Introduction	33
2.2 Spectral analysis of the trivial state	41
2.2.1 Linear stability	42
2.2.2 Example: a reaction-diffusion system	46
2.3 Emergence of a small pattern	46
2.3.1 Fourier expansion and amplitude ODEs	46
2.3.2 The classical center manifold reduction	48
2.4 Evolution of the small pattern outside the CMR regime	51
2.4.1 Beyond classical CMR: a Hopf bifurcation	51
2.4.2 Beyond the Hopf: a homoclinic bifurcation	54
2.5 Capturing the onset of low-dimensional chaos with the ECMR	60
2.5.1 New amplitude equations	61
2.5.2 Example: Revisiting our reaction-diffusion system	63

2.6	Codimension 2 bifurcations	66
2.6.1	Coincidence of the two largest eigenvalues	68
2.6.2	A three-component system	72
2.7	Discussion	77
Appendix		81
A	Sub- or supercritical Hopf bifurcation	81
3 Stability of a benthic layer of phytoplankton		85
3.1	Problem setting	88
3.2	Emergence and evolution of a small colony	90
3.2.1	An evolution law for the emerging population	90
3.2.2	Parametric dependence and stability of the bifurcating pattern	92
3.3	Formation and fate of phytoplankton colonies	94
3.3.1	Linear stability	95
3.3.2	Evolution of DCM profiles	96
3.4	Short-term evolution of bifurcating benthic layers	99
3.4.1	Bifurcating profile	100
3.4.2	Stability	101
3.5	Conclusions	104
3.6	Acknowledgements	105
Appendices		107
A	Approximation of integrals with a localized function	107
B	Approximation of the eigenvalue function	108
C	Nondimensionalization	110
4 Tumor spread with an Allee effect		113
4.1	Introduction	113
4.1.1	Allee effects and tumor growth	113
4.1.2	A new model for malignant tumor invasion	115
4.1.3	Main results	117
4.1.4	Comparison with results for previous models	118
4.1.5	Outline	120
4.2	Model derivation	121
4.3	Type III traveling wave solutions	123
4.3.1	Set-up	124
4.3.2	Layer problem	125
4.3.3	Reduced problem	126
4.3.4	Proof of Theorem 4.3.1	132

4.4	Implications of the strong Allee effect	136
4.4.1	Existence of invasive tumor fronts with well-defined edges	136
4.4.2	Biphasic relationship between invasion speed and background ECM density	139
4.4.3	ODE versus PDE	140
4.4.4	Comparison with models with logistic growth	142
4.5	Discussion and future work	143
4.5.1	Additional biological processes	144
4.5.2	Shortcomings and future work	146
Appendices		149
A	Logistic growth and the Allee effect	149
B	Results for the weak Allee model	151
C	Dimensionless variables and parameters	153
D	Transversality	153
5	Long wave length vegetation patterns	155
5.1	Introduction	155
5.1.1	Existence and stability results of the Gray–Scott model .	158
5.1.2	Outline of this article	160
5.2	Existence of homoclinic traveling multi-pulse patterns	162
5.2.1	Rescaling	163
5.2.2	Slow limit behavior	165
5.2.3	Fast limit behavior	166
5.2.4	Persistence of solutions in the perturbed problem	167
5.3	Existence of traveling multiscale periodic solutions	175
5.4	Stability of singular multiscale patterns	184
5.4.1	The Evans function and associated nonlinear eigenvalue problem	190
5.4.2	Proof of stability theorems	199
5.5	Conclusions and ecological implications	206
5.6	Discussion	209
5.7	Acknowledgments	210
References		211
Samenvatting		227
5.8	Uitgebreide centrumvariëteitreductie	227
5.9	Stabiliteit van een bodemlaag van fytoplankton	229
5.10	Tumorspreiding met een Allee effect	231
5.11	Vegetatiepatronen met een lange golflengte	232

Dankwoord	235
Curriculum Vitae	237

Preface

We can change the world. Although the processes that determine life on earth are not controllable, the impact of human kind is major. We have evolved to an intelligent species that knows exactly how to employ nature as a provider for our survival. Our natural thirst for knowledge has brought us an understanding of many of nature's processes and by virtue of that, prosperity. The population thrives on our innovations and scientific development. In particular since the 18th century, science has flourished and has established to be a valued instrument in the never-ending urge to improve our well-being. And it has been successful; the average life expectancy of humans rises steadily. Scientific discoveries have enabled us to combat diseases and to conquer natural disasters. Intelligent constructing prevents buildings from collapsing during earthquakes, our ships can overcome heavy storms, and, relying heavily on the quality of dykes and levees, we can even live on land that is below sea level. But even on a smaller scale, science delivers; through artificial fertilizer that enhances the growth of our crops, and sunscreen that prevents our skins from the malignant effects of the sun.

However, as beneficial as scientific innovations have been to the growth and health of our population, the human impact on nature is also palpable from much more alarming viewpoints. We arrogantly consider ourselves the most important residents of our planet. To facilitate mass consumption in the world, territories of other species are seized, driving them to extinction; the use of heavy chemicals has contaminated soil, making it unfruitful and the fossil fuel industry that still provides for most of our technology contributes heavily to global warming and all its inherent issues. We seem to have forgotten that our relation to the planet is in fact a symbiosis; the earth is essential to our existence.

The need for a transition of focus of the sciences is hence more urgent than ever. In order to provide for our ever growing community, we need to aim for sustainable development and choose to acknowledge our 'Gaia' as a whole instead of focusing mostly on the people that occupy this planet. In this task there lies an important role for the mathematician, being perhaps the most fundamental of

all scientists. Driven by questions that are posed by experts from ecology, biology or other applied sciences, applied mathematicians identify in complex systems the important mechanisms that are responsible for the process in question. These types of processes frequently refer to, for example, growth or spread with a certain regularity. While other applied scientists often contribute by observing a phenomenon and describing it meticulously, applied mathematicians take another approach. They are not bothered by the exact particulars that define the system, but pay attention to the important driving forces. In many cases, it turns out that the answer a mathematician finds to a specific question, is generally applicable to a much wider range of problems. As an example, think of a meadow with rabbits and foxes. Foxes eat rabbits, but rabbits reproduce faster, so an evident question to ask is what will happen to both populations as time proceeds. To study this, we design a phenomenological model that describes the change of the populations per time unit using two equations; one for foxes and one for rabbits. For the foxes, it incorporates how many foxes are born in that time unit due to reproduction and a diet of fluffy rodents, and a negative term that describes the natural death per time unit. For the rabbits, the equation includes a growth term from reproduction and a negative term that describes not only the natural death, but also death by fox per time unit¹. One could wonder whether the quality of the grass or the size of the meadow should not be taken into the equation², which exemplifies the nontriviality of modeling in the first place. But even when we suppose that only reproduction and the foxes' appetite are of importance, several approaches to this problem are possible. One way is to experimentally measure how many rabbits a fox eats, and what their average life span is, in order to estimate all the numbers that make up the equations. Next, a computer can use these equations to tell you exactly how many foxes and rabbits will survive, given the exact number of both populations at a certain starting point. A mathematician, however, will not be bothered by exactly how many rabbits are born per time unit or how many rabbits are on a fox's menu. Instead, they label all those estimated numbers with a letter so that it becomes a parameter; something that is still variable. Subsequently, we manipulate the abstract equations and draw conclusions that depend on those parameters. Such a conclusion might be that rabbits survive provided that their reproduction rate is at least twice that of a fox. The beauty of this approach is that to a mathematician the actual numbers do not matter. Moreover, a mathematician is less susceptible to drawing biased conclusions because he/she is not troubled by the exact interpretation of the parameters. Experimental data is prone to small

¹This particular model from population dynamics is referred to as the Lotka-Volterra system, proposed separately by Lotka and Volterra in the beginning of the 20th century, see [105, 162]

²pun intended

errors, and a mathematician's results are not affected by that. In fact, the results are so general that they can be applied to any type of predator-prey interaction, other than foxes and rabbits. Furthermore, a mathematician provides results with a certain mathematical rigor. That means that within the laws of the equations, the conclusions come with proofs and are not open to interpretation.

Of course there are disadvantages to this level of abstraction, too. In very complex systems, it is sometimes hard to translate abstract results back to their original application. Also, the rigorous analysis of a mathematician is often nearly impossible in large scale systems with many interaction processes. An essential step in the mathematical modeling of a natural phenomenon is therefore to construct a model that is stripped down from all unnecessary intricacies so that it is manageable, but remains to capture the determining processes. This in itself is a nontrivial task, but there are some ideas to follow. First, we could inspect for any large discrepancies between quantities in the system. Returning to the fox-rabbit model, instead of using general parameters for the reproduction rate of both species, we could include the fact that one is much faster than the other. Such extra information can simplify the model significantly and makes it more controllable. A second approach is to see whether there are some conserved quantities in the system. This could be physical laws like conservation of mass or energy, but it could also be less obvious. In general, any type of extra structure that we lay upon or identify in the system, has the ability to simplify it.

The imperative problems that the expansion of our population brings are obviously hard. The mere issue of prioritizing this large class of questions makes starting to work on them nearly impossible; the diversity in scale and impact is enormous. Not to mention the obstacles that one needs to overcome to model these types of large scale systems. So even though a long history of innovation provides enough confidence that we can indeed change the world and find a way to sustain our planet, it is not going to be easy. The need for interdisciplinary collaborations is evident and the role of an applied mathematician should not be underestimated. Because even when at first sight a model may only bring utter confusion and total chaos, the correct framework and a trained mathematician's eye can provide insight. After all, mathematicians even have a strict definition for chaos.

Introduction

In this thesis, we study several systems with an application in nature. While these applications (phytoplankton growth, tumor spread and vegetation patterns) have little in common, the equations that describe their behavior have strikingly similar features. The models studied in this thesis all comprise two or more coupled differential equations. Differential equations in general are equations that involve not only functions and variables, but also derivatives of functions; they are equations that connect the change of a quantity to the quantity itself. When the equations include derivatives with respect to more than one variable (time, space) they are called partial differential equations. The partial differential equations studied in this thesis are of reaction-diffusion type, which implies that they describe the spread (diffusion) of some quantity over time, under the influence of some interaction (reaction) with, usually, another quantity. Say we label two quantities u and v that interact, and we measure the spread of those quantities over a line segment – a spatial domain parametrized by x – over time t . The equations that describe this may be written as

$$\begin{aligned} u_t &= u_{xx} + f(u, v), \\ v_t &= v_{xx} + g(u, v), \end{aligned} \tag{1.1}$$

where the functions f and g describe exactly how u and v react to each other and a subscript indicates taking the derivative with respect to that variable. The second derivative with respect to the spatial variable models diffusion or natural spreading of the quantities u and v in the absence of any other forces. Furthermore, say we let x be bounded by 0 and 1, and t starts at $t = 0$ and may run up to infinity. To make this system of equations well-posed for solving, we provide boundary and/or initial conditions that prescribes the behavior of the solution at $t = 0$ and at the boundaries of the domain. Also, the system may depend on

parameters. Many types of questions may be posed associated to problems like (1.1). Are there unique solutions to the system (well-posedness)? Could these solutions be periodic in space or time (existence)? Does the character of a solution change significantly under the influence of changing parameters (bifurcations)? Are solutions resilient to small changes in the environment (stability)? In this general form it is hard to answer those questions, because the functions f and g may get very complex. But even in the case that $f = av$ and $g = bu$, with a, b parameters, studying existence of solutions, their bifurcations and their stability is nontrivial.

Therefore, we need some additional information to simplify the general reaction-diffusion model. The models studied in this thesis are all of reaction-diffusion type, but there is more agreement among them. Inherent through the applications, there is a clear separation of scales in all systems. The system is therefore equipped with a special small parameter that we label ε with $0 < \varepsilon \ll 1$. It is for example the size of a phytoplankton colony divided by the depth of the water column. This extra information is essential to the analysis that is presented in this thesis. A system involving such a small parameter is called *perturbed*, and if this small parameter multiplies the highest partial derivative of an equation, we call this *singularly perturbed*. An example of a singularly perturbed reaction diffusion system is

$$\begin{aligned} u_t &= u_{xx} + f(u, v; \varepsilon), \\ v_t &= \varepsilon v_{xx} + g(u, v; \varepsilon). \end{aligned} \tag{1.2}$$

The models studied in this thesis are all singularly perturbed, and the mathematical tools that are used to analyze them exploit that perturbed character. After all, if ε is so small, why not simply set it equal to zero? In singularly perturbed problems, as is obvious in (1.2), simply equating $\varepsilon = 0$ drastically changes the character of the v -equation. It is not even a partial differential equation anymore. Therefore, the results that are derived using the limit problem for $\varepsilon = 0$ need to be studied with care. The mathematical field that is associated with these questions is usually referred to as *asymptotic analysis* or *perturbation analysis*. The results that are derived in this field have a validity regime that can be explicitly estimated in terms of the small parameter ε , as it asymptotically approaches zero.

In this section, we will provide an overview of several techniques from asymptotic analysis that are used throughout this thesis. They can be thought of as the prerequisites to the main part of this thesis, Chapters 2–5. The application of the techniques is not limited to reaction-diffusion systems, but concerns integrals or systems of ordinary differential equations with a small parameter ε . The partial differential equations treated in this thesis are in most cases converted

into systems of ordinary differential equations (for example by introducing a traveling wave coordinate), and after this reduction step, the techniques discussed in this chapter are applied. The techniques discussed in the prerequisites covered below, all define asymptotic results for ε approaching zero, and will in many cases be *leading order results* in ε . In order to quantify exactly what leading order means, we use the following definition.

Definition 1.0.1. Given two functions of a small parameter ε , $f(\varepsilon)$ and $\phi(\varepsilon)$, we say that

$$f(\varepsilon) = \mathcal{O}(\phi(\varepsilon)),$$

if there are constants k and $\bar{\varepsilon}$, both independent of ε , for which holds

$$|f(\varepsilon)| \leq k|\phi(\varepsilon)|, \quad \text{for } 0 < \varepsilon < \bar{\varepsilon}.$$

We say that “ f is big Oh of ϕ ” or “ f is of order ϕ ” as ε approaches zero. In particular, a result holds ‘to leading order in ε ’ if the error term is ‘big Oh’ of a positive power of ε , $\mathcal{O}(\varepsilon^p)$ with $p > 0$. Furthermore, we write $f \sim \phi$ as $\varepsilon \downarrow 0$ if

$$\lim_{\varepsilon \downarrow 0} \frac{f(\varepsilon)}{\phi(\varepsilon)} = 1.$$

These definitions are gained from [77].

1.1 Laplace's method

The first technique that we discuss is one that is not necessarily related to differential equations, but to an operation that is often used to solve them: integrals. Laplace's method is developed to approximate integrals of a product of two functions, say $f(t)h(t)$. Suppose that one of the factors of the product, $h(t)$, is localized; it has a well-defined maximum in the integration interval and the decay away from that maximum is ‘fast’. Then, intuitively, one may expect that the product of $h(t)$ with $f(t)$, which may not be localized, can be approximated by using the value of $f(t)h(t)$ at the location in the integration interval where $h(t)$ is maximal. This is exactly what Laplace's method uses.

An example of a function with a particularly localized character is the exponential. Their growth rate is fast, especially when the argument is very large. A function $h(t) = e^{\frac{g(t)}{\varepsilon}}$, with $g(t)$ some continuous, real-valued function, is thus strongly localized because the exponent grows asymptotically large as ε approaches zero. Laplace's approximation concerns therefore integrals of the form

$$\int_a^b f(t)e^{\frac{g(t)}{\varepsilon}} dt,$$

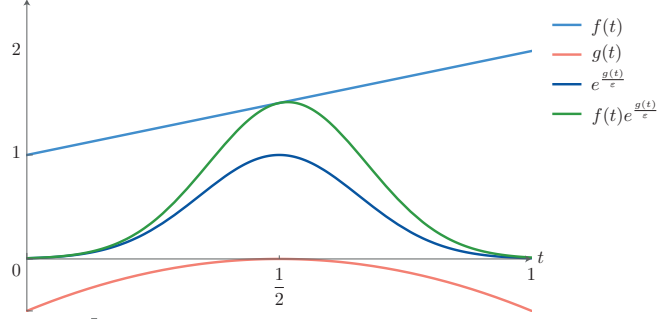


Figure 1.1: Illustration of localized function to which Laplace's method can be applied. Here, $f(t) = t + 1$ and $g(t) = -2(t - \frac{1}{2})^2$ and $\varepsilon = 0.1$.

where $f(t)$ and $g(t)$ are continuous functions over the bounded interval $[a, b]$ with $a < b$. For an illustration of this intuition, see Figure 1.1. We follow the notation from [77]. Laplace's method states that if the maximum of $g(t)$ in the interval $[a, b]$ is attained at some $t_0 \in (a, b)$ and $f(t_0) \neq 0$, then it holds that

$$\int_a^b f(t)e^{\frac{g(t)}{\varepsilon}} dt \sim f(t_0) \sqrt{\frac{2\pi\varepsilon}{g''(t_0)}} e^{\frac{g(t_0)}{\varepsilon}},$$

as $\varepsilon \rightarrow 0$. Note that the maximum value of f does not determine for the approximation but the second derivative of g does. It carries information on the steepness of the decay of g outside t_0 ; it says something about how localized the exponential function really is. This way, Laplace's method provides a direct asymptotic approximation for integrals in terms of local information that can easily be determined.

Say that $f(t) = t + 1$ and $g(t) = -2(t - \frac{1}{2})^2$. Then the maximum of $g(t)$ is attained at $t_0 = \frac{1}{2}$, and the integral $\int_0^1 f(t)e^{\frac{g(t)}{\varepsilon}}$ is approximated by $\frac{3\sqrt{\pi}}{2\sqrt{2}}\sqrt{\varepsilon}$, as $\varepsilon \rightarrow 0$. For $\varepsilon = 0.1$, the error that is made using Laplace's method is $-9.3 \cdot 10^{-4}$, which drops to $6.9 \cdot 10^{-18}$ for $\varepsilon = 0.001$.

It may be the case that the maximum of $g(t)$ is on one of the boundaries of the integration interval. In this case, too, Laplace's method provides estimates. For example, when the maximum of g is attained at the right boundary and , $t_0 = b$, and $g'(b) \neq 0$, we approximate

$$\int_a^b f(t)e^{\frac{g(t)}{\varepsilon}} dt \sim -\varepsilon \frac{f(b)}{g'(b)} e^{\frac{g(b)}{\varepsilon}}.$$

An analogous result exists for a maximum at the left boundary, $t_0 = a$, with a change of sign. Moreover, this result can be extended using higher order estimates if $g'(b) = 0$. Full proofs and higher order terms of this approximation can be found in, for example, [174].

1.2 Center manifold reduction

Upon studying systems of ordinary differential equations, one of the first techniques we learn is how to study the linear stability of fixed points in autonomous systems. That is, in a system of the form

$$\dot{x} = f(x),$$

with $\dot{x} = \frac{dx}{dt}$ and where $x \in \mathbb{R}^n$ and $f(x) : \mathbb{R}^n \rightarrow \mathbb{R}^n$ smooth enough. We learn that the linear stability of a fixed point x^* can be determined by linearizing the function f , that is, studying the Jacobian, $J(x)$. The behavior of the resulting Jacobian evaluated at the fixed point returns the stability of the fixed point. If all eigenvalues of $J(x^*)$ have negative real part, i.e. there are only *stable eigenvalues*, the fixed point is stable. If there is an eigenvalue with positive real part, i.e. an *unstable eigenvalue*, the fixed point is unstable. If, however, any of the eigenvalues has zero real part, a *center eigenvalue*, and there are no unstable eigenvalues, the linear stability analysis is inconclusive. The only way to determine the stability in that case is to do nonlinear stability analysis, and study the behavior of the system using the *center manifold theorem*, Theorem 1.2.2. A detailed proof of this theorem is given in [18], but we will explain the results here.

Suppose we are given a system of which the Jacobian at a fixed point only has n_s stable and n_c center eigenvalues and no unstable eigenvalues. Without loss of generality, we can then translate and rewrite the system in a normal form with a slight abuse of notation like

$$\begin{aligned}\dot{x} &= Ax + f(x, y), \\ \dot{y} &= By + g(x, y),\end{aligned}\tag{1.3}$$

where $x \in \mathbb{R}^{n_c}$ and $y \in \mathbb{R}^{n_s}$. A and B are constant coefficient, square matrices with dimensions n_c and n_s , respectively and the eigenvalues of A all have zero real part, while the eigenvalues of B only have negative real part. Moreover, the functions f and g are strictly nonlinear and smooth. In this normal form, the fixed point is translated to $(x, y) = (0, 0)$ and we have changed the coordinates so that the center and stable behavior are clearly separated. Then, the center manifold theorem states the following.

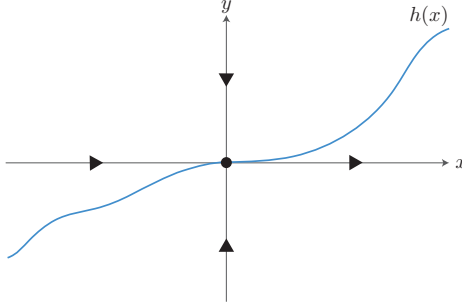


Figure 1.2: Illustration of a center manifold for system (1.3) in the case that $n_c = n_s = 1$. The stable subspace coincides with the y -axis and the center subspace with the x -axis.

Theorem 1.2.1 (Existence of a center manifold). *The system (1.3) has a locally defined, invariant manifold*

$$W^c = \{(x, h(x)) : x \in \mathbb{R}^{n_c}, |x| < \varepsilon\},$$

where $\varepsilon > 0$ is small enough and $h(x) : \mathbb{R}^{n_c} \rightarrow \mathbb{R}^{n_s}$ satisfies

$$h(0) = 0, \quad h_x(0) = 0.$$

That is, there exists a manifold on which the behavior of (1.3) is locally invariant (an initial point on the manifold that follows the flow induced by (1.3), stays on the manifold for some time). This manifold has the dimension of the number of center eigenvalues and is locally a graph over x . Moreover, the center manifold is tangent to the center eigenspace of the fixed point. An illustration of this idea with $n_c = n_s = 1$ is depicted in Figure 1.2

Additional to the existence of such a locally invariant manifold, there exists a theorem that states that the stability of the fixed point $(0, 0)$ of (1.3) can be determined by studying the behavior on that center manifold.

Theorem 1.2.2 (Center manifold reduction theorem). *Locally near $(0, 0)$, the system (1.3) is topologically conjugate to the system*

$$\begin{aligned} \dot{x} &= Ax + f(x, h(x)), \\ \dot{y} &= By. \end{aligned} \tag{1.4}$$

Note that system (1.4) decouples, and for the stability of fixed point $(0, 0)$ it suffices to study the n_c -dimensional system defined by $\dot{x} = Ax + f(x, h(x))$.

That is a reduction of n_s dimensions as opposed to the system (1.3)! Theorem 1.2.2 is a local result, which means that it is only valid if the behavior of matrix B is significantly faster than that of A . That is, the eigenvalues of B must be significantly larger than $\mathcal{O}(\varepsilon)$; there is a spectral gap between the center and stable eigenvalues.

In a more general case, the system depends on parameters and only exhibits center eigenvalues for certain parameter combinations. For those combinations, the system changes stability; there is a bifurcation. Also in the case of a bifurcation, center manifold reduction can be of help, via the following theorem.

Theorem 1.2.3 (Center manifold reduction with parameter dependence). *Consider the system*

$$\begin{aligned}\dot{x} &= A(\mu)x + f(x, y; \mu), \\ \dot{y} &= B(\mu)y + g(x, y; \mu),\end{aligned}\tag{1.5}$$

with $x \in \mathbb{R}^{n_c}$ and $y \in \mathbb{R}^{n_s}$ and $\mu \in \mathbb{R}^k$ a parameter. Let $A(0)$ be a constant coefficient matrix of dimension n_c with only center eigenvalues, and $B(0)$ a constant coefficient matrix of dimension n_s with only stable eigenvalues. Furthermore, let f and g be strictly nonlinear and smooth. Then, there exists a \mathbb{R}^k -dimensional family of locally invariant (i.e. for μ small enough) center manifolds

$$W_\mu^c = \{(x, h(x; \mu)) : x \in \mathbb{R}^{n_c}, |x| < \varepsilon\},$$

and $h(x; 0) = h(x)$ from Theorem 1.2.1. Furthermore, system (1.5) is topologically conjugate with

$$\begin{aligned}\dot{x} &= A(\mu)x + f(x, h_\mu(x); \mu), \\ \dot{y} &= B(\mu)y.\end{aligned}\tag{1.6}$$

This extension can be verified by adding to system (1.5) a auxiliary equation $\dot{\mu} = 0$, and applying Theorems 1.2.1 and 1.2.2. Again, this result is a local one; the reduction only holds for those μ that make the real part of the eigenvalues of B still significantly smaller than those of A . The perturbation by μ may not violate the spectral gap condition. Center manifolds can be determined explicitly, for more details on how to approach this, see for example [98].

1.3 WKB-method

The next perturbation method in this section of mathematical tools is one that approximates solutions to second order, non-autonomous, linear, ordinary

Introduction

differential equations that are singularly perturbed. That is, differential equations of the form

$$\varepsilon^2 y_{xx} - q(x)y = 0, \quad (1.7)$$

with $x \in \mathbb{R}$ with $q(x) > 0$. To gain some intuition, first consider the case that $q(x) = q_0 > 0$, a constant. In that case, equation (1.7) is simply a second order differential equation with constant coefficients. It is solved by exponentials; the general solution is

$$y(x) = c_+ e^{\frac{\sqrt{q_0}}{\varepsilon} x} + c_- e^{-\frac{\sqrt{q_0}}{\varepsilon} x}, \quad (1.8)$$

where c_{\pm} are two constants that depend on the initial conditions. The WKB-method¹ generalizes this idea of using exponentials for a q that depends explicitly on x . Because of the singularly perturbed nature of (1.7), it is expected that there is a separation of scales inherent to the equation. The specific assumption of the WKB-method is that the fastest² behavior is captured by an exponential function as a factor of the solution. Specifically, we assume that the solution is of the form

$$y(x) = e^{\frac{\theta(x)}{\varepsilon}} [y_0(x) + \varepsilon y_1(x) + \mathcal{O}(\varepsilon^2)], \quad (1.9)$$

where $\theta(x)$ and $y_i(x)$ are functions that need to be determined. Upon substituting (1.9) in to (1.7) and collecting terms of the same order in ε , we can rewrite to leading order

$$\varepsilon^2 \left\{ \frac{1}{\varepsilon^2} (\theta')^2 y_0 + \frac{1}{\varepsilon} [\theta'' y_0 + 2\theta' y'_0 + (\theta')^2 y_1] \right\} - q(x) (y_0 + \varepsilon y_1) = 0, \quad (1.10)$$

where ' is the derivative with respect to x . The leading order terms of (1.10) make up the $\mathcal{O}(1)$ equation,

$$(\theta')^2 = q(x), \quad (1.11)$$

which yields $\theta(x) = \pm \int^x \sqrt{q(s)} ds$. The next order equation of (1.10) is

$$\theta'' y_0 + 2\theta' y'_0 + (\theta')^2 y_1 = q(x) y_1, \quad (1.12)$$

but using (1.11), this simplifies to $\theta'' y_0 + 2\theta' y'_0 = 0$, which has solution

$$y_0(x) = \frac{c}{\sqrt{\theta'}},$$

¹WKB stands for Wentzel, Kramers, and Brillouin who worked in the field of quantum mechanics, and used this method to find approximate solutions to the Schrödinger equation. There are, however, several other names for the same technique.

²Here, fast indicates a big change in y over a short x -interval.

where c is an integration constant. Now recall that there are two solutions for $\theta(x)$. This is to be expected in a second order equation without initial conditions; compare with the solution (1.8) which is also a linear combination of two exponentials. Combining the results of the two orders of magnitude in this method and making a linear combination of the two solutions for θ , we find a leading order approximation to (1.7),

$$y(x) = \frac{1}{q^{\frac{1}{4}}(x)} \left[C_+ e^{\frac{1}{\varepsilon} \int^x \sqrt{q(s)} ds} + C_- e^{-\frac{1}{\varepsilon} \int^x \sqrt{q(s)} ds} \right]. \quad (1.13)$$

To find higher order terms of this approximation, we can return to equation (1.10) and collect the next order's terms to solve y_1 and continue. Note that the solution for $y(x)$ is not well-defined for values of x at which $q(x)$ vanishes. In this case, we speak of *turning points*, extra measures are needed and the solution at those x -values is usually approximated using Airy functions. For more details, see [77].

1.4 Geometric singular perturbation theory

In singular perturbed systems, often a separation in (time) scales can be observed. For example, localized behavior of solutions, very steep transitions near boundaries, or oscillations with a fast and a slow part. Taking this type of information into account improves the prospects of solving the system tremendously. By considering both scales of a perturbed problem separately, we can usually derive results much more easily. Moreover, the concatenation of the fast and slow scale is shown to be a good (local) approximation of the original problem. The question that remains is then how the two worlds meet. For at least a class of singularly perturbed problems, geometric singular perturbation theory (GSPT) provides the answer to just that. In this section the main results of the theory are formulated and interpreted. We follow mainly the formulations from [73] and [149], and conclude this subsection with an example where the results are applied to the forced Van der Pol equations.

The focus to which we apply GSPT is a class of systems of ordinary differential equations of the following form,

$$\begin{aligned} \dot{u} &= f(u, v, \varepsilon), \\ \dot{v} &= \varepsilon g(u, v, \varepsilon), \end{aligned} \quad (1.14)$$

where $\dot{\cdot} = \frac{d}{dt}$, $u \in \mathbb{R}^k$ and $v \in \mathbb{R}^l$ with $k, l \geq 1$. For the functions f and g we will require them to be ‘smooth enough’ for the application of the theorems. Furthermore, $0 < \varepsilon \ll 1$ is, of course, a small parameter and f, g are $\mathcal{O}(1)$ with respect to ε .

Upon introducing a new time scale, $\tau = \varepsilon t$, we can rewrite system (1.14) into an equivalent formulation thereof;

$$\begin{aligned}\varepsilon u' &= f(u, v, \varepsilon), \\ v' &= g(u, v, \varepsilon),\end{aligned}\tag{1.15}$$

where $' = \frac{d}{d\tau}$. Since ε is small, τ is a much slower time scale compared to t . Hence, we refer to (1.15) as the slow system, opposing the label ‘fast’ for system (1.14). This is the setting to which GSPT applies.

1.4.1 Fenichel’s theorems

The two equivalent systems (1.14) and (1.15) describe the same behavior, but in a different variable. One could say that the two systems argue from a different viewpoint. Taking the limit $\varepsilon \rightarrow 0$ in (1.14) yields the so-called *layer system*,

$$\begin{aligned}\dot{u} &= f(u, v, 0), \\ \dot{v} &= 0,\end{aligned}\tag{1.16}$$

and is not at all equivalent to the limiting system of (1.15), which we call the *reduced system*,

$$\begin{aligned}0 &= f(u, v, 0), \\ v' &= g(u, v, 0).\end{aligned}\tag{1.17}$$

The layer system has trivial behavior in the v -components, making it significantly easier to study, and the reduced system is a differential-algebraic system, where the dynamics is restricted to the manifold on which $f(u, v, 0) = 0$. This generically l -dimensional manifold, the *critical manifold*,

$$\mathcal{M} = \{(u, v) \in \mathbb{R}^{k+l} : f(u, v, 0) = 0\},\tag{1.18}$$

is, in turn, exactly the set of fixed points of the layer system. Hence, in terms of the layer problem the only nontrivial behavior is in the u -direction, and its direction generically reverts at \mathcal{M} . On the other hand, the reduced problem only takes place on the critical manifold, and the dynamic behavior is dictated by the v -equation. And since (1.16) is associated with the fast, and (1.17) with the slow coordinate, we can conclude that the fast behavior is to leading order trivial in the v -direction and determined by u , while the leading order slow behavior takes place in the lower dimensional state space defined by \mathcal{M} and determined by v .

Definition 1.4.1. Let $\mathcal{M}_0 \subset \mathcal{M}$ be a compact subset of the critical manifold corresponding to system (1.17). If the eigenvalues of the Jacobian $\frac{\partial f}{\partial u}(u, v, 0)|_{\mathcal{M}_0}$ are bounded away from the imaginary axis, then the critical manifold is *normally hyperbolic*.

The evident question to ask now is how to make the results drawn from both limiting systems compatible. This is established by Fenichel's theory [49], and will be explained according to two theorems and one corollary.

Theorem 1.4.1 (Fenichel's first theorem). *Suppose \mathcal{M}_0 is compact and normally hyperbolic. Then, for $\varepsilon > 0$ and sufficiently small there exists a manifold \mathcal{M}_ε which is $\mathcal{O}(\varepsilon)$ close to \mathcal{M}_0 and diffeomorphic to it. Moreover, \mathcal{M}_ε is locally invariant under the flow of (1.14).*

Like the center manifold in section 1.2, the persisting manifold \mathcal{M}_ε is locally a graph over the v -coordinates, say $u = h(v)$; this follows from the Implicit Function Theorem and the fact that \mathcal{M}_0 is normally hyperbolic. Hence, we can reduce the reduced system to

$$v' = g(h(u), v, 0).$$

So, even for $\varepsilon \neq 0$ but small enough, the slow flow may be approximated by (1.17). The slow flow takes place on the locally invariant *slow manifold* \mathcal{M}_ε . For precise statements on the smoothness and invariance of \mathcal{M}_ε , see [82, 84].

It is noteworthy what happens when a critical manifold is not normally hyperbolic. Say, for instance, that \mathcal{M} is folded so the Jacobian has a zero eigenvalue. In most cases, these folds are sets of *jump points*. At those points, the flow starts to follow the fast vector field because that is then the dominant term. However, one needs to be very careful with this assumption because if there is a critical point of the slow flow near the fold, completely different mechanisms can occur. This is further detailed in section 1.4.2 .

The interplay between the slow behavior and the fast phase space that surrounds it, is defined by the stable and unstable manifolds of the points on the critical manifold. Say these sets are $W^{s,u}(\mathcal{M}_0)$, then Fenichel's second theorem specifies their persistence if $\varepsilon \neq 0$.

Theorem 1.4.2 (Fenichel's second theorem). *Suppose $\mathcal{M}_0 \subset \mathcal{M}$ is compact and normally hyperbolic. Then for $\varepsilon > 0$ and sufficiently small, there exist manifolds $W^s(\mathcal{M}_\varepsilon)$ and $W^u(\mathcal{M}_\varepsilon)$ that are $\mathcal{O}(\varepsilon)$ close and diffeomorphic to $W^s(\mathcal{M}_0)$ and $W^u(\mathcal{M}_0)$, respectively. Moreover, these manifolds are locally invariant under the flow of (1.14).*

The stable and unstable manifolds of \mathcal{M}_ε decay to \mathcal{M}_ε with an exponential rate. Often, bounded solutions to (1.14) start in a neighborhood of slow manifold \mathcal{M}_ε , follow $W^u(\mathcal{M}_\varepsilon)$ away from \mathcal{M}_ε and return to it via $W^s(\mathcal{M}_\varepsilon)$. Hence, the intersection $W^s(\mathcal{M}_\varepsilon) \cap W^u(\mathcal{M}_\varepsilon)$ is in many cases a focus of study.

Fenichel's first and second theorem already allow us to draw significant conclusions. If, for example, \mathcal{M}_0 is purely attracting, studying the slow behavior

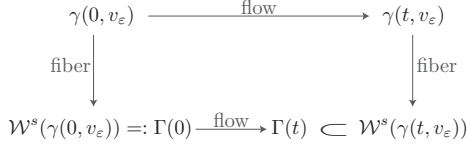


Figure 1.3: Diagram corresponding to Fenichel's third theorem. For $v_\varepsilon \in \mathcal{M}_\varepsilon$, the set that results from flowing forward its fiber is a subset of the fiber of the forward flown initial point v_ε .

on \mathcal{M}_ε may be enough, because all initial points will eventually be attracted to \mathcal{M}_ε . The simple concatenation of pieces of fast and slow orbit for $\varepsilon = 0$ makes up what we label a *singular orbit*. We say that a singular orbit persists for $\varepsilon \neq 0$, if the construction of it is valid for any ε with $0 < \varepsilon < \varepsilon_0$. The proofs of persistence of orbits often rely on the transverse intersections of manifolds, of which we know they persist.

Fenichel's second theorem guarantees persistence of the stable and unstable manifolds of \mathcal{M}_0 as an analogous object. However, this does not imply the persistence of the stable and unstable manifold of a specific point on \mathcal{M}_0 . After all, a critical point v_0 on \mathcal{M}_0 does in general not even perturb to a fixed point for $\varepsilon \neq 0$. Still, Fenichel's third theorem explains that indeed $W^{s,u}(v_0)$ perturb to something analogous in an $\mathcal{O}(\varepsilon)$ neighborhood. As the exact statement of this theorem requires quite some notation, we explain the correspondence using Figure 1.3 and a corollary of the theorem.

Let v_ε be a point in \mathcal{M}_ε , then, by Fenichel's first theorem, there exists a $v_0 \in \mathcal{M}_0$ that can be associated with it in a natural way, and v_0 , being a fixed point of the layer system (1.16), has stable and unstable manifolds $W^{s,u}(v_0)$. Then, Fenichel's third theorem states that there exist manifolds $\mathcal{W}^{s,u}(v_\varepsilon)$ which are diffeomorphic and $\mathcal{O}(\varepsilon)$ close to $W^{s,u}(v_0)$, which we call *fibers* of v_ε . The fibers $\mathcal{W}^{s,u}(v_\varepsilon)$ are not stable and unstable manifolds (since v_ε is not a fixed point) nor are they invariant. There is, however, a weaker sense of invariance available for the fibers, which is explained by Figure 1.3.

Denote any orbit of system (1.14) parametrized by t and with initial point $v_\varepsilon \in \mathcal{M}_\varepsilon$ as $\gamma(t; v_\varepsilon)$. Then, let the corresponding fiber $\mathcal{W}^s(v_\varepsilon)$ be the stable fiber of v_ε . This fiber is in itself a set of initial conditions, say $\Gamma(0)$, where

$$\Gamma(t) = \{\gamma(t, x) : x \in \mathcal{W}^s(v_\varepsilon)\}.$$

Fenichel's theorem states that the set $\Gamma(t)$ is a subset of the fiber of $\gamma(t, v_\varepsilon)$, $\mathcal{W}^s(\gamma(t, v_\varepsilon))$, see Figure 1.3.

From Fenichel's third theorem, the corollary below follows.

Corollary 1.4.3. Suppose \mathcal{M}_ε is a slow manifold as defined in Fenichel's first theorem. Let $\gamma(t, v_\varepsilon) \subset \mathcal{M}_\varepsilon$ be an orbit in the slow manifold with $\gamma(0, v_\varepsilon) = x$, $x \in \mathcal{M}_\varepsilon$. Then there exists a base point $v_\varepsilon^+ \in \mathcal{M}_\varepsilon$ and an orbit $\gamma^+(t, v_\varepsilon^+)$ with $\gamma^+(0, v_\varepsilon^+) = v_\varepsilon^+$ for which there exist constants $C_1, C_2, k > 0$ such that

$$\|\gamma(t, v_\varepsilon) - \gamma^+(t, v_\varepsilon^+)\| \leq C_1 e^{-k/\varepsilon} \quad \text{for } t \geq \frac{C_2}{\varepsilon}.$$

Hence, Fenichel's theorems prescribe the behavior of singularly perturbed systems like (1.14) to leading order. It provides insight in how slow and fast limiting behavior can be 'glued' together. If normal hyperbolicity of the manifold is lost, the theorems are unfortunately no longer applicable. In these cases, the behavior requires canard theory.

1.4.2 Canard theory

When a critical manifold is not normally hyperbolic, see Definition 1.4.1, the fast behavior generically takes over because this is the dominant mechanism. In special cases, however, an orbit remains close to the critical manifold for an $\mathcal{O}(1)$ time, even though it enters a repelling branch of the critical manifold. Such orbits are the focus of study in canard theory. For a clear presentation of this theory, we follow [149] and restrict to three dimensions in (1.14). In particular, we say $k = 1$ and $l = 2$ and study

$$\begin{aligned} \varepsilon u' &= f(u, v_1, v_2, \varepsilon), \\ v'_1 &= g_1(u, v_1, v_2, \varepsilon), \\ v'_2 &= g_2(u, v_1, v_2, \varepsilon), \end{aligned} \tag{1.19}$$

where $' = \frac{d}{d\tau}$. Canard theory applies to GSPT problems of at least dimension 3 in the case that the critical manifold loses normal hyperbolicity. To guarantee that this happens in (1.19) close to the origin in a non-degenerate way, we assume

$$\begin{aligned} f(0, 0, 0, 0) &= 0, & f_u(0, 0, 0, 0) &= 0, \\ f_{v_1}(0, 0, 0, 0) &\neq 0, & f_{uu}(0, 0, 0, 0) &\neq 0, \end{aligned} \tag{1.20}$$

which are simply conditions on the critical manifold \mathcal{M} as defined in 1.4. Making use of the Implicit Function Theorem, we can now parametrize a fold-curve F by $(h_1(v_2), h_2(v_2), v_2) \in \mathbb{R}^3$. Furthermore, we define a transversality criterion,

$$\ell(v_2) := \left\langle \begin{pmatrix} f_{v_1} \\ f_{v_2} \end{pmatrix}, \begin{pmatrix} g_1 \\ g_2 \end{pmatrix} \right\rangle \Big|_{(h_1(v_2), h_2(v_2), v_2, 0)}, \tag{1.21}$$

following [149]. This transversality criterion determines the behavior of the reduced flow near the fold curve. In the case that $\ell(0) \neq 0$, the point on F is a

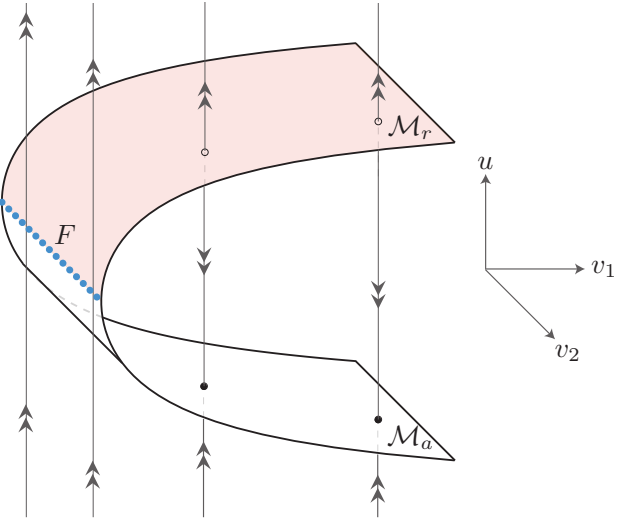


Figure 1.4: Schematic illustration of the folded critical manifold with repelling and attracting branches \mathcal{M}_r and \mathcal{M}_a , and the fold curve F .

jump point, as was discussed in the previous paragraph. If, however $\ell(0) = 0$, it is not, and these points are called *canard points*.

In the case that $\ell(0) = 0$ and (1.20) are satisfied, the system can be transformed into a normal form by a smooth change of coordinates. This normal form is

$$\begin{aligned} \varepsilon u' &= u^2 + v_1 & +\mathcal{O}(\varepsilon v_1, \varepsilon v_2, \varepsilon u, \varepsilon^2, v_1^2 u, u^3, v_1 v_2 u), \\ v'_1 &= au + bv_2 & +\mathcal{O}(v_1, \varepsilon, v_2^2, v_2 u, u^2), \\ v'_2 &= c & +\mathcal{O}(v, \varepsilon, v_2, u), \end{aligned} \quad (1.22)$$

where $a, b, c \in \mathbb{R}$ are explicitly computable. This transformation simply translates F to the v_2 -axis, and uses the fact that the critical manifold is locally parabolic. See a schematic representation in Figure 1.4. The error terms are quantified, but since we work locally around the origin, we will say that (1.22) is to leading order equal to

$$\begin{aligned} \varepsilon u' &= u^2 + v_1, \\ v'_1 &= au + bv_2, \\ v'_2 &= c, \end{aligned} \quad (1.23)$$

for a clear presentation. The critical manifold of (1.23) is

$$\mathcal{M} = \{u^2 + v_1 = 0\} = \{(u, v_1(u, v_2), v_2) \in \mathbb{R}^3\},$$

because it is a graph over (u, v_2) with $v_1(u, v_2) = -u^2$. Differentiating v_1 with respect to τ yields $v'_1 = -2uu'$ and substituting this into (1.23) we reduce on \mathcal{M} to

$$\begin{aligned} -2uu' &= au + bv_2, \\ v'_2 &= c. \end{aligned} \tag{1.24}$$

Which defines the reduced flow on \mathcal{M} in the (u, v_2) field, on which $u = 0$ coincides with the F . For $u = 0$, the system is singular; we desingularize it by reparametrizing the orbits via the substitution $\xi(\tau)$ with $\frac{d\xi}{d\tau} = \frac{1}{2u}$, and obtain the *desingularized system*

$$\begin{aligned} u_\xi &= au + bv_2, \\ v_\xi &= -2cu. \end{aligned} \tag{1.25}$$

The phase portraits of (1.24) and (1.25) are equivalent, apart from the direction of the orbits. If $u > 0$, the direction of orbits in (1.25) needs to be reversed to represent those of (1.24), see Figure 1.5. Note that $(0, 0)$ is an equilibrium of (1.25), but not of (1.24). This defines $(0, 0)$ to be a *folded singularity* in (1.24). The character of the folded singularity is determined by the character of the equilibrium of (1.25). The eigenvalues of the Jacobian of (1.25) at $(0, 0)$ are $\lambda_{1,2} = \frac{1}{2}(a \pm \sqrt{a^2 - 8bc})$. For now, we assume that $bc < 0$, so $(0, 0)$ is a saddle. Consequently, the point $(0, 0)$ in (1.24) is a *folded saddle*. By scaling the saddle back in the τ variable, we find that $(0, 0)$ in fact admits two orbits passing through the fold curve, see Figure 1.5. The solutions of the reduced problem passing from the attracting to the repelling branch of the critical manifold are called *singular canards*, while solutions of the reduced problem that pass from the repelling part of the critical manifold to the attracting branch are *singular faux canards*.

Using blow-up techniques, which are not within the scope of this thesis, it can be shown that, in fact, near a folded saddle, the singular canard persists as a solution of the full system (1.22), see [149]. The theory for three dimensions can be generalized to n , see for example [166].

1.4.3 Example: The forced Van der Pol equations

In this section, we apply GSPT and Canard theory to the forced Van der Pol equation, to exemplify the potential of the theory. It was originally proposed in

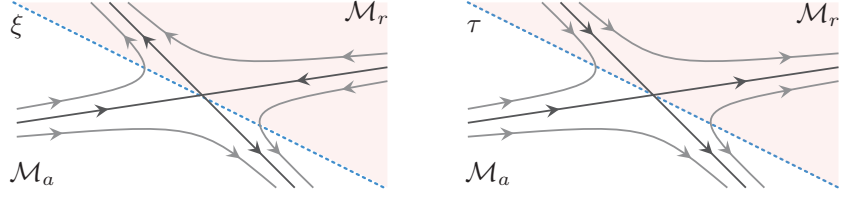


Figure 1.5: Left: Saddle fixed point of the desingularized system (1.25) parametrized by ξ . Right: The corresponding folded saddle of (1.24).

[158] and applies to electrical circuits employing vacuum tubes. Central to this paragraph are thus,

$$\begin{aligned}\dot{u} &= u - \frac{1}{3}u^3 + v_1, \\ \dot{v}_1 &= \varepsilon(-u + \sqrt{2} \cos(v_2)), \\ \dot{v}_2 &= \varepsilon\end{aligned}\tag{1.26}$$

where $\cdot = \frac{d}{dt}$. The system is equivalently posed in the slow time scale $\tau = \varepsilon t$.

$$\begin{aligned}\varepsilon u' &= u - \frac{1}{3}u^3 + v_1, \\ v'_1 &= -u + \sqrt{2} \cos(v_2), \\ v'_2 &= 1.\end{aligned}\tag{1.27}$$

The limiting systems are

$$\begin{aligned}\dot{u} &= u - \frac{1}{3}u^3 + v_1, & 0 &= u - \frac{1}{3}u^3 + v_1, \\ \dot{v}_1 &= 0, & v'_1 &= -u + \sqrt{2} \cos(v_2), \\ \dot{v}_2 &= 0 & v'_2 &= 1.\end{aligned}\tag{1.28}$$

The critical manifold is defined by $v_1 = \frac{1}{3}u^3 - u$ and has two fold curves at $u = \pm 1$ which are parametrized by v_2 . The fast behavior is trivial in the v_1 and v_2 direction while \dot{u} changes sign exactly at the critical manifold. This is depicted in the (u, v_1) -plane in Figure 1.6. On the critical manifold, the singular system that is obtained by differentiating $v_1 = \frac{1}{3}u^3 - u$ defines the slow flow,

$$\begin{aligned}(u^2 - 1)u' &= -u + \sqrt{2} \cos(v_2), \\ v'_2 &= 1,\end{aligned}\tag{1.29}$$

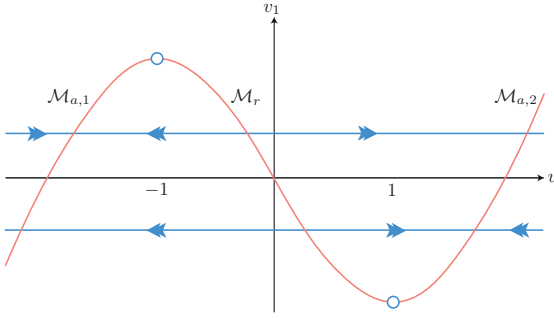


Figure 1.6: Slow manifold and fast singular flow of (1.26) in the (u, v_1) field, for a fixed v_2 . The open circles are fold points of the critical manifold $\mathcal{M} = \mathcal{M}_{a,1} \cup \mathcal{M}_r \cup \mathcal{M}_{a,2}$.

which is desingularized by introducing $\xi(\tau)$ with $\frac{d\xi}{d\tau} = \frac{1}{u^2-1}$, to obtain,

$$\begin{aligned} u_\xi &= -u + \sqrt{2} \cos(v_2), \\ v_{2,\xi} &= u^2 - 1. \end{aligned} \tag{1.30}$$

The desingularized system has equilibria

$$(u, v_2) = \left(1, \pm \frac{\pi}{4} + 2k\pi\right), \quad (u, v_2) = \left(-1, \pm \frac{3\pi}{4} + 2k\pi\right) \quad \text{for } k \in \mathbb{Z}.$$

where $(1, -\frac{\pi}{4} + 2k\pi)$ and $(-1, \frac{3\pi}{4} + 2k\pi)$ are of saddle type, and $(1, \frac{\pi}{4} + 2k\pi)$ and $(-1, -\frac{3\pi}{4} + 2k\pi)$ are foci, see the phase portrait in Figure 1.7.

Changing the direction of the flow for $u < -1$ and $u > 1$ yields the phase portrait of (1.29), where the foci and saddle equilibria turn into folded singularities. Using Fenichel's theorems, we know that \mathcal{M} , as well as its stable and unstable manifolds persist for $\varepsilon \neq 0$, away from the fold lines. Note that if the canard point is a saddle, canard theory implies that a canard solution persists. Hence, there is a canard solution that, for example, $v_2 = -\frac{\pi}{4}$ passes through the canard point from the attracting to the repelling manifold. It then follows the repelling manifold closely for an $\mathcal{O}(1)$ amount of time, before the fast field takes over and sends it to the attracting manifold again. Because v_2 does not change to leading order in the fast behavior, it can even be shown that such a canard solution can be periodic. Projected onto the (u, v_1) -plane, such a solution is depicted in Figure 1.8.

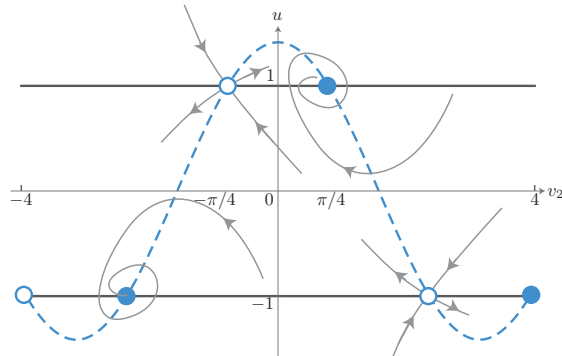


Figure 1.7: Phase portrait of (1.30). The blue closed circles denote foci, while open circles are saddle equilibria. The dashed curve is a nullcline for u , and the horizontals at $u = \pm 1$ are nullclines for v_2 .

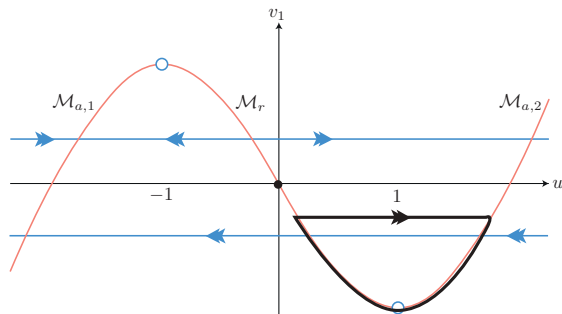


Figure 1.8: Example of a canard solution of (1.26) projected onto the (u, v_1) -plane, which passes through the canard point $(u, v_1, v_2) = (1, -\frac{2}{3}, -\frac{\pi}{4})$.

1.5 Outline of this thesis

This thesis shows an omnibus of studies of singularly perturbed reaction-diffusion systems with applications in various fields. Each system that is studied, requires a different approach using appropriate mathematical tools. Primarily, this is because the corresponding application describes a different type of solution (stationary pulse, traveling front, traveling pulse). Another reason is of a more practical nature; since the singularly perturbed character does not present itself in the same way, not every perturbation technique can be applied effectively. Roughly speaking, the models studied in this thesis have been motivated by three natural phenomena, which we discuss successively.

1.5.1 Blooming phytoplankton

The natural phenomenon that is studied in Chapters 2 and 3 is the blooming of phytoplankton. Among the plankton species, phytoplankton can be distinguished by the feature that it performs photosynthesis; it is a plant in the ocean. It forms the basis of the aquatic food chain and transports enormous amounts of carbon dioxide into the deep ocean and produces oxygen in return. Hence, phytoplankton populations may play a crucial role in understanding climate change, see [47]. Furthermore, field observations describe that phytoplankton colonies always choose a specifically preferred depth in the vertical water column. The two processes that specify this depth are the availability of light and nutrient. If there is an abundance of nutrients, the preferred depth is at the surface of the water column, because it optimizes light, this pattern is called a *surface scum*. If the water column is not very deep and light reaches all the way to the bottom, the phytoplankton prefers to sit at the bottom because of the best availability of nutrients, this state is a *benthic layer*. However, if the water column is very deep and nutrients are limited as well, phytoplankton optimizes its location somewhere in between and we label this a *deep chlorophyll maximum*, [79, 89]. This localized structure, as well as the observation in [78] that deep chlorophyll maxima often oscillate and may even exhibit chaotic behavior, were the inspiration for mathematicians to work on the subject.

Central to Chapters 2 and 3 is a model that consists of two differential equations for the concentration of phytoplankton and its nutrients, respectively. Before the establishment of those chapters, the mathematical framework was laid out in [176] and [177]. In [177], the linear stability of the so-called background state, where there is no phytoplankton and a constant nutrient concentration is studied. The spectrum of the linearized differential operator separates into two sets: one with eigenvalues λ_i (ordered so that $\lambda_i \leq \lambda_{i+1}$) which are $\mathcal{O}(\varepsilon^{1/3})$ apart and depend on parameters, and one with eigenvalues μ_i which are $\mathcal{O}(\varepsilon)$

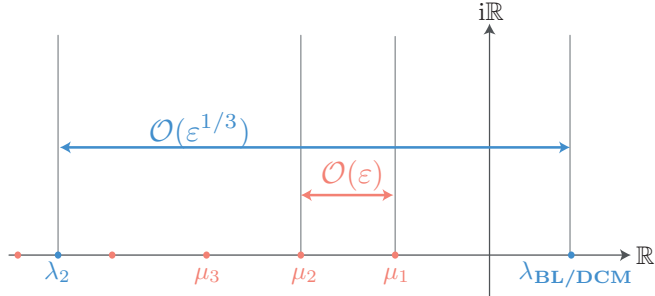


Figure 1.9: Schematic illustration of the spectrum of the background state of the phytoplankton model discussed in Chapters 2 and 3. Depending on parameters, the largest eigenvalue may change type.

interspaced, do not depend on parameters and are always negative. Furthermore, depending on the sinking velocity of the phytoplankton, the largest eigenvalue λ_1 may be either λ_{BL} or λ_{DCM} . That is, depending on that parameter, the primary bifurcation that the backgrounds state can undergo implies either the formation of a benthic layer, or that of a deep chlorophyll maximum, see Figure 1.9 for a illustration. This result is established by approximating the eigenfunctions corresponding to these eigenvalues using the WKB-method, see Section 1.3.

The bifurcation analysis in [177] provides analytic results for the primary (transcritical) bifurcations of the background state. Numerical analysis reported in the same article shows that, in the parameter regime where a DCM bifurcates, there is a secondary bifurcation of Hopf type. That implies that after the emergence of a DCM profile, it starts to oscillate in time. The two bifurcations occur in a $\mathcal{O}(\varepsilon)$ regime in parameter space, see Figure 1.10.

The Hopf bifurcation of the DCMs is studied analytically in [176]. By Fourier decomposing the linear stability problem of the background state into eigenfunctions, the primary, transcritical bifurcation is recovered using center manifold reduction, see Section 1.2. In principle, the local invariance of the center manifold is no longer guaranteed when λ_{DCM} is commensurate with the other eigenvalues μ_i . However, using a novel asymptotic approach and by studying the amplitude equations of the bifurcating profile, the center manifold reduction is extended beyond the spectral gap regime. Then, for $\lambda_{DCM} = \mathcal{O}(\varepsilon)$, the Hopf bifurcation of the DCM profile is found analytically using, among other tools, Laplace's method, see Section 1.1.

In Chapter 2, this method of extending the validity of center manifold reduction is unfolded. We do this using a dummy model that is in some sense

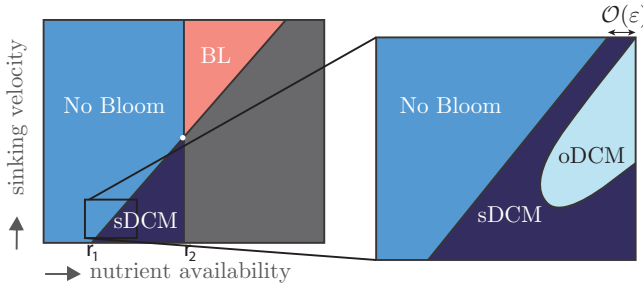


Figure 1.10: Schematic illustration of the bifurcations of the background state of the phytoplankton model discussed in Chapters 2 and 3, depending on the parameters that model nutrient availability and sinking velocity of the phytoplankton. The full model is discussed in Chapters 2 and 3. In the regime 'No Bloom', the background state is stable, the BL regime indicates the emergence of a benthic layer, and sDCM the emergence of stationary deep chlorophyll maxima. Lastly, oDCM is the regime where the DCM has undergone a Hopf bifurcation and oscillates consequently.

more general than the phytoplankton model because the reaction terms are general functions. On the other hand it is also simpler because particular intricacies of the phytoplankton model were not taken into account in order to declutter the presentation of the method. In that chapter we also aptly term this novel method *extended center manifold reduction* (ECMR). Indeed, in the dummy model we recover the classical center manifold reduction that indicates a transcritical bifurcation, as well as requirements for a secondary Hopf bifurcation. Furthermore, to exemplify the strength of ECMR, we apply the method to several other models and study the fate of codimension 2 bifurcations and even find low-dimensional chaos that is described by the extended center manifold reduction. The potential of ECMR is further substantiated by the fact that the low-dimensional chaos in the extended reduction persists in the full PDE model. Chapter 2 was published in full *Physica D* in 2015, see [139].

In Chapter 3 we return to the phytoplankton model and apply ECMR to the regime where a benthic layer emerges from the background state. The clean unfolding of the mechanism in Chapter 2 makes the application of it much more transparent compared to the pioneering article [176]. Chapter 3 reproduces briefly the result that a DCM can undergo a Hopf bifurcation, but also shows in more detail that, conversely, a benthic layer remains stable in the validity regime of ECMR. Because the phytoplankton model is quite detailed, the asymptotic analysis is challenging. Here too, the WKB and Laplace's method are applied.

Chapter 3 was published in full *Chaos* in 2015, see [41].

1.5.2 Spreading of malignant tumor

In ecology, a phenomenon called the *Allee effect* describes a threshold in the growth of a population. The causes of such an effect are numerous. For example, in small populations the gene pool may not be large enough for effective reproduction or finding a mate may be nearly impossible. This Allee effect has been observed in many applications, and recently, evidence has been gathered that in tumor growth this effect plays a role too. Intuitively, this can be motivated by the mere fact that small tumors are expected to be less threatening, but a more extensive literature overview related to the Allee effect in tumor spread can be found in the introduction of Chapter 4.

In modeling tumor spread, we focus on how it invades into its healthy surroundings. In the viewpoint of Chapter 4 it does so via haptotaxis or chemotaxis through the extracellular matrix. That is, the movement of the tumor is in the direction of the gradient of its healthy surrounding. As a simplified representation of the situation, we assume that the focus on a one-dimensional spatial domain is sufficient. This could be attained, for example, for tumors in two-dimension with a certain geometric symmetry that reduces the dimension. Mathematically, an invading tumor corresponds to a traveling front; a fixed spatial profile on an infinitely long, one-dimensional domain with different boundary conditions on both sides, moving with a constant speed. Since the type of tumors considered in Chapter 4, such as melanoma, have a very sharp edge [108], the transition from the left to the right boundary condition should be steep.

Although there are many ways to model the mechanism responsible for the growth of tumors, we study the consequences of incorporating the Allee effect in a model that was proposed in [125] and later adjusted and analysed in [67]. The former is a reaction-advection system and the latter also incorporates diffusion in the two components corresponding to tumor cell density and extracellular matrix. Both models assume that the growth of tumor cells is logistic; the growth term is quadratic so that the growth rate increases until the population gets close to the carrying capacity of the system. After that, the growth rate decreases but the growth term is still positive. For w being tumor cells, this logistic growth term can be presented by $f(w) = w(1 - w)$, if the carrying capacity is scaled to 1. A growth threshold following from the Allee effect is modeled in the system by substituting the quadratic term by a cubic one, $f(w) = w(1 - w)(w - \alpha)$, where α is the strength of the Allee effect.

In [67], the reaction-diffusion-advection tumor model is shown to exhibit four types of traveling wave solutions of which three exhibit a shock. This shock is a very steep transition – the edge of a tumor – and is explained by a canard

solution that is repelled from the repelling branch of a folded slow manifold and touched back upon the attracting branch of that manifold. One of these types of solutions has semi-compact support; on one side of the shock the tumor density is equal to zero, not only exponentially decaying to it. This type of solution is considered the most realistic because it models a sharply defined edge of a tumor. However, three out of four types of traveling wave solutions are deemed stable in [67] because they were observed numerically.

The effect of using an Allee threshold in the tumor growth term is two-fold. Following the methods used in [67], we first prove that only the shock solution with semi-compact support can exist, making the Allee model studied in Chapter 4 already preferable over the logistic growth model. Second, another agreement with experimental observations is found. This observation relates the invasion speed of a tumor to the collagen (the dominant ingredient in the extracellular matrix) density, i.e. the background state of the extracellular matrix. The results show that this relationship is *biphasic*, i.e. not monotonic but with a well-defined maximum. This biphasic relationship is also supported by the Allee model, while not being a feature of the logistic growth model.

The mathematical analysis in Chapter 4 relies heavily on geometric singular perturbation theory and canard theory, as briefly explained in Section 1.4. Chapter 4 was published in full in *Journal of Theoretical Biology* in 2016, see [140].

1.5.3 Traveling vegetation stripes

The last natural phenomenon to which reaction-diffusion models are applied in this thesis sets place in semi-arid regions of the earth. In times that the desert is expanding and this phenomenon is addressed as one of by-products of climate change, these half-barren transition regions are important focus points. Indeed, examples of these types of studies are abundant in literature, not in the least place in the applied mathematical journals.

The transition of vegetated areas into bare soil, *desertification*, occurs in several stages in which the vegetation displays itself in strikingly regular patterns of labyrinth, spotted, or striped character [106]. In the absence of grazing and on gentle slopes, it is mostly striped patterns which are observed, and due to the surplus of water uphill, they slowly migrate upwards. This subphenomenon of desertification is the focal point of Chapter 5.

The model that we use to analyze these patterns is of reaction-diffusion-advection type and models the interaction of water and vegetation density on sloped terrains. It resembles two predecessors; the Klausmeier model [88] and the Gray-Scott model [62], but incorporates the dominant pattern forming mechanisms of both. Our model is defined on a two-dimensional surface – the soil,

but since stripes are trivial in one direction, proving the existence of such solutions is essentially one-dimensional. The type of solution that corresponds to stripe patterns is in the non-trivial spatial direction a periodic repetition of localized pulses, traveling with a constant speed. For the Gray-Scott model, existence and stability of periodic isolated pulses was already studied in [34, 39, 36], and most of the techniques used in Chapter 5 are adapted from those articles. However, a big difference with the Gray-Scott model is the occurrence of an advection term (induced by the slope) in our model. Contrary to the Gray-Scott model, the system studied in Chapter 5 therefore does not possess a reversibility symmetry, on which the proofs in the cited articles rely heavily.

Another motivation to study specifically these types of patterns, is the numerical analysis done in [143], which shows that the stability regime of two-dimensional stripe patterns increases with the slope of the terrain. This indicates that for large enough slopes, the stripe patterns that are solutions to our model could indeed be observed in the field.

Relying on Fenichel's theorems, we first construct a single traveling, localized pulse in an infinite domain; a homoclinic traveling wave as solution of the system. This is later extended to periodic patterns with a long wavelength; the periodic extension of localized pulses. Since the validity of GSPT depends on the scale splitting of a system, a scale analysis of the model is essential and corresponds directly to the fact that the periodic patterns we construct necessarily have a long wave length. To prove the existence of periodic patterns, we cannot carry over the methods used on the Gray-Scott model, because of a lack of symmetry. Hence, a novel approach using a contraction mapping argument is used to guarantee existence of such a periodic pattern.

Lastly, the stability of both those types of traveling wave solutions to the vegetation model is analyzed using an Evans function approach as presented in [35]. Due to the scale separation of the system, the Evans function factorizes in a slow and a fast part, too. The slow component is solved using hypergeometric functions, and a full overview of the stability of periodic patterns is given. The main result is that, despite the numerical results in [143], all the constructed patterns are unstable in a two-dimensional sense. That is, perturbations in the transverse direction destabilize the striped pattern. There are several explanations for this given in the discussion of Chapter 5. Considering only one-dimensional patterns (thereby neglecting the assumed trivial extension in the other direction), there are several destabilization mechanisms possible depending on the parameters. More importantly: there are parameter regimes for which the one-dimensional patterns are stable. Although one dimension is not representing the initial application of the system, vegetation patterns, this is a valuable result in a more abstract sense.

2

Extended center manifold reduction¹

2.1 Introduction

The analysis of pattern formation in evolutionary partial differential equations is directly linked to dynamical systems bifurcation theory. At the onset of patterns, a ‘*trivial state*’ becomes spectrally unstable as a control or bifurcation parameter, R , passes through a critical value $R_{c,1}$. Typically, a ‘*small amplitude pattern*’ bifurcates from this state. When the evolution equation is defined on a bounded domain Ω and the associated spectrum consists of discrete eigenvalues, the very first step in the onset of pattern formation can be studied by a center manifold reduction (CMR). For values of R sufficiently close to $R_{c,1}$, the dynamics of the full infinite-dimensional system can be reduced to the dynamics on an exponentially attracting low-dimensional center manifold. This is due to the existence of a spectral gap between the first eigenvalue(s) crossing the imaginary axis and all other, stable eigenvalues. The presence of this gap makes the analysis of the onset of pattern formation completely equivalent to the study of bifurcations in finite-dimensional dynamical systems (for instance, [9, 18, 160]). Indeed, the small amplitude patterns that originate in this mechanism relate, in general, directly to the standard codimension 1 bifurcations (saddle-node, transcritical, pitchfork and Hopf): the associated center manifolds are one- or two-dimensional.

The center manifold reduction is only valid for R ‘*sufficiently close*’ to the – first – critical value $R_{c,1}$, so that the spectral gap is sufficiently wide. However, in perhaps all examples of pattern forming systems, the pattern originating at $R_{c,1}$ undergoes a next bifurcation at some value $R_{c,2}$ of R et cetera. In other

¹The content of this chapter was published as *Tracking pattern evolution through extended center manifold reduction and singular perturbations* in Physica D. in 2015, see [139].

words, the first bifurcation at onset is followed by a secondary one at $R_{c,2}$. Since this latter concerns the bifurcating pattern and not the trivial state it bifurcated from, it cannot be directly studied through the spectral decomposition for that state. Instead, one now needs stability properties of the pattern bifurcating at $R_{c,1}$. Generally speaking, this is an impossible task – especially for analytical studies of pattern evolution. To overcome that obstacle, formal and/or numerical methods have been developed that are based on spectral properties –eigenvalues and eigenfunctions – associated with the original, trivial background state.

Such secondary, tertiary, et cetera bifurcations cannot be described by CMR, simply because they do not occur in the reduced (center manifold) flow; they take place for values of R violating the spectral gap condition. This is often observed in an explicit setting: the distance between the first, now unstable, eigenvalue and the imaginary axis becomes proportional to that between the next largest eigenvalue(s) and the same axis – note carefully that none of these next eigenvalues needs to actually destabilize for the secondary bifurcation to occur. In the terminology of applied mathematics and/or physics: one *must* account for the evolution of ‘*modes*’ associated with these next eigenvalues and eigenfunctions, as these modes can no longer be ‘*slaved*’ to the one that was first destabilized and that parametrizes the center manifold. In principle, then, studying the full flow through the spectral properties of the trivial state is possible, provided that one extends CMR to a higher-dimensional system by a Galerkin approach. In general, however, there is no ‘*next*’ spectral gap in that extended spectral problem: *all* next eigenvalues are typically commensurable. Accordingly, there is no telling a priori *how many* modes must be accounted for in this extended center manifold Galerkin reduction – certainly not from the analytic point of view. See, for instance, [128] and references therein for a practical study centering on these issues.

Presently, we develop analytical (and asymptotic) extensions of classical CMR. We describe the onset of pattern formation by means of low-dimensional systems governing the dynamics of the full evolutionary system for parameter values violating the spectral gap condition. We term the process by which we derive such simplified systems *extended center manifold reduction (ECMR)*. Our most generic results concern the extension of the one-dimensional CMR associated with a transcritical bifurcation to an explicit two-dimensional flow on an exponentially attracting two-dimensional (local) manifold. We also present explicit classes of systems with codimension 1 bifurcations where this extended center manifold is three- or four-dimensional.

An earlier version of this method was developed in the context of a specific model problem, which concerned the emergence and evolution of localized spatio-temporal patterns in a non-local, coupled, phytoplankton-nutrient model in an oceanic setting,

$$\begin{aligned}\omega_t &= \varepsilon \omega_{xx} - 2\sqrt{\varepsilon} v \omega_x + (p(\omega, \eta, x) - \ell)\omega, \\ \eta_t &= \varepsilon [\eta_{xx} + \ell^{-1} p(\omega, \eta, x)\omega];\end{aligned}\tag{2.1}$$

this is a scaled version of the original model proposed in [78] as well as the focus of chapter 3. In (2.1), $\omega(x, t)$ and $\eta(x, t)$ denote a phytoplankton and a (translated) nutrient concentration; $x \in (0, 1)$ measures ocean depth. The growth of the phytoplankton population is delimited by nutrient and light availability; since light is attenuated with depth and absorbed by phytoplankton, the term $p(\omega, \eta, x)$ is non-local in ω and depends explicitly on depth x . For more details on this model and its boundary conditions (BCs), see [78, 176, 177]. In realistic settings, $\varepsilon \approx 10^{-5}$ while all other parameters – v, ℓ and those entering $p(\omega, \eta, x)$ – can be considered $\mathcal{O}(1)$ with respect to ε [177]. Therefore, (2.1) is studied in [176, 177] as a *singularly perturbed* system. The spectral problem associated with the stability of the trivial state $(\omega(x, t), \eta(x, t)) \equiv (0, 0)$ – no phytoplankton, maximal and constant nutrient concentration – has two distinct sets of (real) eigenvalues: $\mu_m = \mathcal{O}(\varepsilon)$, $m \geq 1$, and $\lambda_n = \lambda_* + \tilde{\lambda}_n$, with $\tilde{\lambda}_n = \mathcal{O}(\varepsilon^{\frac{1}{3}})$ and $n \geq 1$; λ_* can be ‘controlled’ by varying the parameters in (2.1), while $\mu_m < 0$ are parameter-independent and negative. In [177], it is shown through an asymptotic spectral analysis that the trivial state is destabilized by a transcritical bifurcation, at which λ_1 crosses zero. The associated eigenfunction has the strongly localized nature of a (stationary) *deep chlorophyll maximum* (DCM), the pattern playing a central role in the simulations and oceanic observations in [78].

In our terminology above, emergence of the deep chlorophyll maximum represents the onset of pattern formation, and it occurs as the product of the first bifurcation. For the parameter values considered in [78], the deep chlorophyll maximum only exists (as a stable, stationary pattern) in an asymptotically narrow strip of parameter space: the primary bifurcation is almost directly followed by a secondary Hopf bifurcation through which emerges an oscillating DCM [176, 177]. In fact, stationary deep chlorophyll maxima were not even recorded in the numerical simulations of [78] – the bifurcation scenario drawn there starts directly with the oscillating DCM and proceeds with period-doubling cascades and spatio-temporal chaos. In other parameter regimes, not a deep chlorophyll maximum, but a *benthic layer* – a localized maximum at ocean’s bottom – marks pattern formation. Numerical simulations have not indicated a secondary bifurcation of the pattern in this regime. In Chapter 3, we analytically substantiate this phenomenon using the framework described in this chapter.

The predictions in [177] on the transcritical nature of trivial state destabilization were validated in [176], as a first step, by restricting analysis to the regime $0 < \lambda_1 = \mathcal{O}(\varepsilon^\sigma)$ with $\sigma > 1$. In that case, there is a spectral gap driven by the proximity of that primary eigenvalue to the imaginary axis, $\lambda_1 \ll \min_{m \geq 1, n \geq 2} \{|\mu_m|, |\lambda_n|\} = \mathcal{O}(\varepsilon)$; the dynamics of system (2.1) can be reduced to a single amplitude ODE describing the transcritical bifurcation. As $\sigma \downarrow 1$ and λ_1 becomes $\mathcal{O}(\varepsilon)$ like the μ_m 's, the spectral gap breaks down; modes associated with *all* (linearly stable!) μ_m -eigenvalues must now be taken into account. As a consequence, the one-dimensional CMR is expanded dramatically into an a priori infinite-dimensional system. Analysis of that model is nevertheless possible and establishes the existence of a secondary Hopf bifurcation in (2.1), $\mathcal{O}(\varepsilon)$ -close to the primary, transcritical one [176]. The existence of oscillating deep chlorophyll maxima follows. In the present chapter, we show that this surprising fact – that a secondary bifurcation becomes amenable to analysis by extending CMR beyond its classical region of validity – is not due to model specifics but intrinsically tied to the nature of the spectrum associated with the trivial background state. In general, our approach may be developed in the context of systems of the form

$$\frac{\partial}{\partial t} \begin{pmatrix} U \\ V \end{pmatrix} = \begin{pmatrix} \mathcal{L} & 0 \\ \varepsilon \mathcal{K} & \varepsilon \mathcal{M} \end{pmatrix} \begin{pmatrix} U \\ V \end{pmatrix} + \begin{pmatrix} F(U, V; x) \\ \varepsilon G(U, V; x) \end{pmatrix}, \quad (2.2)$$

for a ‘fast’, unknown $U : \Omega \times \mathbb{R}_+ \rightarrow \mathbb{R}^{m_U}$ and a ‘slow’ $V : \Omega \times \mathbb{R}_+ \rightarrow \mathbb{R}^{m_V}$, with $m_U, m_V \geq 1$. The bounded spatial domain $\Omega \subset \mathbb{R}^n$ has a piecewise C^1 boundary $\partial\Omega$. The operators \mathcal{K}, \mathcal{L} and \mathcal{M} are assumed linear, spatial, differential operators and boundary conditions guaranteeing well-posedness must apply. Several specific assumptions on the spectrum of \mathcal{L} and \mathcal{M} and the nonlinearities $F(U, V; x)$ and $G(U, V; x)$ must hold, we refer to Chapter 3 for more details. The aim of this chapter is to present an investigation into the possible impact of the extended center manifold reduction approach. Therefore, we will mainly restrict our analysis to a strongly simplified version of (2.2), i.e. to models of the type

$$\begin{cases} U_t = \mathcal{L}U + \alpha U + F(U, V), \\ V_t = \varepsilon [\mathcal{L}V + \beta U + \gamma V + G(U, V)], \end{cases} \quad (2.3)$$

thus $\mathcal{K} = \beta$, and with a slight abuse of notation, $\mathcal{M} = \mathcal{L} + \gamma$ and the operator \mathcal{L} in (2.2) will be replaced by $\mathcal{L} + \alpha$. The linear differential operator \mathcal{L} in (2.3) – independent of ε – acts on $L^2(\Omega)$, contains spatial derivatives only and is assumed self-adjoint with respect to given boundary conditions. We mostly restrict ourselves to the scalar case $m_U = m_V = 1$. In Section 2.6, however, we will treat an example where $m_U = 2$. By assuming that $0 < \varepsilon \ll 1$ is

asymptotically small, system (2.3) becomes singularly perturbed; the parameters $\alpha, \beta, \gamma \in \mathbb{R}$ are assumed $\mathcal{O}(1)$ with respect to ε . The functions $F(U, V)$ and $G(U, V)$ are assumed sufficiently smooth and at least quadratic in U and V . The Laplace operator Δ subject to Dirichlet boundary conditions is a natural choice for \mathcal{L} , with (2.3) then becoming a reaction-diffusion system. This choice is considered in Sections 2.2.2, 2.4.2, 2.5.2, 2.6.2 to add concreteness to our discussion, but it is not the sole focus of the present work: precise assumptions on \mathcal{L} and Ω are given in Section 2.2.

One may see the simplified model (2.3) as stripping the explicit phytoplankton model (2.1) of its non-locality, heterogeneity and various other intricacies not central to our stated aim. It is for that reason that (2.1) does not precisely fit the framework (2.3). However, it does fit (2.2), and we elaborate further on this in Chapter 3. The main property carried over from (2.1) to (2.3), and also crucial to (2.2), is a decomposition of the (real) eigenvalues in the spectral problem determining stability of the trivial state $(U, V) \equiv (0, 0)$ into distinct, ordered, ‘small’ and ‘large’ sets

$$\mu_k = \mathcal{O}(\varepsilon), \quad \text{and} \quad \lambda_k = \mathcal{O}(1), \quad k \geq 1; \quad (2.4)$$

cf. Section 2.2 and Figure 2.1. It should be noted here that, strictly speaking, only asymptotically many μ_k ’s and λ_k ’s are $\mathcal{O}(\varepsilon)$ and $\mathcal{O}(1)$, respectively, as both sequences diverge to $-\infty$. Similarly to [176], we focus on the destabilization of $(0, 0)$ by the ‘*most unstable*’ large eigenvalue λ_1 , assuming that all other eigenvalues remain in the left half of the complex plane. As in (2.1), destabilization of $(0, 0)$ at $\lambda_1 = 0$ in general occurs through a transcritical bifurcation. This is evident through a standard center manifold reduction, yet we consciously employ a slightly different, equivalent approach as a means of setting the stage for sections 2.4.1 and 2.4.2; see Section 2.3.2 for details.

For our abstract model, 2.3, center manifold reduction remains valid while $\sigma > 1$ just as for (2.1); it breaks down at $\sigma = 1$, see Figure 2.1. Recall also our discussion above on the commensurability of λ_1 and μ_1, μ_2, \dots , where we also briefly mentioned an extension of the one-dimensional center manifold reduction to an infinite-dimensional Fourier system. A Fourier decomposition links every eigenvalue λ_i and μ_i to a corresponding eigenfunction with amplitudes $a_i(t)$ and $b_i(t)$, respectively. Concretely, this means that the ODE governing the evolution in (scaled) time τ of the (scaled) amplitude $a_1(\tau)$ of the λ_1 -eigenmode must, now, be combined with ODEs for $b_k(\tau)$, $k \geq 1$ – the (scaled) amplitudes of the μ_k -eigenmodes. One of the main results in this paper is the identification at leading order in ε of a two-dimensional, exponentially attracting, invariant submanifold for this infinite-dimensional system. Thus, also for $\sigma = 1$, the dynamics of small, $\mathcal{O}(\varepsilon)$ solutions of (2.3) is contained in a low-dimensional manifold.

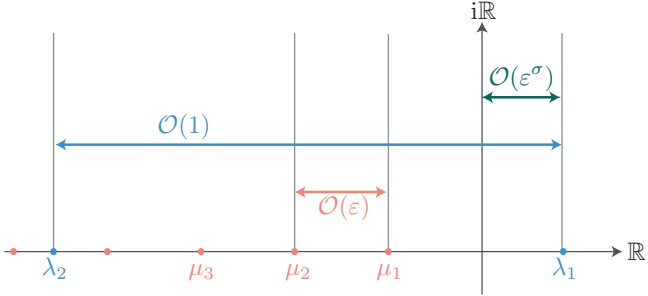


Figure 2.1: Schematic representation of the eigenvalues that determine the stability of $(U, V) = (0, 0)$. The eigenvalues break up into two separate sets. One set of infinitely many $\mathcal{O}(1)$ -interspaced eigenvalues, λ_k , and one set of infinitely many $\mathcal{O}(\varepsilon)$ -interspaced eigenvalues, μ_k . Here, the parameter values are such that all μ_k are negative, while the first $\mathcal{O}(1)$ eigenvalue crossed into the right half-plane but remains small, $\mathcal{O}(\varepsilon^\sigma)$ with $\sigma > 0$.

However, in contrast to the region of classical CMR validity, the dimension of that manifold is 2. As we will see, this increase in the dimensionality of the reduced flow lies at the heart of complex phenomena exhibited by the dynamics of small amplitude solutions of (2.3). The invariant manifold is parametrized by the modes (a_1, b_1) and the flow on it is explicitly deducible. A straightforward analysis reveals that the original pattern bifurcating at onset generically undergoes a Hopf bifurcation, provided that equation coefficients satisfy an explicit sign condition. It follows that the primary transcritical bifurcation is generically succeeded within an $\mathcal{O}(\varepsilon)$ distance by a Hopf bifurcation, exactly as in the phytoplankton model. The sub-/supercritical nature of this bifurcation can also be determined. We finally show that, in such an event, the bifurcating oscillatory pattern necessarily terminates as the control parameter moves further away from both bifurcations (transcritical and Hopf), leaving the attracting two-dimensional manifold unable to sustain bounded behavior. Note that this entire sequence plays out ε -close to the primary bifurcation in parameter space. In that manner, our analysis provides an explicit bound on the region in parameter space where small-amplitude center manifold may be extended: outside it, solutions to the full problem (2.3) can no longer remain small. This is in stark contrast to standard CMR, which cannot provide such an explicit bound.

In the phytoplankton-nutrient model (2.1), the first two bifurcations are only the first steps in a sequence of events leading to low-dimensional spatio-temporal chaos [78]. We investigate the possibility of similar behavior in singularly perturbed systems like (2.3) in the second half of the present chapter. Our results

so far indicate that, near the primary bifurcation, small pattern dynamics are inherently two-dimensional and hence cannot exhibit such phenomena. Even worse, Hopf destabilization of the primary pattern – the second step in the chaotic scenario of (2.1) – is followed by unbounded dynamics: if more complex dynamics is present, it does not play out on the extended center manifold. In contrast, the dimensionality of the long-term dynamics in (2.1) is less clear-cut, and the Hopf destabilization was deduced from a high-dimensional reduced system. Additionally, it was speculated in [176] already that a codimension 2 transcritical bifurcation in (2.1) may be the organizing center of its spatio-temporal chaotic dynamics. Inspired by these observations, we move on from the most simple case of (2.3) and consider two types of systems: first, one with amplified nonlinearities; and second, one where the primary bifurcation is of codimension 2; see sections 2.5–2.6 for the details.

To motivate the first direction, we ascertain that it is the *linear* structure of (2.3) that enables our approach – not the particular form of the nonlinearities. Hence, the introduction of an $\mathcal{O}(1)$ nonlinearity in the PDE for V should not hinder application of our method, and we consider (2.3) with $\varepsilon G(U, V)$ is replaced by an $\mathcal{O}(1)$ nonlinearity $G(U, V)$; see especially system (2.52). This leaves the linear structure unaltered but affects the dimensionality of the reduction strongly. The extended invariant manifold is no longer two-dimensional; in fact, asymptotically many b_k -modes – related to the ‘small’ spectrum $\{\mu_k\}_{k \geq 1}$ – are excited and must be included in the reduced system, resembling the situation in (2.1). As an exploratory example, we consider $G(U, V) = G_{20}U^2$ and ‘tune’ G_{20} by having it depend on x , see Section 2.5.2. In that way, we construct (at leading order in ε) an attracting, linear, five-dimensional, extended center manifold and describe the flow on it by means of the quintuplet $(a_1, b_1, b_2, b_3, b_4)$. Here a_1 and b_i , $i = 1 \dots 4$ are the (rescaled) amplitudes associated with λ_1 and μ_i , respectively. The most unstable mode – which, local to onset, is spanned by a_1 – successfully undergoes a Hopf bifurcation. Depending on parameter values, this Hopf bifurcation can be followed by a sequence of period-doublings resulting in chaotic behavior; exactly like in (2.1). This last result is established numerically, with direct PDE simulations within the chaotic regime revealing a low-dimensional spatio-temporal attractor strikingly similar to the one capturing trajectories of the five-dimensional reduced flow; see Figure 2.9. We conclude that the ECMR accurately describes the dynamics of small amplitude solutions to (2.52), even when this is complex.

Regarding the second direction, we note that the codimension 2 transcritical bifurcation in (2.1) arises as the merging of two transcritical bifurcations generating different localized patterns – a DCM and a *benthic layer* (BL).

We emulate this situation here by tuning the two-component model (2.3) so that the two largest $\mathcal{O}(1)$ eigenvalues, λ_1 and λ_2 , coincide at the origin and the corresponding eigenfunctions are distinct – i.e., the system is *not* in the most general case where one needs to introduce a generalized eigenfunction. Extending the standard center manifold to the ‘gapless’ situation in which $\lambda_1, \lambda_2, \mu_k = \mathcal{O}(\varepsilon)$, we obtain a leading order, attracting, four-dimensional, extended center manifold parametrized by (a_1, a_2, b_1, b_2) – the rescaled amplitudes of modes related to $\lambda_1, \lambda_2, \mu_1$ and μ_2 , respectively – and the flow on that extended center manifold. See also (2.71) and its rich behavior we analyze in Section 2.6. Note, however, that $\mathcal{L} = \Delta$ does not admit a double zero eigenvalue, but examples of (polyharmonic) operators satisfying both conditions are available; see [54] for these facts. Since our prior discussion is rooted in reaction-diffusion systems, we consider in parallel a three-component, reaction-diffusion system of the form (2.3) that admits a double zero eigenvalue. We keep our model as simple as possible, creating a codimension 2 bifurcation by introducing a *vectorial ‘fast’ component* U ,

$$\begin{cases} \partial_t U_1 = D_1 \mathcal{L} U_1 + \alpha_1 U_1 + F_1(U_1, U_2, V), \\ \partial_t U_2 = D_2 \mathcal{L} U_2 + \alpha_2 U_2 + \varepsilon \rho_2 V + F_2(U_1, U_2, V), \\ \partial_t V = \varepsilon [\mathcal{L} V + \beta_1 U_1 + \beta_2 U_2 + \gamma V + G(U_1, U_2, V)]; \end{cases} \quad (2.5)$$

see Section 2.6.2 for more details on this model and its boundary conditions. There exist two sets of large, $\mathcal{O}(1)$ eigenvalues, $\lambda_{1,k}$ and $\lambda_{2,k}$ ($k \geq 1$), where $\lambda_{1,k}$ relates to the linear spectrum of the first equation of (2.5), and $\lambda_{2,k}$ relates to the linear spectrum of the second equation of (2.5). The codimension 2 bifurcation corresponds to the regime $\lambda_{1,1} \approx \lambda_{2,1} \approx 0$. Extending the center manifold, to incorporate the regime where $\lambda_{1,1}, \lambda_{2,1}$ and asymptotically many μ_k ’s are $\mathcal{O}(\varepsilon)$ yields an attracting three-dimensional manifold parametrized by $(a_{1,1}, a_{2,1}, b_1)$. The (rescaled) amplitudes $a_{1,1}(t), a_{2,1}(t)$ and $b_1(t)$ are associated with the eigenvalues $\lambda_{1,1}, \lambda_{2,1}$ and μ_1 , respectively and denote the amplification in the corresponding modes of a Fourier-like decomposition, see (2.74). The flow on it is generated by a rather general quadratic vector field – see (2.85) – containing the celebrated Lorenz system [104] as a special case. A simulation of the full PDE system (2.5) motivated by the classical parameter settings in [104] directly captures the Lorenz attractor; see Figure 2.2. We stress, however, an essential difference between the role of the Lorenz equations relative to the global dynamics here and in [104]. According to our theory, the Lorenz attractor is a global attractor for the (small amplitude) flow induced by the full model (2.5); numerical simulations confirm this, see Figure 2.2. Instead, the same attractor does not attract trajectories of the original convection model in [104], although the Lorenz equations are derived from it through a Galerkin-type reduction – [147], for instance, discusses the differentiating influence of higher-order Galerkin

modes. Small amplitude derivations of the Lorenz system (e.g., [56]) only concern solutions with special characteristics, and thus they also do not result in a three-dimensional flow approximating the full, infinite-dimensional one.

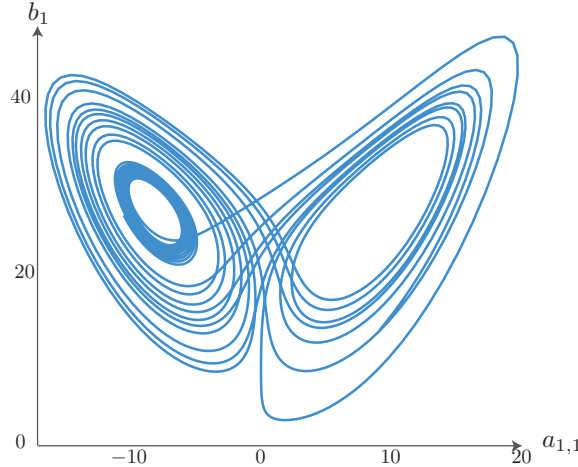


Figure 2.2: Simulation of system (2.5) using MATLAB's PDEPE function with $\mathcal{L} = \Delta$, $\Omega = (0, 1)$ and Dirichlet BCs. Here, $\varepsilon = 0.01$, $D_1 = D_2 = 1$, $\alpha_1 = \pi^2 - 8\varepsilon/3$, $\alpha_2 = \pi^2 - \varepsilon$, $\beta_1 = 0$, $\beta_2 = 10$, $\gamma = \pi^2 - 10$ and $\rho_2 = 28$. The nonlinearities are $F_1(U, V) = (3\sqrt{2}\pi/16)U_2V$, $F_2(U, V) = -(3\sqrt{2}\pi/16)U_1V$ and $G(U, V) = U_1^2$. Plotted are the rescaled amplitudes $a_{1,1}(t)$ and $b_1(t)$, (see (2.74)), of the full solution $(U_1(x, t), U_2(x, t), V(x, t))$ of system (2.5).

As already mentioned at various places in this Introduction, the analysis presented in this chapter is exploratory and formal. Theorems and propositions are provided with proofs, while claims and conjectures are not. We conclude the chapter with a brief discussion of future plans, including rooting this analysis on a rigorous foundation, and of the relevance of our study for phenomena reported in the (mostly reaction-diffusion oriented) literature.

2.2 Spectral analysis of the trivial state

The key to analyzing (2.3) is explicit control over the spectrum and associated eigenfunctions of the linearization around the background state $(U, V) = (0, 0)$. In this section, we formulate the properties that this spectrum must have to enable our analysis; these effectively formalize Figure 2.1. Then, to illustrate these

properties, we introduce a reaction-diffusion example in Section 2.2.2, working out its spectrum methodically.

2.2.1 Linear stability

We write the PDE system (2.3) in matrix form, separating the linear and nonlinear parts,

$$\begin{aligned} \begin{pmatrix} U \\ V \end{pmatrix}_t &= \begin{pmatrix} \mathcal{L} + \alpha & 0 \\ \varepsilon\beta & \varepsilon(\mathcal{L} + \gamma) \end{pmatrix} \begin{pmatrix} U \\ V \end{pmatrix} + \begin{pmatrix} F(U, V) \\ \varepsilon G(U, V) \end{pmatrix} \\ &= \mathcal{DT} \begin{pmatrix} U \\ V \end{pmatrix} + \mathcal{N}(U, V). \end{aligned} \quad (2.6)$$

The linear stability of solution $(0, 0)$ is governed by the spectral problem associated with \mathcal{DT} ,

$$\Lambda u = \mathcal{L}u + \alpha u, \quad (2.7a)$$

$$\Lambda v = \varepsilon \mathcal{L}v + \varepsilon \beta u + \varepsilon \gamma v. \quad (2.7b)$$

Next, we impose boundary conditions and formulate necessary conditions on the operator $\mathcal{L} : H \rightarrow H$ acting on an appropriate Hilbert space H equipped with the standard L^2 -inner product. Consider the scalar spectral problem of \mathcal{L} ,

$$\mathcal{L}\phi(x) = \nu\phi(x), \quad (2.8)$$

where ν is an eigenvalue and $\phi \in H$ is a scalar eigenfunction, i.e. $\phi(x) \in \mathbb{R}$, satisfying boundary conditions adapted from (2.6). We recall that \mathcal{L} does not depend on ε and assume:

A1 \mathcal{L} is self-adjoint.

A2 The solutions of (2.8) (eigenvalues of \mathcal{L}) are ordered with a maximal element,

$$\dots \leq \nu_3 \leq \nu_2 \leq \nu_1 < \infty. \quad (2.9)$$

A3 The invariant subspace associated with any eigenvalue ν_k is one-dimensional.

Moreover, we assume that the boundary conditions are the same for U and V on $\partial\Omega$.

In Section 2.2.2, we will introduce an explicit example system with $\mathcal{L} = \Delta$ and $H = H_0^1(0, 1)$, the Sobolev space of compactly supported, weakly differentiable

functions. Assumptions **A1–A2** are automatically satisfied in this case – see [59]. Note that **A3**, on the other hand, is somewhat strong, as it entails that we do not need to introduce generalized eigenvectors in the case of repeated eigenvalues. In Section 2.6, we will see specific examples by setting $\mathcal{L} = -\Delta^2$ and $H = H_0^2(A_\delta)$ on an annulus $A_\delta = \{(x, y) \in \mathbb{R}^2 : \delta^2 < x^2 + y^2 < 1\}$, $0 < \delta < 1$. The boundary condition is $U = V = 0$ and $\nabla U = \nabla V = 0$ on $\partial\Omega$ [54]. In Remark 2.2, we will comment briefly on more general systems that do not satisfy the assumptions above but are nevertheless expected to generate dynamics beyond the classical CMR similar to model (2.3) – such as the phytoplankton-nutrient model (2.1).

The solutions of equations (2.7) and associated BCs are eigenvectors $(u(x), v(x))^T$ and associated eigenvalues Λ . These eigenvalues are all real-valued, due to the triangular structure of \mathcal{DT} and the condition that \mathcal{L} is self-adjoint. As a matter of fact, solutions to the full spectral problem (2.7) are expressible in terms of the solutions to (2.8).

We normalize the eigenfunctions under the norm of $L^2(\Omega)$,

$$\langle \phi_k, \phi_l \rangle_{L^2} = \delta_{kl}, \quad \text{with } \delta_{kl} \text{ the Kronecker delta.}$$

We define the function space \mathcal{H} spanned by the eigenfunctions of \mathcal{L} ,

$$\mathcal{H} = \text{cl} \left\{ \text{span} \{ \{\phi_k\}_{k \geq 1} \} \times \text{span} \{ \{\phi_k\}_{k \geq 1} \} \right\}, \quad (2.10)$$

define on it an inner product for a Cartesian product of L^2 -spaces,

$$\left\langle \begin{pmatrix} u_1(x) \\ v_1(x) \end{pmatrix}, \begin{pmatrix} u_2(x) \\ v_2(x) \end{pmatrix} \right\rangle_{\mathcal{H}} = \int_{\Omega} (u_1(x)u_2(x) + v_1(x)v_2(x)) \, dx, \quad (2.11)$$

and note the induced norm,

$$\| (u, v)^T \| = \sqrt{\langle (u, v)^T, (u, v)^T \rangle_{\mathcal{H}}}. \quad (2.12)$$

The function space \mathcal{H} equipped with (2.11) is a Hilbert space. From here on, we will omit the subscript in writing the inner product (2.11), because the use of it is never ambiguous. In the case $\mathcal{L} = \Delta$ on $\Omega = (0, 1)$ and with homogeneous Dirichlet BCs, we have $\mathcal{H} = L^2(0, 1) \times L^2(0, 1)$ and the inner product and norm are standard, see Section 2.2.2.

From the assumptions on \mathcal{L} , we can formulate the following proposition.

Proposition 2.2.1. *The eigenvalues determining linear stability of the trivial state $(U, V) = (0, 0)$ of system (2.3) partition into two distinct sets of eigenvalues with asymptotically different interspacing. The eigenvalues $\{\mu_k\}_{k \in \mathbb{N}}$ are $\mathcal{O}(\varepsilon)$ -interspaced, while the remaining eigenvalues $\{\lambda_k\}_{k \in \mathbb{N}}$ are $\mathcal{O}(1)$ -interspaced.*

Assuming $\alpha, \gamma \neq -\nu_k$, for all $k \in \mathbb{N}$, asymptotically many eigenvalues $\{\mu_k\}_{k \in \mathbb{N}}$ and $\{\lambda_k\}_{k \in \mathbb{N}}$ are $\mathcal{O}(\varepsilon)$ and $\mathcal{O}(1)$, respectively. The eigenvalues and the associated normalized eigenfunctions are

$$\left\{ \mu_k = -\varepsilon M_k = \varepsilon(\gamma + \nu_k), \quad s_k = \phi_k(x) \begin{pmatrix} 0 \\ 1 \end{pmatrix} \right\}_{k \geq 1}, \quad (2.13)$$

and

$$\left\{ \lambda_k = \alpha + \nu_k, \quad \sigma_k = \frac{\phi_k(x)}{\sqrt{1+D_k^2}} \begin{pmatrix} 1 \\ D_k \end{pmatrix} \right\}_{k \geq 1}, \quad (2.14)$$

where

$$D_k = \frac{\varepsilon\beta}{\nu_k(1-\varepsilon) + \alpha - \varepsilon\gamma} = \frac{\varepsilon\beta}{\lambda_k - \mu_k}. \quad (2.15)$$

This proposition is proved below. Note that D_k is well-defined under our assumptions that α, γ stay away from $-\nu_k$. The fact that all eigenfunctions can be decomposed as scalar x -dependent functions and a constant vector is noteworthy and becomes fairly important in our analysis. It is due to the same differential operator \mathcal{L} appearing in the U - and the V -equation, both with the same BCs.

The first N μ -eigenvalues are $\mathcal{O}(\varepsilon)$ and $\mathcal{O}(\varepsilon)$ -interspaced, see (2.13). Therefore, we call this part of the spectrum the *small spectrum*. Accordingly, $\{\lambda_k\}_{k \in \mathbb{N}}$ is called the *large spectrum*, which has $\mathcal{O}(1)$ -interspacing. The threshold values for μ_1 and λ_1 to become unstable are the $\mathcal{O}(1)$, fixed values $\gamma = -\nu_1$ and $\alpha = -\nu_1$. Initially, we keep $\gamma < -\nu_1$ fixed, so that the small spectrum is stable. The parameter α is used as a bifurcation parameter and determines the stability of $(0, 0)$. We define

$$\alpha_T = -\nu_1, \quad (2.16)$$

where T stands for ‘transcritical’. The primary eigenvalue of the large spectrum, λ_1 , is unstable for $\alpha > \alpha_T$. Note that the destabilization value for the small spectrum could also be described as $\gamma_T = -\nu_1$, so that the primary eigenvalue of the small spectrum, μ_1 , is unstable for $\gamma > \gamma_T$. By setting $\mu_k = -\varepsilon M_k$, we make the asymptotic magnitude of the small spectrum explicit, and because $\gamma < \gamma_T$ almost everywhere in this chapter, we also make the sign explicit.

Proof of Proposition 2.2.1. This proof uses assumptions **A1–A3** on \mathcal{L} and on the BCs, as well as the solutions of the associated spectral problem (2.8). Due

to the triangular structure of \mathcal{DT} , one set of eigenvectors is of the form

$$s_k(x) := \begin{pmatrix} 0 \\ \zeta_k(x) \end{pmatrix}. \quad (2.17)$$

The eigenvalues corresponding to s_k are μ_k . Equation (2.7a) is satisfied trivially and (2.7b) yields a scalar, self-adjoint spectral problem,

$$(\mu_k - \varepsilon\gamma)\zeta_k = \varepsilon\mathcal{L}\zeta_k. \quad (2.18)$$

We can identify (2.18) as the scalar spectral problem (2.8) with a linear shift. Solutions of (2.18) are therefore the eigenfunctions $\zeta_k(x) = \phi_k(x)$, and the corresponding eigenvalues $\mu_k = \varepsilon(\gamma + \nu_k)$ immediately follow. Normalizing $s_k(x)$ under the norm (2.12) yields (2.13). To derive the second set of eigenvalues and eigenfunctions, we write the eigenfunctions as

$$\sigma_k(x) = \begin{pmatrix} w_k(x) \\ y_k(x) \end{pmatrix}. \quad (2.19)$$

Substitution of (2.19) into (2.7a) yields an ODE for $w(x)$ that decouples from $y(x)$. In this ODE, the scalar problem (2.8) can again be identified, so that,

$$\lambda_k = \alpha + \nu_k \quad \text{and} \quad w_k(x) = c_{1,k}\phi_k(x),$$

with $c_{1,k} \in \mathbb{R}$, a constant depending on the value of ν_k . From this, equation (2.7b) becomes an ODE driven by the inhomogeneity $\varepsilon\beta\phi_k(x)$,

$$\lambda_k y_k(x) = \varepsilon\mathcal{L}y_k(x) + \varepsilon\beta c_{1,k}\phi_k(x) + \varepsilon\gamma y_k(x), \quad (2.20)$$

implying

$$y_k(x) = c_{2,k}\phi_k(x), \quad \text{for some } c_{2,k} \in \mathbb{R}.$$

Substituting into (2.20), we obtain

$$(\alpha + \nu_k)c_{2,k}\phi_k = \varepsilon c_{2,k}\mathcal{L}\phi_k + \varepsilon\beta c_{1,k}\phi_k + \varepsilon\gamma c_{2,k}\phi_k = \varepsilon [c_{2,k}\nu_k + \beta c_{1,k} + \gamma c_{2,k}] \phi_k,$$

so that we find

$$c_{2,k} = \frac{\varepsilon\beta}{\alpha + (1 - \varepsilon)\nu_k - \varepsilon\gamma} c_{1,k} = \frac{\varepsilon\beta}{\lambda_k - \mu_k} c_{1,k}.$$

The constant $c_{1,k}$ is uniquely defined by normalizing σ_k . We then obtain the second set of eigenvalues and eigenfunctions (2.14). \square

2.2.2 Example: a reaction-diffusion system

We illustrate our approach by setting $\mathcal{L} = \Delta$ and $\Omega = (0, 1)$, so that $\mathcal{H} = L_0^2(0, 1)$. Hence, we study the reaction-diffusion system,

$$\begin{cases} U_t = U_{xx} + \alpha U + F(U, V), \\ V_t = \varepsilon [V_{xx} + \beta U + \gamma V + G(U, V)]. \end{cases} \quad (2.21)$$

We assume homogeneous Dirichlet BCs, $U(0) = U(1) = V(0) = V(1) = 0$. The eigenvalue-eigenfunction pairs for the one-dimensional Laplacian ∂_{xx} on the unit interval are

$$\nu_k = -k^2\pi^2 \quad \text{and} \quad \phi_k(x) = \sin(k\pi x), \quad \text{with } k \in \mathbb{N}. \quad (2.22)$$

Normalized under the norm of $L^2(0, 1)$, the eigenfunctions form an orthonormal set in $L^2(0, 1)$,

$$\begin{aligned} & \left\{ \mu_k = \varepsilon(\gamma - k^2\pi^2), \quad s_k(x) = \sqrt{2} \sin(k\pi x) \begin{pmatrix} 0 \\ 1 \end{pmatrix} \right\}_{k \geq 1}, \\ & \left\{ \lambda_k = \alpha - k^2\pi^2, \quad \sigma_k(x) = \frac{\sqrt{2} \sin(k\pi x)}{\sqrt{1 + D_k^2}} \begin{pmatrix} 1 \\ D_k \end{pmatrix} \right\}_{k \geq 1}, \end{aligned} \quad (2.23)$$

where D_k is defined as in (2.15). In this case, $\alpha_T = \gamma_T = \pi^2$, so when $\gamma < \gamma_T$, the small spectrum is stable. This example is used several times in numerical simulations in sections 2.4.2 and 2.5.2, but in the next sections we again turn to an abstract \mathcal{L} .

2.3 Emergence of a small pattern

In Section 2.2, we have obtained explicit control over the spectrum of (2.3) corresponding to the trivial background state $(U, V) = (0, 0)$. In the current section, we set $\lambda_1 = r\varepsilon^\sigma$, with $r > 0$ and $\sigma > 1$, and trace the onset of pattern formation as the background state destabilizes. Since $|\lambda_1| \ll \min_{m,n}\{\mu_m, \lambda_n\}$, there exists a spectral gap and the flow on a center manifold governs the nonlinear dynamics of small initial conditions. As mentioned in the Introduction, we operate slightly different from the textbook center manifold reduction approach but can recover equivalent results – a transcritical bifurcation and the corresponding flow on a one-dimensional center manifold.

2.3.1 Fourier expansion and amplitude ODEs

Consider again the function space \mathcal{H} defined in (2.10). By construction, the eigenfunctions s_k and σ_k , see (2.13) and (2.14), form a basis for it. In contrast

to [176], we choose to *not* work with the eigenbasis but with

$$\left\{ e_k := \begin{pmatrix} \phi_k \\ 0 \end{pmatrix}, \quad e'_k := \begin{pmatrix} 0 \\ \phi_k \end{pmatrix} \right\}_{k \in \mathbb{N}}. \quad (2.24)$$

Although this will lead to linear coupling between modes, it will render the amplitude ODEs more amenable to analysis by eliminating many nonlinearities. This, in turn, makes the analysis of the later obtained amplitude equations much more transparent. Since \mathcal{L} is self-adjoint, this basis is orthonormal:

- $\langle e_l, e_m \rangle = \langle e'_l, e'_m \rangle = \delta_{lm}$, for all $l, m \in \mathbb{N}$;
- $\langle e_l, e'_m \rangle = 0$, for all $l, m \in \mathbb{N}$;
- $\|e_l\| = \|e'_l\| = 1$, for all $l \in \mathbb{N}$.

Here, $\langle \cdot, \cdot \rangle$ and $\|\cdot\|$ denote the inner product and norm on \mathcal{H} as defined in (2.11) and (2.12). With this basis for \mathcal{H} , we can decompose U and V as

$$\begin{pmatrix} U \\ V \end{pmatrix} = \sum_{l \geq 1} A_l(t) e_l + B_l(t) e'_l = \sum_{l \geq 1} \phi_l(x) \begin{pmatrix} A_l(t) \\ B_l(t) \end{pmatrix}. \quad (2.25)$$

In the context of our reaction-diffusion example (2.21), (2.25) amounts to Fourier sine series for U and V . The coefficients A_l and B_l are called *amplitudes* corresponding to e_l and e'_l , respectively, and measure the projection of the solution $(U, V)^T$ along the corresponding eigenspace. For a given solution $(U, V)^T$, the orthonormality relations yield simple formulas for these amplitudes:

$$A_l = \left\langle \begin{pmatrix} U \\ V \end{pmatrix}, e_l \right\rangle, \quad B_l = \left\langle \begin{pmatrix} U \\ V \end{pmatrix}, e'_l \right\rangle.$$

Because each ϕ_l is an eigenfunction of the operator \mathcal{L} , substitution of (2.25) into (2.3) yields

$$\sum_{l \geq 1} \begin{pmatrix} \dot{A}_l \\ \dot{B}_l \end{pmatrix} \phi_l = \sum_{l \geq 1} \begin{pmatrix} \lambda_l & 0 \\ \varepsilon\beta & \mu_l \end{pmatrix} \begin{pmatrix} A_l \\ B_l \end{pmatrix} \phi_l + \mathcal{N}(U, V), \quad (2.26)$$

cf. (2.7a)–(2.7b). Here, the dot (\cdot) denotes differentiation with respect to t . We Taylor-expand the nonlinearity $\mathcal{N} = (F, \varepsilon G)^T$ using

$$\begin{aligned} F(U, V) &= F_{20}U^2 + F_{11}UV + F_{02}V^2 + \mathcal{O}(\|U^2 + V^2\|^{\frac{3}{2}}), \\ G(U, V) &= G_{20}U^2 + G_{11}UV + G_{02}V^2 + \mathcal{O}(\|U^2 + V^2\|^{\frac{3}{2}}), \end{aligned} \quad (2.27)$$

where $\mathcal{O}(\|U^2 + V^2\|^{\frac{3}{2}})$ denotes cubic and higher order terms. Upon substituting (2.25) into these expressions, the nonlinearity becomes

$$\mathcal{N}(U, V) = \sum_{l,m \geq 1} \phi_l \phi_m \left(\frac{F_{20} A_l A_m + F_{11} A_l B_m + F_{02} B_l B_m}{\varepsilon (G_{20} A_l A_m + G_{11} A_l B_m + G_{02} B_l B_m)} \right), \quad (2.28)$$

$+ \mathcal{O}(\|U^2 + V^2\|^{\frac{3}{2}})$ terms. This can now be substituted back into (2.26). Note that the quadratic terms $\phi_l \phi_m$ must also be projected onto $\{\phi_k\}_{k \geq 1}$,

$$\phi_l \phi_m = \sum_{k \geq 1} C_{klm} \phi_k, \quad \text{with } C_{klm} = \int_{\Omega} \phi_k \phi_l \phi_m \, dx, \quad (2.29)$$

where C_{klm} is invariant under index permutations. In the case $\mathcal{L} = \Delta$, $\Omega = (0, 1)$ and with Dirichlet BCs, for example, $C_{111} = 8\sqrt{2}/(3\pi)$ and $C_{klm} = 0$ if $k+l+m$ is even. The resulting system is reducible to an infinite-dimensional system of ODEs for A_k and B_k by taking the inner product with e_k and e'_k , respectively. One thus obtains a pair of coupled ODEs per $k \in \mathbb{N}$:

$$\begin{cases} \dot{A}_k = \lambda_k A_k \\ \quad + \sum_{l,m \geq 1} C_{klm} (F_{20} A_l A_m + F_{11} A_l B_m + F_{02} B_l B_m), \\ \dot{B}_k = -\varepsilon M_k B_k + \varepsilon \beta A_k \\ \quad + \varepsilon \sum_{l,m \geq 1} C_{klm} (G_{20} A_l A_m + G_{11} A_l B_m + G_{02} B_l B_m), \end{cases} \quad (2.30)$$

up to cubic corrections. Note that there is now also *linear coupling* between A_k and B_k , reflecting the fact that $\{e_k, e'_k\}_{k \geq 1}$ is not an eigenbasis of \mathcal{DT} .

2.3.2 The classical center manifold reduction

As discussed in the Introduction, center manifold reduction (CMR) can be used to reduce the flow of a system close to bifurcation, provided that there is a spectral gap between the bifurcating eigenvalues and the other (stable) eigenvalues. To reflect this feature, we rescale

$$\alpha = \alpha_T + r\varepsilon^\sigma, \quad \text{with } r > 0 \text{ and } \sigma > 1, \text{ so that } \lambda_1 = r\varepsilon^\sigma; \quad (2.31)$$

this positions us just beyond destabilization of $(U, V) = (0, 0)$. As we have already remarked, the spectral gap condition is satisfied in this regime; recall Figure 2.1. The results in this section are therefore equivalent to CMR, see [9, 18, 160].

We trace the onset of patterns emerging from a trivial background state, so we expect all amplitudes to be small. To reflect this, we scale all amplitudes by means of

$$\begin{aligned} A_1(t) &= \varepsilon^{\sigma_1} a_1(t), \\ A_k(t) &= \varepsilon^{\sigma_U} a_k(t), \quad k \in \mathbb{N}_{\geq 2}, \\ B_k(t) &= \varepsilon^{\sigma_V} b_k(t), \quad k \in \mathbb{N}, \end{aligned} \tag{2.32}$$

with $\sigma_1 < \sigma_U$. We assumed here that the primary amplitude A_1 is asymptotically larger than all other amplitudes, because it corresponds to the bifurcating eigenvalue. The powers $\sigma_1, \sigma_U, \sigma_V$ are positive and will be determined in terms of σ in the forthcoming analysis. Substituting the rescaled amplitudes into system (2.30) yields,

$$\begin{aligned} \varepsilon^{\sigma_1} \dot{a}_1 &= r \varepsilon^{\sigma_1 + \sigma} a_1 + \varepsilon^{2\sigma_1} C_{111} F_{20} a_1^2 + \varepsilon^{\sigma_1 + \sigma_V} \sum_{m \geq 1} C_{11m} F_{11} a_1 b_m \\ &\quad + \varepsilon^{2\sigma_V} \sum_{l, m \geq 1} C_{1lm} F_{02} b_l b_m + \mathcal{O}(\varepsilon^{\sigma_1 + \sigma_U}, \varepsilon^{\sigma_V + \sigma_U}), \end{aligned} \tag{2.33}$$

$$\begin{aligned} \varepsilon^{\sigma_U} \dot{a}_k &= \varepsilon^{\sigma_U} \lambda_k a_k + \varepsilon^{2\sigma_1} C_{k11} F_{20} a_1^2 + \varepsilon^{\sigma_1 + \sigma_V} \sum_{m \geq 1} C_{k1m} F_{11} a_1 b_m, \\ &\quad + \varepsilon^{2\sigma_V} \sum_{l, m \geq 1} F_{02} C_{klm} b_l b_m + \mathcal{O}(\varepsilon^{\sigma_1 + \sigma_U}, \varepsilon^{\sigma_V + \sigma_U}), \end{aligned} \tag{2.33}$$

$$\varepsilon^{\sigma_V} \dot{b}_1 = -\varepsilon^{1+\sigma_V} M_1 b_1 + \varepsilon^{1+\sigma_1} \beta a_1 + \mathcal{O}(\varepsilon^{1+2\sigma_1}, \varepsilon^{1+\sigma_1+\sigma_V}, \varepsilon^{1+2\sigma_V}),$$

$$\varepsilon^{\sigma_V} \dot{b}_k = -\varepsilon^{1+\sigma_V} M_k b_k + \varepsilon^{1+\sigma_U} \beta a_k + \mathcal{O}(\varepsilon^{1+2\sigma_1}, \varepsilon^{1+\sigma_1+\sigma_V}, \varepsilon^{1+2\sigma_V}),$$

with the higher order corrections originating from the nonlinear terms in (2.30). The *principle of least degeneracy* or of *significant degeneration* [44, 87] suggests that $\sigma = \sigma_1 = \sigma_V$, that $\sigma_U = 2\sigma$ and the rescaling of time $\tau = \varepsilon^\sigma t$. Denoting differentiation with respect to τ by $'$, we find up to corrections of $\mathcal{O}(\varepsilon^\sigma)$,

$$\begin{aligned} a'_1 &= r a_1 + C_{111} F_{20} a_1^2 + F_{11} a_1 \sum_{m \geq 1} C_{11m} b_m + F_{02} \sum_{l, m \geq 1} C_{1lm} b_l b_m, \\ \varepsilon^\sigma a'_k &= \lambda_k a_k + C_{k11} F_{20} a_1^2 + F_{11} a_1 \sum_{m \geq 1} C_{k1m} b_m + F_{02} \sum_{l, m \geq 1} C_{klm} b_l b_m, \\ \varepsilon^{\sigma-1} b'_1 &= -M_1 b_1 + \beta a_1, \\ \varepsilon^{\sigma-1} b'_k &= -M_k b_k. \end{aligned} \tag{2.34}$$

For $\sigma > 1$, the left hand side of all ODEs except the first one is of higher order, compared to their linear terms. This reflects the disparity between the $\mathcal{O}(\varepsilon^\sigma)$ eigenvalue λ_1 and all other eigenvalues, which are at least $\mathcal{O}(\varepsilon)$. It ensures that the long-term, leading order behavior of the corresponding modes are described by algebraic relations – *slaving relations* – because the left-hand sides become higher order compared to the linear terms. The corresponding amplitudes are said to be *slaved* to a_1 , leaving this as the only *dynamic* amplitude and the behavior of (2.34) completely determined by it. Here, the slaving relations assume the form

$$\begin{aligned} b_1 &= \frac{\beta}{M_1} a_1 + \mathcal{O}(\varepsilon^{\sigma-1}), \\ b_k &= 0 + \mathcal{O}(\varepsilon^{\sigma-1}), \\ a_k &= -\frac{C_{k11}H}{\lambda_k} a_1^2 + \mathcal{O}(\varepsilon^{\sigma-1}), \end{aligned} \tag{2.35}$$

where, with a slight abuse of notation, we write

$$H = F_{20} + \frac{F_{11}\beta}{M_1} + \frac{F_{02}\beta^2}{M_1^2}. \tag{2.36}$$

The ODE describing the evolution of a_1 on the center manifold is

$$a'_1 = r a_1 + H C_{111} a_1^2 + \mathcal{O}(\varepsilon^{\sigma-1}), \tag{2.37}$$

obtained by substituting (2.35) into (2.34). At this point, we have recaptured the classical center manifold reduction results. The center manifold is one-dimensional and described by the slaving relations, while the evolution on it is governed by the single ODE for a_1 above. The trivial pattern $(U, V) = (0, 0)$ corresponds to the trivial steady state $a_1 \equiv 0$, and there also exists a nontrivial steady state solution,

$$a_1^* = -\frac{r}{C_{111}H}. \tag{2.38}$$

This state indicates the onset of a nontrivial pattern, because the two steady states exchange stability at $r = 0$ through a transcritical bifurcation. As long as $\sigma > 1$, (2.37) exhibits no other bifurcations in a neighborhood of $(U, V) = (0, 0)$.

Theorem 2.3.1. *The trivial state $(U, V) = (0, 0)$ of system (2.3) undergoes a transcritical bifurcation at $\alpha = \alpha_T$. For $\alpha = \alpha_T + r\varepsilon^\sigma$ with $\sigma > 1$, $r > 0$ and $\gamma < \gamma_T$, the nontrivial, stationary, attracting pattern branching off this trivial state is approximated by*

$$\begin{pmatrix} U \\ V \end{pmatrix} = \varepsilon^\sigma \left[-\frac{r}{C_{111}H} \begin{pmatrix} 1 \\ \beta/M_1 \end{pmatrix} \phi_1(x) + \mathcal{O}(\varepsilon^{\sigma-1}) \right]. \tag{2.39}$$

This result is derived by combining (2.38) and the slaving relations (2.35) with the original expansion (2.25). It also follows from a standard application of center manifold reduction, and therefore we refer to [9, 18, 160] for a full proof.

2.4 Evolution of the small pattern outside the CMR regime

The dichotomy $\sigma > 1$ versus $\sigma = 1$ arises naturally in system (2.34). Indeed, as $\sigma \downarrow 1$, the spectral gap between a_1 and the b_k -amplitudes disappears. What is left are equations for a_1 , b_1 and all b_k with $k \geq 2$. Those b_k -amplitudes naturally remain linearly stable, but they now evolve in the same timescale as a_1 . As a result, (2.34) does not a priori support an exponentially attracting, one-dimensional center manifold anymore.

Below, we use the spectrum of the background state and (2.34) to track the evolution of the small pattern (2.39) emerging from that state well into the regime $\sigma = 1$. We first show that the pattern (conditionally) undergoes a destabilizing Hopf bifurcation at a value $\alpha_H > \alpha_T$ for α , through which a small, stable, temporally oscillatory pattern emerges; see Section 2.4.1. As α increases even further, numerical work show the amplitude and period of the oscillation to increase all the way to a homoclinic bifurcation, at which the oscillatory pattern disappears. Past that α -value, small initial conditions grow unboundedly (in the scaled setting), see Section 2.4.2; this bounds the span of our analysis explicitly.

2.4.1 Beyond classical CMR: a Hopf bifurcation

Setting $\sigma = 1$ in (2.34) and retaining the dynamic equations for the b_k -modes, we obtain, up to $\mathcal{O}(\varepsilon)$ corrections,

$$\begin{cases} a'_1 = ra_1 + C_{111}F_{20}a_1^2 + F_{11}a_1 \sum_{n \geq 1} C_{1n1}b_n + \sum_{m,n \geq 1} C_{mn1}F_{02}b_m b_n, \end{cases} \quad (2.40a)$$

$$\begin{cases} b'_1 = -M_1b_1 + \beta a_1, \end{cases} \quad (2.40b)$$

$$\begin{cases} b'_k = -M_k b_k, \quad \text{where } k \geq 2. \end{cases} \quad (2.40c)$$

The amplitudes a_k with $k \geq 2$ remain slaved. However, since all b_k -modes are now dynamic, each a_k is controlled by both the a_1 - and the b_k -modes,

$$a_k = -\frac{C_{11k}F_{20}a_1^2 + F_{11}a_1 \sum_{n \geq 1} C_{1nk}b_n + \sum_{m,n \geq 1} C_{mnk}F_{02}b_m b_n}{\lambda_k}.$$

In the terminology of center manifold reduction (CMR), one could say that the center manifold dimension has become infinite or, at least, that it cannot be bounded uniformly as $\varepsilon \downarrow 0$ (asymptotically large). Analysis of an infinite-dimensional ODE system is a priori nontrivial. However, in this case all but

one (namely a'_1) of the equations are linear and all but two (namely a'_1 and b'_1) decouple, see also Remark 2.2. Moreover, the ODEs for b_k with $k \geq 2$, see (2.40c), imply exponential decay of those modes at rates increasing with k . Therefore we can conclude that in the long term $b_k = \mathcal{O}(\varepsilon)$ for all $k \geq 2$, see again Remark 2.2, and the evolution of the pattern is controlled by the planar system

$$\begin{cases} a'_1 = ra_1 + C_{111} (F_{20}a_1^2 + F_{11}a_1b_1 + F_{02}b_1^2) + \mathcal{O}(\varepsilon), \\ b'_1 = -M_1b_1 + \beta a_1 + \mathcal{O}(\varepsilon), \end{cases} \quad (2.41)$$

together with the slaving relations

$$a_k = -\frac{C_{11k}}{\lambda_k} [F_{20}a_1^2 + F_{11}a_1b_1 + F_{02}b_1^2] + \mathcal{O}(\varepsilon), \quad b_k = \mathcal{O}(\varepsilon), \quad k \geq 2.$$

The reduced system (2.41) admits two equilibria, namely the zero solution corresponding to the trivial state and the continuation of the pattern (2.39) in this regime,

$$S^*(r) := \left\{ (a_1, b_1) = -\frac{r}{C_{111}H} \left(1, \frac{\beta}{M_1} \right) \right\}; \quad (2.42)$$

recall definition (2.36) for H . The Jacobian of the trivial state has eigenvalues $\Lambda_1 = r$ and $\Lambda_2 = -M_1$, and thus the state changes from stable node to saddle at the transcritical bifurcation ($r = 0$). The stability of S^* is determined by the Jacobian corresponding to (2.41),

$$J(S^*) = \begin{pmatrix} \frac{r}{H}(H - J_1) & -\frac{r}{H}J_2 \\ \beta & -M_1 \end{pmatrix}, \text{ with } J_1 = 2F_{20} + \frac{\beta F_{11}}{M_1} \\ J_2 = F_{11} + 2\frac{\beta F_{02}}{M_1}. \quad (2.43)$$

One of its eigenvalues becomes zero if and only if $r = 0$, as expected because of the transcritical bifurcation, (see Appendix). The branch $S^*(r)$ may further lose stability through a Hopf bifurcation, where limit cycles (periodic amplitudes) are born; this occurs if the eigenvalues form a complex pair crossing the imaginary axis. A straightforward computation gives conditions on r for which the eigenvalues of $J(S^*)$ are purely imaginary complex conjugates:

$$r_H = \frac{HM_1}{H - J_1} \quad \text{and} \quad r_H > 0. \quad (2.44)$$

If $r_H < 0$ instead, S^* remains a stable point for all positive $\mathcal{O}(1)$ values of r . However, we refrain from investigating the fate of S^* in the case that it does not

undergo a Hopf bifurcation. If $r_H > 0$ and $H - J_1 \neq 0$, then a Hopf bifurcation takes place. From [98] we derive a degeneracy condition ensuring that the eigenvalues pass the imaginary axis with nonzero speed, which is always satisfied if $r_H > 0$. The same reference gives rise to a straightforward computation that determines the criticality of the bifurcation [98]. Defining

$$L = (H + r_H F_{20})(2M_1 F_{20} + F_{11}\beta), \quad (2.45)$$

we obtain that the Hopf bifurcation is supercritical if $L < 0$ and subcritical if $L > 0$. We refer the reader to Appendix A for the full derivation of this expression. Our results so far, concerning the evolutionary system (2.3), are summarized in the following proposition.

Claim 2.4.1. *In PDE-systems of the class (2.3), the trivial solution $(U, V) = (0, 0)$, undergoes a transcritical bifurcation as α passes through $\alpha_T = -\nu_1$. When the trivial solution loses stability, the nontrivial branch becomes stable and, under the condition that $r_H > 0$, undergoes a Hopf bifurcation as α increases to*

$$\alpha_H = \frac{HM_1}{H - J_1}\varepsilon - \nu_1.$$

Neither a rigorous proof of this proposition nor validation of the asymptotics are foci of this presentation. The formal work resulting in Claim 2.4.1 establishes that, as long as $r_H > 0$ and $L < 0$, the bifurcating stationary pattern (2.39) starts oscillating periodically in time for parameters $\mathcal{O}(\varepsilon)$ close to the first transcritical bifurcation. As in the case of the phytoplankton-nutrient model (2.1), this behavior is confirmed by direct simulations of the full PDE model; see next section.

Remark 2.1. In system (2.40), the dynamics of the b_k -modes is governed by ODEs. From a different perspective, the b_k -modes represent the leading order original PDE for V , see (2.3), through transformation (2.25). System (2.40) can therefore also be regarded as an ODE (equation (2.40a)) coupled to a PDE (albeit in amplitude form, (2.40b)–(2.40c)). We can reconstruct the PDE to which equation (2.40a) is coupled by writing $V(x, t) = \varepsilon v(x, t)$ and using the correct timescale $\tau = \varepsilon t$ in (2.3). The PDE for v then becomes

$$v_\tau = \mathcal{L}v + \gamma v + \beta a_1(\tau)\phi_1(x) + \mathcal{O}(\varepsilon). \quad (2.46)$$

System (2.40) is thus equivalent to (2.40a) coupled to the inhomogeneous, linear PDE (2.46). The analogue of this compact version of system (2.3) is heavily used in Chapter 3. Note also that all b_k -terms appearing in (2.40a) can in principle be expressed into nonlocal terms of v . We did not work with this representation of the dynamics beyond classical CMR, because of being able to reduce (2.40) to the planar system (2.41).

Remark 2.2. The distinct decoupling between the active b_1 -mode and the exponentially decaying b_k -modes ($k \geq 2$) in the extended center manifold reduction (ECMR) system (2.40) can be traced back to our assumptions on the structure of the basic system (2.3) and its BCs. Since the fast (U) and slow (V) eigenvalue problems are governed by the same operator \mathcal{L} subject to the same BCs, we can employ the Fourier decomposition (2.25) based on the same *scalar* eigenfunctions $\phi_k(x)$ for both the U - and the V -components. In a more general setting – e.g., when the operator and BCs for U differ from those for V – the fast and slow eigenvalue problems do not admit a set of eigenfunctions expressible in terms of the same scalar function. As a consequence, the *leading order* terms in the (beyond CMR) ODEs for b_k may employ the unstable a_1 -mode; in that case, a direct decoupling of the form (2.40) is not ascertained. We encounter that in the phytoplankton-nutrient model (2.1) studied in [78, 176, 177] and Chapter 3 of this thesis. It has, nevertheless, been shown in [176] that, also for (2.1), the full system behavior is essentially two-dimensional. The transcritical bifurcation in (2.1) is also followed by a Hopf destabilization. Although we do not consider the more general case, (2.2) here, we expect it to behave similarly to systems (2.1) and (2.3): essentially two-dimensional dynamics, beyond the classical CMR, which may contain a Hopf bifurcation. The difference between the present, most transparent case (2.3) and the more general (2.2) is expected to mostly be a matter of linear algebra.

2.4.2 Beyond the Hopf: a homoclinic bifurcation

Having successfully tracked the pattern into an $\mathcal{O}(\varepsilon)$ regime beyond the transcritical bifurcation, the question arises whether the ECMR system (2.41) can possibly capture tertiary bifurcations for $\alpha > \alpha_H$. It turns out that, unfortunately, we cannot in general expect (E)CMR to capture the full system dynamics for $r > r_H$. As we will find out, even small initial conditions are no more trapped in a neighborhood of the manifold.

First, we select parameter values ensuring the existence of a supercritical Hopf bifurcation and then trace the stable limit cycle emerging through it. We do not attempt to follow the oscillatory pattern analytically but rely, instead, on numerical ODE continuation toolbox MATCONT to do just that [33]. The first outcome is Figure 2.3, where we have plotted the limit cycle born at α_H for increasing r (or, equivalently, α ; recall (2.31)). Note carefully that these plots correspond to the *reduced*, planar system (2.41) and not to the full PDE model; also, that we have overlaid the limit cycles corresponding to several r -values – this is not a single trajectory. As r increases from r_H , the period of the limit cycle tends to infinity while it accumulates to a homoclinic orbit; this occurs at a well-defined, finite value r_{Hom} . As Figure 2.3 shows, that orbit is homoclinic

to the trivial state $(a_1, b_1) = (0, 0)$. Increasing r beyond r_{Hom} leads amplitudes to grow unboundedly, rendering our asymptotic analysis invalid; indeed, the assumption on the asymptotic magnitude of A_1 and B_1 is then violated, see (2.32).

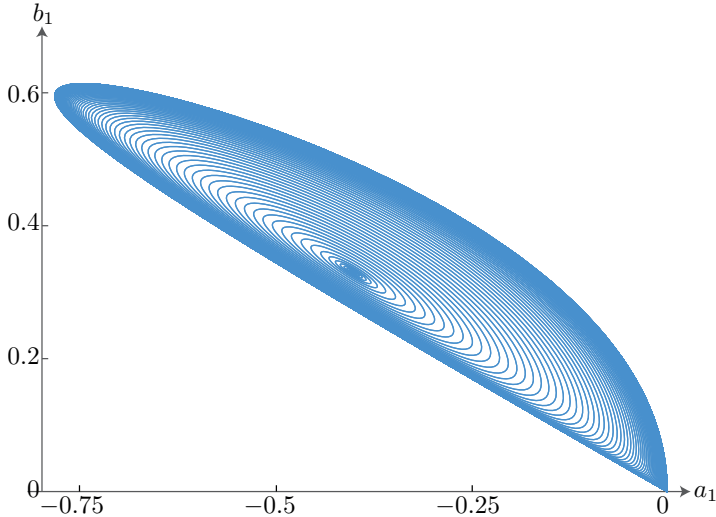


Figure 2.3: A continuation of the attracting limit cycle in system (2.41) that originates at the Hopf bifurcation. The horizontal and vertical axes correspond to a_1 and b_1 , respectively. The parameter values are $\beta = -4$, $\gamma = 5$, $F_{20} = -2$, $F_{11} = 5$, $F_{02} = 12$, so that $r_H > 0$ and $L < 0$. The supercritical Hopf bifurcation occurs at $r_H \approx 0.9596$. The limit cycles accumulate at $r \approx 1.0524$, at which point the period tends to infinity. This indicates the existence of an orbit homoclinic to the trivial state $(0, 0)$. As r increases beyond $r \approx 1.0524$, orbits grow unboundedly.

MATLAB simulations show that the full system (2.3) exhibits similar behavior and has a periodically oscillating spatial structure as attractor. Moreover, the periodic patterns also seem to merge with a homoclinic structure as r increases, see Figure 2.4 where we plot the amplitudes $a_1(\tau)$ and $b_1(\tau)$. Motivated by these observations, we formulate a conjecture concerning the stability of the nontrivial steady state.

Conjecture 2.4.2. *Let $r_H > 0$ and assume that the Hopf bifurcation that (2.41) undergoes is supercritical: $L < 0$, see (2.45). Then, as r increases beyond r_H , the limit cycles grow into a homoclinic orbit at $r = r_{\text{Hom}}$. As r increases beyond*

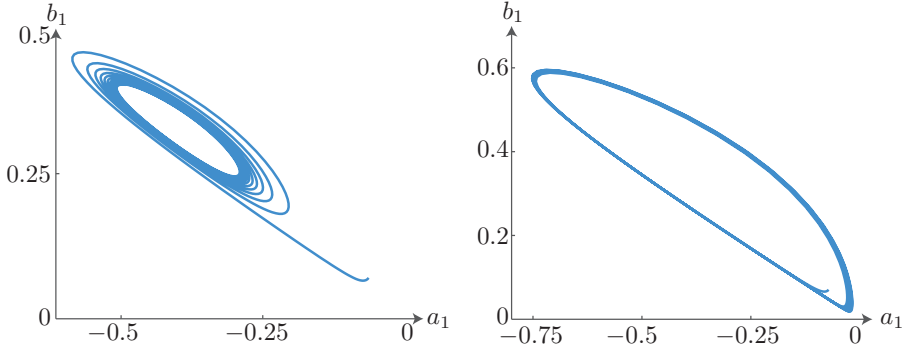


Figure 2.4: PDE simulations of (2.3) using MATLAB’s PDEPE function. Here, $\mathcal{L} = \Delta$ on $\Omega = (0, 1)$ equipped with Dirichlet BCs, and parameters are as in Figure 2.3 and $G_{20} = 1, G_{11} = G_{02} = 0$. Plotted are the amplitudes a_1 (horizontal axis) and b_1 (vertical axis), obtained by projecting the computed $(U(x, t), V(x, t))$ onto $\phi_1(x)$ and rescaling. (a) An orbit evolving to an attracting limit cycle. Additional parameter values are $r = 1$ and $\varepsilon = 0.05$. The initial conditions are $U(x, 0) = -V(x, 0) = -\varepsilon\phi_1(x)$. (b) A similar simulation for $r = 1.09$. For r slightly larger, the limit cycle connects to the origin and orbits continue to grow (data not shown).

that value, all orbits of (2.41) grow unboundedly except for those with initial conditions on the stable manifold of the trivial state $(0, 0)$. Qualitatively, this transition is illustrated in Figure 2.5.

Figures 2.5 contains (hypothetical) phase portraits of a two-dimensional system as it goes through the transcritical, Hopf and homoclinic bifurcations. These portraits are meant to illustrate qualitatively these transitions, not to correspond to (2.41) for specific parameter values. Note that the scenario laid out in Conjecture 2.4.2 has a strong similarity to the behavior of systems near a transcritical codimension 2 Bogdanov-Takens bifurcation point – see [23], for instance. Given the structure of (2.41), this is not surprising. There is, however, a subtle but significant difference between (2.41) and a generic unfolding of a (non-semisimple) codimension 2 bifurcation with two zero eigenvalues as that considered in [23]. Specifically, system (2.41) has been obtained under the assumption that amplitudes a_1 and b_1 , as well as all parameters, are strictly $\mathcal{O}(1)$. For instance, $|r| \ll 1$ will necessarily bring us back to the classical center manifold reduction case of a transcritical (codimension 1) bifurcation of Section 2.3.2. Similarly, it is central to our procedure that M_1 is not ‘small’ – or equivalently that $\mu_1 = \mathcal{O}(\varepsilon)$ but not smaller – as Figure 2.1 clearly illustrates. Therefore, the conjectured occurrence of the homoclinic bifurcation cannot be deduced from

the existence of homoclinic bifurcations near a Bogdanov-Takens point: these are all established by a local analysis zooming into the situation where, in the notation of equation (2.41), $|a_1|$, $|b_1|$, r and M_1 are all ‘*sufficiently small*’. A rigorous proof on the existence of an attracting, extended center manifold as a reduction, is crucial for the validation of our method, but is part of future work.

In fact, the system beyond the center manifold reduction (CMR) obtained in [176] for the phytoplankton - nutrient model (2.1) that inspired the present analysis corresponds to setting $\gamma = 0$ in (2.3), since the small eigenvalues μ_k in (2.1) are parameter-independent and cannot be ‘*tuned*’. Hence, in the case of (2.1), $M_1 = -\pi^2$ and there is no freedom to consider the case $M_1 \rightarrow 0$. Nevertheless, the system beyond CMR obtained in [176] also exhibits the Bogdanov-Takens-like behavior of Conjecture 2.4.2. This is not surprising: it is natural to assume that bifurcation curves existing in a local limit may be extended globally.

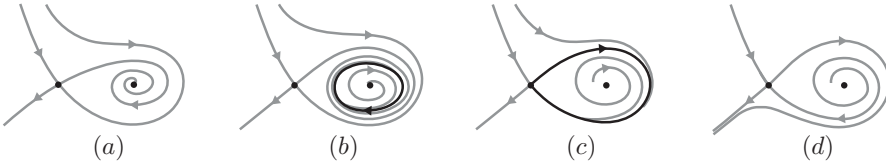


Figure 2.5: Qualitative phase portraits illustrating Conjecture 2.4.2 on the evolution of the stability of the nontrivial steady state S^* . (a) $r \in (\alpha_T, r_H)$; the Hopf bifurcation has not yet occurred, and S^* is a stable focus. (b) $r \in (\alpha_H, r_{\text{Hom}})$; a stable limit cycle has appeared after the Hopf bifurcation, making S^* an unstable focus. (c) $r \approx r_{\text{Hom}}$; the limit cycles have grown into an homoclinic orbit to the origin with attracting initial conditions within its lobe, and S^* is unstable. (d) $r > r_{\text{Hom}}$; now all orbits grow unboundedly, except for the stable manifold of the trivial state.

Other than the numerical evidence, we do not provide an analytical proof for the existence of a homoclinic orbit. We will, however, employ geometric singular perturbation theory (GSPT) and Fenichel’s theorems to show that, if r increases to be asymptotically large, all solutions of (2.41) indeed blow up [49, 82, 84].

We introduce $r = \frac{1}{\delta}$, with $0 < \delta \ll 1$. System (2.41) then becomes singularly perturbed,

$$\begin{cases} a'_1 = \frac{1}{\delta} a_1 + C_{111} (F_{20}a_1^2 + F_{11}a_1b_1 + F_{02}b_1^2) + \mathcal{O}(\varepsilon), \\ b'_1 = -M_1b_1 + \beta a_1 + \mathcal{O}(\varepsilon), \end{cases} \quad (2.47)$$

where the prime denotes differentiation with respect to τ . With a slight abuse of notation, we rescale $A_1 = \delta a_1$ and $B_1 = \delta b_1$ to obtain the associated slow

system,

$$\begin{cases} \delta A'_1 = A_1 + C_{111} (F_{20}A_1^2 + F_{11}A_1B_1 + F_{02}B_1^2), \\ B'_1 = -M_1B_1 + \beta A_1. \end{cases} \quad (2.48)$$

Rescaling time as $\hat{t} = \frac{1}{\delta}\tau$, we obtain the fast system,

$$\begin{cases} \frac{dA_1}{d\hat{t}} = A_1 + C_{111} (F_{20}A_1^2 + F_{11}A_1B_1 + F_{02}B_1^2), \\ \frac{dB_1}{d\hat{t}} = \delta(-M_1B_1 + \beta A_1). \end{cases} \quad (2.49)$$

Using GSPT, we can now conclude the following.

- To leading order in δ , B_1 is constant with respect to the fast dynamics.
- The slow manifold is defined by

$$0 = A_1 + C_{111} (F_{20}A_1^2 + F_{11}A_1B_1 + F_{02}B_1^2), \quad (2.50)$$

which is a conic section (ellipse, hyperbola or parabola). This slow manifold is normally hyperbolic, except at the folds where the slope with respect to B_1 is zero.

- The eigenvalues of the nontrivial equilibrium S^* determined from the fast system are

$$\Lambda_1 = \frac{M_1}{r_H} + \delta \frac{r_H J_1}{H} + \mathcal{O}(\delta^2) \quad \text{and} \quad \Lambda_2 = \delta r_H + \mathcal{O}(\delta^2), \quad (2.51)$$

recall (2.36) and (2.43)–(2.44). In the regime which we consider, $r_H > 0$ and $M_1 > 0$, the equilibrium is a source.

Proposition 2.4.3. *Let $r_H, M_1 > 0$ and $\beta \neq 0$. If a solution $\Gamma(\tau) = (a_1(\tau), b_1(\tau))$ of system (2.47) is bounded, then it lies on the stable manifold of the trivial steady state: $\lim_{\tau \rightarrow \infty} \Gamma(\tau) = (0, 0)$.*

Proof. The proof relies on phase portrait analysis. See Figure 2.6 for two typical configurations of the phase portrait; the situation is similar for a parabolic slow manifold (case not shown). Now, assume $\Gamma(\tau)$ to be bounded and to solve (2.47) but not to limit to the origin. Without loss of generality, we also assume $\Gamma(0)$ to lie on the fast plane and not on the slow manifold. Given that Γ is bounded, the fast flow takes it to a branch of the slow manifold. There, the slow flow cannot further direct it to the trivial steady state, by assumption. Hence, it

carries it to either of the folds of the slow manifold, where the flow of Γ is more subtle. Since there is no other branch of the slow manifold to pick up Γ , that remains unbounded contradicting our assumptions and completing the proof. Note that, in the above argument, we have implicitly assumed Γ to stay away from the nontrivial steady state S^* . The linear analysis (2.51) confirming S^* as a source supports this conclusion, as does Figure 2.6. The same figure, nevertheless, suggests the existence of trajectories limiting to S^* , and thus bounded, when that equilibrium lies at the other side of the folds. This cannot happen in the regime assumed here, $M_1 > 0$ and $r_H > 0$. Indeed, switching occurs at $H - J_1 = 0$ and, in our regime, either $H - J_1 > 0$ or $H - J_1 < 0$: the state remains repelling for all $r_H, M_1 > 0$. \square

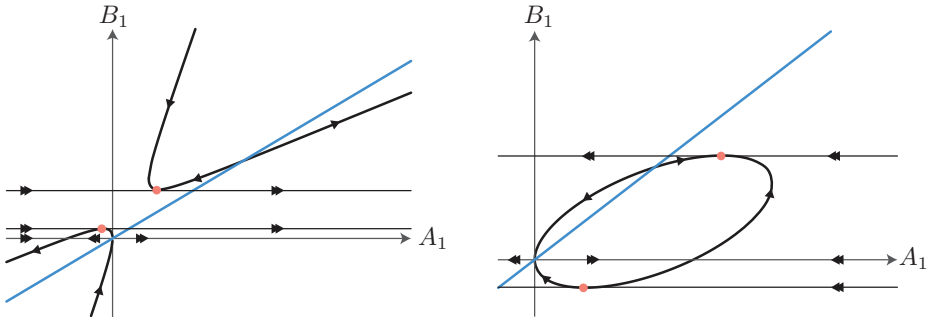


Figure 2.6: Two possible phase portraits of system (2.47). The pink dots mark the folds of the slow manifold. The blue line is $B_1 = \beta A_1 / M_1$, and intersections of it with the conic section are steady states. Left: Here, $F_{20} = 1, F_{11} = 3, F_{02} = 1$ and $\beta = 0.55M_1$, and the conic section is a hyperbola. Right: Here, $F_{20} = -1, F_{11} = 2, F_{02} = -3$ and $\beta = 0.8M_1$, and the conic section is an ellipse. In both cases, the nontrivial steady state is repelling all initial conditions other than itself. The only orbits that do not grow unboundedly are those with initial conditions on the stable manifold of the trivial steady state.

As a corollary of Proposition 2.4.3, every solution of (2.47) not intersecting the stable manifold of the trivial state grows unboundedly. Hence, orbits of system (2.41) with asymptotically large r grow unboundedly, unless they intersect the stable manifold of the trivial state.

2.5 Capturing the onset of low-dimensional chaos with the ECMR

In the previous sections, we have analyzed the onset of patterns arising from a trivial background state in (2.3), finding that it involves a primary (transcritical), a secondary (Hopf) and a tertiary (homoclinic) bifurcation. In this and the next section we demonstrate, first, how a modification in (2.3) creates more complex but equally low-dimensional dynamics and, second, how to track the onset of this dynamics using extended center manifold reduction (ECMR). The first part adds to our ongoing effort to unfold the driving mechanism of low-dimensional chaotic dynamics in (2.1); and indeed, our work puts the spotlight on a wide class of PDE systems exhibiting similar phenomena, see (2.2) and the corresponding Chapter 3. The second part is meant to further highlight this class as one where analysis *is* possible and onset of chaos *may be* understood analytically, for a large part, through ECMR.

As we discussed in the Introduction, the amplitude system (2.40a)–(2.40c) can hardly support more exciting dynamics, as it is essentially two-dimensional through the action of the nonlinearity εG in (2.3). A straightforward choice is amplifying that nonlinearity to G . Note that this does not affect the linear structure of the system near the trivial state – i.e., \mathcal{DT} and thus also the validity of assumptions **A1–A3** – which enabled our analysis in the previous sections. We discuss this modification below, deferring to Section 2.6 the discussion of codimension 2 bifurcations as possible organizing centers for chaos. We start from (cf. (2.3))

$$\begin{cases} U_t = \mathcal{L}U + \alpha U + F(U, V), \\ V_t = \varepsilon \mathcal{L}V + \varepsilon \beta U + \varepsilon \gamma V + G(x, U, V), \end{cases} \quad (2.52)$$

equipped with suitable BCs, and focus for specificity on nonlinearities G that are locally quadratic in U only. Spatial inhomogeneity, modeled here by an x -dependent G and which is also present in (2.1), will become important in Section 2.5.2. As we will see, the corresponding amplitude system is now infinite-dimensional, with all b_k -modes *nonlinearly* coupled to a_1 . To explore the consequences of this dramatic increase in dimensionality, we consider a special case in Section 2.5.2 and recover an essentially five-dimensional reduced system with chaotic dynamics. We conclude this exploratory piece with simulations of the full PDE system, through which we identify spatio-temporal chaos bearing strong similarities to that of the reduced system.

2.5.1 New amplitude equations

In this section, we set $G(x, U, V) = G_{20}(x)U^2$ at leading order in (U, V, ε) , with G_{20} an arbitrary function. We thus study a modification of (2.3) with an $\mathcal{O}(1)$, quadratic nonlinearity in the V -equation,

$$\begin{cases} U_t = \mathcal{L}U + \alpha U + F(U, V), \\ V_t = \varepsilon \mathcal{L}V + \varepsilon \beta U + \varepsilon \gamma V + G_{20}(x)U^2 + \mathcal{O}\left(\varepsilon UV, \varepsilon V^2, ||U^2 + V^2||^{3/2}\right); \end{cases} \quad (2.53)$$

the nonlinearity F is as in (2.27). We again equip the system with suitable BCs guaranteeing conditions **A1–A3**, and we set $\alpha = r\varepsilon^\sigma - \nu_1$ so that $(0, 0)$ destabilizes at $r = 0$.

The analysis proceeds along the same lines as that of system (2.3) in Section 2.3 and 2.4. Using a Fourier-like decomposition in terms of amplitudes and eigenfunctions for U and V – recall (2.25) – system (2.53) is written as an infinite-dimensional system of ODEs,

$$\begin{aligned} \dot{A}_k &= \lambda_k A_k + \sum_{l,m \geq 1} C_{klm} (F_{20} A_l A_m + F_{11} A_l B_m + F_{02} B_l B_m), \\ \dot{B}_k &= -\varepsilon M_k B_k + \varepsilon \beta A_k + \sum_{l,m \geq 1} H_{klm} A_l A_m + \mathcal{O}(\varepsilon A_l B_m, \varepsilon B_l B_m). \end{aligned} \quad (2.54)$$

Here, H_{klm} is the projection of $G_{20}\phi_l\phi_m$ onto ϕ_k ,

$$H_{klm} = \int_\Omega G_{20}(x)\phi_k(x)\phi_l(x)\phi_m(x) dx; \quad (2.55)$$

note that H_{klm} reduces to $G_{20}C_{klm}$ for a constant G_{20} , cf. (2.29). Using rescaling (2.32) with $\sigma_1 = \sigma_V = \sigma$ and $\sigma_U = 2\sigma$,

$$A_1 = \varepsilon^\sigma a_1, \quad A_k = \varepsilon^{2\sigma} a_k, \quad B_k = \varepsilon^\sigma b_k, \quad (2.56)$$

we derive a leading order amplitude system whose only difference from (2.34) is in the nonlinear terms for the b_k 's. Switching to $\tau = \varepsilon^\sigma t$, we obtain a leading order set of amplitude equations,

$$\begin{aligned}
 a'_1 &= ra_1 + C_{111}F_{20}a_1^2 + F_{11}a_1 \sum_{m \geq 1} C_{11m}b_m + F_{02} \sum_{l,m \geq 1} C_{1lm}b_lb_m \\
 &\quad + \mathcal{O}(\varepsilon^\sigma), \\
 \varepsilon^\sigma a'_k &= \lambda_k a_k + C_{k11}F_{20}a_1^2 + F_{11}a_1 \sum_{m \geq 1} C_{k1m}b_m + F_{02} \sum_{l,m \geq 1} C_{klm}b_lb_m \\
 &\quad + \mathcal{O}(\varepsilon^\sigma), \\
 \varepsilon^{\sigma-1} b'_1 &= -M_1 b_1 + \beta a_1 + \varepsilon^{\sigma-1} H_{111}a_1^2 + \mathcal{O}(\varepsilon^\sigma), \\
 \varepsilon^{\sigma-1} b'_k &= -M_k b_k + \varepsilon^{\sigma-1} H_{k11}a_1^2 + \mathcal{O}(\varepsilon^\sigma).
 \end{aligned} \tag{2.57}$$

Here again, a prime represents differentiation with respect to τ and C_{klm} , H_{klm} are reported in (2.29) and (2.55). For $\sigma > 1$, we recover classical center manifold reduction results, as was the case with (2.34). The slaving relations are

$$b_1 = \frac{\beta a_1}{M_1}, \quad b_k = 0, \quad a_k = \frac{C_{111}H}{\lambda_k}a_1^2, \tag{2.58}$$

compare with (2.36). Substituting into the ODE for a_1 and recalling definition (2.36), we can write

$$a'_1 = ra_1 + C_{111}Ha_1^2 + \mathcal{O}(\varepsilon^\sigma). \tag{2.59}$$

Note that, in agreement with theory, the newly introduced nonlinearity does not affect classical center manifold reduction. This changes as $\sigma \downarrow 1$: in that limit, and similar to system (2.34), the b_k -equations in system (2.57) retain their evolutionary character. The system of ODEs governing the behavior of (2.53) in the regime $\lambda_1 = \mathcal{O}(\varepsilon)$ is, up to $\mathcal{O}(\varepsilon)$ corrections,

$$\begin{cases} a'_1 = ra_1 + C_{111}F_{20}a_1^2 + F_{11}a_1 \sum_{n \geq 1} C_{1n1}b_n + \sum_{m,n \geq 1} C_{mn1}F_{02}b_mb_n, \\ b'_1 = -M_1 b_1 + \beta a_1 + H_{111}a_1^2, \\ b'_k = -M_k b_k + H_{k11}a_1^2, \quad \text{for } k \geq 2. \end{cases} \tag{2.60}$$

Asymptotically many b_k -modes interact now nonlinearly with the a_1 -mode *at leading order*. Again, a rigorous proof of the validity of our asymptotic method is necessary, but is not part of this chapter.

Note that system (2.60) resembles but is not identical to the one corresponding to (2.1). The readily apparent differences between the two systems – linear

coupling in (2.60) versus more quadratic terms in the other – are circumstantial and due to our working with (2.24), instead of with the eigenbasis as in [176]. A more appreciable difference concerns their coefficients, as the analogue of (2.29) in [176] involves two sets of eigenfunctions and is less transparent; recall Remark 2.2. Therefore, their corresponding flows may be widely different despite sharing the same functional form, see [66, 98].

In the exploratory spirit of this chapter, we choose not to study (2.60) in full generality but restrict ourselves, once again, to a transparent and highly illustrative special case.

2.5.2 Example: Revisiting our reaction-diffusion system

We work with $\mathcal{L} = \Delta$, $\Omega = (0, 1)$ and homogeneous Dirichlet BCs, as in Section 2.2.2; the eigenfunctions are still given by the simple formulas (2.22). To reach a middle ground between the two-dimensional (2.41) and the infinite-dimensional (2.60), we choose

$$G_{20}(x) = \frac{2\sqrt{2}}{3}A \sin(\pi x) + \sqrt{2}B \sin(2\pi x), \quad \text{with } A, B \in \mathbb{R} \text{ free parameters.}$$

With this choice,

$$\begin{aligned} H_{111} &= A, & H_{112} &= B, \\ H_{113} &= -\frac{1}{3}A, & H_{114} &= -\frac{1}{2}B \\ H_{11k} &= 0, \quad \text{for all } k \geq 5, \end{aligned} \tag{2.61}$$

so that the ODEs for b_k , with $k \geq 5$, only contain higher order nonlinearities: at leading order, $\dot{b}_k = -M_k b_k$. From this we conclude that all b_k with $k \geq 5$ approach exponentially an $\mathcal{O}(\varepsilon)$ value. Thus, we obtain an explicit, exponentially attracting, five-dimensional extended center manifold constraining b_k to $\mathcal{O}(\varepsilon)$ values, for $k \geq 5$, and with flow given by

$$\left\{ \begin{array}{l} a'_1 = ra_1 + C_{111}F_{20}a_1^2 + F_{11}\sum_{l \geq 1}C_{1l1}a_1b_l + F_{02}\sum_{k,l \geq 1}C_{kl1}b_kb_l, \\ b'_1 = -M_1b_1 + \beta a_1 + Aa_1^2, \\ b'_2 = -M_2b_2 + Ba_1^2, \\ b'_3 = -M_3b_3 - \frac{1}{3}Aa_1^2, \\ b'_4 = -M_4b_4 - \frac{1}{2}Ba_1^2. \end{array} \right. \tag{2.62}$$

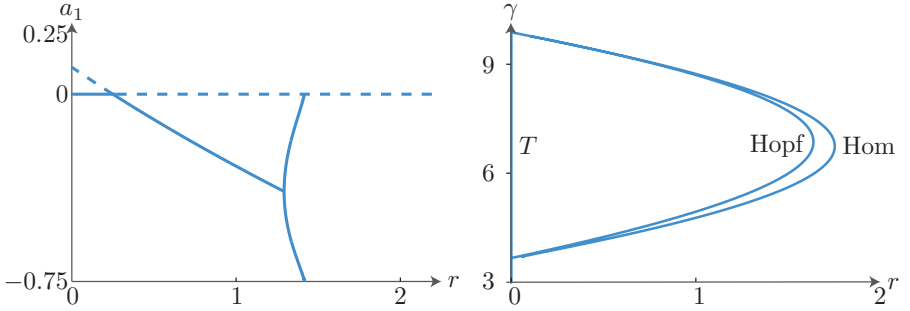


Figure 2.7: Bifurcation figures of system (2.62), with parameters $\beta = -4$, $F_{20} = -2$, $F_{11} = 5$, $F_{02} = 12$, $A = 0.2$ and $B = 0.5$. Left: Steady state diagram in terms of the bifurcation parameter r and the first amplitude a_1 ; here, $\gamma = 5$. Solid (dashed) lines denote stable (unstable) equilibria. The points labeled ‘T’ and ‘Hopf’ indicate a transcritical (coincides with the vertical axis) and a Hopf bifurcation. The solid curves emerging from the Hopf bifurcation measure the minimum/maximun a_1 -values of the bifurcating stable limit cycle. The limit cycle collides with the trivial steady state at ‘Hom,’ yielding a homoclinic bifurcation. Right: A two-parameter continuation in (r, γ) of these three bifurcations; the transcritical one occurs at $r = 0$.

The differential equations for a_1, b_1, b_2, b_3 and b_4 characterize the behavior of the amplitudes in the direction of the modes linking to $\lambda_1, \mu_1, \mu_2, \mu_3$ and μ_4 . Note how the addition of a special, inhomogeneous, $\mathcal{O}(1)$ nonlinearity has yielded a five-dimensional system as our extended center manifold reduction. We study this below using the ODE continuation toolbox MATCONT, discussing two distinct parameter sets in some detail to illustrate behavioral diversity in it. First, we fix $\beta = -4$, $\gamma = 5$, $F_{20} = -2$, $F_{11} = 5$ and $F_{02} = 12$ as in Figures 2.3 and 2.4. Note that these figures concern system (2.3), which only has an $\mathcal{O}(\varepsilon)$, spatially homogeneous nonlinearity. Also note that $\gamma < \gamma_T = \pi^2$, so that the small spectrum is stable. We also fix $A = 0.2$ and $B = 0.5$, leaving r to vary. The left panel of Figure 2.7 provides a bifurcation diagram of the destabilization of the trivial steady state $(a_1, b_1, b_2, b_3, b_4) = (0, 0, 0, 0, 0)$ of (2.62). We track, as r increases, the branches bifurcating from zero using the first amplitude, a_1 , as representative. In this way, we recover qualitatively the destabilization mechanism from Sections 2.2 and 2.4 (small, spatially homogeneous nonlinearity for V). Specifically, as r becomes positive, the trivial and nontrivial steady states exchange stability (transcritical). Tracking the nontrivial steady state for $r > 0$, we encounter a supercritical Hopf bifurcation at $r \approx 1.04$; of the stable limit cycle bifurcating from this point, we have drawn the minimum and maximum values

of a_1 . This limit cycle branch exists up to $r \approx 1.17$, where it becomes an orbit homoclinic to the trivial steady state. For larger r -values, we have found no other attractor. Note that this scenario corresponds precisely (albeit qualitatively) with our results in Sections 2.4.1 and 2.4.2.

The right panel of Figure 2.7 shows the continuation of these three bifurcations in two parameters: r and γ . This figure supports Conjecture 2.4.2 in the present case. If one increases r , starting from a negative value, then one first encounters a transcritical and then a supercritical Hopf bifurcation, which in turn is followed by a homoclinic bifurcation. Beyond this homoclinic bifurcation, orbits grow unboundedly and there seem to be no other attractors. At $(r, \gamma) = (0, \pi^2)$, there exists a transcritical Bogdanov-Takens point, see [23] for its unfolding. For negative values of r the bifurcation diagram is more subtle but we choose not to focus on that because this does not correspond to our analytical work.

For the parameter values reported above, we have seen no significant qualitative differences in the behavior of the reduced system (2.62) and of the original PDE system (2.3). This changes drastically if we retain $A = 0.2$ and $B = 0.5$ but switch to, for instance, $\beta = -2.2$, $\gamma = 6$, $F_{20} = -0.6$, $F_{11} = 3$ and $F_{02} = -3$. Using r as a bifurcation parameter, we observe that the transcritical bifurcation at $r = 0$ persists, see the left panel of Figure 2.8. Tracing the nontrivial steady state stabilized at $r = 0$, we see that it first encounters two saddle-node points at $r \approx 11.55$ and $r \approx 1.80$, before a Hopf bifurcation at $r \approx 5.99$ occurs. This Hopf bifurcation is supercritical, and again we have plotted the minimum and maximum of the limit cycle that arises there. Since this stable limit cycle exists for r -values where the nontrivial steady state is stable, there is bistability of both a steady state and a periodic solution. Contrary to the Hopf bifurcation in the left panel of Figure 2.7, the limit cycle here undergoes several period-doubling bifurcations and becomes chaotic, before terminating again in a homoclinic orbit for larger r -values ($r \approx 30$).

In the right panel of Figure 2.8, we have plotted all five Lyapunov exponents corresponding to the chaotic orbit from $r = 7$ onwards. At $r = 7.34$, the first Lyapunov exponent becomes positive, indicating chaos. Increasing r even further, the chaotic orbit persists and its magnitude grows, until it collides with a saddle steady state at $r = 7.53$. For larger values of r , all orbits escape to infinity. See the left panel of Figure 2.9, where the chaotic orbit itself is plotted for $r = 7.49$. In a simulation of the full PDE (2.3) with the same parameter values, we recover the same period-doubling scenario leading to chaos as in (2.1). However, at $r = 7.49$ the PDE is still in the ‘*double period-regime*’, whereas the ODE reduction already shows a chaotic orbit. This can be understood by the fact that our approach only yields leading order accuracy and $\varepsilon = 0.01$. In principle, the incorporation of higher order terms is expected to improve the correspondence between

the reduced and the full system, especially through the slaving relations for a_k with $k \geq 2$. Note that $a_1 \sim 15\text{--}30$ in the chaotic regime, thus $A_1 = \varepsilon a_1 \sim 0.15\text{--}0.30$, see (2.56) with $\sigma = 1$; this is already near the boundary for which one would expect an asymptotic method to work.

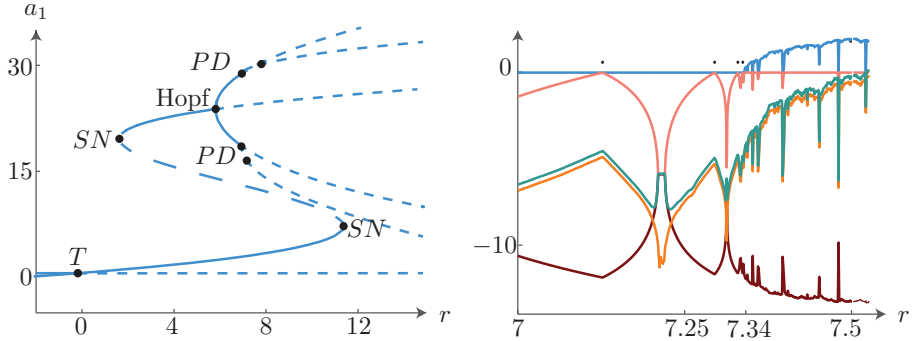


Figure 2.8: Left: A bifurcation diagram corresponding to system (2.62). The parameter set is $\beta = -2.2$, $\gamma = 6$, $F_{20} = -0.6$, $F_{11} = 3$, $F_{02} = -3$, $A = 0.2$ and $B = 0.5$; r is varied. The nontrivial equilibrium first undergoes a transcritical bifurcation (T), then loses stability through a saddle-node bifurcation (SN), and becomes stable again through another saddle-node. After that, a supercritical Hopf bifurcation occurs (Hopf). We have plotted the maximum and minimum value of the stable limit cycles that arise. These undergo period-doubling bifurcations (PD), of which we marked two. Right: The five Lyapunov exponents corresponding to the chaotic orbit, shown with five different colors, varying with r . At $r \approx 7.34$, the first Lyapunov exponent becomes positive. At $r \approx 7.53$, the chaotic orbit collides with a saddle steady state, after which the chaotic orbit no longer exists. The black dots mark the r -values at which period-doubling bifurcations occur.

Remark 2.3. For parameters in a regime where the Hopf bifurcation is subcritical and with β small enough, we observe behavior similar to the right panel of Figure 2.7. In that case, the periodic orbit originating at the Hopf bifurcation exists for $r < r_H$, but it again accumulates onto a homoclinic orbit. The branch of homoclinic bifurcations in (r, γ) -space is now bounded by the transcritical branch to its left and the Hopf branch to its right.

2.6 Codimension 2 bifurcations

As explained in the Introduction, it was analyzed in [177] that the organizing center of chaos in the phytoplankton-nutrient model (2.1) corresponds to a

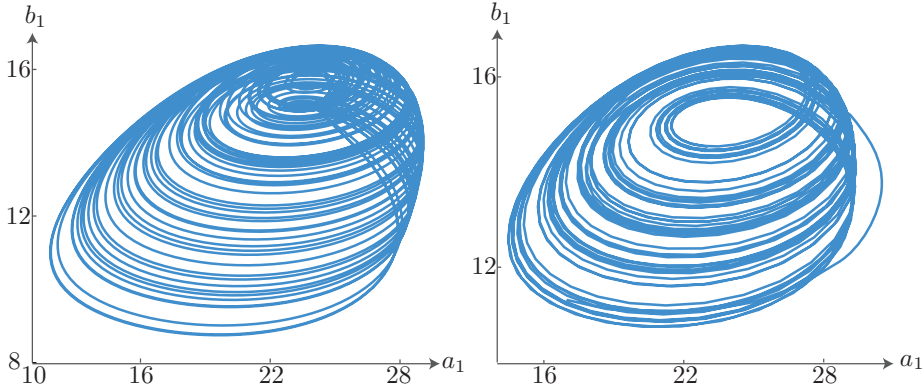


Figure 2.9: Two similar chaotic attractors obtained by simulating the ODE (left) and the PDE (right), with $\beta = -2.2$, $\gamma = 6$, $F_{20} = -0.6$, $F_{11} = 3$, $F_{02} = -3$, $A = 0.2$ and $B = 0.5$. (a) $r = 7.49$. (b) $r = 7.7$, $\varepsilon = 0.01$ and $G_{20}(x) = \frac{2}{3}\sqrt{2}A\sin(\pi x) + \sqrt{2}B\sin(2\pi x)$. The operator is $\mathcal{L} = \Delta$ on the one-dimensional domain $(0, 1)$ and with homogeneous Dirichlet boundary conditions.

codimension 2 bifurcation – a point where two eigenvalues cross the imaginary axis simultaneously. In this section, we investigate the type of phenomena that such points can give rise to, within the context of our model problem (2.3). In the specific case of (2.1), the small spectrum remains contained in the negative semi-axis for all parameter values [176]. We therefore also focus on the case where (also) the second eigenvalue crossing the origin is ‘large’. It is neither our intention nor within the scope of this chapter to offer a complete treatment of all possible transcritical codimension 2 bifurcations in system (2.3). We are primarily interested, instead, in giving an indication of the variety of low-dimensional dynamics exhibited by (2.3) and related models in a codimension 2 setting, which are not captured by classical center manifold reduction.

We present our work below in the general setting of a multidimensional bounded domain $\Omega \subset \mathbb{R}^n$. In Section 2.6.1, we construct and treat an abstract codimension 2 situation, where the two leading eigenvalues λ_1 and λ_2 of \mathcal{DT} cross zero simultaneously in a two-component system (i.e., with scalar U and V), see Proposition 2.2.1 and Figure 2.10. We reduce the PDE system to a four-dimensional ODE one and subsequently consider another type of codimension 2 bifurcation in Section 2.6.2. In this system with an extra component, we find that the flow on the extended center manifold is three-dimensional, illustrating our results further by means of our reaction-diffusion example with an additional component.

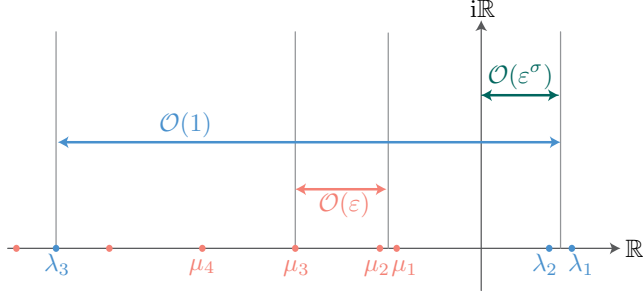


Figure 2.10: Schematic depiction of a codimension 2 bifurcation where λ_1 and λ_2 pass through the origin, while all other eigenvalues remain in the stable half-plane.

2.6.1 Coincidence of the two largest eigenvalues

We first consider the case in which λ_1 and λ_2 cross through the imaginary axis simultaneously, as is depicted in Figure 2.10. Recalling the characterization of eigenvalues in Proposition 2.2.1, we conclude that the two largest eigenvalues of \mathcal{L} – recall the associated spectral problem (2.8) – are necessarily equal, $\nu_1 = \nu_2$. We show that, in this case, our PDE system (2.3) is reducible to a four-dimensional ODE system close to the bifurcation, and we examine the rich dynamics of that reduced system. Note for definiteness that, in our choice of example $\mathcal{L} = \Delta$ with homogeneous Dirichlet BCs on a bounded domain $\Omega \in \mathbb{R}^n$, the first eigenvalues cannot collide [54, 59]. However, there exist combinations of operators, spatial domains and BCs for which assumptions **A1–A3** are satisfied and $\nu_1 = \nu_2$ holds. One such example is $\mathcal{L} = -\Delta^2$ considered on an annulus and with homogeneous BCs for the zeroth and second order derivatives, see [54] for details. Following ideas from that work, we parametrize by a scalar parameter κ a one-dimensional, continuous family of bounded domains $\{\Omega_\kappa\}_\kappa$, with piecewise continuous boundaries. The eigenvalues ν_k corresponding to linear differential operator \mathcal{L} are thus parametrized by κ too, so we write $\{\nu_k(\kappa)\}_k$ for the spectrum of this operator on Ω_κ . To set us up for our analysis, we next assume the existence of a κ^* for which

$$\dots < \nu_3(\kappa^*) < \nu_2(\kappa^*) = \nu_1(\kappa^*),$$

and we further assume, for ν_1 and ν_2 , asymptotic expansions in powers of κ up to first-order:

$$\nu_i(\kappa) = \nu_1(\kappa^*) + (\kappa - \kappa^*)\nu_{i,1}(\kappa^*) + \mathcal{O}(|\kappa - \kappa^*|^2),$$

for $i = 1, 2$ and with $\nu_{1,1}(\kappa^*) \neq \nu_{2,1}(\kappa^*)$. Finally, to avoid introducing generalized eigenfunctions, we further assume that the eigenspaces corresponding to these two eigenvalues do not coincide, as $\kappa \rightarrow \kappa^*$ – this is also the case for $-\Delta^2$ considered in [54]. At $\kappa = \kappa^*$, the equality $\nu_1 = \nu_2$ automatically yields $\lambda_1 = \lambda_2$ and $\mu_1 = \mu_2$ for the eigenvalues of \mathcal{DT} , see (2.13)–(2.14). Note that the equality $\mu_1 = \mu_2$ is an accidental consequence of modeling the evolution of U and V by the same operator \mathcal{L} . We additionally assume the small spectrum to remain ‘harmless’ (negative) and set for our analysis

$$\kappa = \kappa^* + s\varepsilon^\sigma,$$

with $s \in \mathbb{R}$ and $\sigma > 0$. The asymptotic expansions for ν_1 and ν_2 allow us to write, then,

$$\begin{aligned}\nu_1(\kappa) &= \nu_1(\kappa^*) + s\varepsilon^\theta \nu_{1,1}(\kappa^*) + \mathcal{O}(\varepsilon^{2\theta}), \\ \nu_2(\kappa) &= \nu_1(\kappa^*) + s\varepsilon^\theta \nu_{2,1}(\kappa^*) + \mathcal{O}(\varepsilon^{2\theta}).\end{aligned}$$

As usual, we rescale α according to

$$\alpha = r\varepsilon^\sigma - \nu_1(\kappa^*) \quad \text{and also demand that } \gamma < \gamma_T,$$

thus positioning λ_1 and λ_2 at an $\mathcal{O}(\varepsilon^\sigma)$ distance inside the right half of the complex plane. Here again, r is the bifurcation parameter; the eigenvalues are, to leading order,

$$\begin{aligned}\lambda_1(\kappa) &= (r + s\nu_{1,1}(\kappa^*))\varepsilon^\sigma = \varepsilon^\sigma L_1, \\ \lambda_2(\kappa) &= (r + s\nu_{2,1}(\kappa^*))\varepsilon^\sigma = \varepsilon^\sigma L_2.\end{aligned}\tag{2.63}$$

As before, we set $\mu_k = -\varepsilon M_k$ and consider (L_1, L_2) as new and independent bifurcation parameters. Note that varying them is equivalent to varying (r, s) , since $\nu_{1,1}(\kappa^*) \neq \nu_{2,1}(\kappa^*)$ by assumption. Further, we assume the setting of Section 2.4, where the nonlinearity co-driving V is weak. Returning to the basic system (2.3) and substituting amplitude expansion (2.25), then, we again obtain system (2.30) but with two weakly unstable A_k -modes. This is not surprising, as the A_k -modes link directly to the two destabilizing eigenvalues λ_1 and λ_2 ; all other modes remain stable. We thus rescale the amplitudes accordingly,

$$\begin{aligned}A_1 &= \varepsilon^\sigma a_1, & A_k &= \varepsilon^{2\sigma} a_k, & \text{for } k \geq 3 \\ A_2 &= \varepsilon^\sigma a_2, & B_k &= \varepsilon^\sigma b_k, & \text{for } k \geq 1,\end{aligned}\tag{2.64}$$

with $\sigma > 0$. The amplitude system becomes,

$$\begin{aligned} a'_i &= L_i a_i + F_{20}(C_{i11}a_1^2 + 2C_{i21}a_1a_2 + C_{i22}a_2^2) \\ &\quad + F_{11} \left(a_1 \sum_{m \geq 1} C_{i1m}b_m + a_2 \sum_{m \geq 1} C_{i2m}b_m \right) + F_{02} \sum_{l,m \geq 1} C_{ilm}b_l b_m, \\ \varepsilon^\sigma a'_k &= \lambda_k a_k + F_{20} (C_{k11}a_1^2 + 2C_{k12}a_1a_2 + C_{k22}a_2^2) \\ &\quad + F_{11} \left(a_1 \sum_{m \geq 1} C_{k1m}b_m + a_2 \sum_{m \geq 1} C_{k2m}b_m \right) + F_{02} \sum_{l,m \geq 1} C_{klm}b_l b_m, \end{aligned} \tag{2.65}$$

$$\begin{aligned} \varepsilon^\sigma b'_i &= -\varepsilon M_i b_i + \varepsilon \beta a_i, \\ \varepsilon^\sigma b'_k &= -\varepsilon M_k b_k, \end{aligned} \tag{2.65}$$

for $i = 1, 2$ and $k \geq 3$. to leading order and expressed in $\tau = \varepsilon t$. Again, a critical transition occurs when $\sigma = 1$, see (2.34), in which regime the spectral gap condition is violated.

We first consider the case $\sigma > 1$, in which the spectral gap is of sufficient width. The leading order slaving relations are, then,

$$b_1 = \frac{\beta a_1}{M_1}, \quad b_2 = \frac{\beta a_2}{M_2} \quad \text{and} \quad b_k = 0, \quad \text{for } k \geq 3. \tag{2.66}$$

The classical center manifold (recall $\sigma > 1$) is two-dimensional, with the flow on it given by

$$\begin{cases} a'_1 = L_1 a_1 + C_{111}H_{11}a_1^2 + 2C_{121}H_{12}a_1a_2 + C_{122}H_{22}a_2^2, \\ a'_2 = L_2 a_2 + C_{211}H_{11}a_1^2 + 2C_{221}H_{12}a_1a_2 + C_{222}H_{22}a_2^2. \end{cases} \tag{2.67}$$

Here, we have applied the slaving relations and defined the quantities

$$H_{ij} = F_{20} + \frac{F_{11}\beta}{2} \left(\frac{1}{M_i} + \frac{1}{M_j} \right) + \frac{F_{02}\beta^2}{M_i M_j}, \quad \text{for } i, j = 1, 2.$$

This is as expected, for a degenerate codimension 2 transcritical bifurcation of the present type. Moreover, $M_1 = M_2 + \mathcal{O}(\varepsilon^{\sigma-1})$, since $\nu_1 = \nu_2 + \mathcal{O}(\varepsilon^\sigma)$. Hence, $H_{11} = H_{12} = H_{22} = H$ at leading order, cf. (2.36), and (2.67) simplifies to

$$\begin{cases} a'_1 = L_1 a_1 + H(C_{111}a_1^2 + 2C_{112}a_1a_2 + C_{122}a_2^2), \\ a'_2 = L_2 a_2 + H(C_{112}a_1^2 + 2C_{122}a_1a_2 + C_{222}a_2^2). \end{cases} \tag{2.68}$$

Note that the validity of center manifold reduction can, in principle, be rigorously established by classical methods [9, 18, 160]. The trivial state $(U, V) = (0, 0)$, represented by $(a_1, b_1) = (0, 0)$, remains a steady state with eigenvalues $\Lambda_1 = L_1$ and $\Lambda_2 = L_2$. Since steady states now correspond to intersections of two conic sections, there are up to three more steady states (a_1^*, a_2^*) with Jacobian matrix

$$\begin{aligned} J(a_1^*, a_2^*) &= \begin{pmatrix} L_1 + 2H(C_{111}a_1^* + C_{112}a_2^*) & 2H(C_{112}a_1^* + C_{122}a_2^*) \\ 2H(C_{112}a_1^* + C_{122}a_2^*) & L_2 + 2H(C_{122}a_1^* + C_{222}a_2^*) \end{pmatrix} \\ &= \begin{pmatrix} J_{11} & J_{12} \\ J_{12} & J_{22} \end{pmatrix}. \end{aligned} \tag{2.69}$$

Note that the off-diagonal terms are equal; the eigenvalues Λ_{\pm} of matrices of this form are

$$\begin{aligned} \Lambda_{\pm} &= \frac{J_{11} + J_{22} \pm \sqrt{(J_{11} + J_{22})^2 - 4(J_{11}J_{22} - J_{12}^2)}}{2} \\ &= \frac{J_{11} + J_{22} \pm \sqrt{(J_{11} - J_{22})^2 + 4J_{12}^2}}{2}, \end{aligned}$$

and they are necessarily real. Hence, none of the steady states can undergo oscillatory destabilization. The two eigenvalues can, however, change signs when $J_{11}J_{22} = J_{12}^2$, and a fixed point may gain or lose stability.

Next, we analyze the regime $\sigma = 1$ for system (2.65). Here again, the b_k -amplitudes are no longer slaved but evolve in the same timescale as a_1 and a_2 . Up to $\mathcal{O}(\varepsilon)$ corrections,

$$\begin{aligned} a'_i &= L_i a_i + F_{20} (C_{i11}a_1^2 + 2C_{i21}a_1 a_2 + C_{i22}a_2^2) \\ &\quad + F_{11} \left(a_1 \sum_{m \geq 1} C_{i1m} b_m + a_2 \sum_{m \geq 1} C_{i2m} b_m \right) + F_{02} \sum_{l,m \geq 1} C_{ilm} b_l b_m, \\ b'_i &= -M_i b_i + \beta a_i, \\ b'_k &= -M_k b_k, \end{aligned} \tag{2.70}$$

for $i = 1, 2$ and $k \geq 3$. System (2.70) contains two quadratically nonlinear ODEs and infinitely many linear ones. Similar to Section 2.4.1, the b_k -modes for $k \geq 3$ decouple, at leading order, and are slaved to $\mathcal{O}(\varepsilon)$ values. We formally conclude that, in this extended region and codimension 2 setting, the small amplitude flow of the PDE system (2.3) is attracted to a four-dimensional invariant manifold,

the flow on which is approximately described by

$$\begin{aligned} a'_i &= L_i a_i + F_{20} (C_{i11} a_1^2 + 2C_{i21} a_1 a_2 + C_{i22} a_2^2) + F_{11} a_1 (C_{i11} b_1 + C_{i12} b_2) \\ &\quad + F_{11} a_2 (C_{i21} b_1 + C_{i22} b_2) + F_{02} (C_{i11} b_1^2 + 2C_{i12} b_1 b_2 + C_{i22} b_2^2), \\ b'_i &= -M_i b_i + \beta a_i, \end{aligned} \tag{2.71}$$

for $i = 1, 2$. The validity of this reduction is not proved in this study. We refrain from delving into the characteristics of this flow, as the sheer number of parameters ensures the existence of rich dynamics. We do note, however, that the corresponding equilibria will naturally undergo Hopf bifurcations. Thus, also in this codimension 2 case, transcritical bifurcations may generally be followed by Hopf bifurcations within an $\mathcal{O}(\varepsilon)$ neighborhood.

2.6.2 A three-component system

We consider an extended version of system (2.3), namely the 3-component model (2.5) from the Introduction. The operator \mathcal{L} , spatial domain Ω and BCs satisfy assumptions **A1–A3**. The constants α_1 , α_2 , β_1 , β_2 , ρ_2 and γ are all real, and the nonlinearities $F_1(U_1, U_2, V)$, $F_2(U_1, U_2, V)$ and $G(U_1, U_2, V)$ are smooth functions of their arguments. Moreover, we have introduced ‘diffusion’ coefficients $D_1, D_2 > 0$, both of which are $\mathcal{O}(1)$ with respect to ε ; this is natural in reaction-diffusion 3-component models, since $D_1 \neq D_2$ in general. More importantly, we now have the V -component feeding into the U_2 -equation through (weak) linear coupling; cf. the term $\varepsilon \rho_2 V$ in the system. No such mechanism exists for U_1 , as was also the case in system (2.3). The rationale behind this *weak* extension of the core system (2.3) is its becoming significant in the *leading order* extended center manifold reduction (ECMR) we derive below. In that, it highlights how different unfoldings of the primary bifurcation may excite different dynamic modes in the ECMR regime.

By construction, the background state $(U_1, U_2, V) \equiv (0, 0, 0)$ has 3 distinct sets of eigenvalues. Assuming that both $\alpha_2 + D_2 \nu_k$ and $\gamma + \nu_k$ are $\mathcal{O}(1)$ and bounded away from zero, it follows quite straightforwardly that, for $k \geq 1$,

$$\begin{aligned} \lambda_{1,k} &= \alpha_1 + D_1 \nu_k, \\ \lambda_{2,k} &= \alpha_2 + D_2 \nu_k + \mathcal{O}(\varepsilon^2), \\ \mu_k &= \varepsilon(\gamma + \nu_k) + \mathcal{O}(\varepsilon^2) = -\varepsilon M_k + \mathcal{O}(\varepsilon^2), \end{aligned} \tag{2.72}$$

with ν_k the eigenvalue associated with \mathcal{L} – see Proposition 2.2.1 and Figure 2.1. Here, $\lambda_{1,k}$ is associated with the PDE for U_1 and boundary conditions, and $\{\lambda_{2,k}\}_{k \geq 1}$ is the spectrum associated with U_2 and the boundary conditions.

Thus, the ‘new’ term $\varepsilon\rho_2V$ only has an $\mathcal{O}(\varepsilon^2)$ effect on both $\lambda_{2,k}$ and μ_k . In the bifurcational case where we set $\alpha_2 + D_2\nu_1 = r_2\varepsilon^\sigma$, with $\sigma \geq 1$ and $r_2 = \mathcal{O}(1)$, the effect of ρ_2 through $\varepsilon\rho_2V$ is larger – $\mathcal{O}(\varepsilon^{2-\sigma})$. Even though $\gamma + \nu_k \neq 0$ is still $\mathcal{O}(1)$, ρ_2 also impacts μ_1 . In fact, in the critical case $\sigma = 1$, the eigenvalues $\lambda_{2,1}$ and μ_1 are both $\mathcal{O}(\varepsilon)$ and they are the solutions L of the equation

$$L^2 + \varepsilon L(M_1 - r_2) - \varepsilon^2(r_2M_1 + \beta_2\rho_2) = 0. \quad (2.73)$$

However, except for some notational inconveniences, this feature has no effect on our method.

Our aim is to study the codimension 2 transcritical bifurcation in which the ‘large’ primary eigenvalues $\lambda_{1,1}$ and $\lambda_{2,1}$ cross zero simultaneously. Before that, we first understand the codimension 1 case, where only $\lambda_{1,1}$ is $\mathcal{O}(\varepsilon^\sigma)$ close to zero and $\lambda_{2,1}$ far behind it; here, $\sigma \geq 1$ as in Section 2.4. To set up our analysis, we assume that $\alpha_2 + D_2\nu_1 < 0$ and $\gamma + \nu_1 < 0$ are $\mathcal{O}(1)$. Mimicking our approach in Section 2.3, cf. (2.25), we introduce the amplitudes $A_{1,k}(t)$, $A_{2,k}(t)$ and $B_k(t)$ through

$$\begin{pmatrix} U_1(x,t) \\ U_2(x,t) \\ V(x,t) \end{pmatrix} = \sum_{k \geq 1} \phi_k(x) \begin{pmatrix} A_{1,k}(t) \\ A_{2,k}(t) \\ B_k(t) \end{pmatrix}. \quad (2.74)$$

Here the (rescaled) amplitudes $A_{1,k}$, $A_{2,k}$ and B_k link directly to the eigenvalues $\lambda_{1,k}$, $\lambda_{2,k}$ and μ_k . The new coupling term $\varepsilon\rho_2V$ suggests a rescaling differing in the particulars from that of Section 2.3,

$$\begin{aligned} \lambda_{1,1} &= r_1\varepsilon^\sigma, & A_{1,1} &= \varepsilon^\sigma a_{1,1}, & A_{1,k} &= \varepsilon^{2\sigma} a_{1,k}, \\ A_{2,\ell} &= \varepsilon^{1+\sigma} a_{2,\ell}, & B_\ell &= \varepsilon^\sigma b_\ell, \end{aligned} \quad (2.75)$$

for $k \geq 2$ and $\ell \geq 1$. We also write $M_k = -(\gamma + \nu_k)$, as for the two-components system (2.3), and expand the nonlinearities restricting to quadratic terms, cf. (2.27). For $i = 1, 2$, then,

$$\begin{aligned} F_i(U, V) &= F_{i,200}U_1^2 + F_{i,110}U_1U_2 + F_{i,101}U_1V \\ &\quad + F_{i,020}U_2^2 + F_{i,011}U_2V + F_{i,002}V^2, \\ G(U, V) &= G_{200}U_1^2 + G_{110}U_1U_2 + G_{101}U_1V \\ &\quad + G_{020}U_2^2 + G_{011}U_2V + G_{002}V^2. \end{aligned} \quad (2.76)$$

For $\sigma > 1$, classical center manifold reduction is possible with the equivalent of (2.37) being

$$a'_{1,1} = r_1a_{1,1} + C_{111}H_1a_{1,1}^2 + \mathcal{O}(\varepsilon); \quad (2.77)$$

here, the time derivative is taken with respect to $\tau = \varepsilon^\sigma t$ and

$$H_1 = F_{1,200} + \frac{F_{1,101}\beta_1}{M_1} + \frac{F_{1,002}\beta_1^2}{M_1^2}. \quad (2.78)$$

This ODE is coupled to the slaving relations,

$$\begin{aligned} a_{1,k} &= -\frac{1}{\lambda_{1,k}} [C_{11k} H_1 a_{1,1}^2] + \mathcal{O}(\varepsilon), \\ a_{2,1} &= -\frac{\rho_2 \beta_1}{M_1 \lambda_{2,1}} a_{1,1} + \mathcal{O}(\varepsilon^{\sigma-1}), \\ a_{2,k} &= 0 + \mathcal{O}(\varepsilon^{\sigma-1}), \\ b_1 &= \frac{\beta_1}{M_1} a_{1,1} + \mathcal{O}(\varepsilon^{\sigma-1}, \varepsilon^2), \\ b_k &= 0 + \mathcal{O}(\varepsilon^{\sigma-1}), \end{aligned} \quad (2.79)$$

where $k \geq 2$. All $a_{2,k}$ -modes except for the first one then behave as additional b_k -modes for $\sigma > 1$. The eigenvalues $\lambda_{2,k}$, $k \geq 2$ induce the same kind of behavior as the μ_k induce. This changes beyond center manifold reduction, as $\sigma \downarrow 1$. In that regime, the $a_{2,k}$ -modes ($k \geq 2$) remain slaved – now to both $a_{1,1}$ and b_1 – but neither $a_{2,k}$ nor b_k with $k \geq 2$ are higher order anymore; we find that $b'_k = -M_k b_k$ at leading order ($k \geq 2$), similar to (2.40). We therefore have $b_k = \mathcal{O}(\varepsilon)$ for those k -values and may rewrite the three-component system (2.5) as a two-dimensional system of amplitude equations resembling (2.41),

$$\begin{cases} a'_{1,1} = r_1 a_{1,1} + C_{111} (F_{1,200} a_{1,1}^2 + F_{1,101} a_{1,1} b_1 + F_{1,002} b_1^2) + \mathcal{O}(\varepsilon), \\ b'_1 = -M_1 b_1 + \beta_1 a_{1,1} + \mathcal{O}(\varepsilon). \end{cases} \quad (2.80)$$

The evolution of the slaved modes is dictated by this system and the slaving relations,

$$\begin{aligned} a_{1,k} &= -\frac{1}{\lambda_{1,k}} [C_{11k} (F_{1,200} a_{1,1}^2 + F_{1,101} a_{1,1} b_1 + F_{1,002} b_1^2)] + \mathcal{O}(\varepsilon), \\ a_{2,1} &= -\frac{1}{\lambda_{2,1}} [C_{111} (F_{2,200} a_{1,1}^2 + F_{2,101} a_{1,1} b_1 + F_{2,002} b_1^2) + \rho_2 b_1] + \mathcal{O}(\varepsilon), \\ a_{2,k} &= -\frac{1}{\lambda_{2,k}} [C_{11k} (F_{2,200} a_{1,1}^2 + F_{2,101} a_{1,1} b_1 + F_{2,002} b_1^2)] + \mathcal{O}(\varepsilon), \end{aligned}$$

for $k \geq 2$. Thus, we may conclude that the (codimension 1) transcritical bifurcation generates precisely the same behavior in the 3-component model (2.5)

as in the 2-component one (2.3) up to and including the regime $\sigma = 1$ covered by extended center manifold reduction.

We now proceed to analyze the codimension 2 bifurcation. To facilitate our presentation, we introduce the quadratic polynomials (cf. (2.76))

$$\mathcal{F}_j(a, b, c) = F_{j,200}a^2 + F_{j,110}ab + F_{j,101}ac + F_{j,020}b^2 + F_{j,011}bc + F_{j,002}c^2, \quad (2.81)$$

$j = 1, 2$. Note that (2.77), for instance, can now be rewritten as

$$a'_{1,1} = r_1 a_{1,1} + C_{111} \mathcal{F}_1(a_{1,1}, 0, \beta_1 a_{1,1}/M_1) + \mathcal{O}(\varepsilon). \quad (2.82)$$

The polynomials \mathcal{F}_j can be similarly introduced in (2.78), as well as in the slaving relations (2.79). To generate a codimension 2 bifurcation, we tune $D_1, D_2, \alpha_1, \alpha_2$ and introduce r_1, r_2 by

$$\alpha_1 + D_1 \nu_1 = \lambda_{1,1} = r_1 \varepsilon^\sigma \quad \text{and} \quad \alpha_2 + D_2 \nu_1 = r_2 \varepsilon^\sigma, \quad \text{with } \sigma \geq 1, \quad (2.83)$$

cf. (2.72); the spectrum is depicted in Figure 2.11. Note that $\alpha_2 + D_2 \nu_1 \neq \lambda_{2,1}$; the equality only holds at leading order, due to the presence of $\varepsilon \rho_2 V$ in (2.5); cf. (2.72) again. We also set $M_k = -(\gamma + \nu_k)$ and assume M_1 to be $\mathcal{O}(1)$ and nonzero but not necessarily negative.

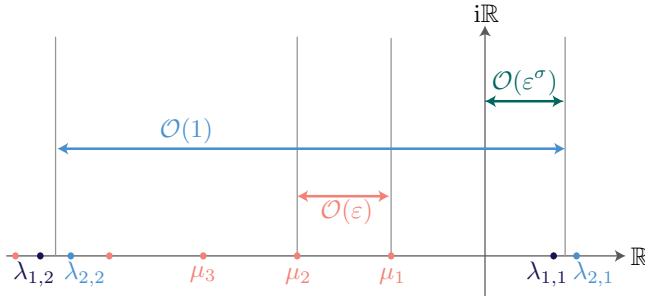


Figure 2.11: Schematic representation of the eigenvalues determining the stability of $(U_1, U_2, V) = (0, 0, 0)$ in system (2.5) and in the codimension 2 setting (2.83). All eigenvalues are negative except for the primary ones, $\lambda_{1,1}$ and $\lambda_{2,1}$, which are positive and $\mathcal{O}(\varepsilon^\sigma)$. All three eigenvalue sets are unbounded below.

We skip the case $\sigma > 1$ (but see Remark 2.4) and proceed immediately to $\sigma = 1$. We rescale as

$$\begin{aligned} A_{1,1} &= \varepsilon^\sigma a_{1,1}, & A_{1,k} &= \varepsilon^{2\sigma} a_{1,k}, \\ A_{2,1} &= \varepsilon^\sigma a_{2,1}, & A_{2,k} &= \varepsilon^{\sigma+1} a_{2,k}, & B_\ell &= \varepsilon^\sigma b_\ell, \end{aligned} \quad (2.84)$$

for $k \geq 2$ and $\ell \geq 1$, see (2.74). The $a_{1,k}$ - and $a_{2,k}$ -modes remain slaved for all $k \geq 2$, while again $b_k = -M_k b_k$ at leading order; the situation is analogous to the two-component case, recall Section 2.4. Following the path we carved in that case, we restrict ourselves naturally to the exponentially attracting subspace $\{b_k = \mathcal{O}(\varepsilon)\}_{k \geq 2}$. Up to $\mathcal{O}(\varepsilon)$ corrections the a priori infinite-dimensional flow then reduces to a three-dimensional one,

$$\begin{cases} a'_{1,1} = r_1 a_{1,1} + C_{111} \mathcal{F}_1(a_{1,1}, a_{2,1}, b_1), \\ a'_{2,1} = r_2 a_{2,1} + \rho_2 b_1 + C_{111} \mathcal{F}_2(a_{1,1}, a_{2,1}, b_1), \\ b'_1 = \beta_1 a_{1,1} + \beta_2 a_{2,1} + (\gamma + \nu_1) b_1. \end{cases} \quad (2.85)$$

It thus turns out that the three-component, codimension 2 equivalent of the two-component, codimension 1 (planar and quadratic) extended center manifold reduction (2.80) is the three-dimensional, quadratic system (2.85). In this chapter, we study neither the dynamics generated by system (2.85) nor the bifurcational structure associated with it in any detail; we have done so for the planar flow generated by (2.80), recall Sections 2.4.1 and 2.4.2. We do, however, observe that the celebrated Lorenz system [104] belongs to the family of systems described by (2.85), as can be seen by setting

$$x(t) = b_1(\tau), \quad y(t) = a_{2,1}(\tau), \quad z(t) = a_{1,1}(\tau),$$

and choosing the $F_{j,klm}$ -coefficients of $\mathcal{F}_j(z, y, x)$, see (2.81), so that

$$C_{111} \mathcal{F}_1(z, y, x) = xy \quad \text{and} \quad C_{111} \mathcal{F}_2(z, y, x) = -xz.$$

Then, (2.85) reduces to

$$\begin{cases} \dot{x} = (\gamma + \nu_1)x + \beta_2 y + \beta_1 z, \\ \dot{y} = \rho_2 x + r_2 y - xz, \\ \dot{z} = r_1 z + xy, \end{cases} \quad (2.86)$$

which is equivalent to the Lorenz system with parameters (σ, b, r) , upon setting

$$(r_1, r_2, \beta_1, \beta_2, \gamma, \rho_2) = (-b, -1, 0, \sigma, -\sigma - \nu_1, r).$$

Note that, at first glance, setting both r_1 and r_2 negative suggests that $\lambda_{1,1}$ and $\lambda_{2,1}$ are stable. However, recall that we have set $\alpha_2 + D_2 \nu_1 = r_2 \varepsilon$, and the eigenvalues of the trivial state are not represented by (2.72) but rather as solutions of (2.73) instead. A direct check yields that $\lambda_{1,1}, \lambda_{2,1}, \mu_1$ indeed correspond directly to the eigenvalues of the unstable critical point $(0, 0, 0)$ of (2.86).

It is apparent in our approach, but we nevertheless underline it here, that there is a significant difference between our derivation of (2.85) and the derivation of the Lorenz model. In particular, the Lorenz model is a *truncation* of the full flow of the infinite-dimensional convective system considered in [104], which approximates neither quantitatively nor qualitatively the dynamics of that original model; see [147] and the Introduction. Instead, (2.85) describes the flow on a three-dimensional manifold which *attracts by construction* the dynamics of small amplitude solutions – scaled as in (2.84) – of the singularly perturbed evolution equation (2.5). It is for this reason that (2.85) *does* approximate the full dynamics of (2.5) asymptotically: see Figure 2.2, where the celebrated Lorenz butterfly is plainly visible. Note that the figure was produced by a direct simulation of the PDE system (2.5), with $\mathcal{L} = \Delta$, $\Omega = (0, 1)$, Dirichlet BCs – similar to Section 2.2.2 – and all parameters tuned to the standard chaotic parameter combination $(\sigma, b, r) = (10, 8/3, 28)$ in the Lorenz model. Indeed, for these parameter values – as in Figure 2.2 – the solutions of (2.73) are $\lambda_{2,1} > 0$ and $\mu_1 < 0$. Moreover, it should be noted that we have also recovered the Lorenz attractor for systems (2.5) with nonlinearities that are more general than the exactly quadratic ones given in the caption of Figure 2.2. Only the leading order quadratic approximations (2.76) need to be as described above, higher order nonlinearities do not have a leading order impact. For example, choosing $F_1(U_1, U_2, V) = 3\sqrt{2}\pi/16 \sin(U_2 V)$ as opposed to $F_1(U_1, U_2, V) = 3\sqrt{2}\pi/16U_2V$ which we have used now, works just as well.

Remark 2.4. The codimension 2 case with $\sigma > 1$ is, due to our rescaling, slightly different from what we expect. All modes are slaved to $a_{1,1}$ – related to the eigenvalue $\lambda_{1,1}$, see Figure 2.11 –, even though this is a codimension 2 situation. This has to do with the fact that, for $\sigma > 1$, the magnitude of $A_{1,k}$ is scaled differently from $A_{2,k}$, see (2.84). We refrain from elaborating further in this chapter.

2.7 Discussion

In this chapter, we have discussed the extension of center manifold reduction (CMR), a classical nonlinear method for dimension reduction. We have chosen, as our setting, the transcritical bifurcation destabilizing a trivial background state of a singularly perturbed, multicomponent, evolutionary PDE model. CMR operates locally to the parameter regime where the destabilization occurs and as long as a certain spectral gap condition is satisfied. We have exemplified its extension to regions in parameter space where that condition is violated and termed our approach *extended* center manifold reduction (ECMR). Our approach was crafted in the context of a number of explicit and closely related model problems, see (2.3), (2.5) and (2.52). However, our work has been inspired

by and builds on an earlier study of a slightly different model, namely the phytoplankton-nutrient model (2.1) sharing with these model problems the same basic structure enabling ECMR. This structure unsurprisingly concerns the *spectrum* determining the stability of the trivial background state and is drawn schematically in Figures 2.1, 2.10 and 2.11. Specifically, ECMR hinges on the assumption that the spectrum in question partitions into families $\{\lambda_k\}_k$ and $\{\mu_k\}_k$ of ‘large’ and ‘small’ eigenvalues, respectively. It is thus expected to be applicable to the general class of systems given in (2.2), see also Chapter 3. In this chapter, and for any fixed k , λ_k and μ_k are $\mathcal{O}(1)$ and $\mathcal{O}(\varepsilon)$, respectively, for an asymptotically small parameter ε .

Our analysis treats situations where one or two of the large eigenvalues initiate a bifurcation by crossing through zero while all others remain stable. Linear theory suffices to pinpoint the codimension 1 or 2 surface (in parameter space) where the bifurcation occurs and, additionally, predicts the ‘shape’ of the bifurcating pattern. The nonlinear extension of center manifold reduction improves on linear theory by predicting the amplitude of that pattern, and tracking it along a larger parametric regime. This regime is restricted, nevertheless, in that the ‘eventual fate’ of the pattern lies even further beyond. The underlying reason is that CMR validity is relying on the existence of a spectral gap of sufficient width; simply put, the critical (i.e. bifurcating) eigenvalues λ_j must be sufficiently closer to the imaginary axis than the largest stable eigenvalue μ_1 . In our setting, this condition reads $|\lambda_j| = \mathcal{O}(\varepsilon^\sigma) \ll \mathcal{O}(\varepsilon) = |\mu_1|$ so $\sigma > 1$. ECMR, in turn, improves this state of affairs by operating in the ‘gapless’ limit $\sigma = 1$. A priori, one would expect a large number of μ_k -modes to be excited in that case, since μ_k scale with ε . In the singularly perturbed setting considered here, however, it turns out that only the μ_1 -mode contributes appreciably to the dynamics. The classical, one-dimensional CMR describing a codimension 1 transcritical bifurcation must hence be extended to a merely two-dimensional extended center manifold. The resulting reduced dynamics attract small initial conditions at an exponential rate and well into the regime $\lambda_j = \mathcal{O}(\varepsilon)$ where secondary and tertiary bifurcations occur.

Using this extended reduction, we showed that the transcritical bifurcation is typically followed by a supercritical Hopf bifurcation of the emerging pattern, similarly to the situation for (2.1) [176]. Additionally, we applied our approach to two systems with codimension 2 (transcritical) bifurcations, finding that the planar CMR must be extended to either a three- or a four-dimensional ECMR attracting small initial conditions exponentially. Motivated by simulations of (2.1) in [78], we have explored various scenarios for the presence of chaotic dynamics in the ECMR flow. Our approach enabled us to construct several such explicit examples, where the full PDE semiflow limits to a low-dimensional

chaotic attractor, i.e. in which the full model exhibits low-dimensional chaotic spatio-temporal dynamics governed by ECMR flows – see Figures 2.2 and the right panel of 2.9.

This chapter has a distinctive exploratory character. We have chosen to investigate the phenomena exhibited by singularly perturbed PDE systems pushed beyond the region of validity of classical CMR associated with a transcritical bifurcation: our analysis is entirely formal. Nevertheless, the backbone of our presentation provides in itself a solid foundation for a rigorous validation. In the context of reaction-diffusion equations, especially, results on the convergence of solutions to N -dimensional Galerkin projections as $N \rightarrow \infty$ seem directly applicable to the present setting, see e.g. [135, 154]. For the codimension 2 case, it is natural to first work out in detail the general case, where eigenfunctions may not span the invariant subspace of the bifurcating eigenvalue. In that situation, one needs to account for generalized eigenfunctions, and we have refrained from doing so in the present chapter.

Another line of future research concerns the application of ECMR to models where the primary bifurcation, associated with the first large eigenvalue λ_1 crossing the imaginary axis, is not transcritical. In principle, ECMR is directly applicable – at least formally – when the trivial state is annihilated/destabilized in a pitchfork or saddle-node bifurcation. Further, although that state cannot undergo a Hopf bifurcation by virtue of \mathcal{L} having been assumed self-adjoint (see **A1** in Section 2.2), a spatially inhomogeneous one could sustain it. We already emphasized that ECMR is enabled by the structure of the spectrum and not by particulars of the basic state. In principle, then, ECMR can also cover this case, as long as the spectrum has a large/small decomposition as depicted in Figure 2.1. A natural question in all of these three contexts is whether the primary bifurcation is also typically followed by a destabilizing Hopf bifurcation already upon an $\mathcal{O}(\varepsilon)$ variation of the bifurcation parameter. This scenario indeed appears natural, see below; it will thus be relevant to study what ECMR can yield in those situations.

Since the present chapter was inspired by the appearance of low-dimensional spatio-temporal dynamics in model (2.1), we finally consider the question of how assistive can ECMR be in understanding analytically the rich spatio-temporal dynamics of evolutionary PDE systems. In Chapter 3, this question is further unfolded. Spatio-temporal dynamics of evolutionary PDE systems are routinely observed in simulations of systems such as (2.3), see for instance [85] and references therein for often encountered reaction-diffusion cases. Scenarios involving a stationary pattern that bifurcates from a basic state, only to be destabilized in a Hopf bifurcation, also appear naturally in reaction-diffusion equations; see, for instance, [45] for an explicit example.

A major question is, of course, how typical is the existence of a stability problem with small and large eigenvalues? A related question is whether the (assumed) existence of such a partition can be used to embed these systems into the singularly perturbed framework necessary for our approach. Given the character of ECMR, we are convinced that it can be applied to explicit (reaction-diffusion) models found in the literature – by assuming certain scaling limits, of course. The most natural candidates are those of Gierer-Meinhardt and Gray-Scott type, which already have the desired singularly perturbed nature; see, for instance, [21, 93, 43] and references therein. The complex dynamics exhibited by these systems is largely dominated by singular solutions of pulse type [121, 161], the spectral stability problem of which does decompose into small and large eigenvalues (on bounded domains) – see, for instance, [80, 157]. Typically, these pulses are destabilized through Hopf bifurcations; one thus needs to adapt ECMR to singular patterns, see our remark above on the nature of the basic state. This appears to be a promising line for future research, especially since the low-dimensional chaotic behavior exhibited by solitary pulses in an extended Gierer-Meinhardt model seems to be driven by large-small spectrum interactions [161].

Appendix

A Sub- or supercritical Hopf bifurcation

In this appendix the character of the Hopf bifurcation as derived in subsection 2.4.1 is determined in full detail. We follow the procedure outlined in [98].

The system that we consider is the subsystem of the first two equations of (2.41) on the invariant center manifold.

$$\begin{cases} a'_1 = ra_1 + C_{111} (F_{20}a_1^2 + F_{11}a_1b_1 + F_{02}b_1^2), \\ b'_1 = -M_1b_1 + \beta a_1. \end{cases} \quad (2.87)$$

The corresponding Jacobian of (2.87) is,

$$J(a_1, b_1) = \begin{pmatrix} r + 2C_{111}F_{20}a_1 + C_{111}F_{11}b_1 & C_{111}(F_{11}a_1 + 2F_{02}b_1) \\ \beta & -M_1 \end{pmatrix}. \quad (2.88)$$

The nontrivial stationary state that becomes stable after the transcritical bifurcation is given in (2.42). Evaluated at this stationary state, the Jacobian (2.88) is:

$$J(a_1^*, b_1^*) = \begin{pmatrix} \frac{r}{H} \left(H - 2F_{20} - \frac{F_{11}\beta}{M_1} \right) & -\frac{r}{H} \left(F_{11} + 2\frac{F_{02}\beta}{M_1} \right) \\ \beta & -M_1 \end{pmatrix},$$

see (2.36) for the definition of H . The eigenvalues of this Jacobian as a function of bifurcation parameter r are,

$$\Lambda_{\pm} = \frac{\text{tr}(J(r)) \pm i\sqrt{4\det(J(r)) - \text{tr}^2(J(r))}}{2} = \mu(r) \pm i\omega(r),$$

where $\text{tr}(J(r))$ and $\det(J(r))$ represent the trace and the determinant of J in

terms of r , respectively. We find that,

$$\text{tr}(J(r)) = \frac{r \left(H - 2F_{20} - \frac{F_{11}\beta}{M_1} \right)}{H} - M_1,$$

$$\det(J(r)) = rM_1.$$

The Hopf bifurcation occurs if $\mu(r_H) = 0$ and $\omega(r_H) = \omega_0 > 0$, where r_H is the value of r at the bifurcation. The first condition is satisfied for

$$r_H = \frac{M_1 H}{-F_{20} + F_{02}\beta^2/M_1^2}.$$

The value of $\omega(r)$ at the bifurcation value is

$$\omega(r_H) = \omega_0 = \sqrt{r_H M_1}.$$

For $\gamma < -\nu_1$, the sign of M_1 is positive, so the requirement for a Hopf bifurcation is that

$$r_H > 0.$$

The following two degeneracy conditions must be satisfied to assure that the Hopf bifurcation is regular.

(C1) $l_1(r_H) \neq 0$, where l_1 is the first Lyapunov coefficient;

(C2) $\mu'(r_H) \neq 0$.

The sign of the first Lyapunov coefficient determines the character of the Hopf bifurcation. If $l_1(r_H) < 0$, the bifurcation is supercritical. That indicates that stable limit cycles bifurcate from the Hopf bifurcation. If $l_1(r_H) > 0$, the bifurcation is subcritical.

Condition (C2) is satisfied for all values of F_{ij} and β , because

$$\mu'(r_H) = \frac{-F_{20} + \frac{F_{02}\beta^2}{M_1^2}}{2H} = \frac{M_1}{r_H}.$$

And if $r_H > 0$, the value $\mu'(r_H)$ is always positive.

Computing the first Lyapunov coefficient is a more involved task. First we translate the variables such that the Hopf bifurcation occurs at the origin. We introduce

$$x_1 = a_1 - a_1^*, \quad \text{and} \quad x_2 = b_1 - b_1^*,$$

with a_1^* and b_1^* the values of the nontrivial stationary state, evaluated at the Hopf bifurcation, i.e. with $r = r_H$. System (2.87) then transforms into

$$\begin{cases} x'_1 = r_H x_1 + C_{111} [F_{20}(x_1^2 + 2a_1^* x_1) \\ \quad + F_{11}(x_1 x_2 + a_1^* x_2 + b_1^* x_1) + F_{02}(x_2^2 + 2b_1^* x_2)] & \equiv F_1(x_1, x_2), \\ x'_2 = -M_1 x_2 + \beta x_1 & \equiv F_2(x_1, x_2). \end{cases} \quad (2.89)$$

Define the symmetric multilinear vector functions of $u, v, w \in \mathbb{R}^2$,

$$B(u, v) = \begin{pmatrix} B_1(u, v) \\ B_2(u, v) \end{pmatrix},$$

$$C(u, v, w) = \begin{pmatrix} C_1(u, v, w) \\ C_2(u, v, w) \end{pmatrix}$$

with

$$B_i(u, v) = \sum_{j, k=1}^2 \frac{\partial^2 F_i((x_1, x_2)^T, r_H)}{\partial x_j \partial x_k} \Bigg|_{x_1=x_2=0} u_j v_k,$$

and

$$C_i(u, v, w) = \sum_{j, k, l=1}^2 \frac{\partial^3 F_i((x_1, x_2)^T, r_H)}{\partial x_j \partial x_k \partial x_l} \Bigg|_{x_1=x_2=0} u_j v_k w_l.$$

For (2.89), these multilinear forms are

$$B(u, v) = \begin{pmatrix} C_{111}(F_{20}u_1v_1 + F_{11}u_1v_2 + F_{11}u_2v_1 + 2F_{02}u_2v_2) \\ 0 \end{pmatrix},$$

$$C(u, v, w) = \begin{pmatrix} 0 \\ 0 \end{pmatrix}.$$

Then the system (2.89) can be represented as

$$x' = J(r_H)x + \frac{1}{2}B(x, x) + \frac{1}{6}C(x, x, x).$$

Define the eigenvectors of $J(r, H)$ and $J^T(r_H)$, q and p respectively, as

$$J(r_H)q = i\omega_0 q, \quad J^T(r_H)p = -i\omega_0 p.$$

A straightforward computation yields that,

$$q = \begin{pmatrix} M_1 + i\omega_0 \\ \beta \end{pmatrix},$$

and with normalization $\langle p, q \rangle = 1$,

$$p = \frac{1}{2\beta M_1} \begin{pmatrix} \beta \\ M_1 + i\omega_0 \end{pmatrix}.$$

Three inner products of these eigenvectors with the multilinear forms are

$$\begin{aligned} g_{20} &= \langle p, B(q, q) \rangle, \\ g_{11} &= \langle p, B(q, \bar{q}) \rangle, \\ g_{21} &= \langle p, C(q, q, \bar{q}) \rangle. \end{aligned}$$

The first Lyapunov coefficient is defined as,

$$l_1(r_H) = \frac{1}{2\omega_0^2} \Re(i g_{20} g_{11} + \omega_0 g_{21}). \quad (2.90)$$

Computing all inner products and evaluating l_1 , we find

$$l_1(r_H) = \frac{C_{111}^2}{2\omega_0 M_1^2} [(2M_1 F_{20} + F_{11}\beta)(HM_1^2 + \omega_0^2 F_{20})].$$

The factor $\frac{C_{111}^2}{2\omega_0 M_1^2}$ is positive because ω_0 is positive, so the sign of the first Lyapunov coefficient is determined by the sign of

$$(2M_1 F_{20} + F_{11}\beta)(HM_1^2 + \omega_0^2 F_{20}).$$

This means that the Hopf bifurcation occurring at $r = r_H$ is

$$\begin{aligned} &\text{supercritical if } (2M_1 F_{20} + F_{11}\beta)(HM_1^2 + \omega_0^2 F_{20}) < 0, \\ &\text{subcritical if } (2M_1 F_{20} + F_{11}\beta)(HM_1^2 + \omega_0^2 F_{20}) > 0. \end{aligned}$$

3

Stability of a benthic layer of phytoplankton¹

Abstract We consider a two-component system of evolutionary partial differential equations posed on a bounded domain. Our system is pattern forming, with a small stationary pattern bifurcating from the background state. It is also equipped with a multiscale structure, manifesting itself through the presence of spectrum close to the origin. Spatial processes are associated with long time scales and affect the nonlinear pattern dynamics strongly. To track these dynamics past the bifurcation, we develop an asymptotics-based method complementing and extending rigorous center manifold reduction. Using it, we obtain a complete analytic description of the pattern stability problem in terms of the linear stability of the background state. Through this procedure, we portray with precision how slow spatial processes can destabilize small patterns close to onset. We further illustrate our results on a model describing phytoplankton whose growth is limited by both nutrient and light. Localized colonies forming at intermediate depths are found to be subject to oscillatory destabilization shortly after emergence, whereas boundary-layer type colonies at the bottom persist. These analytic results are in excellent agreement with numerical simulations for the full model, which we also present.

The interest to model and investigate dynamic processes at the planetary level necessitates the development of analytical tools for multicomponent models. We consider a class of deterministic systems evolving both in time and space and incorporating slow, passive, spatial processes. Exploiting their multiscale structure, we develop a method to study the long-term dynamics of small spatial

¹The content of this chapter was published as *The effect of slow spatial processes on emerging spatiotemporal patterns* in Chaos in 2015, see [41].

patterns as they bifurcate. Our analytic results indicate that passive processes strongly affect and may even destabilize such small patterns over a long timescale. Numerical simulations for an ecologically relevant model of plankton growth in the ocean support these findings, by showing how nutrient diffusion destabilizes deep chlorophyll maxima over a timescale of several years.

As efforts to comprehend how our planet functions intensify, so does the need to comprehend the glaring spatial heterogeneity characterizing it. The trend towards investigating bona fide spatial phenomena, such as mobility or anisotropy, is plainly visible within many core Mathematics of Planet Earth areas [57, 71, 101, 103, 100, 112, 134]. That trend, however, is not always reflected in our modeling efforts. Indeed, modeling studies of natural phenomena often focus on temporal variation, without explicitly accounting for spatial variability. The resulting models can predict, elucidate or quantify temporal trends in the system under investigation, but their ability to incorporate spatial information is, unsurprisingly, limited. Despite these limitations, spatially homogeneous models enjoy wide popularity across a broad range of disciplines. Their evident ability to generate realistic, if crude, information is but one facet of that tenacity. Equally important is the confluence of their inimitable simplicity, which sets the mechanisms underlying complex phenomena in stark relief, and of a rich toolbox that enables their analysis.

Mathematically speaking, such models are typically formulated as nonlinear systems of ordinary differential equations (ODEs). As such, their analysis benefits immeasurably from the advent of dynamical systems theory, an immensely powerful conglomerate of qualitative tools dating back to Poincaré [129]. The inclusion of spatiality, on the other hand, leads to partial differential equation (PDE) models. The theoretical foundation for the qualitative analysis of nonlinear, pattern forming PDEs has been set through the work of Turing [156], but a coherent theory is still largely missing except for sufficiently close to equilibrium. This is particularly pronounced for systems of PDEs, whose global dynamics remain poorly understood and which form the subject of this short communication.

Here, we specifically focus on the dynamics of a system of two evolutionary PDEs posed in a domain of arbitrary dimension. The model is general enough to accommodate various applications, but we conceptualize it in terms of a particular setting in the interest of clarity. In particular, we consider it to track the spatial densities of a consumer and a resource, as they evolve in time and space under the influence of uptake/growth dynamics and spatial processes. We assume these spatial processes of the resource to be strictly linear and to play out much more slowly than the nonlinear dynamics associated with uptake and growth. Our expressed aim is to shed some light on the importance of spatiality, and we embark on this mission by exploring the role played by the slow, spatial

processes. We find these to be crucial, in that they strongly inform the fate of small patterns emerging from the background state. Although such patterns *emerge* when resource availability crosses a certain threshold, as in non-spatial models, their *fate* strongly depends on these processes. Depending on problem specifics, spatiality can effectively “break” what resource availability “makes”.

Our work here also serves as a blueprint for the analytic investigation of post-bifurcation dynamics relatively close to criticality but not close enough to be within reach of rigorous methods. Perhaps somewhat counter-intuitively, this analysis is not obstructed, but rather *facilitated* by the presence of long timescales associated with spatial dynamics. To appreciate this statement, note that the small pattern dynamics become nontrivial only when the unstable and longest stable timescales become commensurate. Here, these longest stable timescales correspond by design to linear spatial processes, a fact that enables us to (formally) reduce the system of two PDEs to an ODE coupled to a PDE. This formulation was also mentioned in Chapter 2, see Remark 2.1. Within that coupled system, the linear PDE dictates the evolution of the resource profile, while the nonlinear ODE dictates that of the amplitude of the emerging pattern. The *intricacy* of the resulting stability problem for that pattern is due to the infinite-dimensional character of the reduced system. Its *tractability*, on the other hand, is largely a result of our ability to generate the Green’s function for the linear PDE problem.

to include *nonlinear* spatial processes. The reduction procedure outlined above carries over to that case, yielding a fully nonlinear ODE–PDE system. Here too, the bifurcating pattern forces the evolution of the resource profile; that, in turn, feeds parametrically into the ODE for the pattern. Such nonlinearities increase in many ways the number of possible evolution scenarios, but they do so at the expense of analytic tractability. Other generalizations, such as wider classes of nonlinear terms, can also be considered. We will refrain from doing so here to keep the discussion simple.

This chapter builds on and extends prior work, most notably [176] and Chapter 2 of this thesis. In [176], we considered an explicit instantiation of the general model considered presently, namely a plankton–nutrient model posed on a water column. Our analysis there began with the derivation of ODEs for the eigenmodes and proceeded with copious amounts of asymptotics. Through that work, we tracked analytically the emerging pattern, a localized plankton population at an intermediate depth called a *deep chlorophyll maximum* (DCM), and showed that it is destabilized shortly after it bifurcates. We recapture a large part of those results much more compactly here by employing our new framework; see Section 3.3.2. In Chapter 2 of this thesis, we worked with a variety of related models. The focus there, however, was on the derivation of

finite dimensional approximations in general and on low-dimensional chaotic dynamics in particular. The part of that work concerning two-component PDE models can, in principle, be made to fit the framework developed here. In contrast to [176], little can be earned by doing that and we do not pursue that direction further. Conversely, our setting here may be easily modified to include bifurcations of higher codimension as in Chapter 2, at the moderate cost of involving *multiple* ODEs in the reduced system. We reserve this work also for a future communication, especially as it relates to the presence of a codimension 2 point in our exemplar phytoplankton-nutrient system [176].

We conclude this introductory section by outlining the work presented here. In Section 3.1, we formulate our model and a number of assumptions relating to it. Then, in Section 3.2.1, we develop an analytical method which allows us to track the emergent pattern beyond the range of validity of classical center manifold reduction. The main result here is an extension of that classical method, in the form of a coupled system composed of a nonlinear ODE and a linear PDE. Using that extension, we discuss the stability of the pattern in Section 3.2.2. In fact, we are able to express that stability problem in a surprisingly simple form, which welds particulars both of the background state and of the spatial processes. In this manner, we extend and streamline prior results from [176] and Chapter 2 where the ODE-PDE structure of the reduced problem was mentioned in 2.1 but not used extensively. Instead, we chose to work with the infinite-dimensional system of ODEs that is equivalent to it. The applicability of our methodology is illustrated in Sections 3.3–3.4, where we consider the phytoplankton–nutrient model. With the help of the theory developed in Section 3.2, we recapture the oscillatory destabilization of DCM patterns in Section 3.3.1. Relatedly, we consider another type of pattern in Section 3.4, namely boundary-layer type, benthic layer (BL) colonies at the bottom whose dynamics were previously unexamined. Such patterns require a deeper analysis that necessarily involves higher-order effects and showcases the advantages of our streamlined approach over our earlier, more direct efforts [176]. Through that analysis, we obtain a new result in itself by finding such colonies to persist in the regime we consider. Section 3.5 concludes the chapter with a summary and critical discussion of our findings.

3.1 Problem setting

We consider a class of nonlinear, slow/fast PDE systems,

$$\begin{bmatrix} u \\ v \end{bmatrix}_t = \begin{bmatrix} \mathcal{L} & 0 \\ \varepsilon\mathcal{K} & -\varepsilon\mathcal{M} \end{bmatrix} \begin{bmatrix} u \\ v \end{bmatrix} - \begin{bmatrix} f(z, u, v; \varepsilon) uv \\ \varepsilon g(z, u, v; \varepsilon) \end{bmatrix} \quad (3.1)$$

postulated for functions $u(z, t) : \Omega \times \mathbb{R}_+ \rightarrow \mathbb{R}$ and $v(z, t) : \Omega \times \mathbb{R}_+ \rightarrow \mathbb{R}$. Here, $\Omega \subset \mathbb{R}^n$ is a given bounded domain with piecewise smooth boundary, \mathbb{R}_+ is the positive timeline and we assume that boundary conditions guaranteeing well-posedness apply. We leave the linear differential operators \mathcal{L} and $-\mathcal{M}$ unspecified but demand that their point spectra are bounded from above. Our main interest lies in reaction–diffusion systems, for which \mathcal{L} and $-\mathcal{M}$ are second-order and elliptic, and we will work with such operators in the ecological application treated in Sections 3.3–3.4. Other choices are possible and have been discussed in Chapter 2. We impose no specific conditions on the linear operator \mathcal{K} other than that, together with \mathcal{M} , it contains the linear dynamics; specifically, $g(z, u, v; \varepsilon) = \mathcal{O}(u^2 + v^2 + \varepsilon^2)$, as $(u, v, \varepsilon) \rightarrow (0, 0, 0)$. In the same vein, we demand that $f_0(z) = f(z, 0, 0; 0)$ is bounded and not identically zero, so that the leading order nonlinearity f_0uv is quadratic. More general nonlinearities, including ones with nonlocalities as in Sections 3.3–3.4, are similarly treatable. For clarity of presentation in this expository chapter, however, we refrain from considering these in detail.

The form assumed by the nonlinearity for u reflects our motivation, which is rooted in the aforementioned ecological problem. In short, u is the concentration of a *consumer* feeding on a spatially distributed *resource*. The concentration v measures resource deviation from a specific spatial profile which, in turn, is attained in the full absence of consumers. This profile represents an offset, as casting our model in terms of resource *deviation* shifts the trivial state to the origin, $(u, v) = (0, 0)$. Additionally, it is optimal for consumer growth, with growth limitations caused by depleted resources reflected in the nonlinearity g . The operator \mathcal{L} models growth under optimal conditions, as well as linear spatial processes such as diffusion and advection. Similarly, $-\mathcal{M}$ models the linear spatial processes affecting the resource, with the minus sign emphasizing their stabilizing character. Here also, more general nonlinearities for u may be analyzed, but we do not pursue this direction at present.

Before proceeding with the analysis, we fix notation, which is slightly abusing compared to Chapter 2. We will write $\sigma_p(\mathcal{L}) = \{\lambda_j\}_{j \geq 0}$ and $\sigma_p(\mathcal{M}) = \{\mu_j\}_{j \geq 0}$ for the point spectra of the differential operators in system (3.1). For the former, we explicitly assume that its primary eigenvalue λ_0 is real and associated with a one-dimensional eigenspace. Further, it is separated by all other eigenvalues in $\sigma_p(\mathcal{L})$ by a spectral gap of sufficient width,

$$\varepsilon \gg \lambda_0 - \operatorname{Re}(\lambda_j) > 0, \quad \text{for all } j \geq 1. \quad (3.2)$$

For $\sigma_p(\mathcal{M})$, we demand it remains bounded away from the imaginary axis as $\varepsilon \downarrow 0$, i.e., $\operatorname{dist}(\sigma_p(\mathcal{M}), i\mathbb{R}) > M$ for some optimally chosen, positive constant M not depending on ε . Additionally, we assume $\sigma_p(\mathcal{M})$ to be bounded from below;

recall our earlier remark. We write $\{u_j\}_{j \geq 0}$ and $\{v_j\}_{j \geq 0}$ for the eigenfunctions of \mathcal{L} and \mathcal{M} , so that $\mathcal{L}u_j = \lambda_j u_j$ and $\mathcal{M}v_j = \mu_j v_j$. Again, note that this is slightly abusive notation compared to Chapter 2. The Banach spaces spanned by $\{u_j\}_{j \geq 0}$ and $\{v_j\}_{j \geq 0}$ are denoted by \mathbb{X}_u and \mathbb{X}_v , respectively, and (3.1) with suitable boundary conditions is well-posed on the product $\mathbb{X}_u \times \mathbb{X}_v$. We also introduce the \mathcal{L} -invariant spaces $\mathbb{X}_{u,0} = \text{span}(u_0)$ and $\mathbb{X}_{u,r} = \text{cl}(\text{span}\{u_j\}_{j \geq 1})$, with the restriction of \mathcal{L} on the latter satisfying $\sigma_p(\mathcal{L}|_{\mathbb{X}_{u,r}}) = \{\lambda_j\}_{j \geq 1}$; in Sections 3.3–3.4, all four spaces will be closed subspaces of $L^2(\Omega)$. Finally, we define a projection $P_0 : \mathbb{X}_u \rightarrow \mathbb{X}_{u,0}$ with $\ker(P_0) = \mathbb{X}_{u,r}$, which strips functions of their components along u_1, u_2, \dots . Lastly, we introduce the ‘projection amplitude’ operator $P_0^a : \mathbb{X}_u \rightarrow \mathbb{R}$ by $P_0 u = (P_0^a u) u_0$. In a Hilbert space setting, this corresponds to the inner product $P_0^a = \langle \cdot, \hat{u}_0 \rangle$, whereas $P_0 = \langle \cdot, \hat{u}_0 \rangle u_0$. Here, the function $\hat{u}_0 \in \mathbb{X}_u$ is the dual of u_0 , i.e. $\langle u_0, \hat{u}_0 \rangle = 1$ and $\langle u_0, \hat{u}_j \rangle = 0$ for all $j \geq 1$.

3.2 Emergence and evolution of a small colony

As discussed in the Introduction, understanding the emergence and interaction of spatial structures in a system helps to shed light on the appearance of complex dynamics in it. To track such patterns, we will employ a scalar parameter quantifying the ability of the environment to sustain consumers. In the model problem we treat in the next sections, this parameter measures resource abundance in the absence of consumers, i.e. it quantifies the resource offset briefly discussed in the last section. This control parameter will affect $\sigma_p(\mathcal{L})$, at the very least, so that we will effectively replace it by λ_0 in what follows: consumer populations can either grow or diminish depending on whether λ_0 is positive or negative.

Center manifold reduction captures the evolution of emerging small populations local to bifurcation – specifically, as long as λ_0 is asymptotically smaller than both $\{\lambda_j\}_{j \geq 1}$ and the bound εM on $\sigma_p(\varepsilon \mathcal{M})$. In that regime, the emerging pattern evolves on the longest timescale present in the system, and all other modes can effectively be considered equilibrated with respect to it. Here, instead, we derive reduced evolution laws that remain valid in the regime where emerging pattern and spatial processes evolve in *commensurate* timescales. In doing that, we demonstrate that the pattern dynamics are enriched substantially by interacting with the spatial component and, concurrently, we extend center manifold reduction in a natural manner.

3.2.1 An evolution law for the emerging population

Our tracking begins with the trivial state $(u, v) = (0, 0)$. Since λ_0 is real and leads all other eigenvalues in $\sigma_p(\mathcal{L})$, it can only enter the right-half complex plane through zero. At that point, the trivial equilibrium is destabilized and develops an unstable direction. For quadratic nonlinearities, such as the ones

3.2 Emergence and evolution of a small colony

we will consider, this is the classical setting for the transcritical bifurcation of a stable equilibrium branch $\{(u^*(z; \lambda_0), v^*(z; \lambda_0))\}$ parametrized by λ_0 . For λ_0 sufficiently small, the full model dynamics are effectively described by a single ODE for the equilibrium amplitude. That amplitude, in turn, scales with λ_0 and the dynamics about it play out on an $\mathcal{O}(1/\lambda_0)$ timescale [98].

These arguments suggest the rescaling

$$\begin{aligned} \lambda_0 &= \varepsilon \Lambda_0, & \tau &= \varepsilon t, \\ u(z, t) &= \varepsilon x(z, \tau), & v(z, t) &= \varepsilon y(z, \tau), \end{aligned}$$

for the regime $\lambda_0 = \mathcal{O}(\varepsilon)$. This is a crucial element in our approach, as classical center manifold reduction is inapplicable for $\lambda_0 = \mathcal{O}(\varepsilon)$. Indeed, in that regime, λ_0 is of the same order as the small eigenvalues $\{\varepsilon \mu_j\}_j$, with spatial processes and pattern dynamics evolving on the same timescale. To emphasize this, we decompose the u -component into eigenfunctions by means of $x(z, \tau) = x_0(\tau)u_0(z) + x_r(z, \tau)$. Here, $x_0u_0 = P_0x \in \mathbb{X}_{u,0}$ is the component of x in the principal eigendirection, while $x_r = (I - P_0)x \in \mathbb{X}_{u,r}$ is a remainder summarizing the components of x along all other eigendirections. Similar to center manifold reduction, the objective of this decomposition is to derive a dynamic equation for x_0 and constrain (*slave*) the remainder x_r . To that effect, we start by reporting the evolution laws for the two components,

$$\begin{aligned} \dot{x}_0 &= \Lambda_0 x_0 - P_0^a(f(z, \varepsilon x, \varepsilon y; \varepsilon))(x_0 u_0 + x_r)y, \\ \dot{x}_r &= \varepsilon^{-1}\mathcal{L}|_{\mathbb{X}_{u,r}}x_r \\ &\quad - (I - P_0)(f(z, \varepsilon x, \varepsilon y; \varepsilon))(x_0 u_0 + x_r)y. \end{aligned}$$

The regime we are interested in is $\Lambda_0 = \mathcal{O}(1)$, where the emerging pattern and the spatial processes evolve in commensurate timescales but the remainder x_r contracts much faster. Indeed, in that regime, the spectrum of $\varepsilon^{-1}\mathcal{L}|_{\mathbb{X}_{u,r}}$ is asymptotically large and resides in the left half of the complex plane, so that the remainder x_r contracts in a relatively short timescale of order $|\varepsilon/\lambda_1| \ll |1/\Lambda_0|$. This formally leads to the slaving relation (compare to [176] and those in Chapter 2)

$$\mathcal{L}|_{\mathbb{X}_{u,r}}x_r = \varepsilon x_0(I - P_0)(f_0 u_0 y), \tag{3.3}$$

at leading order in ε , showing the remainder x_r to be higher-order. This equation supplements the *reduced* dynamic problem

$$\begin{aligned} \dot{x}_0 &= \Lambda_0 x_0 - x_0 P_0^a(f_0 u_0 y), \\ y_\tau &= -\mathcal{M}y + x_0 \mathcal{K}u_0, \end{aligned} \tag{3.4}$$

with the prescribed boundary conditions for y also applying. Note carefully that this evolutionary system is comprised of an ODE for $x_0(\tau)$ coupled to an inhomogeneous PDE for $y(z, \tau)$; that PDE is *linear*, as the nonlinearity $\varepsilon g(z, u, v; \varepsilon)$ has no leading order impact. This systems is analogous to the ODE-PDE system derived for (2.2) as described in Remark 2.1. The advantage of using the ODE-PDE formulation of this reduction is mostly its compactness, although it does take away some of the grip on the amplitude equations. Since the full method is already laid out in Chapter 2, however, the current approach suits the purpose of this chapter best. In the system, the pattern drives the evolution of the profile y whereas, reversely, y forces the pattern parametrically. Note, also, that Λ_0 enters this system both explicitly, through $\Lambda_0 x_0$, and implicitly through u_0 . Typically, though, u_0 can be replaced by its $\lambda_0 = 0$ counterpart, as $\mathbb{X}_{u,0}$ will generically vary with λ_0 slower than at an $\mathcal{O}(1/\varepsilon)$ rate: $\varepsilon ||(I - P_0)du_0/d\lambda_0|| \ll ||u_0||$. In that case, Λ_0 enters system (3.4) only explicitly.

The evolutionary system (3.4) generates a semiflow on an invariant manifold which is local to the origin and a graph over $\mathbb{X}_{u,0} \oplus \mathbb{X}_v$. By construction, that manifold also contains the bifurcating branch of equilibria and the non- (or less) transient dynamics around it. In other words, the ODE–PDE system (3.4) directly extends the one-dimensional ODE center manifold reduction further away from equilibrium and where bifurcating pattern and slow spatial processes interact at leading order. This extension is critical, as we will see below, in that it captures information about pattern evolution that center manifold reduction misses. In principle, the infinite-dimensional ODE systems derived in [176] and Chapter 2 of this thesis can be rederived directly from (3.4) by eigenmode decomposition. Conversely, (3.4) offers itself to any of various Galerkin approaches [135] but maintains a twofold advantage over them. First, it circumvents questions pertaining to the number of modes that must be retained; and second, it allows for a compact analysis by exploiting the linearity and overall simplicity of the PDE problem for y . This will become more apparent both in the next section and in the model treated in Sections 3.3–3.4.

3.2.2 Parametric dependence and stability of the bifurcating pattern

Before proceeding, we introduce the notation $(\mathcal{M} + \xi)^{-1}\mathcal{K}u_0$ for the set of solutions to the problem $(\mathcal{M} + \xi)y = \mathcal{K}u_0$. Here, $\xi \in \mathbb{C}$ is arbitrary and the given boundary conditions for y apply. In particular, $\mathcal{M}^{-1}\mathcal{K}u_0$ is well defined because $0 \notin \sigma_p(\mathcal{M})$ by earlier assumptions. The only values of ξ requiring special attention are, in fact, the isolated values $\{-\mu_j\} = \sigma_p(-\mathcal{M})$, for which the solution set is either empty or a nontrivial affine subspace; this depends on whether or not $\mathcal{K}u_0 \in \text{range}(\mathcal{M} - \mu_j)$ and thus on model particulars. We also define the function

$$a : \mathbb{C} \setminus \sigma_p(-\mathcal{M}) \rightarrow \mathbb{C},$$

$$a(\xi; \Lambda_0) = P_0^a(f_0 u_0 (\mathcal{M} + \xi)^{-1} \mathcal{K} u_0), \quad (3.5)$$

which plays a crucial role below. Note that $a(\xi; \Lambda_0)$ depends only implicitly on Λ_0 through the eigenfunction u_0 ; we will suppress this dependence when no confusion can arise.

All equilibria $(x_0, y) \in \mathbb{R} \times \mathbb{X}_v$ of (3.4) satisfy, at leading order in ε , the system

$$\begin{aligned} x_0 [\Lambda_0 - P_0^a(f_0 u_0 y)] &= 0, \\ x_0 \mathcal{K} u_0 - \mathcal{M} y &= 0. \end{aligned} \quad (3.6)$$

Assuming that

$$a(0) = P_0^a(f_0 u_0 \mathcal{M}^{-1} \mathcal{K} u_0) \neq 0, \quad (3.7)$$

(3.6) has the isolated solutions

$$\begin{aligned} (x_0^0, y^0) &= (0, 0), \\ (x_0^*, y^*) &= \frac{\Lambda_0}{a(0)} (1, \mathcal{M}^{-1} \mathcal{K} u_0). \end{aligned} \quad (3.8)$$

Condition (3.7) ensures that the bifurcating branch of equilibria grows linearly in the direction $(1, \mathcal{M}^{-1} \mathcal{K} u_0)_{\lambda_0=0}$, local to the bifurcation point ($\Lambda_0 \ll 1$); see Theorem 1.7 and 1.18 in [28]. If $\mathbb{X}_{u,0}$ evolves slowly with Λ_0 as in our earlier remark, then the branch evolves approximately linearly also for $\mathcal{O}(1)$ values of Λ_0 .

The spectral stability problem for (x_0^*, y^*) is a parametric ODE–PDE problem,

$$\begin{aligned} \xi \bar{x}_0 &= -x_0^* P_0^a(f_0 u_0 \bar{y}), \\ (\mathcal{M} + \xi) \bar{y} &= \bar{x}_0 \mathcal{K} u_0, \end{aligned} \quad (3.9)$$

involving the eigenfunction $(\bar{x}_0, \bar{y}(z))$, the eigenvalue $\xi \in \mathbb{C}$ and inherited boundary conditions for \bar{y} . Solving the second equation for \bar{y} and substituting into the first one, we derive the associated algebraic equation for ξ dictating the spectral stability properties of the bifurcating branch,

$$\xi a(0) + \Lambda_0 a(\xi) = 0 \quad (3.10)$$

or, equivalently,

$$\left(1 - \frac{a(\xi) - a(0)}{a(\xi)}\right) \xi = -\Lambda_0. \quad (3.11)$$

If \mathbb{X}_u is a Hilbert space, then $P_0^a = \langle \cdot, \hat{u}_0 \rangle$ and

$$a(\xi) = \langle f_0 u_0 (\mathcal{M} + \xi)^{-1} \mathcal{K} u_0, \hat{u}_0 \rangle. \quad (3.12)$$

This last formula will be central to our work in the next sections. Remarkably, it represents a formulation of the stability problem for the small pattern solely in terms of information on the background state that the pattern emerges from. Indeed, both u_0 and \hat{u}_0 relate to the stability problem for that state, and f_0 is the nonlinearity coefficient evaluated at it. Generally, $a(\xi)$ will reflect the infinite-dimensional character of the problem, as it will typically be a transcendental function of ξ and not a polynomial. As will become evident through our treatment of the phytoplankton model, this will allow for richer post-bifurcation dynamics which the one-dimensional center manifold reduction necessarily misses. Note, finally, that $a(\xi)$ can still depend implicitly on Λ_0 through u_0 as per our earlier remark.

3.3 Formation and fate of phytoplankton colonies

We clarify the process laid out above by applying it to a rescaled and dimensionless version of a phytoplankton–nutrient model [78, 176, 177],

$$\begin{bmatrix} p \\ n \end{bmatrix}_t = \begin{bmatrix} \varepsilon \partial_{zz} - 2\sqrt{\varepsilon} v \partial_z + h(z) - \ell & 0 \\ \varepsilon \ell^{-1} h(z) & \varepsilon \partial_{zz} \end{bmatrix} \begin{bmatrix} p \\ n \end{bmatrix} - \begin{bmatrix} 1 \\ \varepsilon \ell^{-1} \end{bmatrix} (h(z) - \mu(z, p, n)) p \quad (3.13)$$

with associated boundary conditions

$$\begin{aligned} (\varepsilon p_z - 2\sqrt{\varepsilon} v p)|_{z=0,1} &= 0, \\ n_z(0) = n(1) &= 0. \end{aligned}$$

Table 3.1 summarizes the correspondence between this model and the general system in Section 3.1. Appendix C shows the nondimensionalization of the original phytoplankton–nutrient model that was used to obtain (3.13).

Here, $z \in [0, 1]$ measures rescaled depth from top to bottom, p phytoplankton concentration and n nutrient deviation from a constant and spatially uniform profile attained for $p = 0$. The function h models growth conditions at maximum nutrient concentration (when there is zero deviation),

$$h(z) = \frac{1}{\eta_H + 1} \frac{1}{1 + j_H e^{\kappa z}},$$

3.3 Formation and fate of phytoplankton colonies

so that growth decreases with depth due to light absorption. The nonlinear factor μ is

$$\mu = \frac{1-n}{n_H + 1-n} \frac{j}{j_H + j},$$

with η_H and j_H dimensionless constants and j the rescaled light intensity at depth z ,

$$j = \exp \left(-\kappa z - r \int_0^z p(s, \tau) ds \right).$$

The dimensionless constants κ and r measure water turbidity and the specific light absorption coefficient of phytoplankton. It is straightforward to verify that the nonlinearity $(\mu - h)p$, modeling nutrient uptake in the water column, is proportional to both n and p as in (3.1).

Section 3.1	Section 3.3
u	p
v	n
\mathcal{L}	$\varepsilon \partial_{zz} - 2\sqrt{\varepsilon v} \partial_z + h(z) - \ell$
\mathcal{M}	$-\partial_{zz}$
\mathcal{K}	$\ell^{-1}h(z)$
$f(z, u, v; \varepsilon)uv$	$(h(z) - \mu(z, p, n))p$
$g(z, u, v; \varepsilon)$	$\ell^{-1}(h(z) - \mu(z, p, n))p$
f_0	$(1 + \eta_H)^{-1}h(z)$
u_j	Es_j (see Appendix)
\hat{u}_j	$E^{-1}s_j$
μ_j	$-M_j = -(j + 1/2)^2\pi^2$
n_j	$\cos(\sqrt{M_j}x)$.

Table 3.1: Notation conversion table.

3.3.1 Linear stability

The nature of the bifurcating profile and of its dynamics after the first bifurcation depend strongly on the value of parameter v . This, in turn, is influenced by both physiological properties of plankton and environmental factors. Buoyant plankton ($v \leq 0$) tends to aggregate near the surface, whereas sinking plankton does so at a well-defined depth $z_* > 0$. As v approaches the threshold value $v^* = h(0) - h(1)$, the bloom shifts toward the bottom monotonically ($z_* \uparrow 1$). For $v > v^*$, the bloom occurs at the bottom ($z_* = 1$) [177]. Depending on

their localization properties, these *stationary* blooms are known as *surface scums* (SS), *deep chlorophyll maxima* (DCM) or *benthic layers* (BL), respectively, and correspond to equilibria of the model.

This state of affairs is reflected in the eigenvalues $\{\lambda_j\}$ and eigenfunctions $\{p_j\}$ of the stability problem for the trivial steady state. Asymptotic expressions for these have been derived elsewhere [177]. At leading order in ε , the primary eigenvalue λ_0 reads

$$\lambda_0 = \begin{cases} \lambda_{BL} &= h(1) - \ell + \mathcal{O}(\varepsilon^{\frac{1}{2}}), & v > v^*, \\ \lambda_{DCM} &= h(0) - \ell - v - \mathcal{O}(\varepsilon^{\frac{1}{3}}), & v < v^*, \end{cases}$$

while the higher-order eigenvalues are given by

$$\lambda_{j \geq 2} = h(0) - \ell - v - \mathcal{O}(\varepsilon^{1/3}),$$

i.e. the eigenvalues $\lambda_{j \geq 2}$ are a mere $\mathcal{O}(\varepsilon^{1/3})$ distance away from λ_{DCM} . The value of v relative to v^* determines the nature of the primary pair (λ_0, p_0) and, therefore, also the nature of the bifurcating profile as the trivial state loses stability.

The eigenvalue set $\{\mu_j\}_j$ is parameter-independent and negative. For this model, both $\{\mu_j\}$ and the associated eigenfunctions $\{n_j\}$ are explicitly computable, see Table 3.1. We finally recall that $P_0^a = \langle \cdot, \hat{p}_0 \rangle$, with \hat{p}_0 the dual of p_0 .

3.3.2 Evolution of DCM profiles

For $0 < v < v^*$, a stable DCM branch emerges at $\lambda_0 = 0$ through a transcritical bifurcation and subsequently undergoes a secondary, destabilizing Hopf bifurcation already for $\lambda_0 = \mathcal{O}(\varepsilon)$ [177]. Both the primary and the secondary bifurcations have been analyzed, and a weakly nonlinear stability analysis was performed by recasting (3.1) as an infinite-dimensional ODE system [176]. In this section, we repeat that analysis along the lines of Section 3.2, so as to benchmark the method detailed there, to compactly recover the oscillatory DCM destabilization mechanism and to further familiarize the reader with the model and the method.

Before delving into details, we compute the function $a(\xi; \Lambda_0)$ introduced in (3.5). Here, this function takes the form (cf. (3.12))

$$a(\xi) = \frac{1}{\ell} \langle f_0 p_0 (\mathcal{M} + \xi)^{-1} (h p_0), \hat{p}_0 \rangle, \quad (3.14)$$

where $(\mathcal{M} + \xi)^{-1}$ is the solution operator to

$$-n_{zz} + \xi n = w(z), \quad n_z(0) = n(1) = 0, \quad (3.15)$$

3.3 Formation and fate of phytoplankton colonies

and with w arbitrary. The solution is

$$((\mathcal{M} + \xi)^{-1}w)(z) = \int_0^1 G(z, s; \xi)w(s)ds,$$

with G the associated Green's function,

$$G(z, s; \xi) = \frac{\cosh(\sqrt{\xi} \min(z, s)) \sinh(\sqrt{\xi}(1 - \max(z, s)))}{\sqrt{\xi} \cosh \sqrt{\xi}}. \quad (3.16)$$

The function $a(\xi; \Lambda_0)$ becomes, then,

$$a(\xi; \Lambda_0) = \frac{1}{\ell} \iint_{[0,1]^2} f_0(r) \hat{p}_0(r) p_0(r) G(r, s; \xi) h(s) p_0(s) ds dr. \quad (3.17)$$

We can readily estimate the integral asymptotically by noting that p_0 and $\hat{p}_0 p_0$ are strongly localized [176]. Through an application of Laplace's method, the localization of p_0 about z_* implies the leading order result

$$\int_0^1 G(r, s; \xi) h(s) p_0(s) ds = G(r, z_*; \xi) h(z_*) \|p_0\|_1;$$

see also [176, Section 3]. By the same token, using that $\hat{p}_0 p_0$ is localized about zero, as well as the identities $\int_0^1 \hat{p}_0 p_0 = 1$ and $h(z_*) = \ell$, we find

$$a(\xi; \Lambda_0) = G(0, z_*; \xi) f_0(0) \|p_0\|_1,$$

see also [176]. This is the desired formula for $a(\xi; \Lambda_0)$, with

$$G(0, z_*; \xi) = \frac{\sinh(\sqrt{\xi}(1 - z_*))}{\sqrt{\xi} \cosh \sqrt{\xi}}.$$

Note that, for $\xi = 0$,

$$G(z, s; 0) = 1 - \max(z, s)$$

and hence also

$$a(0; \Lambda_0) = f_0(0) \|p_0\|_1 (1 - z_*) = \lim_{\xi \downarrow 0} a(\xi; \Lambda_0).$$

Combining this last equation with (3.8), we obtain a leading order result for x_0^* . Recalling, additionally, that the remainder x_r is higher-order by the slaving

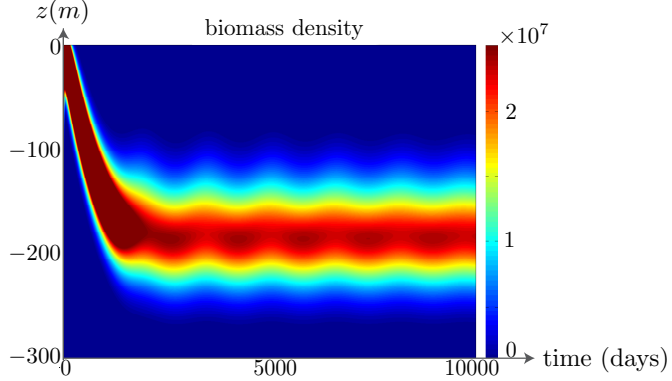


Figure 3.1: Numerical simulation of (3.13) showcasing the growth of an oscillatory DCM from an initial perturbation. Here, depth is dimensional and the parameters are chosen in the DCM regime: $\varepsilon = 9 \cdot 10^{-5}$, $v = 0.063$, $\ell = 0.25$, $\eta_H = 0.4$, $j_H = 0.033$, $\kappa = 4$ and $r = 0.65$. The period of the oscillation is of the order of years, correlating well with the longest diffusive timescale. For the values of the dimensional parameters associated with the nondimensional parameters, see Appendix C.

relation (3.3), we recover the leading order result [176, Eq. (4.9)] describing the nontrivial plankton profile for our phytoplankton-nutrient model,

$$p^*(z) = \varepsilon x^*(z) = \frac{\varepsilon \Lambda_0}{f_0(0)(1-z_*)} \frac{p_0(z)}{\|p_0\|_1}.$$

The biomass contained in that profile is $\int_0^1 p^* dz = \varepsilon \Lambda_0 / (f_0(0)(1-z_*))$, which also matches the prior result [176, Eq. (1.20)]. The stability problem (3.10) for p^* reads

$$\xi(1-z_*) + \Lambda_0 \frac{\sinh(\sqrt{\xi}(1-z_*))}{\sqrt{\xi} \cosh \sqrt{\xi}} = 0 \quad (3.18)$$

which, in turn, is identical to [176, Eq. (4.28)]. An analysis of this equation establishes the destabilization of the bifurcating pattern through a secondary, Hopf bifurcation [176]. This behavior is beautifully captured in Figure 3.1, where a localized structure is shown to develop at a depth of 120 – 220 meters in a oceanic layer with a depth of 300 meter.

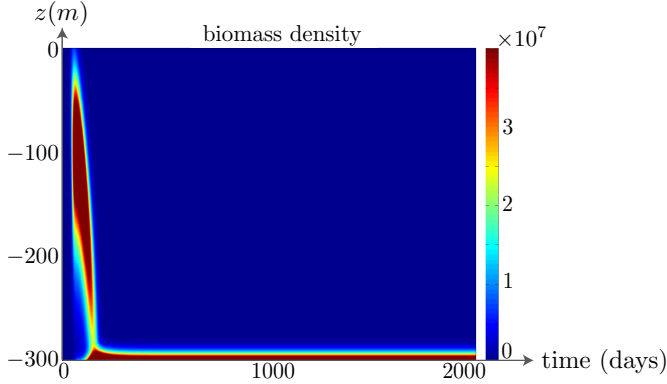


Figure 3.2: Numerical simulation of (3.13), showcasing the growth of a stationary benthic layer from an initial perturbation. The parameters here are chosen in the benthic layer regime ($\varepsilon = 9 \cdot 10^{-5}$, $v = 0.56$, $\ell = 0.25$, $\eta_H = 0.4$, $j_H = 0.033$, $\kappa = 4$, and $r = 0.65$). For the values of the dimensional parameters associated with the nondimensional parameters, see Appendix C.

3.4 Short-term evolution of bifurcating benthic layers

As we mentioned in the previous section, the bifurcating profile and its dynamics depend on the value of v . An elevated sinking speed, decreased production rate or shallower top oceanic layers increase the value of v , potentially changing the profile's qualitative properties. For $v > v^*$, in particular, the localized peak of the eigenfunction migrates to the bottom of the layer ($z = 1$) [177], and the corresponding, primary eigenvalue reads $\lambda_0 = h(1) - \ell + \mathcal{O}(\sqrt{\varepsilon})$. As a result, the small pattern developing past $\lambda_0 = 0$ is shaped as a *benthic layer* (BL), see Figure 3.2.

In this part, we formulate and investigate the stability problem for small patterns of BL-type. Our analysis roughly proceeds as in the last section, but the asymptotic estimates are technically more involved and largely deferred to the Appendix. We find that, contrary to the DCM case, the presence of slow spatial processes does *not* lead to destabilization of BL-type patterns in the regime we examine. Such patterns can and do develop transient oscillatory behavior, evidenced by the complexification of eigenvalues in their spectrum. Nevertheless, the oscillations here remain damped, unlike the sustained oscillations undergone by DCM patterns; eigenvalues cannot escape the left-half complex plane and, accordingly, BL patterns remain stable.

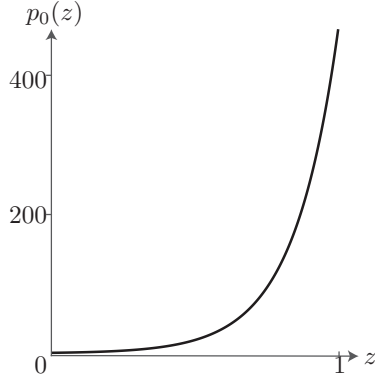


Figure 3.3: Eigenfunction profile p_0 in the case $v > v^*$.

3.4.1 Bifurcating profile

The primary eigenfunction p_0 can be approximated using the WKB method [76], see also Section 7.2 in [176]. First, the Liouville transform $p_0(z) = E(z)s_0(z) = e^{\sqrt{v/\varepsilon}z}s_0(z)$ results in a self-adjoint formulation of the eigenvalue problem, by removing the advection term:

$$\begin{aligned} \varepsilon(s_0)_z - (\ell + v - h(z) + \lambda_0)s_0 &= 0, \\ (s_0)_z(z) - \sqrt{v/\varepsilon}s_0(z)|_{z=0,1} &= 0. \end{aligned} \tag{3.19}$$

The WKB method yields, at leading order,

$$\begin{aligned} s_0(z) &= \frac{\sqrt{2v}}{\varepsilon^{1/4}Q_0^{1/4}(z)}e^{-\int_z^1 \sqrt{Q_0(s)/\varepsilon} ds}, \\ Q_0(z) &= h(1) - h(x) + v + \mathcal{O}(\sqrt{\varepsilon}), \end{aligned} \tag{3.20}$$

where we have normalized $s_0(z)$ under the $L^2(0, 1)$ norm. This profile is depicted in Figure 3.3 for the parameter values of Figure 3.2 but with $\varepsilon = 9 \cdot 10^{-3}$.

The function $a(\xi; \Lambda_0)$, appearing in the stability problem (3.10)–(3.11) is as reported in (3.14). Note that the inner product now corresponds to a projection on the benthic layer profile p_0 . Green's function (3.16) also remains unchanged, since (3.15) does not depend on v . Furthermore, the dual of p_0 assumes the form $\hat{p}_0 = E^{-1}s_0$, due to the self-adjointness of (3.19). According to (3.8), the nontrivial branch of equilibria bifurcating at $\Lambda_0 = 0$ is

$$(x_0^*(z), y^*(z)) = \frac{\Lambda_0}{a(0; \Lambda_0)} \left(1, \frac{1}{\ell} \int_0^1 p_0(s)G(z, s; 0)h(s)ds \right);$$

note, here, that p_0 depends on Λ_0 . Upon bifurcation, the stationary profile of the planktonic component develops in the shape of p_0 , shown in Figure 3.3, and amplitude growth is parametrized by Λ_0 .

3.4.2 Stability

As in Section 3.3.1, the stability properties of the bifurcating profile are governed by (3.10), with $a(\xi; \Lambda_0)$ given in (3.14). However, our asymptotic analysis here is much more involved since, in contrast to that section, it must take into account higher-order terms. A first indication of that is supported by a brief study of the limit $z_* \uparrow 1$ of the DCM case. In that limit, the deep chlorophyll maximum sinks and becomes a benthic layer, but the leading order problem (3.18) becomes trivial, indicating the need of higher-order approximations. In what follows, we work out the stability problem, referring the reader to Appendix A for computational details.

First, since p_0 is strongly localized at $z = 1$, one may estimate $a(\xi)$ by Laplace's method, cf. Section 3.3.2. Leading order asymptotics yield

$$a(\xi) = \varepsilon^{3/4} \frac{e^{\sqrt{v/\varepsilon}} h(1) f_0(1)}{4\sqrt{2}\ell v^{3/4}} + \mathcal{O}(\varepsilon^{5/4}),$$

which implies, as it does not depend on ξ , $a(\xi; \Lambda_0) = a(0; \Lambda_0)$; see Appendix A. With this leading order result, one only captures the single eigenvalue $\xi = -\Lambda_0$ from (3.11). Including the next order term, we find

$$1 - \frac{a(\xi) - a(0)}{a(\xi)} = 1 + \sqrt{\varepsilon} \frac{\sqrt{\xi} \tanh(\sqrt{\xi})}{\sqrt{v}}$$

and (3.11) becomes

$$\left(1 + \sqrt{\varepsilon} \frac{\sqrt{\xi} \tanh(\sqrt{\xi})}{\sqrt{v}}\right) \xi = -\Lambda_0, \quad (3.21)$$

which determines infinitely many other eigenvalues $\xi \in \mathbb{C}$.

We proceed with studying (3.21) in a way that resembles Section 4.4 in [176]. We set $\sqrt{\xi} = \mu = \mu_R + i\mu_I$ and restrict $\arg(\mu)$ to lie in $[0, \pi/2]$, because eigenvalues come in complex conjugate pairs. The stability equation for μ becomes,

$$p(\mu) = -\mu^2 - \sqrt{\frac{\varepsilon}{v}} \mu^3 \tanh(\mu) = \Lambda_0 > 0. \quad (3.22)$$

First, we observe that there are no solutions $\xi \in \mathbb{R}_{>0}$ (equivalently, $\mu > 0$), because p and Λ_0 differ in sign; see Figure 3.4 for an illustration. As $\Lambda_0 \downarrow 0$,

the (real) eigenvalues ξ remain in $\mathcal{O}(\sqrt{\varepsilon})$ neighborhoods of $-\Lambda_0$ and $\sigma_p(-\mathcal{M})$. This is also supported by Figure 3.4, where we have plotted $\{p(\sqrt{\xi})|\xi \in \mathbb{R}_{<0}\}$ (blue curve); real solutions correspond to intersections between that curve and the horizontal at height Λ_0 . The curve approaches vertical asymptotes at the elements of $\sigma_p(-\mathcal{M})$, and becomes unbounded. As $\varepsilon \downarrow 0$, the approach becomes steeper and the intersections of p with the horizontal axis limit to $\{0\} \cup \sigma_p(-\mathcal{M})$.

As Λ_0 increases, the first few eigenvalues complexify and the story takes a turn. We begin by noting the existence of a local maximum for the first curve branch, occurring for some $\xi \in (-\mu_1, 0)$; see Figure 3.4. As the horizontal at height Λ_0 increases, the largest two eigenvalues (intersections) approach each other, collide and develop a nonzero imaginary part; they form a conjugate pair. We have plotted the real part of that pair in red in Figure 3.4. As Λ_0 increases further, the horizontal line at height Λ_0 encounters the local minimum of the second branch. Here, the pair reconnects and splits into two negative eigenvalues, again indicated in blue. The largest of these approaches $-\mu_1$ asymptotically, while the other collides with the third eigenvalue and the process restarts. The smaller the value of ε , the larger the number of these maxima and hence the more eigenvalues are complexified subsequently as Λ_0 increases. For each ε , however, there is a global maximum of p , where the last complex pair is formed, which never returns to the real line.

Importantly, the conjugate pairs thus created do not cross into the right-half complex plane, because (3.22) admits no imaginary solutions. This is supported by Figure 3.4, where the real part of each conjugate pair can be seen to move away from the imaginary axis, as Λ_0 increases. To prove it, we write $\xi = i\hat{\xi} \in i\mathbb{R}_{>0}$ and note that $\mu = \hat{\mu}(1+i)$, for some $\hat{\mu} \in \mathbb{R}_{>0}$. Splitting real and imaginary parts in (3.22) and substituting from one into the other, we find

$$2\hat{\mu}^2 \left(-1 + \sqrt{\frac{\varepsilon}{v}} \hat{\mu} \frac{\sin(2\hat{\mu})}{\sinh^2(\hat{\mu}) + \cos^2(\hat{\mu})} \right) = \Lambda_0. \quad (3.23)$$

No solutions exist because, again, the two sides differ in sign. Since

$$\left| \hat{\mu} \frac{\sin(2\hat{\mu})}{\sinh^2(\hat{\mu}) + \cos^2(\hat{\mu})} \right| < 1,$$

the left member of (3.23) is in $(-1 - \sqrt{\varepsilon/v}, -1 + \sqrt{\varepsilon/v}) \subset \mathbb{R}_{<0}$, for ε small. As we consider $\Lambda_0 > 0$, only there exists no nontrivial solution $\hat{\mu}$ to (3.23), and hence no purely imaginary eigenvalues ξ of (3.21). The real parts of the complex eigenvalues thus never change sign.

Since the spectrum of the stability problem (3.21) remains in the left-half complex plane, we conclude that the benthic layer remains stable for $\mathcal{O}(1)$,

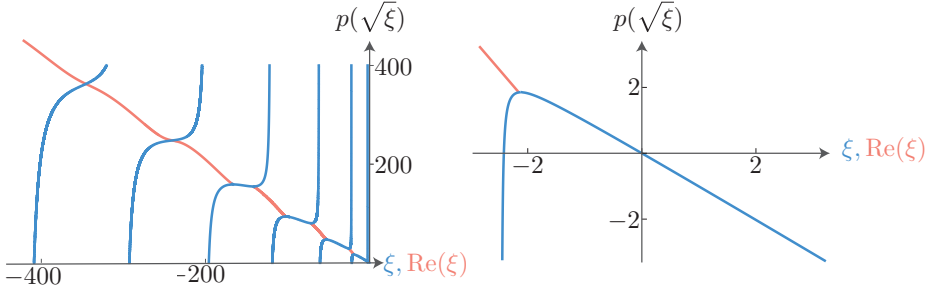


Figure 3.4: Left: In blue, the function $p(\sqrt{\xi})$ for $\xi \in \mathbb{R}$ in a neighborhood of the origin. Red: the function $p(\sqrt{\xi})$, where the argument is no longer purely imaginary, so that $p(\sqrt{\xi})$ is a function over the complex plane. The red curve is the projection of this function onto the $\Im\sqrt{\xi} = 0$ plane. Here, $\sqrt{\varepsilon/v} = 10^{-2}$. Right: In blue, the function $p(\sqrt{\xi})$ for $\xi < 0$ in a neighborhood of the origin. Red: the function $p(\sqrt{\xi})$, where the argument is no longer purely imaginary, so that $p(\sqrt{\xi})$ is a function over the complex plane. The red curve is the projection of this function onto the $\Im\sqrt{\xi} = 0$ plane. Here, $\sqrt{\varepsilon/v} = 10^{-2}$.

positive values of Λ_0 . The reader should contrast this behavior to that of deep chlorophyll maxima which, as we mentioned, undergo oscillatory destabilization soon after they bifurcate. The difference between these two patterns is underlined by numerical simulations, such as those of Figures 3.1 and 3.2. Numerically, one solely observes stationary BL profiles. Stationary DCM profiles are also present, but can only be detected in a targeted manner as they only exist in an asymptotically small parametric region.

In the region $v \approx v^*$, one expects the system dynamics to exhibit interplay between BL and DCM patterns. In that region, the two first eigenvalues cross the imaginary axis in close succession. This is what was referred to as a codimension 2 bifurcation in earlier work [176], where the existence of such patterns was hypothesized but not proved. Figure 3.5 demonstrates what is possibly one such pattern, where a rather shallow DCM and a BL alternate in a periodic fashion. This simulation serves as numeric indication of the existence and stability of such mixed patterns in (3.13). At the same time, it very possibly illuminates the wide chasm separating nonlinear reality, on one hand, from attempts to explore it through linear analysis on the other. As we briefly mentioned in the Introduction, we expect that the method developed here will prove helpful in covering some of that ground. At present, we defer all analysis to future work.

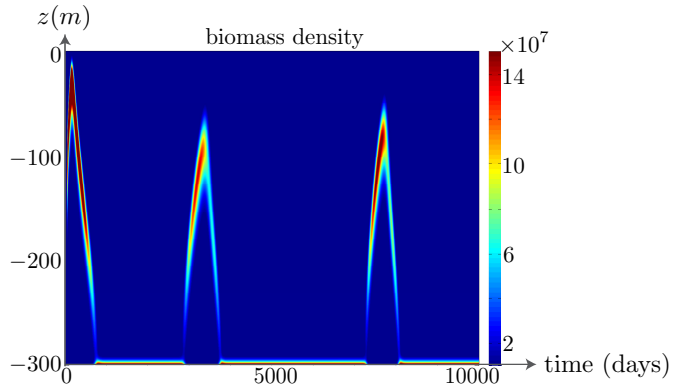


Figure 3.5: Numerical simulation close to the codimension 2 bifurcation showcasing the appearance of a periodic state that interpolates a DCM and a BL. The specific parameters values for this simulation are $\varepsilon = 9 \cdot 10^{-5}$, $v = 0.32$, $\ell = 0.25$, $\eta_H = 0.3$, $j_H = 0.033$, $\kappa = 4$ and $r = 0.65$. For the values of the dimensional parameters associated with the nondimensional parameters, see Appendix C.

3.5 Conclusions

In this chapter, we considered the evolution of small amplitude patterns bifurcating from a trivial state in evolutionary PDE systems. In that direction, we specifically developed a novel analytical framework to study their dynamics beyond the range of applicability of classical, one-dimensional, center manifold reduction. Our main insight is that, in general PDE systems such as (3.1), classical reduction can and must be extended to capture dynamically significant behavior. The result of that process is the reduced model (3.4), comprised of a nonlinear ODE and a linear PDE. The two govern, respectively, the amplitude of the emerging pattern and the slow spatial processes mentioned in the title of this communication. The coupling between them is strong and describes accurately the interactions between pattern and ambient environment.

Using that framework, we next examined the infinite-dimensional eigenvalue problem determining pattern stability. We were able to encapsulate that in a transcendental equation that elegantly conflates information from the background state and the generator of the spatial processes. This analytical result is expressed in (3.10)–(3.12), and its solutions correspond to eigenvalues of the stability problem. As such, it extends, streamlines and simplifies similar results where the infinite-dimensional system was used to work with, instead of the ODE–PDE

formulation, see [176] and Chapter 2.

Finally, we applied our general method to a specific example describing the interaction of phytoplankton and nutrient in a water column [78, 177, 176]. This enabled us to recover swiftly the onset of oscillations in *deep chlorophyll maxima*, a phenomenon previously observed and simulated [78] as well as analyzed by less elaborate methods [176]. Moreover, our method allowed us to extend earlier insights [78, 176, 177] by considering the more degenerate dynamics of *benthic layers*.

3.6 Acknowledgements

We wish to thank Prof. Huib de Swart and Brianna Liu (University of Utrecht, IMAU) for generously providing the simulator for (3.1). LS acknowledges the support of NWO through the *Nonlinear Dynamics in Natural Systems* (NDNS⁺) cluster.

Appendices

A Approximation of integrals with a localized function

The primary eigenfunction $p_0(z)$ associated with a benthic layer has a very narrow, large amplitude at $z = 1$, see Figure 3.3. In this appendix, we will write p_0 as,

$$p_0(z) = A(z)e^{-\frac{1}{\sqrt{\varepsilon}}H(z)} \quad (3.24)$$

with $H(z) = \int_z^1 \sqrt{Q(s)}ds - \sqrt{v}z$ and $A(z) = \sqrt{2v\varepsilon^{-1/4}}Q(z)^{-1/4}$.

We use the localized structure of p_0 to our advantage in approximating integrals of the form

$$\int_0^x f(z)p_0(z)dz = \int_0^x F(z)e^{-\frac{1}{\sqrt{\varepsilon}}H(z)}, \quad (3.25)$$

where $f(z)$ is (with a slight abuse of notation) any real, continuous function and $F(z) = f(z)A(z)$. The technique used for approximation is called *Laplace's method* [174, 76] and was applied repeatedly in earlier work on phytoplankton patterns [176]. The idea behind this method is to evaluate an integral with an exponentially decaying factor only at its maximum, because the error is exponentially small. In our case, the exponential in (3.25) is maximal where $H(z)$ is minimal. $H(z)$ is monotonically decreasing, hence the minimum of $H(z)$ for $z \in [0, x]$ is at $z = x$. We Taylor expand,

$$\begin{aligned} H(z) &= H(x) + \sum_{n \geq 0} a_n(z-x)^{n+1}, \\ F(z) &= \sum_{n \geq 0} b_n(z-x)^{n+\alpha-1}, \end{aligned} \quad (3.26)$$

with $\alpha > 0$ and compute $a_0 = -\sqrt{Q(x)} - \sqrt{v}$ and $a_1 = -\frac{1}{4}\frac{Q'(x)}{2\sqrt{Q(x)}}$. Laplace's

method yields, up to $\mathcal{O}(\varepsilon^{\frac{\alpha}{2}+1})$ corrections,

$$\int_0^x F(z) e^{-\frac{H(z)}{\sqrt{\varepsilon}}} dz = \begin{aligned} & -e^{-\frac{H(x)}{\sqrt{\varepsilon}}} \varepsilon^{\frac{\alpha}{2}} \left(\Gamma(\alpha) \frac{b_0}{a_0^\alpha} + \sqrt{\varepsilon} \frac{\Gamma(\alpha+1)}{a_0^{\alpha+1}} \left[b_1 - \frac{(\alpha+1)a_1 b_0}{a_0} \right] \right), \end{aligned} \quad (3.27)$$

as $\varepsilon \rightarrow 0$ [174, 76]. Note the Gamma function $\Gamma(n) = (n-1)!$ for natural numbers n .

B Approximation of the eigenvalue function

The eigenvalue function $a(\xi; \Lambda_0)$ is defined in equation (3.5),

$$a(\xi; \Lambda_0) = \frac{1}{\ell} \left\langle f_0 p_0 \int_0^1 G(z, s; \xi) h(s) p_0(s) ds, \hat{p}_0 \right\rangle,$$

but due to the definition of $G(z, s; \xi)$, we need to split the inner integral into separate integrals taking care of $\min(z, s)$ and $\max(z, s)$. After that, we use Laplace's method to approximate $\int_0^1 G(z, s; \xi) h(s) p_0(s) ds$, and then perform it once more to find $a(\xi)$. The leading order result is:

$$a(\xi) = \varepsilon^{3/4} \frac{e^{v/\varepsilon} h(1) f_0(1)}{4\sqrt{2}\ell v^{3/4}}. \quad (3.28)$$

Note that this leading order term does not depend on ξ , hence $a(0)$ has the same leading order term.

For the stability equation (3.11), we therefore consider the difference

$$\begin{aligned} \ell(a(\xi) - a(0)) &= \left\langle f_0 p_0 \int_0^1 G(z, s; \xi) h p_0 ds, \hat{p}_0 \right\rangle \\ &\quad - \left\langle f_0 p_0 \int_0^1 G(z, s; 0) h p_0 ds, \hat{p}_0 \right\rangle \\ &= \int_0^1 f_0 s_0^2 \int_0^1 h p_0 [G(z, s; \xi) - G(z, s, 0)] ds dz \end{aligned} \quad (3.29)$$

For $\xi \rightarrow 0$, the Green's function becomes $G(z, s; 0) = \lim_{\xi \rightarrow 0} G(z, s; \xi) = 1 - \max(z, s)$.

$$\begin{aligned}
 & \int_0^1 f_0 s_0^2 \int_0^1 G(1, 1-s+z; \xi) h p_0 ds dz \\
 & - \int_0^1 f_0 s_0^2 \int_0^1 G(1, 1-s+z; 0) h p_0 ds dz \\
 & + \int_0^1 f_0 s_0^2 \int_0^1 (G(-z, s; \xi) - G(-z, s; 0)) h p_0 ds dz,
 \end{aligned}$$

because $G(1, 1-s+z; \xi)$ is zero for $z \leq s \leq 1$ and $\min(-z, s)$ and $\max(-z, s)$ do not change for $0 \leq s, z \leq 1$. We shall evaluate separately for every Green's function. Define

$$\begin{aligned}
 I_{1,i} &= \int_0^1 G(1, 1-s+z; i) h(s) p_0(s) ds, \\
 I_{2,i} &= \int_0^1 G(-z, s; i) h(s) p_0(s) ds.
 \end{aligned}$$

with $i \in \{\xi, 0\}$. Integrals $I_{1,i}$ and $I_{2,i}$ are of the form (3.25) and we use the following table to approximate them with Laplace's method.

	α	b_0	b_1
$I_{1,\xi}$	2	$\sqrt{\xi} \frac{h(z)}{Q^{1/4}(z)}$	$\frac{h(z)Q'(z)}{4Q^{5/4}(z)} - \frac{h'(z)}{Q^{1/4}(z)}$
$I_{1,0}$	1	$\frac{h(z)}{Q^{1/4}(z)}$	—
$I_{2,\xi}$	2	$-\sqrt{\xi} \frac{h(1)}{v^{1/4}}$	$-\sqrt{\xi} \frac{h'(1)h(1)}{4v^{5/4}-v^{1/4}}$
$I_{2,0}$	1	$\frac{h(1)}{v^{1/4}}$	—

The higher order coefficients of $I_{1,0}$ and $I_{2,0}$ are not needed for the approximation, compared to $I_{1,\xi}$ and $I_{2,\xi}$ (compare $\alpha = 1$ versus $\alpha = 2$). Substituting the Taylor coefficients into approximation (3.27) and combining terms yields

$$\begin{aligned}
 \ell(a(\xi) - a(0)) &\rightarrow \frac{1}{2} \sqrt{2} (\varepsilon v)^{\frac{1}{4}} h(1) e^{\sqrt{\frac{v}{\varepsilon}}}. \\
 & \int_0^1 \frac{f_0(z)}{\sqrt{Q(z)}} e^{-\frac{2}{\sqrt{\varepsilon}} \int_z^1 \sqrt{Q(s)} ds} \left(1 - \frac{\cosh(\sqrt{\xi}z)}{\cosh(\sqrt{\xi})} \right) dz
 \end{aligned} \tag{3.30}$$

which is a second order Laplace approximation. The integral over z , which is left, is not of the form (3.25), as the exponential is now

$$e^{-\frac{2}{\sqrt{\varepsilon}} \int_z^1 \sqrt{Q(s)} ds}.$$

The factor $\int_z^1 \sqrt{Q(s)} ds$ is also monotonically decreasing, and hence we can estimate (3.30) at $z = 1$. Using Taylor approximations, we find $\alpha = 2$, and Laplace's method yields

$$\begin{aligned} & \ell(a(\xi) - a(0)) \rightarrow \\ & -\varepsilon^{\frac{5}{4}} e^{\sqrt{\frac{V}{\varepsilon}}} \frac{(h(1))^2 \eta_H}{4\sqrt{2}(1+\eta_H)\ell v^{3/4}} \sqrt{\xi} \tanh(\sqrt{\xi}). \end{aligned} \quad (3.31)$$

C Nondimensionalization

The system analyzed in sections 3.3 and 3.4 is a nondimensionalized version of a phytoplankton-nutrient model as stated in [78] and [177],

$$\begin{aligned} W_{\hat{t}} &= DW_{\hat{z}\hat{z}} - VW_{\hat{z}} + \left[\hat{\mu}P(L, N) - \hat{\ell} \right] W, \\ N_{\hat{t}} &= DN_{\hat{z}\hat{z}} - \alpha \hat{\mu}P(L, N)W, \end{aligned} \quad (3.32)$$

with

$$\begin{aligned} L(\hat{z}, \hat{t}) &= L_I e^{-K_{\text{bg}}\hat{z} - R \int_0^{\hat{z}} W(\xi, \hat{t}) d\xi}, \\ P(L, N) &= \frac{LN}{(L + L_H)(N + N_H)}. \end{aligned} \quad (3.33)$$

The coordinates \hat{z} and \hat{t} represent depth $-\hat{z} \in (0, z_B)$ and time. The system (3.32) is subject to boundary conditions,

$$\begin{aligned} DW_{\hat{z}} - VW|_{\hat{z}=0, z_B} &= 0, \\ N_{\hat{z}}|_{\hat{z}=0} &= 0, \\ N|_{\hat{z}=z_B} &= N_B. \end{aligned} \quad (3.34)$$

Here, W and N are the phytoplankton and nutrient concentration in a water column of depth z_B , and the system is assumed to be in a turbulent mixing regime. The parameters V , $\hat{\ell}$, α and $\hat{\mu}$ measure the sinking speed of phytoplankton, the species-specific loss rate, the conversion factor and the maximum specific production rate, respectively. The function L models the light intensity, where L_I is the light intensity at the surface, R is the shading due to plankton and K_{bg} is the light absorption coefficient. Lastly, L_H and N_H are half-saturation constants of light and nutrient, respectively.

The relevant parameter values used in [78] and their units are reported in C.1. By introducing new parameters and coordinates, we rescale system (3.32) to a nondimensional system.

Indicent light intensity	L_I	600	m^2/s
Background turbidity	K_{bg}	0.045	m^{-1}
Absorption coeff. phyto	R	$6 \cdot 10^{-10}$	m^2/cell
Depth	z_B	300	m
Vert. turbulent diffusivity	D	$1.2 \cdot 10^{-5}$	m^2/s
Max. specific growth rate	$\hat{\mu}$	$1.11 \cdot 10^{-4}$	s^{-1}
Half-sat. light	L_H	20	m^2/s
Half-sat. nutrient	N_H	$2.5 \cdot 10^{-2}$	m^{-3}
Specific loss rate	$\hat{\ell}$	$2.78 \cdot 10^{-6}$	s^{-1}
Nutrient content phyto	α	$1 \cdot 10^{-9}$	$\text{mmol}/\text{cell}^3$
Sinking velocity	V	$1.17 \cdot 10^{-5}$	m/s
Bottom nutrient supply	N_B	10	m^{-3}

Table C.1: Dimensional parameters of (3.32) used in [78] for a simulation in which the phytoplankton seems to behave chaotically.

$$\begin{aligned}
 z &= \frac{\hat{z}}{z_B} & \ell &= \frac{\hat{\ell}}{\hat{\mu}}, \\
 t &= \hat{\mu}\hat{t} & v &= \frac{V^2}{4\hat{\mu}D}, \\
 p(z, t) &= \frac{\hat{\ell}\alpha z_B^2}{DN_B} W(\hat{z}, \hat{t}) & \eta_H &= \frac{N_H}{N_B} \\
 n(z, t) &= 1 - \frac{N(\hat{z}, \hat{t})}{N_B} & \kappa &= K_{\text{bg}}z_B, \\
 \varepsilon &= \frac{D}{\hat{\mu}z_B^2} & r &= \frac{RDN_B}{\hat{\ell}\alpha z_B}.
 \end{aligned} \tag{3.35}$$

Note that n rescales N as the offset of nutrient from the maximum at the bottom, N_B . The rescaling transforms systems (3.32) to

$$\begin{aligned}
 p_t &= \varepsilon p_{zz} - 2\sqrt{\varepsilon} vp_z + (\mu(z, p, n) - \ell)p, \\
 n_t &= \varepsilon n_{zz} + \varepsilon \ell^{-1} \mu(z, p, n)p.
 \end{aligned} \tag{3.36}$$

with

$$\mu(z, p, n) = \frac{j(1-n)}{(j-j_H)(\eta_H+1-n)}, \quad j = e^{-\kappa z - r \int_0^z p(\xi, t) d\xi}.$$

parameter	Figure 3.1	Figure 3.2	Figure 3.5
L_I	600	600	600
K_{bg}	$1.33 \cdot 10^{-2}$	$1.33 \cdot 10^{-2}$	$1.33 \cdot 10^{-2}$
R	$6 \cdot 10^{-10}$	$6 \cdot 10^{-10}$	$6 \cdot 10^{-10}$
z_B	300	300	300
D	$9 \cdot 10^{-5}$	$9 \cdot 10^{-5}$	$9 \cdot 10^{-5}$
$\hat{\mu}$	$1.11 \cdot 10^{-4}$	$1.11 \cdot 10^{-4}$	$1.11 \cdot 10^{-4}$
L_H	20	20	20
N_H	4	4	3
$\hat{\ell}$	$2.78 \cdot 10^{-6}$	$2.78 \cdot 10^{-6}$	$2.78 \cdot 10^{-6}$
α	$1 \cdot 10^{-9}$	$1 \cdot 10^{-9}$	$1 \cdot 10^{-9}$
V	$1.59 \cdot 10^{-5}$	$4.74 \cdot 10^{-5}$	$3.59 \cdot 10^{-5}$
N_B	10	10	10

Table C.2: Dimensional parameters used in the Figures 3.1, 3.2 and 3.5.

The boundary conditions transform according to (3.35), too.

$$\begin{aligned} \varepsilon p_z - 2\sqrt{\varepsilon v p} \Big|_{z=0,1} &= 0, \\ n_z(0) &= 0, \\ n(1) &= 0. \end{aligned} \tag{3.37}$$

For the figures 3.1, 3.2, 3.5, the dimensional parameters that are used to simulate the model are reported in the table C.2.

Tumor spread with an Allee effect¹

4.1 Introduction

4.1.1 Allee effects and tumor growth

A recent article in *Nature Reviews Cancer*, [94], has highlighted how a well-established concept in ecology—the Allee effect [2]—is also relevant to tumors but has yet to be incorporated into their modelling. In its strong form, the Allee effect refers to the observation that there is a population threshold below which a species has negative population growth, driving it to extinction. The weak form of the Allee effect describes a species that has small (but not negative) population growth at low populations [25]. The ecological causes of Allee effects (which are observed within small populations) are multitudinous: the inability to find a mate; the negative impact on co-operative behaviors such as anti-predator vigilance; the increased sensitivity to demographic stochasticity; and, the lack of diversity in the extant gene pool [26, 86, 148]. Evidence for the strong [12, 27, 65, 81, 99] and weak [2, 5, 30, 151, 152] Allee effects are plentiful across many taxa; additional reviews are available in [64, 95]. Consequently, there is a proliferation of mathematical models of the Allee effect in ecology [7, 8, 29, 70, 96, 102, 130, 175, e.g.]. While studies in ecology often worry about factors that might push a threatened species below the (strong) Allee threshold and thereby towards extinction [137, e.g.], an intriguing possibility in cancer research is whether the Allee effect could be harnessed for controlling or negating the growth of cancerous cells [94], consonant with recent experiments in bacteria [146].

¹The content of this chapter was published as *Influences of Allee effects in the spreading of malignant tumours* in Journal of Theoretical Biology in 2016, see [140].

While seldom stated, hints of the Allee effect are numerous in the cancer research literature. Firstly, at the most anecdotal level, a tumor is only deemed threatening if it is above a certain size, which is an implicit presumption of a strong Allee threshold. More concrete illustrations are available in clinical trials for papillary and follicular thyroid cancers [107], in which risk-of-spread versus initial tumor size figures indicate that the risk is effectively zero until a minimum primary tumor size is reached. Secondly, studies of tumor dormancy suggest the presence of mechanisms such as a restrictive apoptosis/proliferation equilibrium (a cell density at which natural cell death balances new cell production) or a minimum angiogenic potential requirement for blood vessel formation in the tumor [136]. Such biological considerations translate to the inability of the tumor to grow unless a strong Allee threshold is reached. Thirdly, it has been shown experimentally that in the growth of blebs (spherical protrusions forming along the front boundary of tumors), there is a minimum surface tension below which the blebs cannot expand [155]. Since this surface tension is governed by a variety of poorly understood factors such as available myosin [155], the existing microenvironment can be thought of as essentially imposing an Allee effect. Fourthly, [6] and [127] provide evidence of the co-operation between nearby subclones in the early evolution of tumors through the production and exchange of growth factors. Since co-operation is adversely impacted at low populations, tumor cells must—as in ecological systems—encounter the Allee effect. Fifthly, deleterious mutations accumulate more in smaller tumors [94], thereby driving the population to extinction with much higher probability than larger tumors. Sixthly—and at a much broader level—the very fact that cancers depend on genetic heterogeneity, mutations and subsequent evolution [15, 63, 113], pinpoints the necessity of having a large enough gene pool for successful growth, that is, the requirement of an Allee effect². For example, numerical results from a recent integral equation model that models the number of cells in clones with different mutation rates, indicate that there is a threshold genetic mutation rate below which the cancer cells suffer extinction [4]. It is important to note that most evolutionary models of cancer (see the reviews by [113] and [116]) neglect the spatial structure, which is problematic given that tumors are clinically classified depending on their shape [24]. One way of incorporating genetic mutation information within a spatial spreading model is to treat the stochastic mutations as creating an effective strong Allee threshold.

There are a variety of tumor growth models which examine the roles of additional effects such as acidity [53, 111, 13], adhesion [20, 55, 141], non-local interactions [150, 55], cell plasticity in proliferation versus migration [50, 72, 153,

²This is stating that genetic diversity produces an implicit Allee effect, different from studies on the impact of a *separately imposed* Allee effect on genetic diversity [172, 173].

110], in a range of tumor types. Most models fall into two classes: those which simulate a network of cells [72, 153], and those which rely of continuum modelling [20, 53, 110, 111, 141, 150, e.g.], although some models that make a connection between the two exist, [10, 46, 122, e.g.]. Very recently, a spatio-temporal tumor cell growth model incorporating micro-environmental influences has been studied. That analysis reveals an Allee effect depending on the cell motility versus local cell density, [14].

4.1.2 A new model for malignant tumor invasion

In light of this emergent viewpoint on the relevance of the Allee effect in cancers, we offer in this manuscript, one of the first (see also [17]) cancer spreading model that explicitly includes the Allee effect. Specifically, we examine how the inclusion of the Allee effect changes conclusions in comparison to the commonly used logistic growth model. For our comparison – the first of its kind – we choose to examine a model of a malignant, solid tumor invading through the extracellular matrix (ECM) via haptotaxis or chemotaxis, as opposed to the more complex, metastatic dissemination regime [170]. In particular, our analysis applies to the spread of tumors in which haptotaxis or chemotaxis is the dominant mechanism of cell migration, such as melanoma [109, 125]. We focus on the behavior of the tumors on a long time scale; we do not analyse the transient dynamics.

We assume that an invasive tumor front can be modeled, mathematically, by a traveling wave solution (TWS) with constant speed c . TWSs correspond to stationary solutions in an appropriately moving frame and are defined on a one-dimensional, unbounded spatial domain. While this choice of domain is a simplification of the geometry of tumor invasion, it is a reasonable approximation, while still yielding a model that is amenable to mathematical analysis.

We build on a model of malignant tumor invasion derived in [126] and subsequently studied in [67, 109]. In these articles, a logistic growth term is used to model the growth of the cancer cells (see paragraph 4.1.4); Allee effects are neglected. Here, we replace this logistic growth term with an Allee growth term and study the existence of TWSs of the following dimensionless model for malignant tumor invasion (see section 4.2 for the derivation):

$$\begin{aligned} \frac{\partial u}{\partial t} &= \underbrace{-u^2 w}_{\text{proteolysis}} + \underbrace{\varepsilon \beta \frac{\partial^2 u}{\partial x^2}}_{\text{diffusion}}, \\ \frac{\partial w}{\partial t} &= \underbrace{f(u, w)}_{\text{growth}} - \underbrace{\frac{\partial}{\partial x} \left(\underbrace{\frac{\partial u}{\partial x} w}_{\text{haptotaxis}} \right)}_{\text{haptotaxis}} + \underbrace{\varepsilon \frac{\partial^2 w}{\partial x^2}}_{\text{diffusion}}, \end{aligned} \quad (4.1)$$

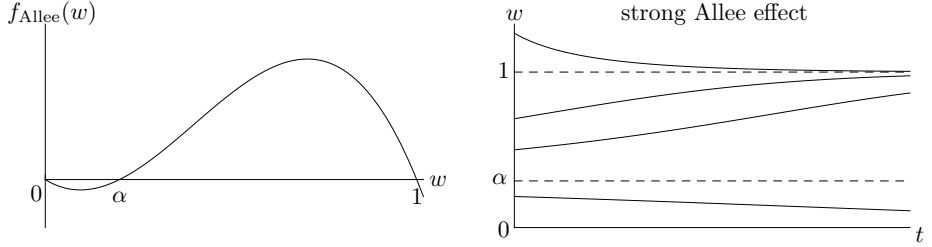


Figure 4.1: Left-hand panel: Sketch of $f_{\text{Allee}} = w(1 - w)(w - \alpha)$ for $0 < \alpha < 1$. Observe that $f_{\text{Allee}} > 0$ for $\alpha < w < 1$. Right-hand panel: Sketch of the solutions to $w' = w(1 - w)(w - \alpha)$ with $0 < \alpha < 1$. Initial conditions larger than α approach the carrying capacity (which is scaled to one), while initial conditions smaller than α die out and approach $w = 0$.

with

$$f(u, w) = f_{\text{Allee}}(w; \alpha) := w(1 - w)(w - \alpha), \quad |\alpha| < 1. \quad (4.2)$$

The dependent variables $u \geq 0$ and $w \geq 0$ represent the dimensionless ECM and cancer cell densities, respectively. The independent variables $t > 0$ and $x \in \mathbb{R}$ represent time and one-dimensional space, respectively. Both species are assumed to diffuse slowly, which is modeled by the small parameter ε : $0 \leq \varepsilon \ll 1$. We further assume that the ECM diffuses more slowly than the cancer cells: $0 \leq \beta \leq 1$ and independent of ε . Observe that our analysis is also able to capture the situation of the ECM not diffusing, i.e. $\beta = 0$. The observed migration of the cancer cells up the gradient of ECM is modeled by the haptotaxis term. As the cancer cells migrate they break down the ECM; this is modeled by the proteolysis term. The cubic function describing the growth of the cancer cells, (4.2), models the Allee effect, with different values of α corresponding to different strengths. Consistent with the definition in Section 4.1.1, the Allee effect modeled by (4.2) describes the following.

A positive α models the strong Allee effect. Since the carrying capacity of the cancer cell density has been scaled to one in (4.2), we require $\alpha < 1$. The strong Allee effect imposes a growth threshold on the tumor, whereby the cancer cell population only increases (at a given location) if $\alpha < w < 1$, since otherwise $f_{\text{Allee}} \leq 0$. See also Figure 4.1. In the context of tumor invasion, $\alpha \gtrsim 0$ is the most appropriate representation of the strong Allee effect as it is unlikely that a large threshold value (relative to the carrying capacity) is needed for the proliferation of cancer cells.

A negative α models the weak Allee effect. Unlike the strong Allee effect,

the weak Allee effect does not impose a growth threshold. Instead, it models a population with a growth rate that is initially positive and increases with population increase for *small* populations, until crowding effects take over and cause the growth rate to decrease with further population increase. Hence, we require $\alpha > -1$, with $\alpha \gtrapprox -1$ corresponding to the most appropriate representation of the weak Allee effect. For further discussion and more precise definitions of the strong and weak Allee effects, see [25] and Appendix A.

4.1.3 Main results

The focus of this chapter is to compare the Allee model (4.1)–(4.2) with the logistic model, developed in [126], with respect to its ability to capture the behavior of malignant tumor invasion. Furthermore, we compare our results to a different modification of the logistic model, studied in [108], where competition between the species is included in $f(u, w)$ in (4.1). For convenience, we refer to (4.1)–(4.2) with $\alpha \gtrapprox 0$ and $\alpha \gtrapprox -1$ as the strong and weak Allee models, respectively. We present evidence that the strong Allee model provides a better model of tumor invasion than these previously proposed models, while the weak Allee model provides no significant improvement. The following sections provide a summary of the main results that lead to these conclusions.

Strong Allee model

For the strong Allee model, we find that:

- Only invasive tumor fronts with well-defined edges [108] (so-called *Type III waves*, see Section 4.1.4) exist, rather than the whole family that exists for the previously studied models of malignancies such as melanoma [67, 108, 109, 126]; and,
- A non-monotonic (biphasic) relationship between the background ECM density and the invasion speed of the tumor is evident, consistent with the experiments on a HT1080 fibrosarcoma cell line invading collagen gels as reported in [125, 108]. In contrast, models without the Allee effect predict a monotonic relationship [67, 126, 109]. See in particular Figure 11 in [67].

These results are illustrated in Figure 4.2. The numerical method used to simulate (4.1)–(4.2) uses a vertex-centered finite volume discretisation in space, with upwinding to approximate u and w at the faces of the control volumes, on a linear mesh with $\Delta x = 1/80$. The resultant ODEs are integrated in time using MATLAB's inbuilt ODE solver `ode45` (which uses a variable-order Runge–Kutta algorithm with adaptive timestepping).

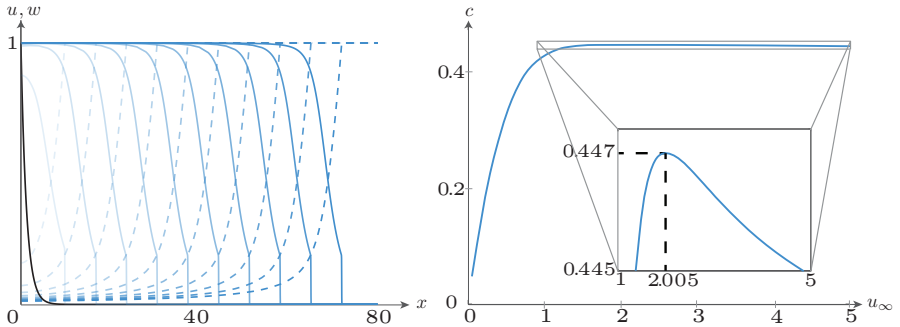


Figure 4.2: Left-hand panel: A *Type III wave* with a biologically justified, well-defined edge and speed $c \approx 0.43$, obtained by numerically simulating (4.1)–(4.2) with $\varepsilon = 0.001$, $\alpha = 0.05$ and $\beta = 0.5$. The dashed lines correspond to u -profiles and the solid lines to w -profiles, with solutions plotted at $t = 0$ (black), 16 (lightest), 32, . . . , 160 (darkest). Right-hand panel: The leading order ($\varepsilon = 0$) component of the speed of traveling wave solutions of (4.1)–(4.2) (c) versus the background ECM density (u_∞), with $\alpha = 0.05$, illustrating a biphasic relationship.

Weak Allee model

In contrast, the main result relating to the weak Allee model is that it offers no notable benefits over the previously studied models for tumor invasion such as melanoma and, so, due to its added complexity, is a less preferable model of malignant invasion. Consequently, we omit the derivation of the results from the main body of the chapter; we present them briefly in Appendix B. The key findings that lead to our conclusion are as follows.

- There exists a family of invasive tumor fronts (so-called *Type I–IV waves*), which includes some that have non-sharp fronts but that appear (numerically) to be stable and, hence, observable within the system.
- The relationship between the background ECM density and the invasion speed of the tumor fronts with sharp edges is monotonically increasing, contrary to an experimentally observed biphasic relationship [125].

4.1.4 Comparison with results for previous models

In the models for malignant tumor invasion studied in [67, 109, 125, 126], the cancer cells are assumed to grow logistically, governed by the dimensionless

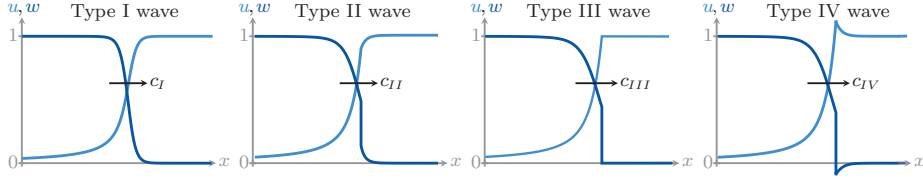


Figure 4.3: Schematics of the four types of traveling wave solutions discussed in this chapter. This figure is an adaptation of Figure 6 in [67]. Copyright ©2014 Society for Industrial and Applied Mathematics. Reprinted with permission. All rights reserved.

kinetic function

$$f(u, w) = f_{\text{logistic}}(w) := w(1 - w). \quad (4.3)$$

In the model studied in [108], an interaction term between the ECM (u) and cancer cells (w) is added to (4.3) to signify the competition for space between the two species. Subsequently, the growth of the cancer cells is governed by the dimensionless kinetic function

$$f(u, w) = f_{\text{competition}}(w) := w(1 - w) - \gamma uw. \quad (4.4)$$

Thus, the models studied previously are (4.1), with (4.3) or (4.4) in place of (4.2)³. Henceforth, for convenience, we refer to the former as the logistic model and the latter as the competition model.

In [67], it is shown that the logistic model admits a continuous family of traveling wave solutions (TWSs). This family is classified into four distinct types, according to qualitative differences in the cancer cell density profiles, in the singular limit $\varepsilon \rightarrow 0$; see Figure 4.3. A *Type I wave* has a smooth, exponentially decaying cancer cell density profile. A *Type II wave* has a cancer cell density profile with a shock but that remains positive and decays exponentially to zero as $x \rightarrow \infty$. A *Type III wave* has a cancer cell density profile with a shock and semi-compact support. A *Type IV wave* has a cancer cell density profile with a shock and that decays exponentially to zero as $x \rightarrow \infty$ but with densities that are negative after the shock. Preliminary numerical results suggest that the Type I–III waves are stable, in the sense that they are observable in the system, while the Type IV waves are not [67].

Remark 4.1. The labelling of the four wave types depicted in Figure 4.3 refers to those waves identified in [67] for the logistic model. However, the classifications

³In [109, 126, 108], it is assumed, for simplicity, that $\varepsilon = 0$. In [67], $\beta = 1$.

that underpin this terminology apply more generally, for example, to TWSs of (4.1) with $0 \leq \varepsilon \ll 1$ and $0 \leq \beta \leq 1$. Thus, we adopt the labels Type I–IV and henceforth use them to refer to any waves with equivalent features to those described in [67], outlined above.

A similar family of Type I–IV waves exists for the competition model, studied in [108]⁴. Moreover, numerical simulations suggest that in certain, broad parameter regimes, the Type I–III waves are stable and, hence, observable in the system. Although the Type IV solution is not observable and a negative density has no interpretation in the current application of system (4.1), we consider this type of solution for the sake of completeness.

From a biological perspective, Type III waves are considered to be most realistic for tumors which are expected to possess a well-defined edge; such as melanomas, see for example [108]. In contrast to the logistic, competition and weak Allee models, the strong Allee model automatically *selects* tumors with sharply defined edges.

In [125], a *biphasic relationship* between the background collagen (the predominant ingredient in ECM) density and the invasion speed of malignant tumors is observed experimentally. These experimental results indicate that the invasion speeds of malignant tumors do not increase monotonically with the background collagen (and, hence, ECM) density. Instead, there is some critical density up to which the invasion speed increases but over which the invasion speed decreases. The competition model was proposed in [108] to mathematically replicate this biphasic relationship, which is not a feature of the logistic model [67, 109, 108]. The logistic model exhibits a monotonically increasing relationship between the speed of the Type III waves c_{III} and the background ECM density u_∞ , similar to the weak Allee model. By studying only the Type III waves, the desired biphasic relationship is revealed in [108]. Mathematically, this result is facilitated by the existence to two Type III waves, with different u_∞ , for certain, fixed speeds.

4.1.5 Outline

The remainder of the chapter is set out as follows. In Section 4.2, we derive the dimensionless model (4.1) from a dimensional model for malignant tumor invasion proposed in [126]. In Section 4.3, we set up the mathematical framework that is required to prove the main results of the strong Allee model, described in Section 4.1.3. We prove (in a mathematically rigorous way) that the strong Allee model only admits Type III traveling wave solutions. The framework we follow exploits the separation of scales between the haptotaxis or chemotaxis and diffusion terms. It is based on that described in [167] and uses geometric singular perturbation

⁴Only Type III waves are considered in [108] but, using methods developed in [167] and used in [67] and here, it can be shown that Type I, II and IV waves also exist.

theory (GSPT) [73, 82, 84] and canard theory [11, 97, 149, 166]. The results for the strong Allee model are further analysed in Section 4.4, including the biological implications of our findings in relation to previously studied models. In Section 4.5, we discuss the extension of our results to a more general class of models, the limitations of our work and topics for future research.

Remark 4.2. The mathematical derivation contained within Section 4.3 is not prerequisite to following the arguments and discussions contained within the subsequent sections. Thus, we invite the less mathematically inclined reader to skip over it.

4.2 Model derivation

Our decision to study (4.1) is inspired by [126], where, after a quasi-steady state approximation, the following dimensional model of malignant tumor invasion is studied (using the notation in [67]):

$$\begin{aligned}\frac{\partial \hat{u}}{\partial \hat{t}} &= -k_4 \hat{u}^2 \hat{w}, \\ \frac{\partial \hat{w}}{\partial \hat{t}} &= \hat{k}_1 \hat{w}(k_2 - \hat{w}) - k_3 \frac{\partial}{\partial \hat{x}} \left(\frac{\partial \hat{u}}{\partial \hat{x}} \hat{w} \right),\end{aligned}\tag{4.5}$$

Here, \hat{x} represents one-dimensional space (in metres, m) and \hat{t} represents time (in seconds, s). The dependent variable \hat{u} (kg m^{-3}) represents the ECM density and \hat{w} (cells m^{-3}) represents the cancer cell density. Diffusion of the species is assumed to be small and therefore neglected. The parameter $k_3 > 0$ ($\text{m}^5 \text{kg}^{-1} \text{s}^{-1}$) measures the strength of the haptotaxis or chemotaxis term, which models the observed migration of cancer cells up the gradient of ECM. The nonlinear function $-k_4 \hat{u}^2 \hat{w}$ models the degradation of the ECM via proteolysis at rate $k_4 > 0$ ($\text{m}^6 \text{kg}^{-1} \text{cells}^{-1} \text{s}^{-1}$)⁵. The proliferation of the cancer cells is modeled by the nonlinear function $\hat{k}_1 \hat{w}(k_2 - \hat{w})$: without spatial influences and independent of the other species, the cancer cells grow logistically to their carrying capacity $k_2 > 0$ (cells m^{-3}), with (constant) proliferation rate $\hat{k}_1 k_2 > 0$ (s^{-1}). We refer to [126] for a more detailed derivation of (4.5).

We wish to study the influence of incorporating an Allee effect into the description of the growth of the cancer cells. We assume the same nonlinearity for proteolysis but replace the cancer cell growth function with an Allee term. Following [167], we reintroduce the small amount of diffusion of both the ECM

⁵An enzyme–protease—that is produced in the presence of cancer cells, breaks down the ECM in a process called proteolysis. However, the protease reaction evolves on a much faster time scale than the other processes within the tumor and so a quasi-steady state reduction is applied; see [126] for more details.

and cancer cells that was neglected in (4.5). With these adaptations, the model under investigation becomes

$$\begin{aligned}\frac{\partial \hat{u}}{\partial \hat{t}} &= -k_4 \hat{u}^2 \hat{w} + D_1 \frac{\partial^2 \hat{u}}{\partial \hat{x}^2}, \\ \frac{\partial \hat{w}}{\partial \hat{t}} &= k_1 \hat{w} (k_2 - \hat{w}) (\hat{w} - k_6) - k_3 \frac{\partial}{\partial \hat{x}} \left(\frac{\partial \hat{u}}{\partial \hat{x}} \hat{w} \right) + D_2 \frac{\partial^2 \hat{w}}{\partial \hat{x}^2},\end{aligned}\tag{4.6}$$

with $k_i > 0$ for $i \in \{1, \dots, 5\}$, $|k_6| < k_2$ and $0 \leq D_1 \leq D_2$ ($\text{m}^2 \text{s}^{-1}$). We will allow for the ECM to have both no diffusion ($D_1 = 0$), and small diffusion, in comparison to the cancer cells.

Here, k_2 (cells m^{-3}) is still the carrying capacity of the cancer cell density, while $k_1 k_2 k_6 (\hat{w}/k_6 - 1)$ (s^{-1}) is the (density dependent) proliferation rate. This density dependent proliferation rate, in contrast to the constant proliferation rate assumed by logistic growth, is the main difference between the two models, (4.5) and (4.6). For $k_6 > 0$, k_6 (cells m^{-3}) represents a growth threshold, below which the cancer cell density decreases, consistent with the strong Allee effect. For $k_6 < 0$, the interpretation of k_6 is less clear. However, the effect of the term $(1 + \hat{w}/(-k_6))$ is to increase the proliferation rate, relative to the (constant) rate $k_1 k_2 (-k_6)$, with this increase more pronounced as the cancer cell density increases, consistent with the weak Allee effect; see [25] for further discussion of the weak (and strong) Allee effects and their mathematical representation.

We introduce

$$u = \frac{\hat{u}}{U}, \quad w = \frac{\hat{w}}{W}, \quad t = \frac{\hat{t}}{T}, \quad x = \frac{\hat{x}}{X},\tag{4.7}$$

with

$$U = \frac{k_1 k_2}{k_4}, \quad W = k_2, \quad T = \frac{1}{k_1 k_2^2}, \quad X = \sqrt{\frac{k_3}{k_2 k_4}},$$

and define

$$\alpha := \frac{k_6}{k_2} < 1, \quad \beta := \frac{D_1}{D_2} \leq 1, \quad \varepsilon := \frac{k_4}{k_1 k_2 k_3} D_2.$$

This nondimensionalisation transforms (4.6) to (4.1)–(4.2), restated here for convenience:

$$\begin{aligned}\frac{\partial u}{\partial t} &= -u^2 w + \varepsilon \beta \frac{\partial^2 u}{\partial x^2}, \\ \frac{\partial w}{\partial t} &= w(1 - w)(w - \alpha) - \frac{\partial}{\partial x} \left(\frac{\partial u}{\partial x} w \right) + \varepsilon \frac{\partial^2 w}{\partial x^2},\end{aligned}\tag{4.8}$$

with $(x, t) \in (\mathbb{R}, \mathbb{R}^+)$, $|\alpha| < 1$, $0 \leq \beta \leq 1$ and $0 < \varepsilon \ll 1$. The new variables u , w , x and t , and parameters α , β and ε are dimensionless; see Appendix C. Moreover, α and β are assumed to be $\mathcal{O}(1)$ with respect to ε : (loosely speaking) for $\alpha, \beta > 0$ they are independent of ε and do not approach zero in the limit $\varepsilon \rightarrow 0$. Due to the choice of nondimensionalisation, the carrying capacity of the cancer cells has been scaled to one and the strength of the Allee effect is solely measured by the parameter α .

The significant reduction in the number of parameters from eight in (4.6) to three in (4.8) makes the latter (dimensionless) model considerably more amenable to mathematical analysis.

4.3 Type III traveling wave solutions

In this section, we provide the mathematical foundation to derive the results for the strong Allee model ((4.8) with $\alpha \gtrsim 0$, $0 \leq \beta \leq 1$ and ε sufficiently small), stated in Section 4.1.3. We prove that this model only admits Type III traveling wave solutions (TWSs).

In the strong Allee model the homogeneous equilibria $(u, w) = (0, 1)$ and $(u_\infty, 0)$, with $u_\infty \in \mathbb{R}$, represent an all-cancer state and a cancer-free state, respectively. When studying invasive tumor fronts, we are interested in connections between these two states. From a mathematical standpoint, we study the existence of right-moving TWSs of (4.1)–(4.2) that travel with constant speed: $c > 0$. Such solutions correspond to stationary solutions in the moving frame $z = x - ct$ and so satisfy

$$\begin{aligned} -cu_z &= -u^2w + \varepsilon\beta u_{zz}, \\ -cw_z &= w(1-w)(w-\alpha) - (u_z w)_z + \varepsilon w_{zz}, \end{aligned} \tag{4.9}$$

TWSs also satisfy the asymptotic boundary conditions

$$\lim_{z \rightarrow -\infty} (u, w) = (0, 1), \quad \lim_{z \rightarrow \infty} (u, w) = (u_\infty, 0), \quad u_\infty \in \mathbb{R}^+, \tag{4.10}$$

where u_∞ represents the (variable) background ECM density, as in [67]. Thus, TWSs of (4.1)–(4.2) or (4.8) correspond to heteroclinic connections of (4.9) that satisfy (4.10).

Theorem 4.3.1. *For $0 < \varepsilon \ll 1$ sufficiently small and $0 < \alpha < 1$, $0 \leq \beta \leq 1$ and $\mathcal{O}(1)$ with respect to ε , the only possible solution of (4.9)–(4.10) corresponds to a Type III traveling wave solution of (4.1)–(4.2).*

We prove Theorem 4.3.1 using a method outlined in [167], which was subsequently used in [67] to study the logistic model. The foundation of this method

lies in geometric singular perturbation theory (GSPT) [73, 82, 84], which provides a geometric approach to singular perturbation problems. The benefit of using GSPT lies in the rigorous theory that underpins it, which exploits the geometric structure embedded in models such as (4.1) and allows us to prove that the leading order solutions we construct are good approximations of the full solutions with $0 < \varepsilon \ll 1$. Canard theory [11, 97, 149, 166] is also used when the standard GSPT, known as Fenichel theory [49, 82], becomes invalid due to a loss of normal hyperbolicity of the critical manifold. Conditions on the vector field of (4.9) that guarantee the existence of Type III TWSs are also derived.

4.3.1 Set-up

System (4.9) is singularly perturbed, due to the different asymptotic scalings of the diffusion and haptotaxis or chemotaxis terms, with perturbation parameter $0 \leq \varepsilon \ll 1$. Singularly perturbed systems exhibit an inherent separation of scales. In Figures 4.2 and 4.3, for example, we observe two spatiotemporal scales: the *fast scale* captures the dynamics where rapid changes occur, which, in the singular limit, correspond to shocks in the solutions; and, the *slow scale* relates to the dynamics away from the shocks (in the singular limit), or where less rapid changes occur.

The separation of slow and fast behavior becomes more evident when we write the w -equation of (4.9) as a balance law

$$(\varepsilon w_z - u_z w + cw)_z = -w(1-w)(w-\alpha).$$

So, we define two new variables,

$$p := u_z \quad \text{and} \quad v := \varepsilon w_z - pw + cw,$$

(see [67] and [167] for a further rationale behind the rescaling above). This way, we can write (4.9) as a four-dimensional system of first-order ordinary differential equations (ODEs):

$$\begin{aligned} u_z &= p, \\ v_z &= -w(1-w)(w-\alpha), \\ \varepsilon p_z &= \frac{1}{\beta}(u^2 w - cp), \\ \varepsilon w_z &= v + (p - c)w. \end{aligned} \tag{4.11}$$

For $\beta = 0$, the equation for p in (4.11) becomes singular. This has to do with the fact that the u -equation of (4.9) is only first order for $\beta = 0$, as opposed to second order for $\beta > 0$. We assume from now on that $\beta > 0$, and discuss

the proof of Theorem 4.3.1 for $\beta = 0$ (which goes along the same lines as for $\beta > 0$) in some more detail in Remark 4.4. Following standard terminology from geometric singular perturbation theory (see for example [82, 84]) we label (4.11) the *slow system*, with z the *slow traveling wave coordinate*. Provided $\varepsilon \neq 0$, we can equivalently write (4.11) in terms of the fast scale by introducing the *fast traveling wave coordinate*, $y = z/\varepsilon$:

$$\begin{aligned} u_y &= \varepsilon p, \\ v_y &= -\varepsilon w(1-w)(w-\alpha), \\ p_y &= \frac{1}{\beta}(u^2 w - cp), \\ w_y &= v + (p-c)w. \end{aligned} \tag{4.12}$$

So, (u, v) are the slow variables and their equations determine the dynamics away from the shock, while the equations for the fast variables (p, w) determine the dynamics around the shock. While (4.11) and (4.12) are equivalent for $\varepsilon \neq 0$, in the singular limit $\varepsilon \rightarrow 0$, they reduce differently depending on the spatiotemporal scale. In Section 4.3.2–4.3.3, we study the singular limits of (4.12) and (4.11), respectively. The results of these sections determine the leading order behavior of the heteroclinic connections in the appropriate regimes. In Section 4.3.4, the results from Section 4.3.2–4.3.3 are combined to prove Theorem 4.3.1.

4.3.2 Layer problem

On the fast scale, taking the singular limit ($\varepsilon \rightarrow 0$) of the so-called *fast system*, (4.12), yields a two-dimensional ODE system, termed the *layer problem*:

$$\begin{aligned} p_y &= \frac{1}{\beta}(u^2 w - cp), \\ w_y &= v + (p-c)w, \end{aligned} \tag{4.13}$$

with two parameters $u, v \in \mathbb{R}$. Since u and v are parameters in (4.13), they remain constant along any shocks in the TWSs of (4.1)–(4.2) with $\varepsilon = 0$.

The equilibria of (4.13) form a two-dimensional surface in (u, v, p, w) -space, referred to as the *critical manifold*, which can be represented as a graph over the original variables (u, w) :

$$S := \left\{ (u, v, p, w) \mid v = \left(c - \frac{u^2 w}{c}\right) w, \quad p = \frac{u^2 w}{c} \right\}. \tag{4.14}$$

The left-hand panel of Figure 4.4 shows a projection of S into (u, v, w) -space.

Lemma 4.3.2. *The critical manifold S is folded around the so-called fold curve,*

$$F := \{(u, w) \mid 2u^2w - c^2 = 0\}. \quad (4.15)$$

In other words, at F , two branches of equilibria $(p_{\pm}(u, v; c), w_{\pm}(u, v; c))$ of (4.13) originate in a saddle-node bifurcation, see for example [98] for the conditions of a saddle-node bifurcation. The equilibria $(p_{-}(u, v), w_{-}(u, v))$ are unstable, or repelling, with respect to (4.13) and, hence, we label this branch of S as S_r . The other branch of S , given by $(p_{+}(u, v; c), w_{+}(u, v; c))$, is stable, or attracting, and is labelled S_a . S is symmetric in w around F with $w_{-} \geq w_{+}$.

Proof. The proof follows from [167], and is similar to the proof of Lemma 2.2 in [67]; we refer to these works for the details. Briefly: the folded structure of S follows from checking that the standard conditions for a saddle-node (SN) bifurcation are met [98, e.g.]; the stability of S is evident from the eigenvalue structure of the linearisation of (4.13); and, the symmetry is a consequence of the definition of S . \square

The folded structure of S allows heteroclinic connections between S_r and S_a . Such a connection transports a point $(u_{-}, v_{-}, p_{-}, w_{-})$ on S_r to the point $(u_{+}, v_{+}, p_{+}, w_{+})$ on S_a , with $u_{+} = u_{-}$ and $v_{+} = v_{-}$ (since u and v are constant in (4.13)), and

$$\begin{aligned} p_{+} &= \frac{u_{-}^2 w_{+}}{c} = c - p_{-}, \\ w_{+} &= \frac{c^2}{u_{-}^2} - w_{-} = 2F(u_{-}) - w_{-}. \end{aligned} \quad (4.16)$$

These conditions follow from the definition of S and are equivalent to the Routh–Hugoniot and Lax entropy conditions for shocks for the strictly hyperbolic system (4.1)–(4.2) with $\varepsilon = 0$; see [67, 109, 167]. The second equation in (4.16) highlights the symmetry of S around F . The right-hand panel of Figure 4.4 provides a schematic of S and an example heteroclinic connection between S_r and S_a via the dynamics of (4.13).

4.3.3 Reduced problem

On the slow scale, taking the singular limit of (4.11) yields a differential–algebraic system with two ODEs coupled to two algebraic constraints, termed the

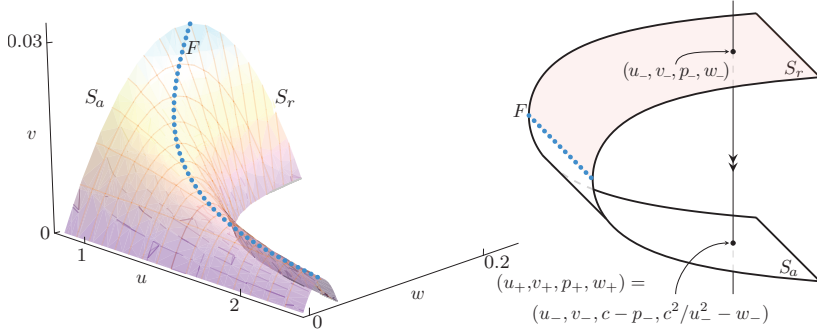


Figure 4.4: The critical manifold S , defined in (4.14). S is folded around the fold curve F , defined in (4.15) and represented by the blue dotted line. It is symmetric in w around F , with one repelling side (S_r) and one attracting side (S_a). Left-hand panel: Projection of the S into (u, v, w) -space, highlighting the folded structure. Right-hand panel: A schematic of S and an example of a flow connecting a point on S_r to the corresponding point on S_a . This is an adaptation of Figure 4 in [68]. ©IOP Publishing & London Mathematical Society. Reproduced with permission. All rights reserved.

reduced problem:

$$\begin{aligned} u_z &= p, \\ v_z &= -w(1-w)(w-\alpha), \\ 0 &= \frac{1}{\beta}(u^2w - cp), \\ 0 &= v + (p-c)w. \end{aligned} \tag{4.17}$$

As expected from geometric singular perturbation theory, the algebraic constraints define S . Herein lies the geometric structure of the model. When viewed on the slow scale, the flow along S is evident and governed by (4.17).

Since S is given as a graph over the original model variables (u, w) , we restrict our investigation of (4.17) to these coordinates, where the slow behavior is governed by

$$\begin{aligned} u_z &= \frac{u^2w}{c}, \\ \left(c - \frac{2u^2w}{c}\right)w_z &= -w(1-w)(w-\alpha) + \frac{2u^3w^3}{c^2}. \end{aligned} \tag{4.18}$$

Consequently, the analysis of the reduced dynamics reduces to a two-dimensional, (u, w) -phase plane analysis. In this projection, the phase space consists of two distinct regions corresponding to S_a and S_r , separated by F ; see, for example, Figure 4.8.

The equilibria of (4.18) in the first quadrant are

$$(u_\infty, 0), \quad (0, \alpha), \quad (0, 1), \quad u_\infty \in \mathbb{R}^+.$$

The stability of these equilibria is determined via the associated Jacobian matrix, appended with a perturbation analysis in the case of a zero eigenvalue:

- $(u_\infty, 0)$ has an unstable eigenvalue and a zero eigenvalue (related to the translation in the u direction);
- $(0, \alpha)$ has a stable eigenvalue with eigenvector pointing in the direction of the invariant w -axis and center-unstable outgoing trajectories, directed into the first quadrant; and,
- $(0, 1)$ has an unstable eigenvalue with eigenvector pointing in the direction of the invariant w -axis and center-unstable outgoing trajectories, directed into the first quadrant.

System (4.18) is singular along F , because the left-hand side of the w -equation vanishes here. In general, solution trajectories approaching F have w -derivatives that blow-up in finite time. The isolated points on F at which the right-hand side of (4.18) also vanishes, referred to as *canard points* [11, 166], form the exception to this rule.

To understand solution trajectories of (4.18) interacting with these canard points, we introduce a new variable \bar{z} , defined via

$$\frac{dz}{d\bar{z}} = c - \frac{2u^2w}{c}.$$

With this change of coordinate system, (4.18) transforms to the so-called *desingularised system*

$$\begin{aligned} \frac{du}{d\bar{z}} &= \frac{u^2w}{c} \left(c - \frac{2u^2w}{c} \right), \\ \frac{dw}{d\bar{z}} &= -w(1-w)(w-\alpha) + \frac{2u^3w^3}{c^2}. \end{aligned} \tag{4.19}$$

This system is more amenable to analysis than (4.18) as it is no longer singular. Canard points of (4.18) correspond to equilibria of (4.19) on F . They are

classified according to the nature of the corresponding equilibrium in (4.19). For example, if (4.19) has a saddle equilibrium on F , then the corresponding canard point of (4.18) is called a *folded saddle canard point* (FS). Similarly, we have *folded focus canard points* (FF), *folded node canard points* (FN), etc.. Two trajectories of a system with a FS can pass through F at such a canard point, thereby flowing from S_a to S_r and *vice versa* [166]. The former trajectory is labelled the *canard solution* and the latter the *faux canard solution*. Trajectories are not able to pass through F at a FF, while a *funnel* of trajectories pass through F at a FN [165, 166]. Figure 4.5 provides a schematic of a FS, FF and FN and illustrates their connection with regular equilibria.

Remark 4.3. The flows of (4.18) and (4.19) differ only in their parametrization. The flows are topologically equivalent in forward \bar{z} if $dz/d\bar{z} > 0$ and topologically equivalent in backward \bar{z} if $dz/d\bar{z} < 0$. It is straightforward to see that $dz/d\bar{z} = c^2 - 2u^2w < 0$ on S_r , or above F in the (u, w) -plane, while $dz/d\bar{z} = c^2 - 2u^2w > 0$ on S_a , or below F in the (u, w) -plane. Thus, the (u, w) -phase plane of (4.18) is obtained from the (u, w) -phase plane of (4.19) by reversing the direction of the trajectories on S_r , or above F in the (u, w) -plane; see Figure 4.8 for an illustration.

Lemma 4.3.3. *For $0 < \alpha < 1$, (4.18) has two canard points if $0 < c < c^+(\alpha)$, and no canard points otherwise, where*

$$c^+ = c^+(w^+(\alpha), \alpha) := 2\sqrt{2w^+}(1 - 2w^+ + \alpha) \quad (4.20)$$

and

$$w^+ = w^+(\alpha) := \frac{1}{6} \left(1 + \alpha + \sqrt{(1 + \alpha)^2 + 12\alpha} \right).$$

The w -components of both canard points are larger than α and smaller than 1.

Proof. Canard points of (4.18) correspond to equilibria of (4.19) on F . The w -components of these equilibria are real positive roots of

$$q(w) := \sqrt{2}(1 - w)(w - \alpha) = c\sqrt{w} =: s(w), \quad (4.21)$$

and the corresponding u -components are given by $u = c/\sqrt{2w}$. The number of solutions to (4.21) changes in a saddle-node (SN) bifurcation as $q(w)$ and $s(w)$ become tangent, which occurs at $c = c^+(\alpha)$. From the shapes of the graphs of $q(w)$ and $s(w)$ (parabolic and monotonically increasing, respectively) for different values of c , it follows that the smaller root of (4.21) lies between α and $w^+(\alpha)$, while the larger root lies between $w^+(\alpha)$ and 1. As $c \rightarrow 0$, the roots approach α and 1, and as $c \rightarrow c^+(\alpha)$, they approach $w^+(\alpha)$. \square

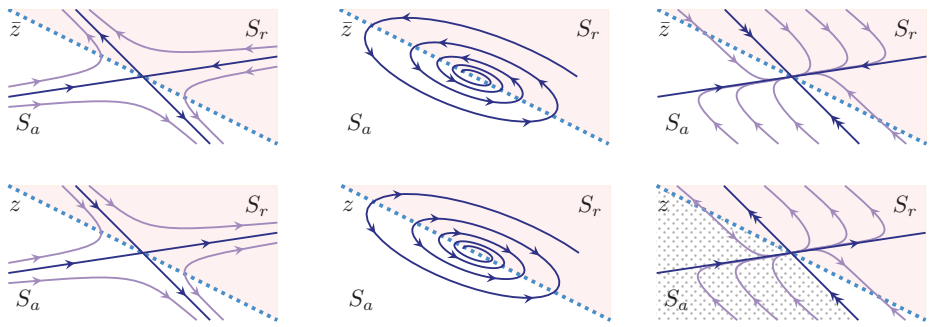


Figure 4.5: Schematics of some types of canard points. The blue dotted line represents F , the upper-right, shaded region S_r and the lower-left, unshaded region S_a . The upper panels show standard equilibrium points (saddle, focus, node), which lend their names to the corresponding canard points shown in the lower panels (folded saddle, folded focus, folded node). The difference between the upper and lower panels is the direction of the trajectories on S_r due to the parametrization, \bar{z} or z . A folded saddle admits two trajectories through it, along the stable and unstable manifolds of the corresponding saddle. A folded focus does not admit any trajectories. A folded node admits a *funnel* (dotted region) of trajectories between the stronger stable (or unstable) manifold of the corresponding node and F , which follow the weaker stable (or unstable) manifold. This is an adaptation of Figure 10 in [68]. ©IOP Publishing & London Mathematical Society. Reproduced with permission. All rights reserved.

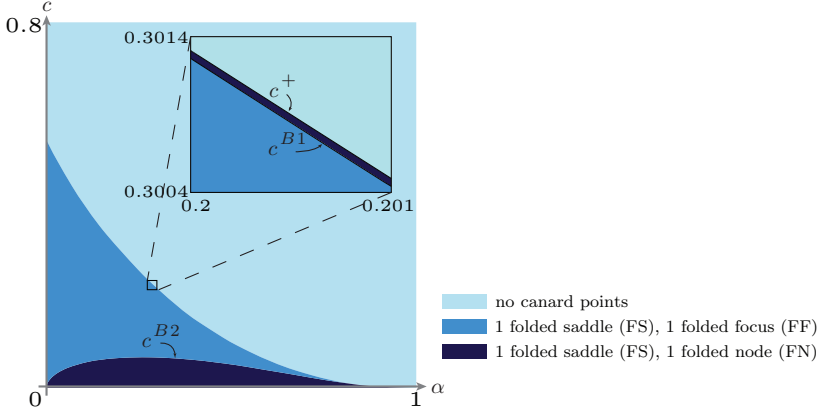


Figure 4.6: The type of canard points of (4.18), in the (α, c) -plane. The canard points are created in a saddle-node bifurcation as c decreases through $c = c^+(\alpha)$, defined in (4.20). The folded node becomes a folded focus at $c = c^{B1}(\alpha)$ and a folded node once again at $c = c^{B2}(\alpha) < c^{B1}(\alpha)$.

We determine the type of the canard points by numerically computing the eigenvalues of the corresponding equilibria of (4.19). Since the canard points are created in a SN bifurcation, we observe a folded saddle (FS) and a folded node (FN) near the bifurcation point, $c = c^+(\alpha)$. Just after the SN bifurcation, at $c = c^{B1}(\alpha) < c^+(\alpha)$, the FN becomes a FF (while the FS remains a FS). The FF transitions back to a FN at $c = c^{B2}(\alpha) < c^{B1}(\alpha)$; see Figure 4.6. While $c^+(\alpha)$ is determined analytically, and defined in (4.20), $c^{B1}, c^{B2}(\alpha)$ are determined numerically⁶.

Lemma 4.3.4. *For $0 < \alpha < 1$ and $0 < c < c^+(\alpha)$, with $c^+(\alpha)$ defined in (4.20), (4.18) admits a solution trajectory connecting $(0, 1)$ to the FS.*

Proof. For $0 < \alpha < 1$ and $0 < c < c^+(\alpha)$, Lemma 4.3.3 implies that (4.18) has two canard points, (u_{FS}, w_{FS}) and (u_F, w_F) , with $\alpha < w_F, w_{FS} < 1$. It is straightforward to show that the FS, (u_{FS}, w_{FS}) , is the canard point with the larger w -component. Since F corresponds to a monotonically decreasing function of w as u increases, $u_{FS} < u_F$. Consequently, (u_{FS}, w_{FS}) lies above and to the left of (u_F, w_F) in the (u, w) -phase plane. From (4.18) it follows that $w' > 0$ for $w, c > 0$ and that $w' < 0$ along $w = w_F$ for $0 < u < u_F$. Consequently,

⁶In principle, it may be possible to determine c^{B1}, c^{B2} analytically: the canard points correspond to roots of (4.21) and these roots are a subset of the roots of a quartic polynomial. However, these expressions are so complicated they offer little insight

the trajectory leaving $(0, \alpha)$ does not connect to (u_{FS}, w_{FS}) . Since the u -axis is repelling, it intersects F below and to the right of (u_F, w_F) . The w -nullcline connecting $(0, 1)$ with the FS is strictly decreasing and the stable eigenvector of the FS lies below that nullcline for $u \lesssim u_{FS}$. As a result, there is a trajectory leaving $(0, 1)$ that connects to (u_{FS}, w_{FS}) . \square

This solution trajectory (that leaves $(0, 1)$, connects to (u_{FS}, w_{FS}) and, hence, continues onto S_r) is the canard solution, which we label T_o . It is the only solution trajectory of (4.18) that (partly) lives on S_r and connects to $(0, 1)$.

In the remainder of this chapter, we do not consider regimes where FNs are present: $0 < c < c^{B2}$ and $c^{B1} < c < c^+$. Although we expect that our results are valid for $0 < c < c^+$, the analysis of FNs is beyond the scope of this chapter.

Remark 4.4. In the case $\beta = 0$, the u -equation of (4.9) is of first order. In this case, u_z is simply $\frac{u^2 w}{c}$ and the singularly perturbed system becomes three-dimensional.

$$\begin{aligned} u_z &= \frac{u^2 w}{c}, \\ v_z &= -w(1-w)(w-\alpha), \\ \varepsilon w_z &= v - cw + \frac{u^2 w^2}{c}. \end{aligned} \tag{4.22}$$

Consequently, the layer problem becomes one-dimensional, but the definition of S and the symmetry it has around the fold curve F remain unchanged. Hence, the reduced system and the slow behavior are independent of β , and for $\beta = 0$ are described by (4.18). This is also supported by the simulations of the full PDE system with $\beta = 0$, see Figure 4.7 which has identical parameter values as Figure 4.2, besides $\beta = 0$. The case $\beta = 0$ applies to tumors of which the dominant mechanism of cell migration is haptotaxis rather than chemotaxis, like some solid tumors.

4.3.4 Proof of Theorem 4.3.1

Traveling wave solutions (TWSs) are identified in the four-dimensional phase space of (4.11) or (4.12) as heteroclinic connections between the equilibria

$$(u, v, p, w) = (0, c, 0, 1) \quad \text{and} \quad (u, v, p, w) = (u_\infty, 0, 0, 0).$$

To leading order, flow in the four-dimensional phase-space can be represented by concatenations of the fast flow of (4.13) with u, v constant, describing the TWSs around the shock, and the slow flow of (4.17), describing the TWSs away from the shock. This *glueing together* of solution segments from (4.13) and (4.17)

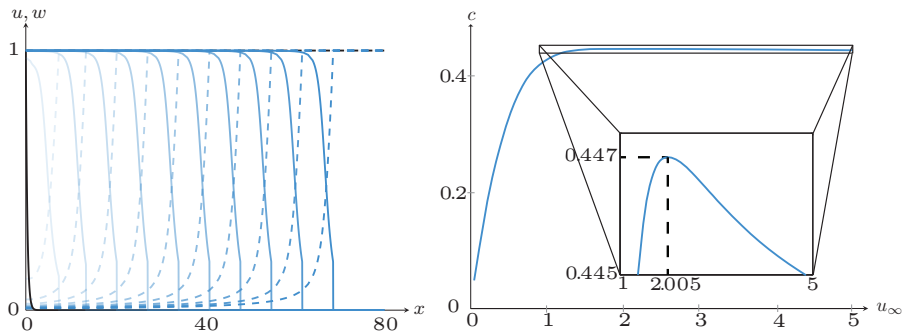


Figure 4.7: Left-hand panel: A *Type III wave* with a biologically justified, well-defined edge and speed $c \approx 0.43$, obtained by numerically simulating (4.1)–(4.2) with $\varepsilon = 0.001$, $\alpha = 0.05$ and $\beta = 0$. The dashed lines correspond to u -profiles and the solid lines to w -profiles, with solutions plotted at $t = 0$ (black), 16 (lightest), 32, ..., 160 (darkest). Note that this is very similar to the left panel of Figure 4.2, because only the fast dynamics is influenced by β , see (4.13). Right-hand panel: The leading order ($\varepsilon = 0$) component of the speed of traveling wave solutions of (4.1)–(4.2) (c) versus the background ECM density (u_∞), with $\alpha = 0.05$, illustrating a biphasic relationship. This is exactly the same as the right-hand panel of Figure 4.2 as the leading order component is independent of β , see (4.18).

is how we construct leading order approximations of TWSs of (4.1)–(4.2). The validation of this approach follows from GSPT and canard theory.

Since both equilibria lie on S_a , they both have two-dimensional stable manifolds in (4.13) and a two-dimensional center manifold corresponding to the slow variables. Consequently, a heteroclinic connection cannot be made between the two equilibria purely within (4.13). Similarly, since $(u_\infty, 0)$ in (4.18) has a one-dimensional unstable manifold (since $\alpha > 0$) and a one-dimensional center manifold corresponding to translation in the u -direction, a heteroclinic connection cannot be made between the two equilibria purely within (4.18). Instead, a connection must contain solution segments from both systems. Consequently, no TWSs exist when no canard points are present ($c > c^+(\alpha)$) and TWSs of (4.1)–(4.2) can only be Type III waves since the final part of the heteroclinic connection for $\varepsilon = 0$ has to be a trajectory of (4.13).

According to Lemma 4.3.2 and (4.16), the fast flow is directed from S_r to S_a and the w -component is symmetric in F , while the u -component is constant. Hence, a heteroclinic connection to $(u_\infty, 0, 0, 0)$ on S_a via (4.13) must *take-off* from $(u_\infty, 0, 0, c^2/u_\infty^2)$ on S_r . The canard solution is the only solution of the slow flow that (partly) lives on S_r and that connects to S_a in backward z . So, to construct a heteroclinic connection between $(0, c, 0, 1)$ and $(u_\infty, 0, 0, 0)$, we need the canard solution (in four-dimensional space) to intersect $(u_\infty, 0, 0, c^2/u_\infty^2)$. In the original, (u, w) -coordinates, this means that the canard solution of (4.18) (T_o) must intersect the *jump curve*: $J := c^2/u_\infty^2$. In Figure 4.8, the phase plane of (4.18) and J are shown for particular values of α and c ; T_o and J intersect, yielding a heteroclinic connection of (4.9)–(4.10) with $\varepsilon = 0$ and, hence, a Type III TWS of (4.1)–(4.2) with $\varepsilon = 0$.

With $\varepsilon > 0$, the end states $(0, 1)$ and $(u_\infty, 0)$ do not perturb. Geometric singular perturbation theory implies that the (invariant) manifolds S_a and S_r perturb to the $\mathcal{O}(\varepsilon)$ -close, locally invariant manifolds $S_{a,\varepsilon}$ and $S_{r,\varepsilon}$, respectively, provided S_a and S_r are normally hyperbolic and ε is sufficiently small. Along F , S loses normal hyperbolicity. However, canard theory guarantees that T_o persists [167].

If the unstable manifold of $(0, 1)$ and the stable manifold of $(u_\infty, 0)$ have a transverse intersection for $\varepsilon = 0$, the heteroclinic connection for $\varepsilon = 0$ persists as a solution of (4.9)–(4.10) with $0 < \varepsilon \ll 1$. This condition is equivalent to J and T_o intersecting transversally. In D, we show that this *transversality condition* holds, provided $c \neq u_\infty\sqrt{\alpha}$. Hence, a TWS that is constructed for $\varepsilon = 0$, persists as a TWS of (4.1)–(4.2), with $0 < \varepsilon \ll 1$ sufficiently small, provided $c \neq u_\infty\sqrt{\alpha}$, with the former providing a leading order approximation of the latter.

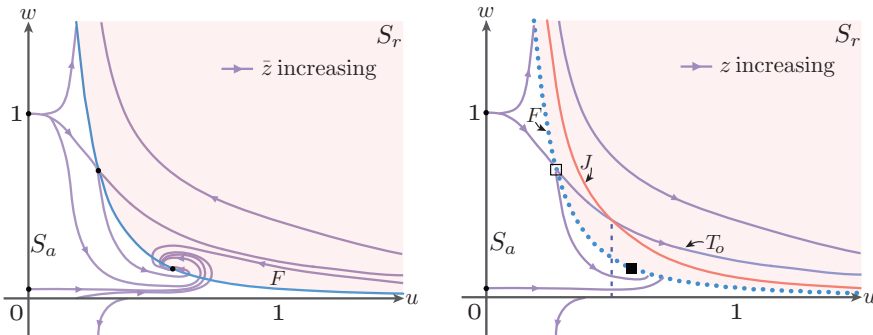


Figure 4.8: Phase planes of (4.19) (left) and (4.18) (right), for $\alpha = 0.05$ and $c = 0.33$. The blue line is the fold curve (F), which is dotted on the right to illustrate its singularity. Black dots represent equilibria. The black open square is a folded saddle and the solid black square is a folded focus. F divides S into a repelling side (S_r , shaded) and an attracting side (S_a , not shaded). The canard solution is labelled T_o (take-off). The curve J given by $w = J(u) = c^2/u^2$ and is a reflection of the u -axis in F . An intersection between J and T_o determines the u_∞ for which a Type III traveling wave solution (with speed c) exists. Here, only one intersection exists.

4.4 Implications of the strong Allee effect

In the previous section, we introduced the mathematical framework to study invasive tumor fronts, or traveling wave solutions (TWSs), of the strong Allee model (4.1)–(4.2) with $0 \lesssim \alpha < 1$, $0 \leq \beta \leq 1$ and $0 \leq \varepsilon \ll 1$ sufficiently small) connecting the all-cancer state $(0, 1)$ and the cancer-free state $(u_\infty, 0)$ with $u_\infty \in \mathbb{R}^+$. It was shown, in a mathematically rigorous way, that the strong Allee model cannot admit Type I, II or VI TWSs (see Theorem 4.3.1); only TWSs where the w -component has a well-defined edge—Type III waves—can exist. This result is due to the stability of the states $(u_\infty, 0)$. While Type III waves are the only possible TWSs of the strong Allee model, their existence is not guaranteed. In Section 4.3, we derived a condition for the existence of Type III waves.

In this section, we establish the main results presented in Section 4.1.3. We demonstrate the existence of Type III TWSs in the strong Allee model and investigate the relationship between their speed and the background ECM density (u_∞) , for different values of ε . We also make a qualitative comparison between the results for the strong Allee model and results for the logistic model, (4.1) with (4.3), [67] and the competition model, (4.1) with (4.4), [108], and review the impact of the inclusion of the strong Allee effect.

4.4.1 Existence of invasive tumor fronts with well-defined edges

Type III TWSs of the strong Allee model exist if a transverse intersection between two specific curves in the phase plane of the ODE system

$$\begin{aligned} u_z &= \frac{u^2 w}{c}, \\ \left(c - \frac{2u^2 w}{c}\right) w_z &= -w(1-w)(w-\alpha) + \frac{2u^3 w^3}{c^2} \end{aligned} \tag{4.23}$$

exists; see Section 4.3 for the derivation of this condition. The two curves are the so-called *canard solution*, denoted T_o in Figure 4.9, and the so-called *jump curve*, denoted $J := c^2/u^2$ in Figure 4.9. Here, u and w still represent the ECM and cancer cell densities, c is the invasion speed of the tumor and $z = x - ct$ is a new variable—the so-called *traveling wave coordinate*—that corresponds to a coordinate frame moving along with the TWS. Note that (4.23) can also be obtained from the strong Allee model by setting $\varepsilon = 0$ and looking for stationary solutions in the z -coordinate frame.

A consequence of the requirement of an intersection between the canard solution and the jump curve is that no TWSs exist for c greater than a critical value, $c = c^+(\alpha)$, defined in (4.20), as the canard solution does not exist in this regime; see Section 4.3. The behavior of c^+ as a function of α is shown as the

transition curve between the light and dark green regions in Figure 4.6, which shows that $c^+(\alpha)$ is a decreasing function of the Allee threshold α . Tumors requiring a larger threshold to grow, therefore have a slower maximum speed potential. Henceforth, we only consider speeds $c^{B2}(\alpha) < c < c^{B1}(\alpha) < c^+(\alpha)$, where $0 < c \leq c^{B2}(\alpha)$ and $c^{B1}(\alpha) \leq c < c^+(\alpha)$ are narrow regions where the mathematical analysis becomes more involved and is beyond the scope of this chapter. The analytic expression $c^+(\alpha)$ hence yields an upper bound on the speed of the invading waves. Consequently, the model does not support traveling waves that go faster than this upper limit. So, the expression $c^+(\alpha)$ can be used as a crude measure to give an upper bound on how far an invading wave has traveled at any time without any significant computation. Because $c^+(\alpha)$ is decreasing, a larger α gives a lower upper bound on the speed.

With $c^{B2}(\alpha) < c < c^{B1}(\alpha)$, the canard solution is the only solution trajectory of (4.23) that leaves the all-cancer state $(0, 1)$ and crosses the so-called *fold curve*, denoted $F := c^2/2u^2$ in Figure 4.9. (This fold is a projection in two dimensions of the fold F of the critical manifold as shown in Figure 4.4). Other trajectories leaving $(0, 1)$ also hit the fold curve, but do not cross it due to the singular nature of (4.23); at the point where the canard solution crosses the fold curve both the left- and right-hand sides of the second equation in (4.23) vanish. This point is a *folded saddle canard point* (FS).

A TWS of the strong Allee model corresponds (to leading order in ε) to the canard solution until it intersects the jump curve, at say $(u, w) = (u_*, c^2/u_*^2)$, at which point it jumps to $(u_\infty, 0)$. This jump corresponds to a shock in the w -component of the (leading order) TWS that connects to zero, while the u -component stays constant ($u = u_*$), creating a Type III TWS with cancer-free state $(u_\infty, 0) = (u_*, 0)$ and speed c (to leading order); see Figure 4.9. The length of the shock is c^2/u_*^2 , which is double the distance between the u -axis and the fold curve at $u = u_*$. In other words, the jump curve is the reflection of the u -axis around the fold curve.

Figure 4.9 provides an example phase plane of (4.23) for given α and c , and a schematic of the Type III TWS that the strong Allee model admits for this parameter set. The fold curve is indicated by the green dotted line. The solid blue lines are solution trajectories of (4.23) and the unique solution trajectory crossing the fold curve (the canard solution) is labelled T_o . Potential shocks are indicated by the dashed blue lines. Due to the symmetry of the shock, the length of the dashed blue lines is twice the distance between the canard solution and the fold curve and the given u -coordinate. Since $(u_\infty, 0)$ are repelling equilibrium points of (4.23), trajectories of (4.23) cannot connect to the u -axis as $z \rightarrow \infty$. Consequently, only shocks landing exactly on the u -axis create TWSs; such TWSs are Type III TWSs.

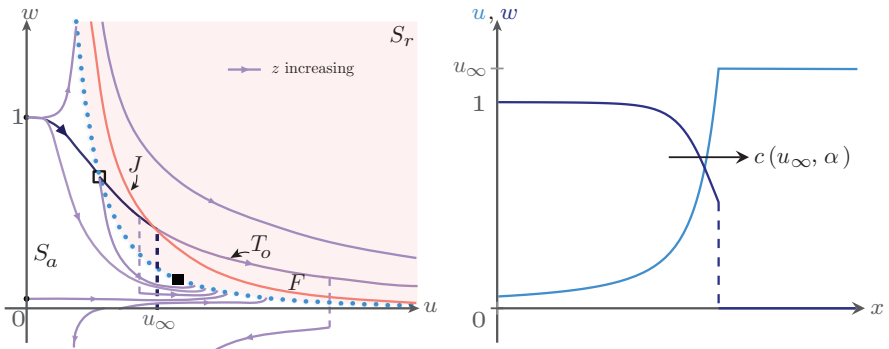


Figure 4.9: Left-hand panel: An example phase plane of (4.23), with $\alpha = 0.05$ and $c = 0.33$. The green dotted line represents the fold curve, labelled F , and the open black square represents the folded saddle, at which the canard solution, labelled T_o , crosses the fold curve. The solid blue lines correspond to trajectories of (4.23) and the dashed blue lines correspond to shocks. The jump curve, labelled $J := c^2/u^2$, is shown in orange. A Type III traveling wave solution of the strong Allee model exists since the jump curve and the canard solution intersect transversally. The solid black square is a folded focus canard point, which does not play a role in the construction of traveling wave solutions. Right-hand panel: An illustration of the Type III traveling wave solution (as a function of x) that is obtained from the dark blue trajectory in the phase plane. The w -component has semi-compact support and $u_\infty > 1$ is chosen arbitrarily.

The connection to the u -axis occurs if and only if $u_* = u_\infty$; only if the canard solution intersects the jump curve is a Type III TWS created. The jump curve is indicated by the orange curve in Figure 4.9. For the given parameters, there is a unique intersection between the canard solutions and the jump curve. Therefore, with $\alpha = 0.05$, the strong Allee model admits a unique Type III TWS that travels with speed $c = 0.33$ and asymptotes to the cancer-free state $(u_\infty, 0) = (u_*, 0)$ (to leading order).

4.4.2 Biphasic relationship between invasion speed and background ECM density

In the previous section, we discussed how Type III traveling wave solutions (TWSs) are created. However, several questions remain:

1. For a given α and c , does an intersection between the canard solution and the jump curve always exist, such that a Type III TWS is created?
2. If such an intersection exists, is it unique?
3. Can different speeds yield TWSs that asymptote to the same cancer-free state $(u_\infty, 0)$ with α fixed?

The first question is answered Section 4.3 and discussed in the previous section. For $c > c^+(\alpha)$, there is no canard solution and, thus, no TWSs exist. However, neither Section 4.3 nor the previous section guarantee that the required intersection exists for $c^{B2}(\alpha) < c < c^{B1}(\alpha) < c^+(\alpha)$, despite the canard solution existing in this regime. An investigation of the phase portraits of (4.23) for different values of α and c provides further insight into this, and the other questions. The results are presented in Figure 4.10, where the (leading order) speed of the Type III TWS c (if such a TWS exists) is indicated, for the chosen values of α and u_∞ .

Figure 4.10 suggests that there is an upper limit $c = c^{\text{trans}}(\alpha)$ on the values of c for which there exists an intersection between the canard solution and the jump curve. This upper limit appears to be less than $c^{B1} < c^+(\alpha)$ and satisfies the transversality condition derived in D. Consequently, the corresponding value of $u_\infty = u_\infty^{\text{trans}}$ is related to c^{trans} via $c^{\text{trans}} = \sqrt{\alpha}u_\infty^{\text{trans}}$. Moreover, for fixed α , different values of c yield different u_∞ -values and it appears that TWSs to all cancer-free states $(u_\infty, 0)$ can be constructed. For a given α , the relationship between the invasion speed of the tumor (c) and the background ECM density (u_∞) has a single turning point—a maximum—at $u_\infty = u_\infty^{\text{trans}}(\alpha)$ with speed $c^{\text{trans}} = \sqrt{\alpha}u_\infty^{\text{trans}}$. This *biphasic* relationship qualitatively resembles experimental results for malignant tumor invasion reported in [125], where the relationship between the collagen concentration and invasion distance of HT1080 is measured

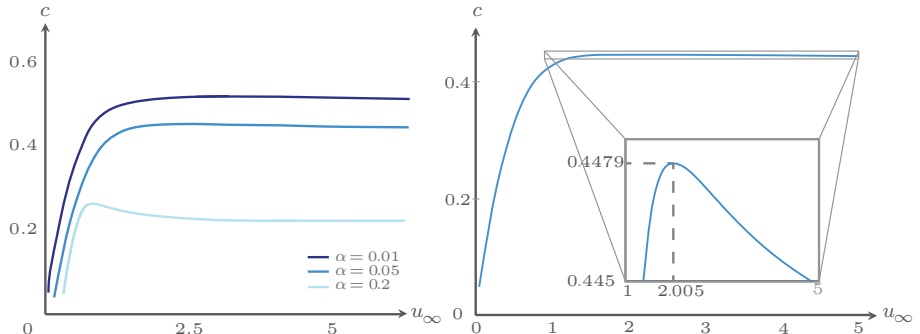


Figure 4.10: Left-hand panel: The leading order speed of the invasive tumor fronts as a function of the background ECM density, for $\alpha = 0.01, 0.05, 0.2$. For increasing α , the *biphasic relationship* between c and u_∞ becomes more prominent and the wavespeed for a given u_∞ decreases. Right-hand panel: A close-up of the $\alpha = 0.05$ -curve in the left-hand panel, highlighting the biphasic relationship.

to be non-monotonic. Moreover, the non-monotonicity becomes more pronounced as α increases. Consequently, there is no intersection between the canard solution and the jump curve for $c > c^{\text{trans}}$, and, therefore, no TWS. For $c < c^{\text{trans}}$ there is a narrow region where two intersections exist, which implies the existence of two TWSs, with different end states, that travel with identical speed. However, since the relationship between u_∞ and c illustrated in Figure 4.10 is a graph over u_∞ , each background state $(u_\infty, 0)$ corresponds to a single invasion speed. Hence, for a given α and u_∞ , we obtain a unique TWS. Figure 4.10 indicates that for increasing α and for fixed u_∞ , this speed decreases.

4.4.3 ODE versus PDE

The phase plane and wave shape illustrated in Figure 4.9 as well as the wave-speed results presented in Figure 4.10 are for the strong Allee model with $\varepsilon = 0$. However, provided we are not near the turning point of the biphasic relationship, where transversality between the canard solution and the jump curve is lost, the shape and speed of these traveling wave solutions (TWSs) are good approximations of TWSs of strong Allee model with $0 < \varepsilon \ll 1$; see Section 4.3.4. It is probable that even near the turning points, the $\varepsilon = 0$ -solutions are good approximations of the $\varepsilon > 0$ -solutions. The location of the turning point will simply shift. However, further mathematical analysis is required to confirm this.

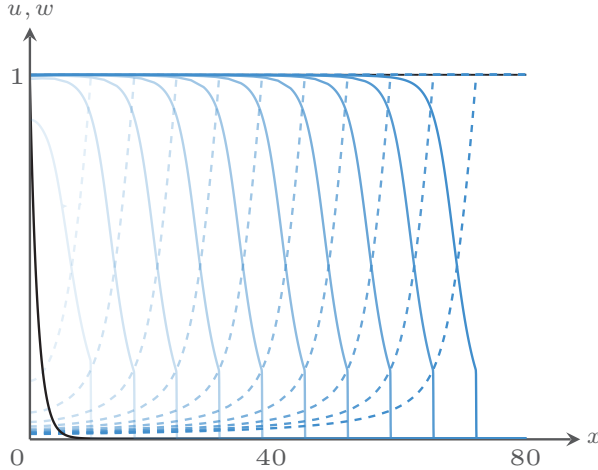


Figure 4.11: A numerical simulation of (4.1)–(4.2), with $\alpha = 0.05$, $\beta = 0.5$, $\varepsilon = 0.001$, $u_\infty = 1$ and a measured speed $c \approx 0.43$, consistent with the ODE results. The dashed lines correspond to u -profiles and the solid lines to w -profiles, with solutions plotted at $t = 0$ (black), 16 (lightest), 32, . . . , 160 (darkest).

Figure 4.11 provides an example simulation of (4.1), the strong Allee model with $\varepsilon > 0$, away from the turning point. This simulation shows the evolution of a Type III wave with a speed that agrees with that predicted by the phase plane analysis, to $\mathcal{O}(\varepsilon)$. The figure also suggests that the invasive tumor front is stable, in the sense that it is observable in the system. The initial conditions for this particular simulation are $(u, w) = (u_\infty, e^{-x})$. However, the same invasive tumor front, with the same speed, appears to evolve from any exponentially decaying w -initial condition, or a w -initial condition with semi-compact support.

Figure 4.12 depicts the results of further numerical simulations for a range of ε and u_∞ values, $\alpha = 0.05$ and $\beta = 0.5$; the right-hand panel is a close-up of the left-hand panel. The solid curve is the biphasic relationship for $\varepsilon = 0$ and $\alpha = 0.05$, given in Figure 4.10. The markers indicate the measured speed of the Type III TWS that evolves from the numerical simulation of strong Allee model, with $\varepsilon > 0$ as indicated. These results demonstrate that for a given u_∞ and α , the invasion speed is an $\mathcal{O}(\varepsilon)$ perturbation of the $\varepsilon = 0$ -speed, as expected; see Section 4.3.4. Moreover, they suggest that near the maximum of the solid curve, Type III TWSs continue to exist for $\varepsilon > 0$ with speeds close to the $\varepsilon = 0$ -speed.

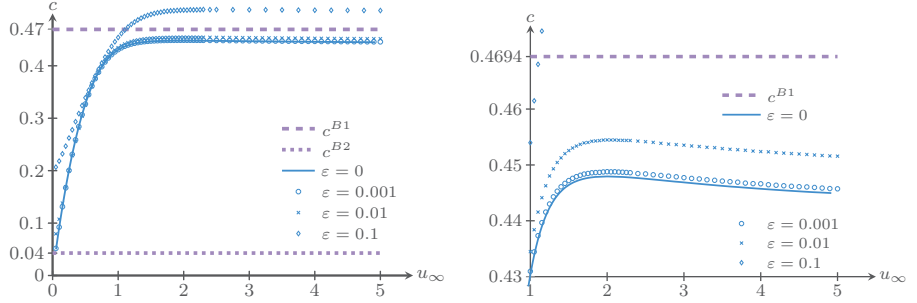


Figure 4.12: The relationship between u_∞ and the measured speed c for Type III traveling wave solutions obtained by numerically simulating (4.1)-(4.2) with $\alpha = 0.05$, $\beta = 0.5$ and ε as indicated, together with bifurcation values of c for $\alpha = 0.05$; see Section 4.3.3. The solid curve indicates the relationship between u_∞ and c for Type III traveling wave solutions with $\alpha = 0.05$ and $\varepsilon = 0$, given in Figure 4.10. The right-hand panel is a close-up of the left-hand panel. The biphasic relationship is clearly visible for small ε .

This observation supports our previous claim that while the mathematical analysis breaks down near the maximum, the results are not significantly altered.

The light blue dashed and dotted curves in Figure 4.12 are values of c at which the phase plane of (4.23) changes qualitatively, for $\alpha = 0.05$; see Figure 4.6. For c values between these lines, the folded focus canard point (FF) denoted by the filled black square in Figure 4.9, remains a FF. The values of c between the light blue dashed and dotted curves ($c^{B2}(\alpha) < c < c^{B1}(\alpha)$) represent the regime analysed mathematically in Section 4.3. Thus, we require that for a given α , u_∞ is chosen in such a way that the resulting TWS has a speed in this regime. Based on Figure 4.12, for $\alpha = 0.05$, the minimum value of u_∞ appears to be less than 0.05 (the smallest value we tested). Since $c^{\text{trans}} < c^{B1}$, there does not appear to be an upper bound on u_∞ . The $c^{B1, B2}$ lines will perturb for $\varepsilon > 0$, which may affect the range of appropriate choices of u_∞ . However, the appearance of qualitatively similar TWSs of the strong Allee model for a range of ε values suggests that our analysis remains valid for reasonably large ε values (say, $\varepsilon = 0.1$).

4.4.4 Comparison with models with logistic growth

In this section, we make a qualitative comparison between the strong Allee model and the logistic ((4.1) with (4.3)) and competition ((4.1) with (4.4)) models. The logistic model, where cancer cell growth is modeled by a logistic growth term, is

studied extensively in [67]. The competition model, where a term representing the competition for space between the ECM and cancer cells is appended to a logistic growth term, is studied in [108]. The results of the previous sections, for the strong Allee model, differ from those derived previously, in two main aspects.

For the logistic and competition models, there exists a range of traveling wave solutions (TWSs) with different speeds for a given background ECM density, varying from Type I–IV. This is in contrast to the unique TWS for the strong Allee model. Moreover, this unique TWS is of Type III, the most biologically relevant type, and appears to be stable in the sense that this kind of TWS is observed in numerical simulations of the PDE system, for a wide range of initial conditions. In contrast, for both the logistic and competition models all the Type I–III TWSs appear to be stable. See, for example, Figure 1 in [67] where stable Type I–III TWSs are shown.

The biphasic relationship observed experimentally in malignant tumor invasion [126], occurs in the competition model [108, fig. 10] but not in the logistic model. For the logistic model, the relationship between the invasion speed of the Type III waves and the background ECM density is monotonically increasing [67, fig. 11]. Thus, we conclude that the relationship between u_∞ and c has changed qualitatively due to the Allee effect, in comparison with logistic growth.

4.5 Discussion and future work

In this chapter, we proposed, what is to our knowledge, one of the first model of malignant tumor invasion that explicitly includes Allee effects, [17]. The analysis and results lead us to the conclusion that this model, with the strong Allee effect, is a better model of types of malignant tumor invasion in which haptotaxis or chemotaxis is the dominant mechanism of cell migration than similar, previously studied models: the logistic model [67, 109, 126] and the competition model [108]. This conclusion is based on the strong Allee model’s ability to replicate experimentally observed features of malignant tumor invasion more effectively than the previous models. In particular, the two main results that lead to this conclusion are:

1. The strong Allee model only admits Type III waves, the most biologically relevant invasive tumor fronts, rather than the whole family of Type I–IV waves that is admitted by the logistic and competition models.
2. The relationship between the invasion speed of these Type III waves and the background ECM density is biphasic, which is consistent with experimental observations, contrary to the corresponding relationship for the logistic model.

The results for the weak Allee model are less impressive; see Appendix B. They lead to the conclusion that the weak Allee model is similar to the logistic or competition models as a model of malignant tumor invasion. It admits the same family of traveling wave solutions, including those that are not biologically relevant, and does not exhibit the experimentally justified biphasic relationship between the speed of the Type III waves and the background ECM density.

4.5.1 Additional biological processes

The kinetic function for the cancer cells that we study is a general representation of a cubic function with zero constant term, negative cubic term and positive quadratic term:

$$f_{\text{Allee}}(\hat{w}) = -k_1\hat{w}^3 + k_1(k_2+k_6)\hat{w}^2 - k_1k_2k_6\hat{w} =: K_1\hat{w}^3 + K_2\hat{w}^2 + K_3\hat{w}, \quad (4.24)$$

with $K_1 < 0$ and $K_2 > 0$. Thus, appropriate modifications to the second equation in (4.6) (in the form of linear, quadratic or cubic terms in \hat{w}) can be expressed and studied using (4.1)–(4.2); the interpretation of the parameters simply changes. Consequently, the results of the Allee model apply more generally and we may use them to infer the effects of including (appropriate) additional biological processes to (4.6).

For example, the death of the cancer cells as a result of treatment or therapy can be modeled by the linear death term $-k_7\hat{w}$, with $k_7 > 0$ (s^{-1}). Appending this term to the \hat{w} -equation of (4.6) yields

$$\begin{aligned} \frac{\partial \hat{u}}{\partial \hat{t}} &= -k_4\hat{u}^2\hat{w} + D_1 \frac{\partial^2 \hat{u}}{\partial \hat{x}^2}, \\ \frac{\partial \hat{w}}{\partial \hat{t}} &= k_1\hat{w}(k_2 - \hat{w})(\hat{w} - k_6) - k_7\hat{w} - k_3 \frac{\partial}{\partial \hat{x}} \left(\frac{\partial \hat{u}}{\partial \hat{x}} \hat{w} \right) + D_2 \frac{\partial^2 \hat{w}}{\partial \hat{x}^2}. \end{aligned} \quad (4.25)$$

Upon applying the nondimensionalisation

$$u_d = \frac{\hat{u}}{U_d}, \quad w_d = \frac{\hat{w}}{W_d}, \quad t_d = \frac{\hat{t}}{T_d}, \quad x_d = \frac{\hat{x}}{X_d}, \quad (4.26)$$

with

$$\begin{aligned} U_d &= \frac{k_1}{k_4}W_d, \quad W_d = \frac{1}{2} \left(k_2 + k_6 + \sqrt{(k_2 - k_6)^2 - 4\frac{k_7}{k_1}} \right), \\ T_d &= \frac{1}{k_1 W_d^2}, \quad X_d = \sqrt{\frac{k_3}{k_4 W_d}}, \end{aligned}$$

and

$$\alpha_d := \frac{k_2 + k_6}{W_d} - 1, \quad \beta_d := \frac{D_1}{D_2} = \beta, \quad \varepsilon_d := \frac{k_4}{k_1 k_3 W_d} D_2,$$

and dropping the subscript d, (4.25) transforms to the Allee model, (4.1)–(4.2). We assume $k_7 < k_7^* = k_1(k_2 - k_6)^2/4$ so that W_d is real-valued.

To interpret the effect of the additional death term, we analyse how the dimensionless variables and parameters change between (4.7) and (4.26), keeping the remaining dimensional parameters k_i , $i \in \{1, 2, \dots, 6\}$ fixed. The death rate k_7 appears directly in W_d and indirectly via W_d in the other terms (excluding $\beta_d = \beta$). It is straightforward to see that a death rate k_7 decreases W_d compared to W : $W_d < W$. Consequently,

$$U_d < U, \quad T_d > T, \quad X_d > X, \quad \alpha_d > \alpha, \quad \beta_d = \beta, \quad \varepsilon_d > \varepsilon.$$

As expected, the expression for W_d corresponds to the background state of (4.25) that represents the carrying capacity of the cancer cell density; the cancer cell density in (4.2) has been scaled to one so the *representative* cancer cell density $W_{[.]}$ used in the nondimensionalisation must correspond to this background state. In terms of their relationship to W_d , the other quantities in the nondimensionalisation remain unchanged.

The parameter α_d represents the ratio of the two nontrivial w -background states of (4.25), consistent with α in (4.2). Consequently, for $\alpha_d > 0$, this parameter still imposes a growth threshold. However, in terms of the dimensional variables, the growth threshold is no longer represented by $k_6 > 0$ but by $k_6 + k_7/(k_1 k_2) > 0$. Increasing k_7 causes the two nontrivial \hat{w} -background states of (4.25) to approach each other on the \hat{w} -axis, until they collide and become complex-valued at $k_7 = k_7^*$. In (4.2), since the greater background state is scaled to one, increasing k_7 increases the value of the lesser nontrivial \hat{w} -background state, which has been scaled to α . Consequently, to obtain results for (4.25) we take $\alpha < \alpha_d < 1$ (with $\alpha_d \rightarrow 1$ as $k_7 \rightarrow k_7^*$). As evidenced by Figure 4.10, for $\alpha > 0$, increasing α causes an overall decrease in the speed of the waves. Thus, adding a linear death term to the strong Allee model slows the invasive tumor fronts.

On more speculative terms we may conclude that, as incorporating a growth threshold yields a better match between experimental data and model data, cancer treatment may be improved. If indeed tumor cells cannot survive when the density is low, therapy only needs to be applied until the density is below this threshold. If more experimental data would be available, these thresholds can be determined.

4.5.2 Shortcomings and future work

In this chapter, we proposed a model of malignant tumor invasion that we argue is an improvement on previously studied models of its kind. However, our proposed model is still far from a complete description of malignant tumor invasion; any mathematical model describing a biological process is highly simplified. It is rarely possible to identify the exact mechanisms that are involved in a given process and parameter values such as reaction-rates are often only known to several orders of magnitude. Even if the biology is completely understood, it remains a challenge to represent it mathematically in a way that is both accurate and manageable. For example, irregularities in the border of malignant tumors can be important [3, e.g.], contributing to the speed and severity of the tumor. However, to capture these irregularities, two- or three-dimensional models must be used. Such models are highly complex and not conducive to rigorous mathematical analysis. In the quickly developing field of cancer research, the correct formulation of a model is an ongoing debate. We chose to model the Allee effect with the cubic function (4.2). However, other functional forms may also be used; see, for example, [25] and references therein. Nevertheless, simple models, such as the Allee model, still provide useful information. In this case, we demonstrate that using the strong Allee effect instead of logistic growth has strong implications on the modelling of malignant tumor invasion. They also provide a stepping stone towards understanding more realistic, complex models.

The mathematical methods in this chapter focus on proving the existence of traveling wave solutions. Although the PDE simulations provide an indication of which of these solutions are stable, a rigorous stability analysis remains to be undertaken. One method of inferring stability results for models such as (4.1) is based on an Evans function computation. Such a method is at the time of publishing under development; see [69]. A related aspect that is not discussed in this chapter is the *transient dynamics* of the traveling wave solutions. We do not discuss how an initially small, localised patch of cancer cells evolves into an invading tumor front or how the cancer cells come to be present in the first place. Instead, we investigate the possible long term behaviors of pre-existing tumors. An alternative model is necessary to describe the early stages of tumor development; the prime feature of the strong Allee effect is the growth threshold it imposes, which causes populations less than the threshold value to become extinct. The stability and transient dynamics of the traveling wave solutions studied here are topics for future research.

Finally, our analysis is only valid for sufficiently small values of ε . The numerical simulations suggest that our results remain (at least qualitatively) sound for quite large values of ε , say, $\varepsilon = 0.1$ (see, for example, Figure 4.12). However, we purposely avoid specifically defining *sufficiently small* as this goes

4. Discussion and future work

beyond the scope of this chapter. An investigation of the effect of larger ε is left for future research.

Appendices

A Logistic growth and the Allee effect

To gain an understanding of the influence of the Allee effect, in comparison to logistic growth, consider the two ordinary differential equations (ODEs)

$$\frac{dw}{dt} = f_{\text{logistic}}(w) = w(1-w) \quad \text{and} \quad \frac{dw}{dt} = f_{\text{Allee}}(w) = w(1-w)(w-\alpha). \quad (4.27)$$

Both ODEs are separable and can be solved analytically; sketches of the solutions are given in Figure A.1. The ODEs with logistic growth and the weak Allee effect yield growth (or decay) to the dimensionless carrying capacity ($w = 1$) for any positive initial condition. In contrast, the ODE with the strong Allee effect yields growth (or decay) to the dimensionless carrying capacity only if an initial condition is greater than the threshold value $\alpha > 0$; initial conditions less than $\alpha > 0$ result in the extinction of the species. The differences between logistic growth and the strong and weak Allee effects are further explained by looking at the *per capita growth rate* (pcgr) of w , in the absence of spatial (or other) effects. The pcgr of w is defined as

$$\text{pcgr}(w) := \frac{1}{w} \frac{dw}{dt} = \frac{d(\log w)}{dt},$$

where $\log w$ represents the natural logarithm of w . We determine the pcgr of w for the two cases, logistic and Allee, using dw/dt defined in (4.27):

$$\text{pcgr}_{\text{logistic}}(w) = 1 - w, \quad \text{pcgr}_{\text{Allee}}(w) = (1 - w)(w - \alpha).$$

Figure A.2 provides an illustration of these curves for $w \geq 0$.

For $0 < \alpha < 1$, the pcgr curve for the strong Allee effect is negative in a neighbourhood of $w = 0$, before becoming positive at $w = \alpha$. This negativity, which corresponds to negative population growth, characterizes the strong Allee effect. For $-1 < \alpha < 0$, the pcgr curve for the weak Allee effect decreases almost everywhere except for a small increasing part for $w \in [0, (1 + \alpha)/2]$. This increase characterizes the weak Allee effect.

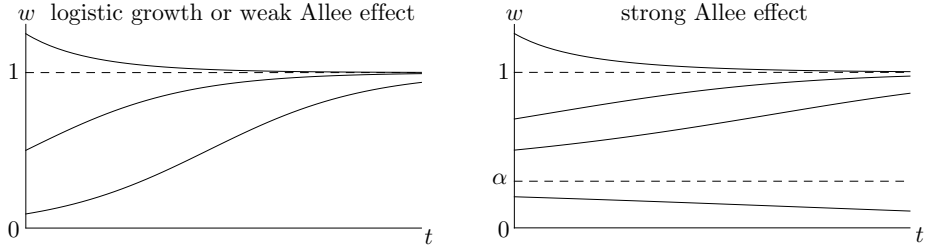


Figure A.1: Sketches of the solutions to the ODEs in (4.27). Left-hand panel: The ODEs with logistic growth and the weak Allee effect yield growth (or decay) to the carrying capacity (scaled to one) for all positive initial conditions. Right-hand panel: The ODE with the strong Allee effect only yields growth to the carrying capacity for initial conditions larger than the threshold value $\alpha > 0$. Initial conditions smaller than $\alpha > 0$ result in the extinction of w .

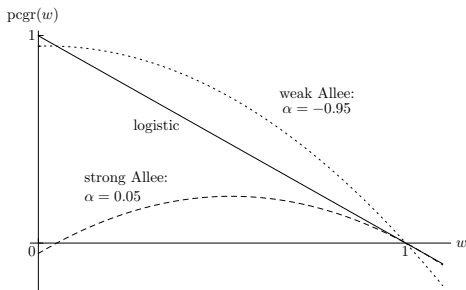


Figure A.2: The pcgr curves for logistic growth (solid), the strong Allee effect (dashed) and the weak Allee effect (dotted). The negativity of the dashed curve for $w < \alpha$ characterizes the strong Allee effect. The turning point in the dotted curve at a *small* value of w relative to the carrying capacity (in this case, at $w = 1/40$), combined with the positive intercept (at $w = 0$), characterizes the weak Allee effect.

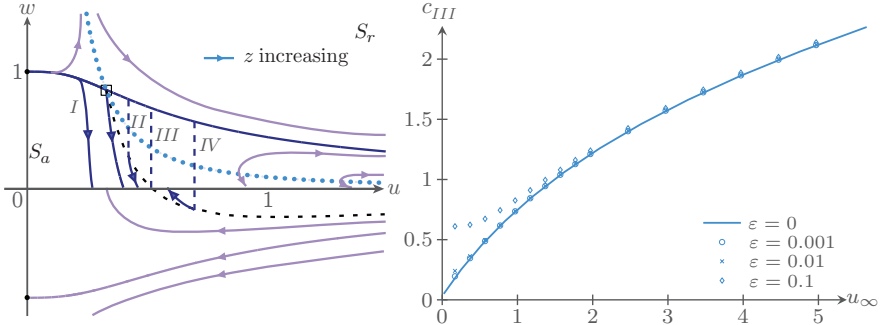


Figure B.1: Left-hand panel: Phase plane of (4.18), parametrized by z , with $\alpha = -0.95$, $c = 0.43$. The green line is the fold curve (F), which is dotted to illustrate its singularity. Black dots represent equilibria. The black open square is a folded saddle. F divides S into a repelling side (S_r , shaded) and an attracting side (S_a , unshaded). There exist a family of heteroclinic connections corresponding to Type I–IV traveling wave solutions. Right-hand panel: The relationship between the background ECM density (u_∞) and the speed of a Type III wave (c_{III}), with $\alpha = -0.95$. The solid curve is obtained from ODE simulations of (4.19); the markers are obtained from PDE simulations of the weak Allee model.

B Results for the weak Allee model

The mathematical techniques outlined in Section 4.3 can be directly applied to the weak Allee model ((4.1)–(4.2) with $\alpha \gtrapprox -1$). With $\alpha < 0$, the equilibrium $(u, w) = (0, \alpha)$ lies on the negative w -axis and the equilibria $(u_\infty, 0)$ are center stable, in contrast to the case presented in Section 4.3 with $\alpha > 0$. This means that the phase planes of the reduced problem in the weak and strong cases differ considerably, especially near the u -axis. In the weak case, trajectories can approach $(u_\infty, 0)$ via either the fast or slow dynamics, instead of only the fast. For $|\alpha|$ sufficiently large (see Remark 4.5), one canard point exists on F : a folded saddle. The left-hand panel of Figure B.1 illustrates these features and depicts an example phase plane for the weak Allee model.

The configuration of canard points and end states $(u_\infty, 0)$ for the weak Allee model is equivalent to that of the logistic model. Consequently, the analysis of the former is very similar to the latter, which is described in detail in [67]. By glueing together trajectories of the reduced and layer problems, as in Section 4.3.4, we construct a family of Type I–IV traveling wave solutions, parametrized

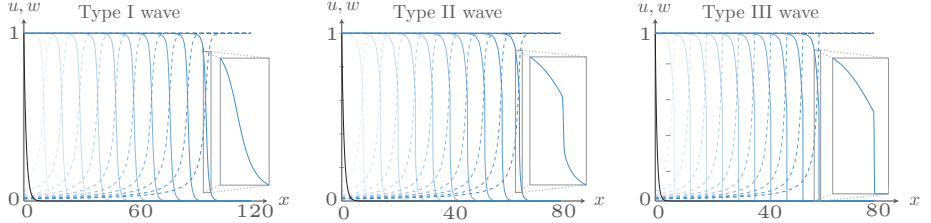


Figure B.2: Type I–III waves with speeds $c \approx 1.2, 0.80$ and 0.73 , respectively, obtained by numerically simulating (4.1) with $\varepsilon = 0.001$, $\alpha = -0.95$ and $\beta = 0.5$. The only imposed difference between the three simulations is the initial condition, in particular, the steepness of the w -component; steeper w -components lead to slower waves. The dashed lines correspond to u -profiles and the solid lines to w -profiles, with solutions plotted at $t = 0$ (black), 8 (lightest), $16, \dots, 80$ (darkest).

by c , for a given u_∞ and $\varepsilon = 0$. The Type III waves correspond to solutions that approach $(u_\infty, 0)$ via the fast dynamics, similar to the Type III waves in the strong Allee model. The Type I, II and IV waves correspond to solutions that approach $(u_\infty, 0)$ via the slow dynamics.

The persistence of these solutions follows from geometric singular perturbation theory and canard theory, using very similar arguments to those presented in [67]. One difference arises from a *transversality condition*, which is automatically satisfied in the logistic model but is violated in the weak Allee model if $u_- = u_+ = c/\sqrt{1+\alpha}$, where u_\pm is the u -coordinate of the shock; see Section 4.3.2. The full implications of this loss of transversality remain to be determined. One immediate implication is the breakdown of the proof of persistence for $0 < \varepsilon \ll 1$ for any traveling wave solutions that violate the transversality condition. Another implication appears to be the existence of nonunique solutions, that is, two possible traveling wave solutions for a given α , c , u_∞ and $\varepsilon = 0$: one with a shock and one without. Numerical simulations of the weak Allee model with $0 < \varepsilon \ll 1$ suggest that the Type I–III waves are stable; see Figure B.2.

The right-hand panel of Figure B.1 provides a plot of the speed of the Type III waves c_{III} as a function of the background ECM density u_∞ , for fixed $\alpha = -0.95$. This monotonically increasing relationship resembles the corresponding relationship for the logistic model, rather than the experimentally justified biphasic relationship.

Remark 4.5. The above discussion of the weak Allee effect requires $|\alpha|$ to be sufficiently large. This is ensure that there exists exactly one canard point on F . For $-7 + 4\sqrt{3} \approx -0.072 < \alpha < 0$, there may exist three canard points on

F , depending on the value of c . As c increases, the number of canard points on F changes from one to three and back to one via two saddle-node bifurcations. Although this regime may be mathematically interesting, it is not biologically relevant since the weak Allee effect requires $\alpha \gtrapprox -1$; see A. Consequently, we do not consider it here.

C Dimensionless variables and parameters

$$\begin{aligned}
 [u] &= [\hat{u}] \frac{[k_4]}{[k_1][k_2]} = \frac{\text{kg}}{\text{m}^3} \times \frac{\text{m}^6}{\text{kg} \times \text{cells} \times \text{s}} \times \frac{\text{cells} \times \text{s}}{\text{m}^3} = 1 \\
 [w] &= [\hat{w}] \frac{1}{[k_2]} = \frac{\text{cells}}{\text{m}^3} \times \frac{\text{m}^3}{\text{cells}} = 1 \\
 [x] &= [\hat{x}] \sqrt{\frac{[k_2][k_4]}{[k_3]}} = \text{m} \times \sqrt{\frac{\text{cells}}{\text{m}^3} \times \frac{\text{m}^6}{\text{kg} \times \text{cells} \times \text{s}} \times \frac{\text{kg} \times \text{s}}{\text{m}^5}} = 1 \\
 [t] &= [\hat{t}] [k_1][k_2]^2 = \text{s} \times \frac{\text{m}^3}{\text{cells} \times \text{s}} \times \frac{\text{cells}}{\text{m}^3} = 1 \\
 [\alpha] &= \frac{[k_6]}{[k_2]} = \frac{\text{cells}}{\text{m}^3} \times \frac{\text{m}^3}{\text{cells}} = 1 \\
 [\beta] &= \frac{[D_1]}{[D_2]} = \frac{\text{m}^2}{\text{s}} \times \frac{\text{s}}{\text{m}^2} = 1 \\
 [\varepsilon] &= \frac{[k_4]}{[k_1][k_2][k_3]} [D_2] = \frac{\text{m}^6}{\text{kg} \times \text{cells} \times \text{s}} \times \frac{\text{cells} \times \text{s}}{\text{m}^3} \times \frac{\text{kg} \times \text{s}}{\text{m}^5} \times \frac{\text{m}^2}{\text{s}} = 1
 \end{aligned}$$

D Transversality

The curves J and T_o intersect at $(u, w) = (u_\infty, c^2/u_\infty^2)$. Since T_o follows the vector field, this intersection is transverse (not tangent) if

$$\left. \frac{dJ}{du} \right|_{u=u_\infty} - \left. \frac{dw}{du} \right|_{(u,w)=(u_\infty,c^2/u_\infty^2)} \neq 0,$$

where dw/du is the ratio of the ODEs in (4.19). A straightforward computation shows that the above express is given by

$$\frac{2c^2}{u_\infty^3} + \frac{c^2(1 - c^2/u_\infty^2)(c^2/u_\infty^2 - \alpha) - 2u_\infty^3 c^4/u_\infty^4}{u_\infty^2(2u_\infty^2 c^2/u_\infty^2 - c^2)} = \frac{(u_\infty^2 - c^2)(c^2 - \alpha u_\infty^2)}{u_\infty^6} \neq 0.$$

So, transversality is lost if $c = u_\infty$ or $c = \sqrt{\alpha} u_\infty$. The former case implies that the take-off point of the jump is $(u, w) = (c, 1)$, which is only possible if $c = 0$.

Thus, given $u_\infty, c > 0$, transversality is violated only if $c = \sqrt{\alpha} u_\infty$. This speed corresponds to a take-off point of the jump at $(u, w) = (u_\infty, \alpha)$.

Long wave length vegetation patterns¹

5.1 Introduction

Human activity and climate change have stressed life on the Earth's surface. Especially in the drylands the effects are tangible, as persistent soil degradation has led to barren areas, unsuitable for agriculture. To combat this process of desertification is set as one of seventeen global goals on the United Nations' sustainable development agenda [119]. The need for a better insight in arid ecosystems is thus widely acknowledged. In the absence of grazing, vegetation growth is mainly limited by scarcity of water and nutrient. Therefore, homogeneously vegetated areas may turn into bare soil as a result of decreasing precipitation. Several intermediate stages, where the terrain is partly vegetated and partly barren, are observed, all with strikingly regular patterns [106]. In the case of a flat terrain, the transition from homogeneous vegetation to bare soil goes via hole, labyrinth, and spot patterns, [132, 138]. On a sloped terrain, however, the labyrinth patterns self-organize spatially as stripe patterns, parallel to the terrain's contours, [171]. Moreover, patterns on flat terrain have been reported to be stationary, while the stripe patterns slowly move uphill, [88]. Although the evolution from fertile to barren soil is not instantaneous, it is catastrophic in the sense that it is nearly irreversible; an increase of water availability does not automatically cultivate barren terrain to be fertile again. Therefore, vegetation patterns not only announce an early warning signal for desertification, but conversely provide a starting for the development of a homogeneously vegetated state.

The mathematical models developed to study the mechanisms responsible

¹The content of this chapter was submitted under the title *Spatially periodic multi-pulse patterns in a generalized Klausmeier-Gray-Scott model*.

for this pattern formation are mostly of reaction-diffusion type. Some models are two-component systems regarding the interaction of plant density with water density, [178, 133, 163, e.g.], while others include competition for surface water, see [75, 131], or [58, 114, e.g.]. The effect of grazing of the region in question is also expected to have a significant impact, and is taken into account in [58, 115, e.g.]. Typically, the patterns arise as a heterogeneous perturbation destabilizes the homogeneous, vegetated state; a Turing bifurcation, [156]. The catastrophe is then explained by the fact that there is a bistable parameter regime, in which both a vegetation pattern and the bare soil state are attracting [132, 138, e.g.]. As water availability decreases to some bifurcation point, the vegetation pattern destabilizes, causing it to collapse to the bare soil state; a process that is not simply reverted if water increases, because the bare soil state is also stable. The water availability should be increased as far as beyond the bistable regime to be able to configure into a vegetation pattern again. This is also referred to as hysteresis.

The focus of this article is on the striped vegetation patterns, which are observed on terrains with a gentle slope, [171]. This slope induces a downwards flow of precipitation in the form of surface water, which is then modeled by an advection term, and was introduced by C.A. Klausmeier in 1999, [88]. His model has two components, for water U , and vegetation V , and is subjected to a rescaling in [159], after which it is of the form

$$\begin{aligned} U_t &= A(1 - U) - UV^2 + CU_x, \\ V_t &= D\Delta_{x,y}V - BV + UV^2, \end{aligned} \tag{5.1}$$

where A controls water input, B is the natural death rate of vegetation, C is the rate at which water flows downhill and D is a diffusion coefficient. All coefficients are positive. The diffusion Δ models vegetation spread on a two-dimensional, infinite domain, $(x, y) \in \mathbb{R}^2$. Naturally, $t \in \mathbb{R}^+$ is the temporal coordinate.

The observation that vegetation patterns also occur in the absence of a slope, motivated an extension of model (5.1). By introducing (nonlinear) diffusion of water the spread is also modeled by a term that has no preferred direction. Extended comparisons in [159] show that nonlinear diffusion does not induce significant differences to the model. This motivates that in this article, we focus specifically on linear diffusion of water, i.e. we study

$$\begin{aligned} U_t &= \Delta_{x,y}U + A(1 - U) - UV^2 + CU_x, \\ V_t &= \delta^2\Delta_{x,y}V - BV + UV^2. \end{aligned} \tag{5.2}$$

Because it is natural to assume that water diffuses faster than vegetation, $0 < \delta \ll 1$ is a small parameter. The homogeneous background state $(U, V) = (1, 0)$ is

interpreted as a desert state; a constant water availability, yet with no vegetation. The main parameter, A , relates to precipitation, B models the vegetation's death rate and C models advection of water induced by a sloped terrain. Furthermore we assume $A, B > 0$, and $C \geq 0$. Under the assumption $A > 4B^2$, there are two more homogeneous steady states, (U_{\pm}, V_{\pm}) which are vegetated. We refer to (5.2) as the *generalized Klausmeier–Gray–Scott (gKGS) model*, because for $C = 0$, the model reduces to the Gray–Scott model, [62]. The model in [62] describes autocatalytic reactions, but as their setting is in a continuously stirred tank reactor, no diffusion is taken into account [62]. The Gray–Scott ODE system, extended with diffusion, is what is currently referred to as the Gray–Scott model, and was introduced in [19, 124].

It is widely known that both the Gray–Scott and the Klausmeier model exhibit a plethora of spatial patterns, [88, 123], and the gKGS-model captures patterns on both sloped (Klausmeier) and flat (Gray–Scott) terrains. To describe this phenomena mathematically, the existence of solutions with certain properties (wave number, amplitudes) is usually proved. However, stability analysis of these patterns is a necessary follow-up, as one does not expect to observe patterns which are unstable. To bridge the gap between existence of regular patterns in a mathematical setting and observable patterns, we consider the so-called *Busse balloon*, introduced in [16] and generalized to reaction-diffusion equations in [40, 117]. This balloon is a region in (wave number, parameter)-space in which patterns are stable against perturbations. In the context of vegetation patterns, the natural choice for the parameter is precipitation, A . Multistability of patterns with different wavelengths explains the hysteresis mentioned earlier. The onset of patterns, an extremum of the Busse balloon, occurs through a Turing bifurcation, while at the other end of the balloon, only patterns with very small wave numbers, are stable. The latter coincides with the homoclinic limit of periodic patterns confirmed by, for example [90, 91, 120, 157].

Research in the setting of system (5.2) has been fruitful at the interface of ecology and mathematics. Several Busse balloons for the gKGS system were derived using numerical continuation in [159]. In the same article, analytic control over the beginning of pattern formation is gained through the analysis of the complex Ginzburg-Landau equation associated with the pattern's amplitude. Although system (5.2) is written in a slightly different way in [143, 145], the instability mechanism for stripe patterns is unfolded further in these two articles. Using numerical continuation and simulations, [145] reports an extensive study of the destabilization of stripe patterns under the influence of a slowly decreasing parameter A . For flat terrains, the existence of nontrivial two-dimensional patterns of stripe and rhomb type and to some extent also their stability, is established in [143].

An analytical result is formulated in Theorem 3 of that article, which states that stripe patterns are unstable in the Gray–Scott model, i.e. on flat terrain, described by the $C = 0$ case of (5.2). For nonzero slope C , however, the stability is derived only using numerical continuation. These numerics suggest that as the slope of the terrain increases, the stability regime of stripe patterns spreads from the Turing bifurcation down. Eventually, for a slope large enough, even patterns with the smallest wave numbers are stable. Observations in nature also support this theory, because stripe patterns occur on sloped terrain [32]. Yet, analytical results on existence and stability of stripe patterns with small wave numbers have not been reported so far. To justify both numerics and to test the ability of the gKGS model to describe natural observations, this analysis is precisely the focus of the current paper. Our methods are based on those used for multiscale pulses in the Gray–Scott model, which as a long history of analytical studies that are discussed in section 5.1.1. Due to the advective term in (5.2), this truly is a nontrivial task; the symmetries that are used extensively in the proofs in for example [34, 39], break as soon as $C \neq 0$. Hence, the proof of existence of pulse patterns with small wave numbers in (5.2) – Theorem 5.3.1 of this paper – requires mathematical methods that go beyond the classical framework of geometric singular perturbation theory.

5.1.1 Existence and stability results of the Gray–Scott model

In this article, we exploit the singularly perturbed nature of (5.2), (recall that $0 < \delta \ll 1$) and use asymptotic analysis to prove existence and stability of stripe patterns. Our approach mainly follows the techniques developed for generalized Gray–Scott type systems in [34, 35, 36, 39, 117]. It involves geometric singular perturbation methods as well as an Evans function formulation, using the slow/fast structure of the problem and the evaluation of the solutions of a *nonlocal eigenvalue problem*.

In order to clearly compare the results, we summarize briefly the relevant results derived in for the Gray–Scott model, (5.2) with $C = 0$. In one spatial dimension, the existence of homoclinic N -pulses with $N \geq 1$ is largely covered in Theorem 4.1 of [39], see also Figure 5.1. These pulse solutions correspond to a single strip or N stripes of vegetation in an elsewhere bare terrain. An N -pulse is constructed as a homoclinic solution to the desert background state $(U, V) = (1, 0)$ that makes N fast excursions in a small spatial regime in which V is large. Already in the early publications on existence of pulses in the Gray–Scott model, the asymptotic scaling of the parameters and variables proves to be a crucial step in the analysis; a feature we also encounter for $C \neq 0$ throughout this article. In terms of the small parameter δ , the V -component of the pulse solutions constructed in [39] have asymptotically large amplitudes

in a small spatial interval, while being exponentially small outside the pulse region. The pulse solutions of [117] have less restrictions on relative magnitude of the U and V -component, and in [90, 91], an even broader parameter spectrum is analyzed in which pulse solutions exist. The rescaled, singularly perturbed system gives rise to a geometric singular perturbation analysis, where solutions of the limiting slow and fast system are concatenated according to classical Fenichel theory [82, 48, 49]. Periodic extensions of the N -pulses are characterized by slow components with long length scaled with a negative power of δ , in which the V -coordinate is exponentially small. That is, the slow/fast structure of these periodic solutions remains to be clearly distinguished. As stated in Theorem 4.2 of [39], there exists a 1-parameter family of stationary periodic solutions, and the proof relies highly on the reversible symmetry of (5.2) with $C = 0$. With a trivial extension in y -direction, the existence proof remains valid for two dimensions, but of course the extra spatial freedom gives way to more complex patterns. The existence of spot and multispot patterns on bounded two-dimensional domains have been proved in [168, 169]. The stability of homoclinic and periodic pulse patterns in the one-dimensional Gray–Scott is further analyzed in [34], where again scaling is essential, especially the relative magnitude of parameter B . From the stability problem, a nonlocal eigenvalue problem (NLEP) is formulated, and the eigenfunctions are constructed using matched asymptotic expansions. The NLEP is subsequently solved using hypergeometric functions, which reveals that for B small enough with respect to A , the 1-pulse is stable. There is a Hopf bifurcation through which it loses/gains stability in a specific B -regime, and the 1-pulse is unstable if B becomes larger than that. In the more general setting, the terminology of a Busse balloon for patterns in the Gray–Scott model was used as early as in [117]. Of course, as the authors are considering only one spatial dimension, the stability results do not necessarily hold for two-dimensional solutions, albeit with a trivial extension in the y -direction, as perturbations in the transverse direction are not taken into account. For spot and stripe patterns in two dimensions, the instability mechanisms of the Gray–Scott model are analyzed in [92] and in more detail in [22].

Another method to calculate the eigenvalues in a setting like this, is using the Evans function, see [1]. The embedding of this a priori formal stability analysis using the NLEP into the Evans function approach is established in [36], and studied in full detail in a more general context in [35].

As stated earlier, the one-dimensional patterns are trivially (constantly), extended in the transverse y -direction form 2D stripe patterns. To show existence of these patterns, no extra analysis is needed compared to the 1D existence proof. Stability, however, now needs to be tested against perturbations in both the x - and y -direction.

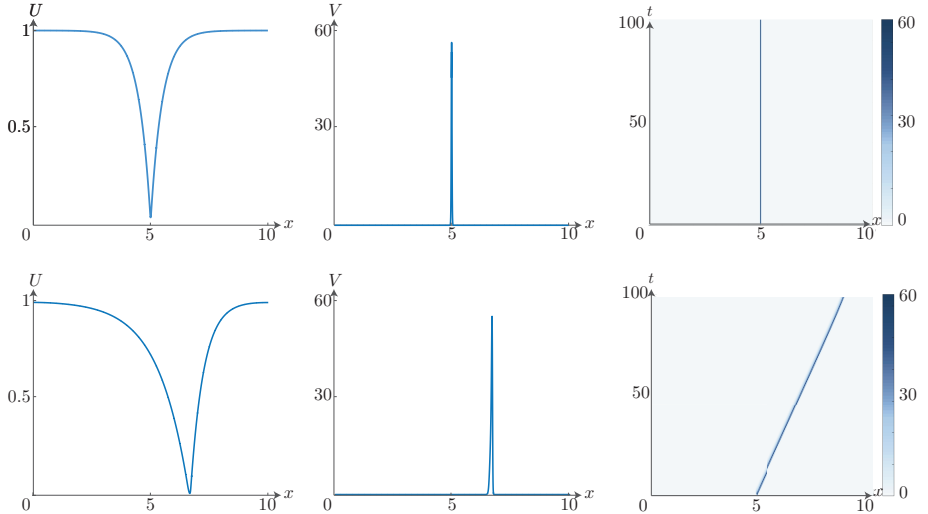


Figure 5.1: Simulations of homoclinic 1-pulses in system (5.2) in one spatial dimension x and $\delta = 0.01$ with $C = 0$ (Gray-Scott) in the top panels and $C = 1$ (gKGS) in the bottom panels. Left, a plots of U at $t = 50$ are depicted, in the middle V at $t = 50$ is depicted, and on the right we see a surface plot of V against both x and t . As parameter values we have used the sets $A = 4, B = 1.8, C = 0$ in the Gray-Scott case, and $A = 1.4, B = 0.6, C = 1$ in the gKGS case. Note that the V -pulse is stationary for $C = 0$, and travels with a constant speed to the right for $C = 1$. For the gKGS case, the values of A, B, C may, for instance, be equivalently represented by $a \approx 0.28, b = 0.25, c \approx 0.45$ with $\gamma \approx -0.174$ and $\beta \approx -0.190$ via rescaling (5.7).

This analysis is done in [143], and in the parameter regimes considered in that article, the transverse perturbations cause instability.

5.1.2 Outline of this article

In this article, we exploit the singularly perturbed nature of the system (recall δ is a small parameter), and analytically prove the existence of traveling stripe patterns on a sloped terrain, with a singular character. That is, we establish the existence of single pulses with an asymptotically large amplitude, as well as periodic extensions of these pulses. For the N -pulse, our approach goes along the lines of [39]. However, the advection term breaks the reversible symmetry so that the solutions now travel with a constant wavespeed, S , in x -direction, which we

introduce by setting $\chi = x - St$. Figure 5.1 shows a numerical simulation of the model where the symmetry breaking and constant travel speed is clearly visible. Furthermore, by focussing on stripe patterns and choosing the y -coordinate along the patterns, the spatial derivatives with respect to y vanish. Hence, we use the following system to construct stripe patterns,

$$\begin{aligned} 0 &= U_{xx} + A(1 - U) - UV^2 + (C + S)U_x, \\ 0 &= \delta^2 V_{xx} - BV + UV^2 + SV_x, \end{aligned} \tag{5.3}$$

where we make specific choices for the magnitude of the parameters and coordinates with respect to δ , in section 5.2.1. Note that the homogeneous, stationary state $(U, V) = (1, 0)$ is still a solution. Due to the loss of symmetry, the existence analysis for the spatially periodic solutions requires a novel approach. Using a contraction argument, we show that, for each given slope C , there is an interval of speeds S , for which traveling periodic pulse solutions exist.

In section 5.4, we analyze the Evans function to evaluate the eigenvalues corresponding to the stability of homoclinic and periodic pulse patterns. We require the constructed pulse patterns to have a sufficiently long wave length so that solutions to the stability problem are exponentially small in between the pulses. This implies that every family of eigenvalues one would expect in the stability analysis of spatially periodic patterns may be asymptotically approximated by a single discrete eigenvalue. See also section 5.4.1 and, for a rigorous validation, [31, 51, 52, 157]. Using the slow/fast splitting of the solutions, a leading order approximation of the eigenvalue problem is then formulated. This is equivalent with again an NLEP, that can be solved using hypergeometric functions. Similar to the results for the Gray–Scott model, the stability of patterns depends on the asymptotic magnitude of B , but the slope also affects the stability. The results are presented in Theorems 5.4.1–5.4.3. One of the findings is that perturbations with (asymptotically) large transverse wave numbers eventually destabilize any pattern. This confirms in some sense the numerical results of [143], which state that stripe patterns can only be stable on very steep slopes; a parameter regime that is not covered by the scaling restrictions of our asymptotic analysis. Moreover, one may argue that not all perturbations are representative to model ecological resilience of a pattern. Therefore, we also present Corollary 5.4.5, which analyzes the stability with respect to a more restrictive and specifically chosen function space. Since it is the transverse perturbations that form the main destabilization mechanism of stripe patterns, Theorems 5.4.2 and 5.4.3 restrict to one-dimensional patterns for which we derive saddle-node and Hopf bifurcations in several parameter regimes. Lastly, a detailed characterization of destabilization through a decrease of A or C is discussed in section 5.5. One of the conclusions that can be drawn is that indeed, a larger

value of both precipitation and slope is preferable for stripe patterns, confirming the natural observations.

5.2 Existence of homoclinic traveling multi-pulse patterns

In this section, we construct N -pulse solutions and periodic solutions of (5.3) that consist of slow and fast components. Specifically, these solutions have large χ -intervals for which the V -solution is close to zero. The building block for these solutions is the 1-pulse, i.e. a solution homoclinic to $(1, 0)$, with a localized pulse where V is $\mathcal{O}(1)$ or larger compared to δ and U small within the localized χ -interval. In this section, we will prove the following theorem.

Theorem 5.2.1 (Existence of 1-pulse patterns). *Let $A = \delta^{2\gamma}a$, $B = \delta^\beta b$, $C = \delta^\gamma c$, and $S = \delta^{1-\frac{3}{2}\beta+2\gamma}s$, where γ, β satisfy the following assumptions, also illustrated by Figure 5.2*

A1 $\beta < \gamma$,

A2 $\beta > \frac{2}{3}(\gamma - 1)$,

A3 $\beta \geq 2(\gamma - 1)$,

and $a, b, c, s \in \mathcal{O}(1)$. Then, there exists a δ_0 , such that for all $\delta < \delta_0$ and a, b, c given, there exists a uniquely determined speed s such that the four-dimensional dynamical system (5.3) has a homoclinic solution to the critical point $(U, U_\chi, V, V_\chi) = (1, 0, 0, 0)$. This solution corresponds to a traveling wave solution $\gamma_{hom}(\chi)$ of (5.2), with speed s . Its spatial profile is in x biasymptotic to $(U, V) = (1, 0)$, and trivially extends into the y -direction. The orbit γ_{hom} consists of two slow components and a single fast excursion. The magnitude of the U and V components during the fast excursion are $\delta^{1+\frac{3}{2}\beta-\gamma}$ and $\delta^{-1-\frac{1}{2}\beta+\gamma}$, respectively. Moreover, the traveling speed of this wave is to leading order in δ given by

$$s = \frac{c\sqrt{c^2 + 4a}}{6b\sqrt{b}}. \quad (5.4)$$

During the fast excursion, the U -component is constant to leading order, $U = \delta^{1+\frac{3}{2}\beta-\gamma}u_0$, with

$$u_0 = \frac{6b\sqrt{b}}{\sqrt{c^2 + 4a}}. \quad (5.5)$$

In the remainder of this section, we prove this theorem using geometric singular perturbation techniques.

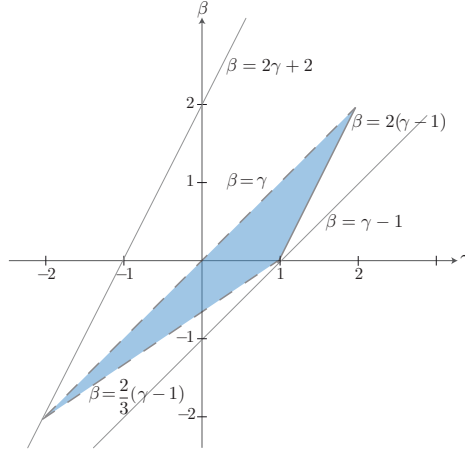


Figure 5.2: Scaling regime in the (γ, β) -plane, that satisfies assumptions **A1–A3** in Theorem 5.2.1.

5.2.1 Rescaling

The model proposed by Klausmeier, (5.1), is in dimensionalized form, meaning that it does not take into account the relative magnitudes of parameters and coordinates. However, in the case of Gray–Scott models, patterns are observed in regimes where not all quantities are $\mathcal{O}(1)$. In fact, scaling is essential for the analysis and plays an important role in the results. Hence, scaling of all parameters and coordinates is also appropriate in system (5.2), and here too, it is crucial for the analysis.

In the system (5.3), which already incorporates traveling solutions with a trivial y -extension, we introduce a new traveling coordinate,

$$\xi = \delta^{\frac{1}{2}\beta-1} \chi, \quad (5.6)$$

which we will refer to as the fast variable. The original χ will be referred to as the super slow variable. Furthermore, we introduce the following rescaled parameters and coordinates,

$$\begin{aligned} S &= \delta^{1-\frac{3}{2}\beta+2\gamma} s, & U &= \delta^{1+\frac{3}{2}\beta-\gamma} u, & V &= \delta^{-1-\frac{1}{2}\beta+\gamma} v \\ A &= \delta^{2\gamma} a, & B &= \delta^\beta b, & C &= \delta^\gamma c, \end{aligned} \quad (5.7)$$

where a, b, c, s, u, v are $\mathcal{O}(1)$. This specific scaling is motivated by arguments derived from simulations and observations, as well as earlier work on the Gray–Scott model, see [34, 39]. Most important is assumption **A1**, without which our

rescaled system would not have distinct slow and fast behavior. This assumption makes it possible to perform geometric singular perturbation analysis in the first place. The fact that A is scaled quadratically compared to C , is the most significant choice because this is the only way that neither the effects of a nor those of c (the most important parameters) are negligible. The factor $\delta^{1-\frac{3}{2}\beta+2\gamma}$ of s is chosen such that the speed has a measurable effect in the two-dimensional Hamiltonian system associated with the fast dynamics. Furthermore, we require the U -equation to exhibit slow behavior with small amplitudes in the fast interval as opposed to the fast dynamics with large amplitudes governed by the V -equation, this results in assumptions **A2** and **A3**, respectively. Lastly, we balance BV and UV^2 , so that the two-dimensional Hamiltonian system associated with the fast V -equation has a homoclinic orbit for $\delta \rightarrow 0$ and we take into account the forthcoming matching of slow and fast behavior, which leads to the specific choices of the scalings of U and V . The details of the limit behavior in the slow and fast variable, are laid out in sections 5.2.2 and 5.2.3, respectively. In the end, all quantities are scaled with only two scaling parameters, β and γ , combined with three assumptions **A1–A3**. Note that the calibration of the scalings is largely consistent with that of the Gray–Scott case, where only the scaling parameter β was left undetermined. Upon introducing an extra parameter, the slope C , one may expect the degree of freedom in scaling to increase by one which is indeed the case here. In Figure 5.2, the allowed regime of β, γ according to the assumptions is graphically outlined.

Rescaling system (5.3) according to (5.7) gives rise to,

$$\begin{aligned} u_{\xi\xi} &= \delta^{2(\gamma-\beta)} \left[uv^2 - \delta^{2+\beta} a (\delta^{\gamma-\frac{3}{2}\beta-1} - u) - \delta^{1-\gamma+\frac{3}{2}\beta} c u_\xi - \delta^2 s u_\xi \right], \\ v_{\xi\xi} &= bv - uv^2 - \delta^{2(\gamma-\beta)} s v_\xi. \end{aligned} \quad (5.8)$$

Note that $\gamma > \beta$ (**A1**), so that the right hand side of u -equation is indeed asymptotically small for $0 < \delta \ll 1$. The homogeneous equilibrium state $(U, V) = (1, 0)$ is now represented by $(u, v) = (\delta^{-1-\frac{3}{2}\beta+\gamma}, 0)$. We label this desert state P . We write (5.8) as a four-dimensional system of first order differential equations, by introducing the variables p, q .

$$\begin{aligned} u_\xi &= \delta^{\gamma-\beta} p, \\ p_\xi &= \delta^{\gamma-\beta} \left[uv^2 - \delta^{2+\beta} a (\delta^{\gamma-\frac{3}{2}\beta-1} - u) - \delta^{1+\frac{1}{2}\beta} c p - \delta^{2+\gamma-\beta} s p \right], \\ v_\xi &= q, \\ q_\xi &= bv - uv^2 - \delta^{2(\gamma-\beta)} s q. \end{aligned} \quad (5.9)$$

Assumptions **A1–A3** guarantee that the right hand side of the equation for p_ξ is always asymptotically small. We now introduce a second slow variable, see **A1**, to write system (5.9) in the slow form,

$$\zeta = \delta^{\gamma-\beta} \xi.$$

Note that ζ is, however, faster or of the same speed as χ because of **A3**,

$$\chi = \delta^{1-\frac{1}{2}\beta} \xi \lesssim \zeta = \delta^{\gamma-\beta} \xi \ll \xi.$$

From now on, we work with ζ, ξ exclusively and refer to those as the slow and fast variable, respectively. In terms of the slow variable ζ , (5.9) becomes

$$\begin{aligned} u_\zeta &= p, \\ p_\zeta &= uv^2 - \delta^{2+\beta} a(\delta^{\gamma-\frac{3}{2}\beta-1} - u) - \delta^{1+\frac{1}{2}\beta} cp - \delta^{2+\gamma-\beta} sp, \\ \delta^{\gamma-\beta} v_\zeta &= q, \\ \delta^{\gamma-\beta} v_\zeta &= bv - uv^2 - \delta^{2(\gamma-\beta)} sq. \end{aligned} \tag{5.10}$$

Using the limiting behavior for $\delta \rightarrow 0$ of the two equivalent systems (5.9) and (5.10), we will establish the existence of solutions for $\delta \neq 0$.

5.2.2 Slow limit behavior

For $\delta \rightarrow 0$, the last two equations of system (5.10) become,

$$\begin{aligned} 0 &= q, \\ 0 &= bv - uv^2, \end{aligned} \tag{5.11}$$

which define two two-dimensional critical manifolds in \mathbb{R}^4 , $\{v = 0, q = 0\}$ and $\{v = b/u, q = 0\}$. Since P is on the former, and as the latter is not normally hyperbolic for all v, q , we focus on the dynamics on

$$\mathcal{M} = \{u \geq 0, v = 0, q = 0\}, \tag{5.12}$$

where we restrict to $u \geq 0$ because this is the only ecologically relevant regime for u . Fenichel theory [9, 48, 49], guarantees the persistence of \mathcal{M} for $0 < \delta \ll 1$ as a slow manifold. In the present case, (5.12) exactly defines the invariant slow manifold associated to the full problem. Fenichel theory and its implications are discussed in more detail in section 5.2.4.

The slow dynamics on \mathcal{M} is described by

$$\begin{aligned} u_\zeta &= p, \\ p_\zeta &= -\delta^{2+\beta} a(\delta^{\gamma-\frac{3}{2}\beta-1} - u) - \delta^{1+\frac{1}{2}\beta} cp, \end{aligned} \tag{5.13}$$

from which we can derive that P is a saddle point on \mathcal{M} , with eigenvalues

$$\Lambda_{\pm} = \frac{1}{2} \delta^{1+\frac{1}{2}\beta} \left(-c \pm \sqrt{c^2 + 4a} \right),$$

and eigenvectors through P in the (u, \hat{p}) -plane,

$$\begin{aligned} \ell^u : \hat{p} &= \frac{1}{2} \left(c - \sqrt{c^2 + 4a} \right) (1 - \delta^{1+\frac{3}{2}\beta-\gamma} u), \\ \ell^s : \hat{p} &= \frac{1}{2} \left(c + \sqrt{c^2 + 4a} \right) (1 - \delta^{1+\frac{3}{2}\beta-\gamma} u). \end{aligned} \quad (5.14)$$

with a new variable $\hat{p} = \delta^{\beta-\gamma} p$. When assumption **A2** is satisfied, the eigenvectors do not depend on u in the leading order. The point P then has an asymptotically large u -value, and hence in the (\hat{p}, u) -plane $\ell^{s,u}$ are vertical at leading order. This is depicted in the middle panel of Figure 5.3. However, as $\beta = \frac{2}{3}(\gamma - 1)$, the fixed point comes into frame and $U = u$. In this case the eigenvectors do depend on u , see the right panel in Figure 5.3. This case is also explained in more detail in remarks 5.1 and 5.2. Contrary to the Gray–Scott case, where $c = 0$, the behavior on \mathcal{M} is in both panels of Figure 5.3 not symmetric about the u -axis.

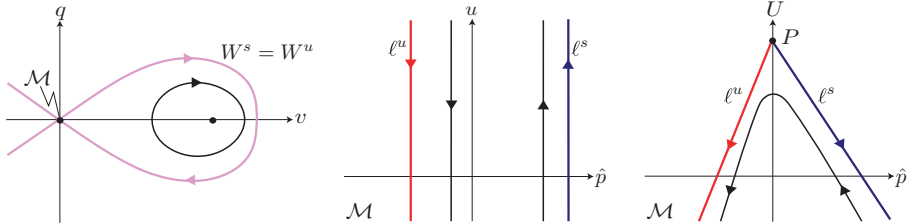


Figure 5.3: Left: The phase plane corresponding to (5.16), with in purple the homoclinic orbit to $(v, q) \in \mathcal{M}$. Center: Dynamics on \mathcal{M} dictated by (5.13) in the (\hat{p}, u) plane when **A2** is satisfied. The equilibrium P has an asymptotically large u -value and does not appear in this frame. To leading order, all dynamics, as well as $\ell^{s,u}$ are vertical. Right: Dynamics on \mathcal{M} in the (\hat{p}, U) plane, when $\beta = \frac{3}{2}(\gamma - 1)$ and $u = U$. The equilibrium P is $\mathcal{O}(1)$ and the eigenvectors vary with U .

5.2.3 Fast limit behavior

The limiting fast problem, system (5.9) with $\delta \rightarrow 0$, implies that u and p are constant, to leading order, i.e.

$$u(\xi) \equiv u_0, \quad p(\xi) \equiv p_0. \quad (5.15)$$

Hence, the fast dynamics is determined by

$$\begin{aligned} v_\xi &= q, \\ q_\xi &= bv - u_0 v^2, \end{aligned} \tag{5.16}$$

where u_0 occurs as a parameter. The fast limit problem (5.16) is Hamiltonian, with conserved quantity

$$H(v, q) = \frac{1}{2}q^2 - \frac{1}{2}bv^2 + \frac{1}{3}u_0v^3. \tag{5.17}$$

Note that there exists a symmetry in (5.16),

$$q \rightarrow -q, \quad \xi \rightarrow -\xi. \tag{5.18}$$

The equilibrium of (5.16) of our focus, $(v, q) = (0, 0)$, has $H = 0$ and is a saddle. There is a homoclinic connection to $(0, 0)$, and we find an explicit solution by integrating $H(v, q) = 0$ with respect to ξ ,

$$\begin{aligned} v_0(\xi) &= \frac{3b}{2u_0} \operatorname{sech}^2\left(\frac{1}{2}\sqrt{b}\xi\right), \\ q_0(\xi) &= -\frac{3b\sqrt{b}}{2u_0} \operatorname{sech}^2\left(\frac{1}{2}\sqrt{b}\xi\right) \tanh\left(\frac{1}{2}\sqrt{b}\xi\right). \end{aligned} \tag{5.19}$$

The phase plane of (5.16) is depicted in the left panel of Figure 5.3. Since the homoclinic orbit exists for any u_0 and p_0 , the equilibrium $(v, q) = (0, 0)$ represents the entire critical manifold \mathcal{M} (5.12). The critical manifold has three-dimensional stable and unstable manifolds, $W^{u,s}(\mathcal{M})$. Because the homoclinic orbit exists for all u_0, p_0 , we find $W^u(\mathcal{M}) = W^s(\mathcal{M})$ in the limit $\delta \downarrow 0$. This is represented in three dimensions in the left hand panel of Figure 5.4.

5.2.4 Persistence of solutions in the perturbed problem

With the results of sections 5.2.2 and 5.2.3, we construct a singular homoclinic orbit to P with both slow and fast parts obtained by the $\delta = 0$ limits. For $\delta \downarrow 0$, the eigenvectors $\ell^{s,u}$ tend to and eventually collide on the u -axis. In other words, the stable and unstable manifolds of P , restricted to \mathcal{M} are in fact the u -axis in this limit. To construct a singular slow/fast homoclinic solution to P , we may match any point on the u -axis to the fast homoclinic excursion, because for $\xi \rightarrow \pm\infty$, the eigenvectors $\ell^{s,u}$ will connect it to P . As a result, we have a one parameter family of singular homoclinic connections to P , parametrized by the value of u at the concatenation point of the slow and fast parts, say u_0 .

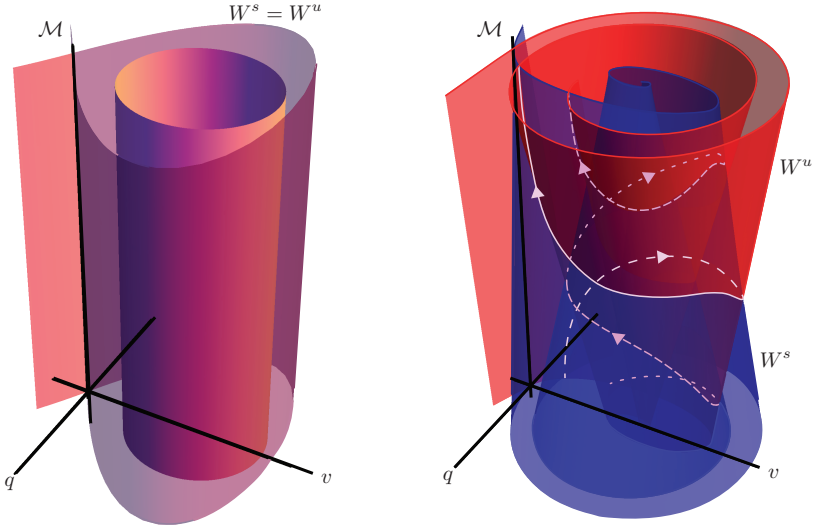


Figure 5.4: Schematic three-dimensional representation of the intersection of $W^u(\mathcal{M})$ and $W^s(\mathcal{M})$ of (5.9) for $\delta = 0$ (left) and $0 < \delta \ll 1$ in four dimensions. In reality, \mathcal{M} , here the one-dimensional vertical axis, is two-dimensional. Left: The stable and unstable manifolds of \mathcal{M} are three-dimensional, and coincide. For every point on \mathcal{M} there exists a fast homoclinic connection. Right: The stable (blue) and unstable (red) manifolds persist, but no longer coincide. Their intersections correspond with fast N -pulses, homoclinic to \mathcal{M} . Here, only the first two intersections are drawn: the 1-pulse, in white, and the 2-pulse in purple.

For $\delta \neq 0$, the stable and unstable manifolds of \mathcal{M} persist as $W_{\delta}^{s,u}(\mathcal{M})$ according to Fenichel theory [48, 49], but they no longer coincide. Instead, the intersection of $W_{\delta}^{s,u}(\mathcal{M})$ perturbs, like depicted in Figure 5.4. A fast connection to \mathcal{M} is thus no longer guaranteed for every pair (u, \hat{p}) .

A solution homoclinic to P , with a slow/fast structure must leave P via the perturbed ℓ^u on \mathcal{M} , connect to a fast orbit homoclinic to \mathcal{M} , and returning to \mathcal{M} exactly such that it enters P along the perturbed stable manifold, ℓ^s . These eigenvectors $\ell^{s,u}$ have also perturbed with δ , and no longer coincide on the u -axis. Schematically, we represent a homoclinic slow/fast solution in four dimensions in a three-dimensional illustration in the left hand panel of Figure 5.5.

Although the fast connection to \mathcal{M} generally does not persist, a perturbed

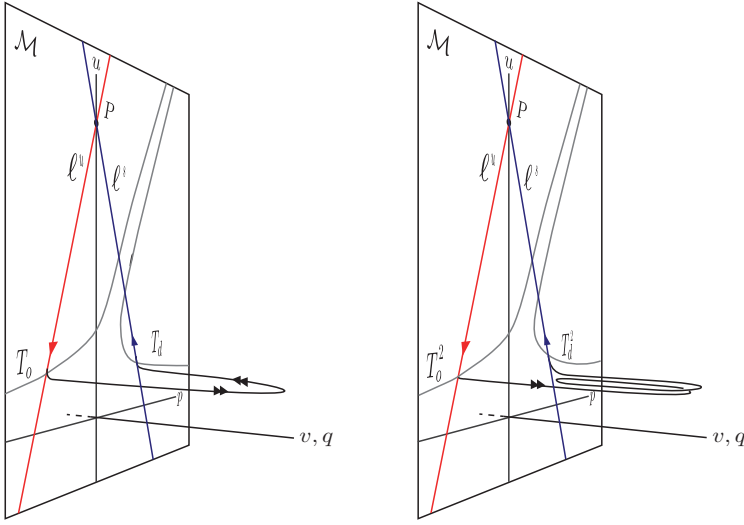


Figure 5.5: Schematic representation of a 1-pulse (left) and a 2-pulse (right); a slow/fast homoclinic connection to P , with a fast component that has one (left) or two (right) maxima. On \mathcal{M} , the solution follows ℓ^u before taking off into the fast field, where v and q become large. After that, the solution lands back on \mathcal{M} at ℓ^s , which limits to P .

homoclinic orbit is still approximated by the $\delta = 0$ solution in the fast field, (5.19). To prove the statement of Theorem 5.2.1, we show that there still exists a homoclinic solution to P for $0 < \delta \ll 1$. We label this solution $\gamma_{\text{hom}}(\xi) = (u(\xi), p(\xi), v(\xi), q(\xi))$. Without a loss of generality, we choose $\gamma_{\text{hom}}(0) = (u_0, p_0, v_{\max}, 0)$. That is, we select the $\xi = 0$ point exactly there where $q = 0$; it is at the maximum value of the V -pulse.

We first show that there exists a one-dimensional manifold for which $W_\delta^s(\mathcal{M})$ and $W_\delta^u(\mathcal{M})$ intersect transversally in the hyperplane $\{q = 0\}$. Then, following the approach developed in [35, 39], we construct take-off and touch-down curves that dictate how to connect the intersection $W_\delta^s(\mathcal{M}) \cap W_\delta^u(\mathcal{M}) \cap \{q = 0\}$ to the slow stable and unstable manifolds of P restricted to \mathcal{M} , which are the eigenvectors $\ell^{s,u}$.

Lemma 5.2.2. *Assume the conditions on a, b, c from Theorem 5.2.1 are satisfied. Then there exists a $\delta_0 > 0$ such that for all $0 < \delta < \delta_0$ the stable and unstable manifold of \mathcal{M} in system (5.9) intersect transversally in $\{q = 0\}$; the (u_0, p_0)*

coordinates of this one-dimensional intersection are at leading order given by

$$p_0 = \delta^{\gamma-\beta} s u_0. \quad (5.20)$$

In other words, the homoclinic connection of (5.16) to \mathcal{M} persists for $\delta > 0$ in (5.9) if (5.20) is satisfied.

For $0 < \delta \ll 1$, the critical manifold \mathcal{M} , as well as the stable and unstable manifolds $W^{s,u}(\mathcal{M})$ persist as a slow manifold \mathcal{M}_δ and $W_\delta^{s,u}(\mathcal{M})$ in an $\mathcal{O}(\delta^{\gamma-\beta})$ -neighborhood. This follows directly from Fenichel's first and second theorem, see [48, 82]. In fact, we may choose $\mathcal{M}_\delta = \mathcal{M}$, because $v = q = 0$ is still invariant under the flow for $0 < \delta \ll 1$. This is not the case for $W_\delta^{s,u}(\mathcal{M})$; the stable and unstable manifolds that used to coincide (see the left hand side of Figure 5.4), no longer do so. In general, the two three-dimensional manifolds intersect in two-dimensional surfaces, and in these intersections lie the only trajectories that are biasymptotic (homoclinic) to \mathcal{M} , see an illustration of such a perturbation and a persisting connection in the right-hand panel of Figure 5.4.

To detect these intersections, and hence proving Lemma 5.2.2, we apply a Melnikov method, much like [35, 39]. We will work with the fast variable ξ and define the fast interval I_f , as

$$I_f = \left[-\frac{1}{\delta^\mu}, \frac{1}{\delta^\mu} \right], \quad \text{with } 0 < \mu < \gamma - \beta. \quad (5.21)$$

If $\gamma(\xi)$ is a solution of (5.9), then, for $\xi \in I_f$, u and p are constant and equal to u_0, p_0 at leading order. We measure the distance between $W^s(\mathcal{M})$ and $W^u(\mathcal{M})$ in the hyperplane $\{q = 0\}$, using the Hamiltonian (5.17) and the fact that on \mathcal{M} , $H \equiv 0$ even though $\delta \neq 0$, see (5.17). We now determine the first order corrections of u and p in the fast variable ξ . That is, we write

$$\begin{aligned} u(\xi) &= u_0 + \delta^{\gamma-\beta} u_1(\xi) + \text{h.o.t.}, \\ p(\xi) &= p_0 + \delta^{\gamma-\beta} p_1(\xi) + \text{h.o.t.}, \end{aligned} \quad (5.22)$$

and determine $u_1(\xi), p_1(\xi)$. We assume $u(0) = u_0$, and set $u_j(0) = 0$ for all $j \geq 1$. Using a standard asymptotic analysis and the boundary conditions that U and V must remain bounded on the real line, we find that $u_1(\xi) \equiv 0$. From the leading order analysis of section 5.2.2, we derive that $p = \mathcal{O}(\delta^{\gamma-\beta})$, so $p_0 = 0$. As a matter of fact, $p_1 = \hat{p}$, the variable introduced in section 5.2.2.

We compute \hat{p} from the first order terms of system (5.9),

$$\begin{aligned}\hat{p} = \int_0^\xi \hat{p}_\xi d\xi + \hat{p}(0) &= \int_0^\xi u_0 v_0^2(\xi) d\xi + \hat{p}(0), \\ &= \frac{3b\sqrt{b}}{2u_0} \tanh\left(\frac{1}{2}\sqrt{b}\xi\right) \left(2 + \operatorname{sech}^2\left(\frac{1}{2}\sqrt{b}\xi\right)\right) + \hat{p}(0),\end{aligned}\quad (5.23)$$

to leading order in δ . Now we can measure the change in the Hamiltonian H in I_f over the fast homoclinic orbit. For $\delta \neq 0$, it is given by

$$H_\xi = \delta^{2(\gamma-\beta)} \left(\frac{1}{3}v^3\hat{p} - sq^2 \right), \quad (5.24)$$

which implies

$$\begin{aligned}\Delta H &= \delta^{2(\gamma-\beta)} \int_{I_f} \left(\frac{1}{3}v^3\hat{p} - sq^2 \right) d\xi, \\ &= \delta^{2(\gamma-\beta)} \frac{6b^2\sqrt{b}}{5u_0^2} \left(\frac{2\hat{p}(0)}{u_0} - s \right),\end{aligned}\quad (5.25)$$

where ΔH means the change in H over I_f . Hence, for given $p_0 = \delta^{\gamma-\beta}\hat{p}(0)$, ΔH changes sign once and in a transversal way at

$$\hat{p}(0) = \frac{1}{2}su_0, \quad (5.26)$$

which implies that $W_\delta^s(\mathcal{M})$ and $W_\delta^u(\mathcal{M})$ indeed intersect transversally. This proves Lemma 5.2.2.

Note that equation (5.25) is actually the first moment we explicitly focus on the construction of a 1-pulse, by measuring the change in H over exactly one fast excursion. In Corollary 5.2.4, we explain how this step changes to establish the existence of N -pulses with $N > 1$.

Lemma 5.2.3 (Take-off and touch-down curves). *Let $\Gamma(\xi; u_0)$ be the one-parameter family of solutions of (5.9) with $\Gamma(0; u_0)$ in $W_\delta^s(\mathcal{M}) \cap W_\delta^u(\mathcal{M}) \cap \{q = 0\}$. In other words, let $\Gamma(0; u_0) = (u_0, \frac{1}{2}\delta^{\gamma-\beta}su_0, v(0), 0)$ at leading order, see (5.26). Moreover, let $\Gamma^{o,d}(\xi; u^{o,d}, p^{o,d})$ be trajectories strictly on \mathcal{M} with initial condition at $(u^{o,d}, p^{o,d})$. Then, there exist two curves $T_o(u)$ and $T_d(u)$ on \mathcal{M} , such that there are $\Gamma^{o,d}$ satisfying*

$$\begin{aligned}||\Gamma(\xi; u_0) - \Gamma^o(\xi; u_0, T_o(u_0))|| &< k_1 e^{k_3 \delta^{\beta-\gamma}}, \quad \text{for } -\xi \geq \mathcal{O}(\delta^{\beta-\gamma}), \\ ||\Gamma(\xi; u_0) - \Gamma^d(\xi; u_0, T_d(u_0))|| &< k_2 e^{k_3 \delta^{\beta-\gamma}}, \quad \text{for } \xi \geq \mathcal{O}(\delta^{\beta-\gamma}),\end{aligned}\quad (5.27)$$

for some $\mathcal{O}(1)$ constants $k_{1,2,3} > 0$. The curves $T_o(u)$ and $T_d(u)$ are called take-off and touch-down curve, respectively, and are given by

$$\begin{aligned} T_o(u) &= \frac{1}{2}\delta^{\gamma-\beta} \left(su - \frac{6b\sqrt{b}}{u} \right), \\ T_d(u) &= \frac{1}{2}\delta^{\gamma-\beta} \left(su + \frac{6b\sqrt{b}}{u} \right), \end{aligned} \tag{5.28}$$

to leading order.

Thus, this lemma explicitly describes trajectories on \mathcal{M} , for which the distance to a solution homoclinic to \mathcal{M} gets exponentially small as ξ gets large in either the negative or the positive half-line.

Proof. The existence of the take-off and touch-down curves is established by Fenichel theory, where the points in T_o and T_d are referred to as base points of the Fenichel fibers, see [48, 49]. The geometry of $W^s(\mathcal{M}) \cap W^u(\mathcal{M})$ implies that T_o and T_d can indeed be characterized as graphs over u . Their quantification is obtained by explicitly determining the change of p from the $\xi = 0$ point in the intersection $W_\delta^s(\mathcal{M}) \cap W_\delta^u(\mathcal{M}) \cap \{q = 0\}$, over half a fast pulse, to an exponentially small neighborhood of \mathcal{M} for both negative and positive ξ ,

$$\int_{-\frac{1}{\delta^\mu}}^0 p_\xi d\xi = \int_0^{\frac{1}{\delta^\mu}} p_\xi d\xi,$$

for $\xi < 0$ and $\xi > 0$, respectively. The boundaries of the integrals are the boundaries of I_f , see (5.21). The fast behavior is symmetric to leading order, see (5.18), so both integrals are half of the integral over the full fast interval, and equal to

$$\begin{aligned} \frac{1}{2} \int_{I_f} p_\xi d\xi &= \frac{1}{2} \delta^{\gamma-\beta} \int_{I_f} u_0 v_0(\xi)^2 d\xi + \text{h.o.t.}, \\ &= \frac{1}{2} \delta^{\gamma-\beta} \frac{6b\sqrt{b}}{u_0} + \text{h.o.t.} \end{aligned} \tag{5.29}$$

So, combining this rate of change of p with $p(0)$ from (5.23), we arrive at (5.28). The estimates of (5.27) are derived from Fenichel theory, and the constant k_3 is related to the largest eigenvalue of the fast field. \square

Using Lemmas 5.2.2 and 5.2.3, we now prove Theorem 5.2.1.

Proof. (of Theorem 5.2.1). From all the solutions $\gamma(\xi)$ that are biasymptotic to \mathcal{M} , the homoclinic 1-pulse γ_{hom} is by construction exactly that one that connects to ℓ^u for $\xi < 0$ and to ℓ^s for $\xi > 0$. Thus, we need

$$T_o(u_0) = \ell^u(u_0) \quad \text{and} \quad T_d(u_0) = \ell^s(u_0).$$

This happens when

$$u_0 = \frac{6b\sqrt{b}}{\sqrt{c^2 + 4a}}, \quad \text{and} \quad s = \frac{c\sqrt{c^2 + 4a}}{6b\sqrt{b}}, \quad (5.30)$$

to leading order in δ , see the left panel of Figure 5.5. \square

Corollary 5.2.4 (Existence of N -pulse patterns). *Let A, B, C satisfy the assumptions **A1–A3**.*

Then there exists a δ_0 , such that for all $\delta < \delta_0$, and for each N of $\mathcal{O}(1)$, there exists a solution $\gamma_{N,\text{hom}}$ of (5.3) homoclinic to $(U, U_\chi, V, V_\chi) = (1, 0, 0, 0)$ for a uniquely defined speed s_N . The orbit $\gamma_{N,\text{hom}}$ corresponds to a traveling wave solution of (5.2). Its spatial profile that is in x biasymptotic to $(U, V) = (1, 0)$, and trivially extends into the y -direction. It consists of two slow components and N fast excursions. The traveling speed of this wave is given by

$$s_N = \frac{c\sqrt{c^2 + 4a}}{6Nb\sqrt{b}}. \quad (5.31)$$

During the fast excursions, the U -component is constant to leading order, $U = \delta^{1+\frac{3}{2}\beta-\gamma} u_0$, with

$$u_{0,N} = \frac{6Nb\sqrt{b}}{\sqrt{c^2 + 4a}}. \quad (5.32)$$

For $N = 2$ the homoclinic orbits to P are schematically drawn in the right hand panels of Figures 5.4 and 5.5. The key principle to realize is that manifolds $W^s(\mathcal{M})$ and $W^u(\mathcal{M})$ may intersect more than once in $\{q = 0\}$. In [35], it is shown, using the symmetry of the fast system, that indeed, there may be many intersections $W^s(\mathcal{M}) \cap W^u(\mathcal{M}) \cap \{q = 0\}$, all of dimension 1. Following ξ in forward and backward time along W^s and W^u , starting from \mathcal{M} , the first intersection corresponds to the 1-pulse of Theorem 5.2.1 and has $v = \mathcal{O}(1)$. The second intersection happens for $0 < v \ll 1$, and corresponds to the 2-pulse, the third intersection has again $v = \mathcal{O}(1)$ and corresponds to the 3-pulse, et cetera.

Proof. The condition (5.23) must still hold, but since the trajectory makes N circuits in the fast regime, we must measure the change of p a total of N times.

Symmetry (5.18) makes that we can construct take-off and touch-down curves for every N , as follows

$$T_o^N(u) = \frac{1}{2} \delta^{\gamma-\beta} \left(su - \frac{6Nb\sqrt{b}}{u} \right), \quad T_d^N(u) = \frac{1}{2} \delta^{\gamma-\beta} \left(su + \frac{6Nb\sqrt{b}}{u} \right).$$

Again, an intersection of T_o^N, T_d^N with $\ell^{s,u}$ constructs the homoclinic N -pulse, and we arrive at the conditions for $u_{0,N}$ and s_N as stated in the theorem. \square

As opposed to the homoclinic 1-pulse, we will not dive into the details of the existence of periodic extensions of these N -pulses nor their stability. The main reason for this is the fact they can be argued to be unstable by a simple argument, explained in section 5.4.1.

Remark 5.1. Even in the case that $\beta = \frac{2}{3}(\gamma - 1)$, when **A2** is violated, homoclinic pulse solutions continue to exist. In that case, the expressions for $\ell^{s,u}$ from (5.14) depend on u in the leading order and the behavior on \mathcal{M} is as described by the right panel of Figure 5.3. The fast limit results remain unchanged but the fine tuning for the values (5.30) is slightly different. In both cases, the touch-down curve intersects ℓ^s twice, while the take-off curve intersects ℓ^u just once. By tuning s and u_0 , there are two solutions

$$\begin{aligned} u_0^- &= \frac{1 - \sqrt{1 - 24\delta^{\gamma-\frac{2}{3}\beta-1}b\sqrt{b}(c^2 + 4a)^{-1/2}}}{2\delta^{\gamma-\frac{2}{3}\beta-1}}, & s^+ &= c\delta^{\gamma-\frac{2}{3}\beta-1} \left(\frac{1}{u_0^-} - 1 \right), \\ u_0^+ &= \frac{1 + \sqrt{1 - 24\delta^{\gamma-\frac{2}{3}\beta-1}b\sqrt{b}(c^2 + 4a)^{-1/2}}}{2\delta^{\gamma-\frac{2}{3}\beta-1}}, & s^- &= c\delta^{\gamma-\frac{2}{3}\beta-1} \left(\frac{1}{u_0^+} - 1 \right). \end{aligned} \tag{5.33}$$

When **A2** is satisfied, only the pair (u_0^-, s^-) is an eligible solution because u_0^+ is not $\mathcal{O}(1)$. To leading order in δ , this results exactly in (5.30).

However, as $\beta = \frac{2}{3}(\gamma - 1)$, both intersections u_0^\pm are $\mathcal{O}(1)$, so there are two solutions under the condition that

$$\frac{24b\sqrt{b}}{\sqrt{c^2 + 4a}} \leq 1. \tag{5.34}$$

$$\begin{aligned} u_0^- &= \frac{1 - \sqrt{1 - 24b\sqrt{b}(c^2 + 4a)^{-1/2}}}{2}, & s^+ &= c \left(\frac{1}{u_0^-} - 1 \right), \\ u_0^+ &= \frac{1 + \sqrt{1 - 24b\sqrt{b}(c^2 + 4a)^{-1/2}}}{2}, & s^- &= c \left(\frac{1}{u_0^+} - 1 \right). \end{aligned} \tag{5.35}$$

Both solutions correspond to a homoclinic 1-pulse solution of (5.3), and (5.34) defines the parameter combination at which the solutions merge in a saddle-node bifurcation, see also [39].

5.3 Existence of traveling multiscale periodic solutions

Given that the origin of system (5.3) is the description of vegetation patterns, the existence of periodic patterns is perhaps more relevant than the homoclinic N -pulse patterns. After all, homoclinic patterns represent N relatively nearby stripes that are isolated in an elsewhere completely bare desert. The stripe patterns, as they are observed in the field, are naturally much better represented by periodic pulse patterns, [143]. The periodic patterns still have a slow/fast structure, and we will construct periodic patterns as depicted in Figure 5.6. That is, the slow parts of the period patterns lie close to \mathcal{M} and connect to a fast excursion. Furthermore, we use that the fast parts of the constructed solutions are nearly homoclinic to the slow manifold \mathcal{M} ; solutions stay in a neighborhood of \mathcal{M} for an $\mathcal{O}(\delta^{-1+\frac{1}{2}\beta-\gamma})$ amount of time in ξ . By definition, a periodic orbit cannot be homoclinic to \mathcal{M} , but we use in our construction that it is exponentially close to $W^u(\mathcal{M}) \cap W^s(\mathcal{M})$, see also [38]. We focus on the periodic solution that consists of one fast excursion from the slow manifold \mathcal{M} , and one long, slow segment near \mathcal{M} , per period. This periodic orbit may be distinguished from an N -pulse by the distance between the fast pulses. After their fast excursions, periodic solutions constructed in this section remain exponentially close to \mathcal{M} for a long time in ξ before making another excursion that actually marks a new period of the pattern. Therefore, the wavelength of the constructed patterns is algebraically large in δ^{-1} . The N -pulses, however, do not return to an exponentially small neighborhood of \mathcal{M} after a fast excursion, since N -pulses only approach \mathcal{M} to an algebraically small distance in δ between consecutive fast excursions. The distance between pulses of an N -pulse is thus only logarithmically large in δ . It is only after the N -th excursion that the N -pulse returns to \mathcal{M} , indefinitely.

In this section, we prove the following theorem.

Theorem 5.3.1. *Let $a, b, c, s \in \mathcal{O}(1)$ be given and let **A1–A3** and*

$$s < \frac{c\sqrt{c^2 + 4a}}{6b\sqrt{b}}, \quad (5.36)$$

be satisfied. Then, there exists a δ_0 , such that for all $\delta < \delta_0$, there exists a unique periodic solution $\gamma_{p,s}(\xi)$ of (5.8) with a slow/fast structure. That is, for any s satisfying (5.36), there exists a traveling wave solution of (5.2), with a spatial profile which is periodic.

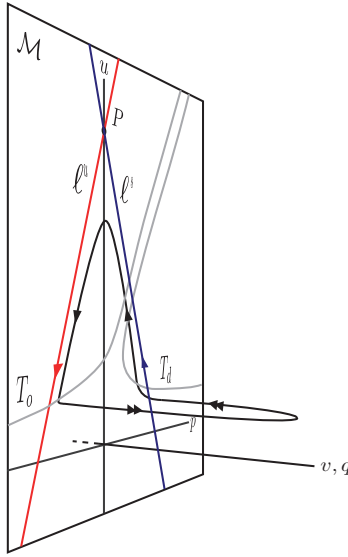


Figure 5.6: Schematic representation of a periodic slow/fast solution of which the slow part is close to the manifold \mathcal{M} . During the fast excursion the coordinate u is constant to leading order.

Figure 5.7 shows a simulation of (5.2) representing a solution like $\gamma_{p,s}$.

Because v, q are exponentially small during the largest part of the period of the constructed solution, the leading order behavior of the slow parts is still governed by (5.13), and the derivation of the take-off and touch-down curves remains valid. We use the explicit formulas we have for T_o and T_d to construct periodic solutions and prove Theorem 5.3.1. As an illustrative guide to the proof, we use Figure 5.8.

First, note that the slow segments of the periodic solution must lie in the area enclosed by ℓ^s and ℓ^u , because they are separatrices in the slow manifold. Within this area, the take-off curve is monotonous as a function of p , while the touch-down curve is not. This fact is key in the existence of periodic solutions.

Second, note that the geometry of $T_{o,d}$ and $\ell^{s,u}$ determines the eligible u -values for which the periodic pattern will make the fast excursion. For a given s , the maximum of the interval of eligible u -values is always

$$\tilde{u} = \sqrt{\frac{6b\sqrt{b}}{s}} \quad (5.37)$$

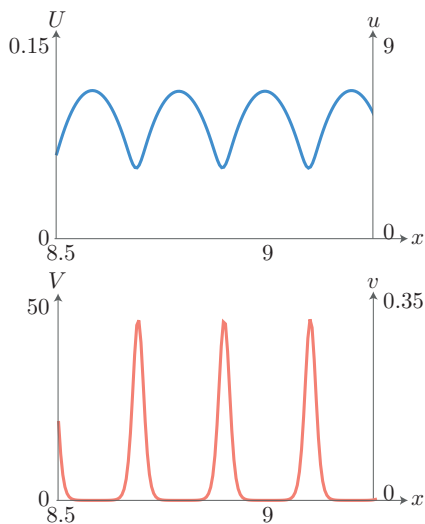


Figure 5.7: Simulation of (5.2) with $A = 15$, $B = 1.8$, $C = 1$ and $\delta = 0.01$, or, $a = 3$, $b = 0.75$, $c \approx 0.447$ with $\gamma \approx -0.174$, $\beta \approx -0.190$. The simulation was done on a spatial domain of length 10, and the patterns travel to the right over time. The left y -axes denote the unscaled U_0 (blue) and V - (red) values while the right y -axes denote the values of the scaled u and v for our choices of β, γ .

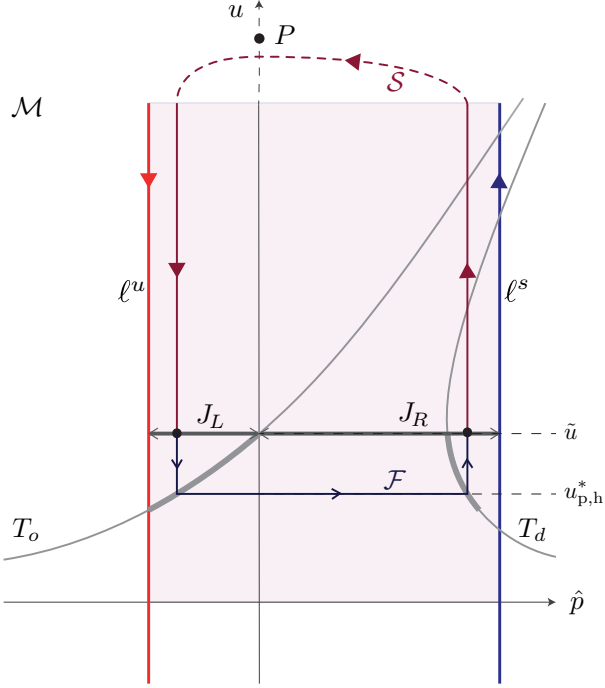


Figure 5.8: Schematic illustration of the construction of a periodic solution of (5.8). Depicted is the slow manifold \mathcal{M} with the stable and unstable eigenvectors $\ell^{s,u}$ and take-off and touch-down curves $T_{o,d}$. In dark red, a schematic representation of the slow function \mathcal{S} is sketched, and the fast function \mathcal{F} is dark blue. The point P is at an $\mathcal{O}(\delta^{-1-\frac{3}{2}\beta+\gamma})$ -distance, hence the dashed lines.

, i.e. the intersection of T_o with the $\{\hat{p} = 0\}$ -axis. Condition (5.36) implies that the minimum is always the u -value corresponding to $\ell^u \cap T_o$, see Figure 5.8.

Due to the lack of reversible symmetry, the methods developed in [38] do not provide sufficient control over the slow system to prove Theorem 5.3.1. We therefore employ a different approach making use of a contraction argument.

We define a horizontal line segment in the (\hat{p}, u) -plane, i.e. on \mathcal{M} enclosed by ℓ^u and ℓ^s , and at the $u = \tilde{u}$ level.

$$J = \left\{ \hat{p} \in \left(c - \sqrt{c^2 + 4a}, c + \sqrt{c^2 + 4a} \right), \quad u = \tilde{u} \right\}. \quad (5.38)$$

and J_R and J_L as the parts of J , where \hat{p} is positive, resp. negative, see Figure 5.8. On these intervals, we define two functions. Firstly, a map $\mathcal{S} : J_R \rightarrow J_L$.

Let J_R represent a line of initial conditions of the slow flow, see (5.13). Note that $u_\xi = 0$ for $p = 0$. As the slow flow is linear and P is a saddle point on \mathcal{M} , we know that all orbits with an initial point in J_R have an intersection with J_L as well. In fact, this is a one-to-one correspondence. The map \mathcal{S} assigns to every point $(\tilde{u}, p) \in J_R$, the corresponding intersection in J_L , and this is a bijection.

Secondly, in the parameter regime where (5.36) holds, define the map

$$\mathcal{F} : J_L \rightarrow J_R, \quad \mathcal{F}(\tilde{u}, p) = \left(\tilde{u}, p + \frac{24sb\sqrt{b}}{p + \sqrt{p^2 + 24sb\sqrt{b}}} \right). \quad (5.39)$$

This map represents the fast flow indicated by the take-off and touch-down curves. For initial values in J_L , the map is based on a concatenation of three steps. To leading order, p does not change by the evolution of the slow flow. Furthermore, T_o is monotonous, so by following the slow flow the initial points on J_L correspond bijectively to points T_o . This is the first step of \mathcal{F} . As the second step, dictated by the fast flow, the point on T_o that results from the first step is sent to a point on T_d , which is also well-defined since the u -value remains, at leading order, constant during the fast excursion. Lastly, the slow flow takes all these touch-down points to J_R . Condition (5.36) implies that the range of \mathcal{F} is guaranteed to be within J_R . Hence, the map \mathcal{F} keeps solutions in the bounded area of \mathcal{M} , shaded in Figure 5.8. By inverting the expressions for T_o and T_d , it can be verified that \mathcal{F} indeed acts as given in (5.39).

Lemma 5.3.2. *Both maps $\mathcal{S} : J_R \rightarrow J_L$ and $\mathcal{F} : J_L \rightarrow J_R$ are contractions.*

Proof. Naturally, we use the Euclidian metric on J_L and J_R . As explained, the map \mathcal{S} is a bijection. However, the size of the domain, J_R is $c + \sqrt{c^2 + 4a}$, which is smaller than the size of codomain J_L , which is $c - \sqrt{c^2 + 4a}$. Since P is a saddle, the flow on \mathcal{M} is linear and orbits cannot intersect, the initial points in J_R remain ordered after they intersect the nullcline $p = 0$. By explicitly evaluating \mathcal{S} , we indeed find that for every pair $X, Y \in J_R$,

$$|\mathcal{S}(X) - \mathcal{S}(Y)| < |X - Y|,$$

and \mathcal{S} is a contraction.

For the map \mathcal{F} it suffices to check that

$$\frac{\partial}{\partial p} \left(p + \frac{24sb\sqrt{b}}{p + \sqrt{p^2 + 24sb\sqrt{b}}} \right) = \frac{p}{\sqrt{p^2 + 24sb\sqrt{b}}} < 1.$$

A derivative smaller than 1 implies contraction, so the function \mathcal{F} is a contraction, too. \square

Lemma 5.3.2 allows us to establish the first ingredient of the proof of Theorem 5.3.1 about the existence of periodic solutions. The composition $\mathcal{F} \circ \mathcal{S} : J_R \rightarrow J_R$ is a contraction as well. By Banach's fixed point theorem, this contraction has a unique fixed point in J_R , say $\hat{p} = \hat{p}_{p,h}^* \in J_R$. This implies that $(\tilde{u}, \hat{p}_{p,h}^*)$ is an initial point for a slow segment in \mathcal{M} which intersects the take-off and touch-down curves in the same u -value. We label this u -value $u_{p,h}^*$ so that

$$(u_{p,h}^*, \hat{p}_{p,h}^*) = \left(u_{p,h}^*, \frac{1}{2} \left(s u_{p,h}^* + \frac{6b\sqrt{b}}{u_{p,h}^*} \right) \right). \quad (5.40)$$

Note that $u_{p,h}^*$ is always larger than the u_0 of (5.30), because u_0 marks the left boundary of J_L , in which T_o is monotonically increasing. In sections 5.4 and 5.5, we show that this has implications for the stability of the solutions and links directly to Ni's conjecture [120].

A concatenation of the slow and fast parts of the constructed orbit associated with $(u_{p,h}^*, \hat{p}_{p,h}^*)$ does not immediately result in a periodic orbit, because the orbit is derived using the intersection of $W^s(\mathcal{M}) \cap W^u(\mathcal{M})$ for $T_{o,d}$. The constructed orbit, we label it $\gamma_{p,h}(\xi)$, is depicted in Figure 5.9, and is rather than being periodic, homoclinic to the manifold \mathcal{M} . That means that it makes only one excursion in the fast field, after it has returned to a neighborhood of \mathcal{M} it only gets closer and closer. Note that actually, $\gamma_{p,h}(\xi)$ depends on the choice of s . We label the speed corresponding to $\gamma_{p,h}$ as $s_{p,h}$.

We reset the initial point of $\gamma_{p,h}$ so that it is at the point where v is maximal, i.e. $q = 0$. That is, we write

$$\gamma_{p,h}(0) = (u_{p,h}(0), p_{p,h}(0), v_{p,h}(0), 0).$$

We will show that a true periodic orbit exists with initial point exponentially close to $\gamma_{p,h}(0)$. This orbit is $\gamma_{p,s}(\xi)$ that is defined in the statement of theorem 5.3.1.

The proof of Theorem 5.3.1 is inspired by that of Theorem 3.1 in [38], but cannot be carried over immediately. The advection term in (5.2) breaks the reversible symmetry, which is crucial to the proofs in [38]. In the present, not symmetric case, more delicate arguments are developed to resolve that issue.

Proof. (of Theorem 5.3.1)

We prove the existence of periodic orbits by using arguments of intersecting manifolds, similar to the proof of Theorem 5.2.1. The aim is to show (in four dimensions) that there is a one-dimensional periodic orbit that lies close to $\gamma_{p,h}(\xi)$.

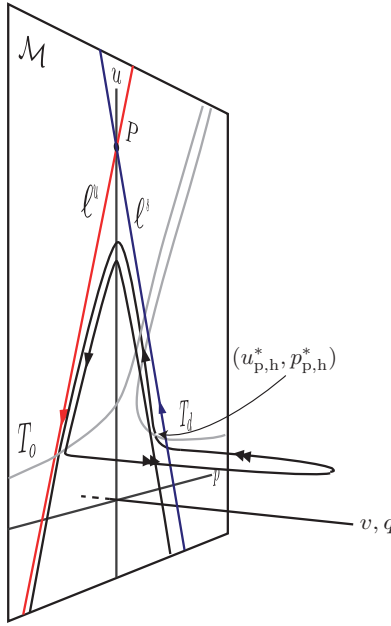


Figure 5.9: Schematic representation of the four-dimensional orbit $\gamma_{p,h}$ in three dimensions. The orbit makes one fast excursion and is homoclinic to the manifold \mathcal{M} .

Define the exponentially small, two-dimensional rectangle γ as follows,

$$\begin{aligned} \gamma = & \{u = u_{p,h}(0)\} \times \left(p_{p,h}(0) - k_1 e^{-k\delta^{-1+\frac{1}{2}\beta-\gamma}}, p_{p,h}(0) + k_2 e^{-k\delta^{-1+\frac{1}{2}\beta-\gamma}} \right) \\ & \times \left(v_{p,h}(0) - k_3 e^{-k\delta^{-1+\frac{1}{2}\beta-\gamma}}, v_{p,h}(0) - k_4 e^{-k\delta^{-1+\frac{1}{2}\beta-\gamma}} \right) \\ & \times \{q = 0\}, \end{aligned} \quad (5.41)$$

with $k, k_i > 0$ and $k_3 > k_4$. The value k is associated with the eigenvalues of the fast limit system. Figure 5.10 shows the rectangle γ in the rescaled $e^{-k\delta^{-1+\frac{1}{2}\beta-\gamma}}(v, p)$ -plane. Note that $-1 + \frac{1}{2}\beta - \gamma < 0$ in the regime defined by **A1-A3** (Figure 5.2), so $-k\delta^{-1+\frac{1}{2}\beta-\gamma}$ is very large and negative, and γ is indeed exponentially small.

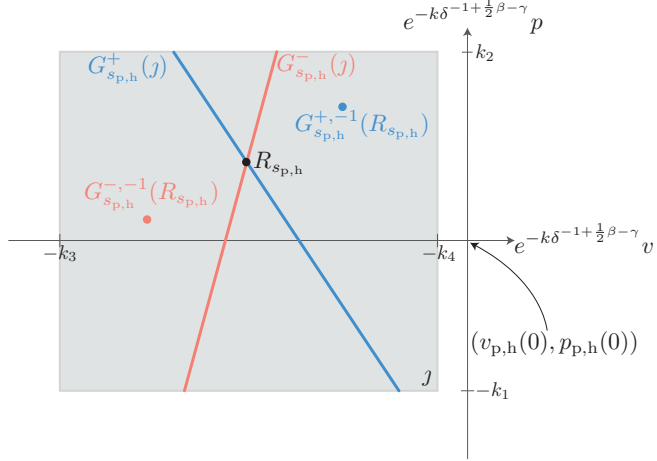


Figure 5.10: Schematic representation of the rectangle \mathcal{J} (gray) with $G_{s_{p,h}}^+(\mathcal{J})$ and $G_{s_{p,h}}^-(\mathcal{J})$ as one-dimensional curves in \mathcal{J} in red and blue, respectively. The point $G_{s_{p,h}}^{+,-1}(R_{s_{p,h}})$ is the original in \mathcal{J} that was sent to $R_{s_{p,h}}$ following the forward flow and is therefore red, while $G_{s_{p,h}}^{-,-1}(R_{s_{p,h}})$ is the original under G^- and is therefore associated with the blue curve and colored accordingly.

We use \mathcal{J} as a set of initial conditions that lie exponentially close to the intersection $W^u(\mathcal{M}) \cap W^s(\mathcal{M}) \cap \{q = 0\}$. All orbits formed by flowing initial condition in \mathcal{J} forward, remain exponentially close to $W^s(\mathcal{M})$ as long as ξ does not become larger than $\mathcal{O}(\delta^{1-\frac{1}{2}\beta+\gamma})$. Because of the exact closeness estimate of $\mathcal{O}(e^{-k\delta^{-1+\frac{1}{2}\beta-\gamma}})$, it remains close to $W^s(\mathcal{M})$ exactly long enough to make an $\mathcal{O}(\delta^{\gamma-\beta})$ change in p . This is the same order of magnitude that p changes during the slow part of $\gamma_{p,h}$. The three-dimensional manifold is obtained from flowing \mathcal{J} forward is labeled J^+ . The flow depends directly on the speed of $\gamma_{p,h}$, i.e. $s_{p,h}$, so J^+ does so as well.

By choosing k_i appropriately, J^+ will return to an exponentially small neighborhood of \mathcal{J} , since it is exponentially close to $W^u(\mathcal{M})$. Thus, J^+ intersects \mathcal{J} in a one-dimensional manifold $\mathcal{J} \cap J^+$; a curve in \mathcal{J} . We define the map $G_{s_{p,h}}^+ : \mathcal{J} \rightarrow \mathcal{J}$ that maps points in \mathcal{J} to their next intersection with \mathcal{J} when the forward flow induced by (5.8) is followed. Hence we find

$$G_{s_{p,h}}^+(\mathcal{J}) = J^+ \cap \mathcal{J},$$

see Figure 5.10.

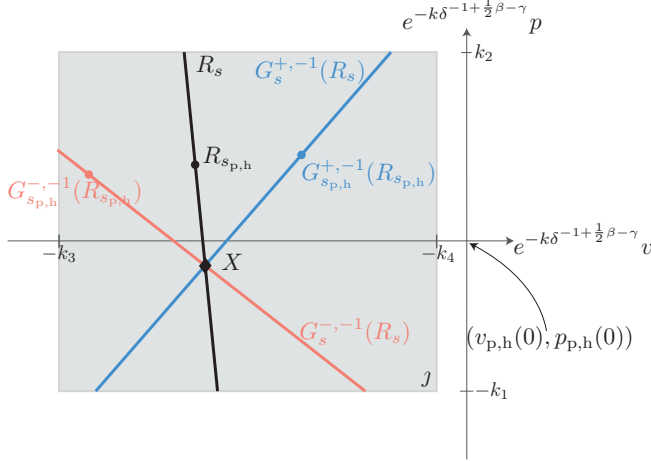


Figure 5.11: Representation of the rectangle \mathcal{J} (gray) with $G_s^{+, -1}(R_s)$ and $G_s^{-, -1}(R_s)$ as one-dimensional curves in \mathcal{J} in red and blue, respectively. $R_{s_{p,h}}$ is the original intersection $G_{s_{p,h}}^+(\mathcal{J}) \cap G_{s_{p,h}}^-(\mathcal{J})$ in \mathcal{J} associated with the speed $s_{p,h}$ of orbit $\gamma_{p,h}(\xi)$. The points $G_{s_{p,h}}^{\pm, -1}(R_{s_{p,h}})$ are the pre-images of $R_{s_{p,h}}$ and the curves are parametrized by s . The intersection of the curves is the point X , which is associated to an initial condition for the periodic orbit $\gamma_p(\xi)$, and is indicated with a black diamond.

Similarly, we can define J^- by flowing \mathcal{J} backwards in ξ . Again, appropriate k_i will make sure that J^- intersects \mathcal{J} and we label this analogous map $G_{s_{p,h}}^-(\mathcal{J}) : J^- \rightarrow \mathcal{J}$, so that we have

$$G_{s_{p,h}}^-(\mathcal{J}) = J^- \cap \mathcal{J}.$$

See again Figure 5.10 for an illustration. The curves $G_{s_{p,h}}^{\pm}(\mathcal{J})$ are one-dimensional and generically intersect in a point in \mathcal{J} , say $R_{s_{p,h}}$. The intersection point $R_{s_{p,h}}$ is the point in \mathcal{J} that in both in forward and backward time returns to \mathcal{J} . Since $R_{s_{p,h}}$ is on $G_{s_{p,h}}^+(\mathcal{J})$, there is a point in \mathcal{J} that is flown forward to $R_{s_{p,h}}$, say $G_{s_{p,h}}^{+, -1}(R_{s_{p,h}})$, as it is a the pre-image of $R_{s_{p,h}}$. On the other hand, since $R_{s_{p,h}}$ is on $G_{s_{p,h}}^-(\mathcal{J})$ as well, there is a point in \mathcal{J} that is flown backward to $R_{s_{p,h}}$, which we label $G_{s_{p,h}}^{-, -1}(R_{s_{p,h}})$. However, $G_{s_{p,h}}^{-, -1}(R_{s_{p,h}})$ and $G_{s_{p,h}}^{+, -1}(R_{s_{p,h}})$ are both zero-dimensional in \mathcal{J} and hence a priori do not intersect. The point $R_{s_{p,h}}$ generally is thus not an initial value for a periodic orbit.

We do know, however, that if we consider exponentially small deviations in s from $s_{p,h}$, the points $G_{s_{p,h}}^{-, -1}(R_{s_{p,h}})$ and $G_{s_{p,h}}^{+, -1}(R_{s_{p,h}})$ move in \mathcal{J} , along curves

parametrized by s , see Figure 5.11. These curves, $G_s^{\pm,-1}(R_{s_{p,h}})$, generically intersect in γ for a specific s_p , say in the point X . Exactly when this happens, both the forward flow map G^+ and backward flow map G^- have X as a fixed point. Of course, that also implies that the intersection $G_{s_p}^+(\gamma) \cap G_{s_p}^-(\gamma)$ occurs exactly in X so $R_{s_p} = X$.

This point $X = (v^X, p^X)$ is associated to a periodic orbit with an initial value $(u_{p,h}(0), p^X, v^X, 0)$. This periodic orbit is $\gamma_p(\xi)$ and it has a speed that is exponentially close to $s_{p,h}$. Note that, by our choice of rectangle γ , we do fix the initial condition of the periodic solution at the maximum value of v (since $q = 0$) and that the u -value at that point is equal to the u -value of $\gamma_{p,h}$ where $v_{p,h}$ is maximal.

Using the direct method as developed in [37], or the exchange lemma approach with exponential errors of [83], it is possible to show that indeed this X exists for a certain s_p . Moreover, this s_p is unique, but we refrain from going into the details any further. \square

Remark 5.2. As for the existence of homoclinic singular pulse solution, see 5.2.1, we have assumed through **A2** that $\beta > \frac{2}{3}(\gamma - 1)$. When $\beta = \frac{2}{3}(\gamma - 1)$ the construction of a homoclinic singular pulse solution is still possible, see Remark 5.1. The same holds for periodic patterns. As the assumption **A2** attains equality, the construction of periodic solutions remains valid as the rectangle γ remains exponentially small. The only difference to take into account is that condition (5.36) changes into

$$u_{\min} < \frac{2c}{2c + s},$$

where u_{\min} is the u -value corresponding to the intersection of T_o with ℓ^u in \mathcal{M} .

5.4 Stability of singular multiscale patterns

Although the existence of many types of stripe patterns in system (5.3) is guaranteed by the analysis of sections 5.2 and 5.3, not all will be relevant in light of vegetation patterns. Of course, an unstable solution of a simplified model like (5.3) can never be observed in a natural system. In this section, we test the linear stability of the constructed patterns from the previous sections against two-dimensional perturbations. We formulate the Evans function corresponding to the linear stability problem, and make extensive use of the slow/fast structure of our solutions to evaluate it. This method is developed and described in full detail for reversible systems in [34, 35, 36]. However, like in the existence problem, the advection term breaks the symmetry, so the theory cannot be carried over completely. Nevertheless, we show that this approach can be extended and we decompose the Evans function in a fast and a slow component. As in the

literature, the slow component of the Evans function is determined explicitly in terms of hypergeometric functions.

Let (U_0, V_0) be a traveling solution of (5.2) corresponding to a single stripe $(U_{\text{hom}}, V_{\text{hom}})$ of vegetation or a periodic pattern (U_p, V_p) of vegetation stripes in \mathbb{R} , trivially extended in a second spatial dimension. Since N -pulse solutions with $N > 1$ are unstable (this is motivated in section 5.4.1), we do not consider the stability of these patterns in the current section. The solutions γ_{hom} and $\gamma_{p,s}$ that have been established in Theorems 5.2.1 and 5.3.1 may be rescaled back into U, V coordinates according to (5.7) to obtain $(U_{\text{hom}}, V_{\text{hom}})$ and (U_p, V_p) , respectively; both solutions of (5.2) could be substituted for (U_0, V_0) . Due to the trivial structure of (U_0, V_0) in y -direction we can use a Fourier ansatz and perturb the solutions as,

$$(U(\chi, y, \tau), V(\chi, y, \tau)) = \left(U_0 + e^{\hat{\lambda}\tau+i\hat{\ell}y} \hat{u}(\chi), V_0 + e^{\hat{\lambda}\tau+i\hat{\ell}y} \hat{v}(\chi) \right), \quad (5.42)$$

where χ is the super slow traveling coordinate. Here we must make the following clarification. For periodic patterns, any perturbation in the direction transverse to the pattern (that is the y -direction), may be represented by $\hat{\ell} \in \mathbb{R}$ and a $\hat{\gamma} \in S^1$, taking into account the so-called ‘ $\hat{\gamma}$ -eigenvalues’ [31]. We may then speak of eigenvalues $\hat{\lambda}(\hat{\gamma}, \hat{\ell})$ for each $\hat{\gamma}, \hat{\ell} \in (\mathbb{R}, S^1)$. However, since the fundamental interval of our periodic solutions is asymptotically large and the exponential decay of U and V is fast enough so that they are both exponentially small outside I_f , the entire family $\hat{\lambda}(\hat{\gamma}, \hat{\ell})$ is exponentially close to one specific value $\hat{\lambda}(\hat{\ell})$ for each $\hat{\ell}$. We quantify this in section 5.4.1. Then, for every fixed $\hat{\ell} \in \mathbb{R}$ there exists an eigenvalue $\hat{\lambda}(\hat{\ell})$ that determines the stability of the solution (U_0, V_0) , also in the case that (U_0, V_0) is a spatially periodic pattern. For more details on this approach, see [31, 51, 52, 157].

If $\hat{\lambda}$ has negative real part for every $\hat{\ell} \in \mathbb{R}$ – apart from the trivial translation eigenvalue $\hat{\lambda}(0) = 0$ – the pattern is (spectrally) 2D-stable. Conversely, if there is one $\hat{\ell}$ for which an eigenvalue $\hat{\lambda}(\hat{\ell})$ has positive real part, the pattern is 2D-unstable. Note that the reduction $\hat{\ell} = 0$ in (5.42) implies only perturbations in the χ -direction. The results for $\hat{\ell} = 0$ therefore correspond to 1D-stability. In what follows, we derive the stability problem of (U_0, V_0) and subsequently formulate three theorems that summarize the results. In section 5.4.1, the Evans function framework is established and analyzed for 1-pulse patterns. These results are expanded to also be valid for periodic patterns, so that the proofs of the theorems can be presented for all stripe patterns constructed in this article in section 5.4.2.

Substituting (5.42) into (5.3) and linearizing, yields the linear stability prob-

lem for (\hat{u}, \hat{v}) ,

$$\begin{aligned} 0 &= \hat{u}_{xx} + (C + S)\hat{u}_x - (A + \hat{\ell}^2 + \hat{\lambda} + V_0^2)\hat{u} - 2U_0V_0\hat{v}, \\ 0 &= \delta^2\hat{v}_{xx} + S\hat{v}_x + (2U_0V_0 - \delta^2\hat{\ell}^2 - \hat{\lambda} - B)\hat{v} + V_0^2\hat{u}. \end{aligned} \quad (5.43)$$

Rescaling according to (5.7), and introducing

$$\begin{aligned} U_0 &= \delta^{1-\gamma+\frac{3}{2}\beta}u_0, & \hat{u} &= \delta^{1-\gamma+\frac{3}{2}\beta}u, & \hat{\lambda} &= \delta^\beta b\lambda, \\ V_0 &= \delta^{-1+\gamma-\frac{1}{2}\beta}v_0, & \hat{v} &= \delta^{-1+\gamma-\frac{1}{2}\beta}v, & \hat{\ell} &= \delta^\theta\sqrt{b}\ell, \end{aligned} \quad (5.44)$$

we derive a linear, non-autonomous, four-dimensional system of first order differential equations in the fast variable ξ , much like system (5.9),

$$\begin{aligned} u_\xi &= \delta^{\gamma-\beta}p, \\ p_\xi &= \delta^{\gamma-\beta} \left[2u_0v_0v + v_0^2u + \delta^{2+\beta}au + (\delta^{2+2\theta+\beta-2\gamma}\ell^2 + \delta^{2+2\beta-2\gamma}\lambda)bu \right. \\ &\quad \left. - \delta^{1+\frac{1}{2}\beta}cp - \delta^{2+\gamma-\beta}sp \right] \\ v_\xi &= q, \\ q_\xi &= [b(\lambda + 1) - 2u_0v_0]v + v_0^2u - \delta^{2+2\theta-\beta}b\ell^2v - \delta^{2(\gamma-\beta)}sq. \end{aligned} \quad (5.45)$$

Here, the new scaling parameter θ is a dummy parameter to make the magnitude of $\hat{\ell}$ explicit. In principle, 2D-stability is only guaranteed if we can make a stability statement for all $\theta \in \mathbb{R}$. In order to perform our slow/fast analysis, however, we restrict to a subclass of transverse perturbations by assuming,

$$\theta > \gamma - \frac{1}{2}\beta - 1. \quad (5.46)$$

That is, we test stability against perturbations with a transverse wave number that may be arbitrarily small, but is not larger than $\mathcal{O}(\delta^{\gamma-\frac{1}{2}\beta-1})$. Since we have assumed (**A3**) that $\gamma - \frac{1}{2}\beta - 1 \geq 0$, this is an asymptotically large bound. Restricting to this subclass in general weakens the stability statements. However, we find that also for θ within this bound, there always exist unstable perturbations. That implies that the restriction to this subclass does not change anything for the 2D-stability of (U_0, V_0) .

Concerning the stability of solutions $(U_0(\xi), V_0(\xi))$ of (5.2), we formulate the following theorems.

Theorem 5.4.1. *Let the assumptions **A1–A3** be satisfied and let δ be small enough. Let (U_0, V_0) be a slow/fast solution of (5.2), either of a 1-pulse type, or a spatially periodic pattern with asymptotically large wave length of $\mathcal{O}(\delta^{\frac{1}{2}\beta-1-\gamma})$ as established in Theorems 5.2.1 and 5.3.1. Then there is an $\hat{\ell}$ such that there is a bounded solution to (5.42) for a $\hat{\lambda}(\hat{\ell})$ with positive real part. That is, the 1-pulse and periodic stripe patterns constructed in this article, are 2D-unstable.*

For $\hat{\ell} = 0$, the stability of a solution (U_0, V_0) is tested for perturbations without a component in the y -component. Since we have assumed the constructed solutions in this article have a trivial extension in the y -direction, results for $\hat{\ell} = 0$ correspond to the stability of one-dimensional patterns. For this 1D-stability of a spatially one-dimensional pattern, which we will, slightly abusive, also label (U_0, V_0) , we formulate Theorem 5.4.2.

For a clear presentation of the results, we introduce,

$$C_1 = \frac{\bar{u}^2}{6b}, \quad C_2 = \frac{c^2 + 4a}{b}. \quad (5.47)$$

where \bar{u} is the value of $\delta^{\gamma - \frac{3}{2}\beta - 1} U_0$ in the fast regime I_f , where U_0 is to leading order constant, see 5.9. In the case that $(U_0, V_0) = (U_{\text{hom}}, V_{\text{hom}})$, the value of \bar{u} is in fact reported in (5.30).

Theorem 5.4.2. *Let the assumptions **A1** and **A3** be satisfied and let $\beta \geq \frac{2}{3}(\gamma - 1)$. Let (U_0, V_0) be a slow/fast 1-pulse solution of (5.2) in one spatial dimension. That is, let (U_0, V_0) be $(U_{\text{hom}}, V_{\text{hom}})$ established in Theorem 5.2.1 without the trivial extension in the y -direction. The 1D-stability of this pattern can be summarized as follows.*

- (i) *If $\beta < \gamma - \frac{1}{2}$, there is a bounded solution to (5.42) with $\Re(\hat{\lambda}) > 0$, so (U_0, V_0) is 1D-unstable.*
- (ii) *If $\beta > \gamma - \frac{1}{2}$ and **A2** is satisfied, all nontrivial eigenvalues $\hat{\lambda}$ corresponding to pattern (U_0, V_0) have negative real part, so the pattern is 1D-stable.*
- (iii) *If $\beta = \gamma - \frac{1}{2}$ and **A2** is satisfied, then a pair of eigenvalues $\hat{\lambda}_{1,2}$ passes through the imaginary axis (i.e. a Hopf bifurcation occurs) if $C_1 = 2H^*$. Here, H^* is given as the explicit solution of an expression in terms of hypergeometric functions, and $H^* \approx 0.661$. Using (5.30), we equivalently formulate that for $\sqrt{\frac{b}{c^2+4a}} < 2H^*$, the pattern (U_0, V_0) is 1D-stable.*
- (iv) *If $\beta > \gamma - \frac{1}{2}$ and $\beta = \frac{2}{3}(\gamma - 1)$, then an eigenvalue $\hat{\lambda}$ passes through zero if*

$$C_1 \sqrt{C_2} = 1. \quad (5.48)$$

The pattern (U_0, V_0) is 1D-stable if $C_1\sqrt{C_2} < 1$. This implies, using (5.35) that the pattern with $\bar{u} = u_0^+$ is 1D-unstable, and the pattern with $\bar{u} = u_0^-$ is 1D-stable. The bifurcation occurs exactly at the saddle-node bifurcation, at which u_0^\pm collide.

- (v) If $\beta = \gamma - \frac{1}{2}$, $\beta = \frac{2}{3}(\gamma - 1)$ and $C_2 > C_2^*$, which is a explicit solution of an equation in terms of hypergeometric functions and $C_2^* \approx 1.333$, then an eigenvalue $\hat{\lambda}$ passes through zero if (5.48) is satisfied. This implies, using (5.35) that the pattern with $\bar{u} = u_0^+$ is 1D-unstable, and the pattern with $\bar{u} = u_0^-$ is 1D-stable. The bifurcation occurs exactly when (5.34) is an equality; where u_0^\pm collide.
- (vi) If $\beta = \gamma - \frac{1}{2}$, $\beta = \frac{2}{3}(\gamma - 1)$ and $C_2 \leq C_2^*$ as defined in case (v), then a pair of eigenvalues $\hat{\lambda}_{1,2}$ passes through the imaginary axis (i.e. a Hopf bifurcation occurs) if

$$C_1 = Z(C_2) := \frac{1}{\sqrt{4i\bar{\kappa}(C_2) + C_2}} \left(\frac{9}{K \left(2\sqrt{i\bar{\kappa}(C_2) + 1} \right)} - 1 \right). \quad (5.49)$$

Here, the function $\bar{\kappa}(C_2)$ is the function that assigns to every $C_2 \in (0, C_2^*)$ the imaginary part of the eigenvalues at the Hopf bifurcation, and $K(P)$ is defined in (5.77). The bifurcation never occurs for patterns with u_0^+ of (5.35), and the pattern with $\bar{u} = u_0^+$ is 1D-unstable. The pattern with $\bar{u} = u_0^-$ may undergo the Hopf bifurcation and is 1D-stable if $C_1 < Z(C_2)$.

For a schematic representation of the stability results in different scaling regimes from Theorem 5.4.2, see Figure 5.12.

Theorem 5.4.3. Let the assumptions **A1** and **A3** be satisfied and let $\beta \geq \frac{2}{3}(\gamma - 1)$. Let (U_0, V_0) be a slow/fast periodic solution of (5.2) in one spatial dimension with wave length of $\mathcal{O}(\frac{1}{\delta^{1+\gamma-\frac{1}{2}\beta}})$. That is, let (U_0, V_0) be $(U_{p,s}, V_{p,s})$ as established in Theorem 5.3.1 without the trivial extension in the y -direction. The 1D-stability of this pattern can be summarized as follows.

- (i) If $\beta < \gamma - \frac{1}{2}$, there is a solution to (5.42) with $\Re(\hat{\lambda}) > 0$, so (U_0, V_0) is 1D-unstable.
- (ii) If $\beta > \gamma - \frac{1}{2}$ and $\beta < 2\gamma$, all eigenvalues $\hat{\lambda}$ corresponding to pattern (U_0, V_0) have negative real part, so the pattern is 1D-stable.
- (iii) If $\beta = \gamma - \frac{1}{2}$ and $\beta < 2\gamma$, then a pair of eigenvalues $\hat{\lambda}_{1,2}$ passes through the imaginary axis (i.e. a Hopf bifurcation occurs) if $C_1 = 2H^*$. Here, H^* is

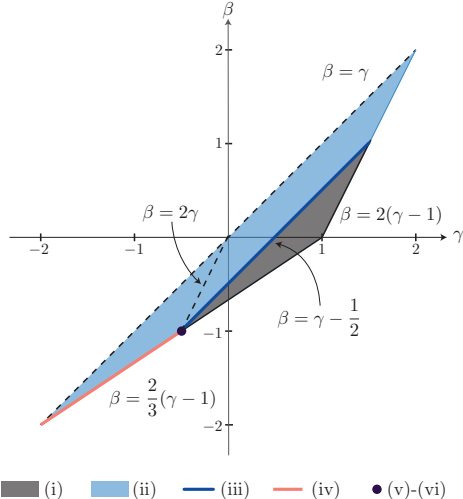


Figure 5.12: Schematic representation of 1D-stability regimes as described in Theorems 5.4.2 and 5.4.3. The shaded regimes are the regimes in the (γ, β) -plane where stripe patterns exist, defined by assumptions **A1**, **A3** and $\beta \geq \frac{2}{3}(\gamma - 1)$. Stripe patterns with scaling parameters in the gray shaded areas are 1D-unstable. Stripe patterns with scaling parameters in the blue shaded area are 1D-stable. Stripe patterns with scaling parameters on the borders may undergo a bifurcation when parameters change as described in Theorem 5.4.2. The regimes (i)–(vi) correspond to the subresults with the same labels in Theorem 5.4.2, and the regimes (i)–(iii) with those of Theorem 5.4.3.

given as the explicit solution of an expression in terms of hypergeometric functions, and $H^* \approx 0.661$. For $C_1 < 2H^*$, the pattern (U_0, V_0) is 1D-stable.

Note that the cases (i)–(iii) of Theorem 5.4.3 do not cover the entire triangular scaling regime defined by assumptions **A1–A3** and Figure 5.2, due to the extra assumptions $\beta < 2\gamma$ in cases (ii) and (iii). This is associated with the validity regime of the slow/fast approximation of the Evans function, and is explained in more detail in section 5.4.1.

Remark 5.3. In the case of the homoclinic pulses of Theorem 5.4.2, the fact that the operator is sectorial immediately establishes nonlinear stability if the pattern is spectrally stable, [36, 74]. We refrain from going into details about the nonlinear stability of the periodic patterns and two-dimensional patterns: stability statements in Theorem 5.4.3 and upcoming Corollary 5.4.5 concern only

spectral stability with respect to $\mathcal{O}(1)$ eigenvalues. This follows the approach of [34], and more details are reported in [31].

5.4.1 The Evans function and associated nonlinear eigenvalue problem

For the proof of Theorems 5.4.1–5.4.3, we establish an Evans function framework for the 1-pulse patterns, $(U_{\text{hom}}, V_{\text{hom}})$ constructed in section 5.2. In section 5.4.1 we will show how this framework can be in essence carried over to periodic patterns with periods of sufficient asymptotic length, after which we may proceed to section 5.4.2 for the proofs of the Theorems 5.4.1, 5.4.2. To make use of the slow/fast structure of the system in an efficient way, we will use the four-dimensional formulation of the stability problem, (5.45).

Homoclinic 1-pulse solutions

As an equivalent representation of (5.45), we write

$$\frac{\partial}{\partial \xi} \phi(\xi; \lambda, \ell) = \mathcal{A}(\xi; \lambda, \ell) \phi(\xi; \lambda, \ell), \quad (5.50)$$

where $\phi(\xi; \lambda, \ell) = (u(\xi), p(\xi), v(\xi), q(\xi))$, and \mathcal{A} is a 4×4 matrix. We will lay out the stability analysis in terms of the fast variable ξ . For ξ outside I_f , the solution v_0 is exponentially close to zero. Moreover, every term of (5.45) that involves u_0 , which varies outside the fast regime, is multiplied with v_0 . Hence, the matrix $\mathcal{A}(\xi; \lambda, \ell)$ approaches a constant matrix outside that fast regime;

$$\lim_{\xi \rightarrow \pm\infty} \mathcal{A}(\xi; \lambda, \ell) = \mathcal{A}_\infty(\lambda, \ell),$$

with

$$\mathcal{A}_\infty(\lambda, \ell) = \begin{pmatrix} 0 & \delta^{\gamma-\beta} \\ \delta^{2-\gamma+\beta} [\delta^{2\gamma-\beta} a + b(\delta^{2\theta-\beta} \ell^2 + \lambda)] & -\delta^{1+\gamma-\beta} (\delta^{\frac{1}{2}\beta} c + \delta^{1+\gamma-\beta} s) \\ 0 & 0 \\ 0 & 0 \\ b(\lambda + 1 + \delta^{2+2\theta-\beta} \ell^2) & -\delta^{2(\gamma-\beta)} s \end{pmatrix} \quad (5.51)$$

The matrix \mathcal{A}_∞ has four eigenvalues $\Lambda_{1,2,3,4}$. Two of those eigenvalues are asymptotically small and two are $\mathcal{O}(1)$. Their leading order approximations are,

$$\begin{aligned}\Lambda_1 &= \sqrt{b(\lambda + 1 + \delta^{2+2\theta-\beta}\ell^2)} + \text{h.o.t.} \\ \Lambda_2 &= \frac{1}{2}\delta^{1+\gamma-\frac{1}{2}\beta} \left[-c + \sqrt{c^2 + 4a + 4\delta^{\beta-2\gamma}(\delta^{2\theta-\beta}b\ell^2 + b\lambda)} \right] + \text{h.o.t.} \\ \Lambda_3 &= \frac{1}{2}\delta^{1+\gamma-\frac{1}{2}\beta} \left[-c - \sqrt{c^2 + 4a + 4\delta^{\beta-2\gamma}(\delta^{2\theta-\beta}b\ell^2 + b\lambda)} \right] + \text{h.o.t.} \\ \Lambda_4 &= -\sqrt{b(\lambda + 1 + \delta^{2+2\theta-\beta}\ell^2)} + \text{h.o.t.}\end{aligned}\tag{5.52}$$

Assumptions **A1–A3** and (5.46), imply that indeed $\Lambda_{2,3} \ll 1$, while $\Lambda_{1,4} = \mathcal{O}(1)$. Furthermore, the eigenvalues $\Lambda_{1,2}$ have by definition positive real part and are unstable, while $\Lambda_{3,4}$ have negative real part and are stable. The corresponding eigenvectors are

$$\begin{aligned}E_{1,4} &= (0, 0, 1, \Lambda_{1,4})^T, \\ E_{2,3} &= (1, \delta^{\beta-\gamma}\Lambda_{2,3}, 0, 0)^T.\end{aligned}\tag{5.53}$$

The essential spectrum associated with (5.50) coincides with all $\lambda(\ell)$ for which \mathcal{A}_∞ has an eigenvalue $\Lambda_i \in i\mathbb{R}$, that is,

$$\sigma_{\text{ess}} = \bigcup_{k,\ell \in \mathbb{R}} \left\{ -1 - \delta^{2+2\theta-\beta}\ell^2 - k^2, \frac{1}{4\delta^{\beta-2\gamma}b}(-4a - 4\delta^{2\theta-2\gamma}b\ell^2 + 2cik - k^2) \right\}\tag{5.54}$$

Depending on whether $\beta \gtrless 2\gamma$, the maximal real part of the essential spectrum is -1 or $-\delta^{2\gamma-\beta}\frac{a}{b}$, see a schematic representation of both cases in \mathbb{C} in 5.13. The full linear stability problem (5.50), has four independent (vector-)solutions $\phi_j(\xi; \lambda, \ell)$. The theory in [35, 36] explains that we may introduce eigenvectors ϕ_j such that,

$$\begin{aligned}\lim_{\xi \rightarrow -\infty} \phi_j(\xi, \lambda, \ell) e^{-\Lambda_j \xi} &= E_j \quad \text{for } j = 1, 2, \\ \lim_{\xi \rightarrow \infty} \phi_j(\xi, \lambda, \ell) e^{-\Lambda_j \xi} &= E_j \quad \text{for } j = 3, 4.\end{aligned}\tag{5.55}$$

In particular, this implies that $\phi_{1,2} \rightarrow (0, 0, 0, 0)$ as $\xi \rightarrow -\infty$ and $\phi_{3,4} \rightarrow (0, 0, 0, 0)$ as $\xi \rightarrow \infty$. Because Λ_1 is the largest, positive eigenvalue, a general solutions ϕ

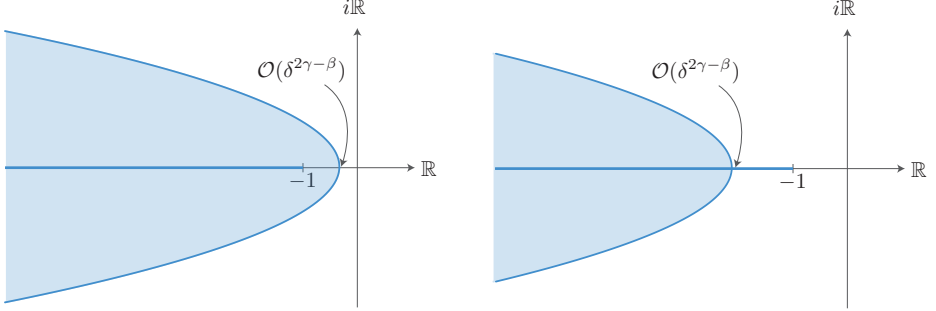


Figure 5.13: Schematic representation of the essential spectrum, (5.54) in \mathbb{C} . On the left, the case that $2\gamma > \beta$, so the maximal real part of the essential spectrum is $-\delta^{2\gamma-\beta} \frac{a}{b}$. On the right the case $2\gamma < \beta$, so the maximal real part of the essential spectrum is -1 .

will grow as $e^{\Lambda_1 \xi}$ as $\xi \rightarrow \infty$. We define the *fast transmission function* $t_f(\lambda, \ell)$, which is an analytic function over λ as,

$$\lim_{\xi \rightarrow \infty} \phi_1(\xi; \lambda, \ell) e^{-\Lambda_1 \xi} = t_f(\lambda, \ell) E_1(\lambda, \ell). \quad (5.56)$$

Not all ϕ_i necessarily grow with the largest rate, though. In the case that $t_f(\lambda, \ell) \neq 0$, we can define ϕ_2 uniquely by assuming it does not grow like $e^{\Lambda_1 \xi}$, i.e.

$$\lim_{\xi \rightarrow \infty} \phi_2(\xi; \lambda, \ell) e^{-\Lambda_1 \xi} = (0, 0, 0, 0)^T. \quad (5.57)$$

In other words, the only vector solution that grows with the fast rate as $\xi \rightarrow \infty$ is $\phi_1(\xi)$, because (5.55) has already put a boundary condition on ϕ_2 and ϕ_3 . A detailed justification of this procedure follows especially from Lemma 3.7 in [35]. Generically, the behavior of the second solution ϕ_2 is dominated by the slow growth rate Λ_2 for $\xi > 0$. Hence, we define a *slow transmission function*, $t_s(\lambda, \ell)$.

$$\lim_{\xi \rightarrow \infty} \phi_2(\xi; \lambda, \ell) e^{-\Lambda_2 \xi} = t_s(\lambda, \ell) E_2(\lambda, \ell). \quad (5.58)$$

The Evans function is the determinant of the four independent solutions of \mathcal{A}_∞ ,

$$\mathcal{D}(\lambda, \ell) = \det [\phi_1, \phi_2, \phi_3, \phi_4] e^{-\int_0^\xi \text{Tr}(\mathcal{A}(\eta; \lambda, \ell)) d\eta}, \quad (5.59)$$

see [35]. The Evans function is only defined for λ outside of the essential spectrum, (5.54). Since

$$\text{Tr}(\mathcal{A}(\eta; \lambda, \ell)) = \sum_j \Lambda_j = -\delta^{2(\gamma-\beta)} s,$$

and because the Evans function is independent of ξ , see [1], (5.59) is equivalent to,

$$\begin{aligned} \mathcal{D}(\lambda, \ell) &= \lim_{\xi \rightarrow \infty} \det [\phi_1 e^{-\Lambda_1 \xi}, \phi_2 e^{-\Lambda_2 \xi}, \phi_3 e^{-\Lambda_3 \xi}, \phi_4 e^{-\Lambda_4 \xi}] \\ &= \det [t_f(\lambda, \ell) E_1(\lambda, \ell), t_s(\lambda, \ell) E_2(\lambda, \ell), E_3(\lambda, \ell), E_4(\lambda, \ell)] \quad (5.60) \\ &= \delta^{\beta-\gamma} t_s(\lambda, \ell) t_f(\lambda, \ell) ((\Lambda_4 - \Lambda_1)(\Lambda_3 - \Lambda_2)), \end{aligned}$$

to leading order. Zeros of the Evans function coincide with eigenvalues $\lambda(\ell)$. Since outside of the essential spectrum σ_{ess} , see (5.54), the Λ_i never coincide, we conclude that the Evans function is zero only if the product of the transmission functions, $t_s t_f$ is zero. For the fast transmission function, the zeros can simply be found in literature. The associated fast reduced stability problem, that can be obtained from (5.45) by taking the limit $\delta \rightarrow 0$ and setting $u \equiv 0$, is

$$v_{\xi\xi} + 2\bar{u}v_0v - b(\lambda + 1)v = 0. \quad (5.61)$$

Which equivalent to those reported in [35, 36, 143]. The fast isolated eigenvalues are

$$\lambda_f^0 = \frac{5}{4}, \quad \lambda_f^1 = 0, \quad \lambda_f^2 = -\frac{3}{4}. \quad (5.62)$$

Paradoxically, the positive eigenvalue λ_f^0 does not immediately imply instability of (u_0, v_0) , because the slow transmission is not analytic but merely meromorphic and has a pole at λ_f^0 , as we will show below. This zero-pole cancellation is explained in full detail in [35, 36]. In [35], it is also shown that N -pulses pick up the same fast eigenvalues but with multiplicity N , which are not canceled by the order 1 poles of the slow transmission function. Hence, N -pulses are unstable. For more details on this mechanism, see [38].

Zeros of the slow transmission function

We determine the zeros of the slow transmission function by matching the values of u and p in- and outside the fast interval I_f , see (5.21). The change in u and p is measured by the uniquely determined fundamental solution ϕ_2 . We know that it does not grow with the fast rate, see (5.57), so outside I_f and with $\xi > 0$,

$$\phi_2(\xi) = t_s e^{\Lambda_2 \xi} E_2 + \tilde{t}_s e^{\Lambda_3 \xi} E_3 + \tilde{t}_f e^{\Lambda_4 \xi} E_4,$$

where $\tilde{t}_{s,f}$ are also transmission functions of λ and ℓ . The Λ_4 -term does not contribute to the leading order behavior, however, because Λ_4 is large and negative. In fact, outside I_f , $e^{\Lambda_4 \xi}$ is already exponentially small. On the other side outside of I_f , where $\xi < 0$, we know by (5.55)

$$\phi_2(\xi) = e^{\Lambda_2 \xi} E_2,$$

up to exponentially small corrections. We measure the change of ϕ_2 over I_f from outside of I_f (in the slow regime) first. We define the slow difference function Δ_s as follows,

$$\Delta_s \begin{pmatrix} u \\ p \\ v \\ q \end{pmatrix} = \lim_{\xi \downarrow \delta^{-\mu}} (t_s e^{\Lambda_2 \xi} E_2 + \tilde{t}_s e^{\Lambda_3 \xi} E_3 + \tilde{t}_f e^{\Lambda_4 \xi} E_4) - \lim_{\xi \uparrow -\delta^{-\mu}} e^{\Lambda_2 \xi} E_2. \quad (5.63)$$

Upon assuming **A1–A3** and (5.46), we can always choose a $\mu > 0$ (recall (5.21)) such that

$$\begin{aligned} \Delta_s u &= t_s e^{\Lambda_2 \delta^{-\mu}} E_2 + \tilde{t}_s e^{\Lambda_3 \delta^{-\mu}} E_3 + \tilde{t}_f e^{\Lambda_4 \delta^{-\mu}} E_4 - e^{\Lambda_2 \delta^{-\mu}} E_2, \\ &= t_s + \tilde{t}_s - 1, \end{aligned} \quad (5.64)$$

to leading order. We know that during the fast transition, the u -component does not change (recall (5.45)), therefore

$$\tilde{t}_s = 1 - t_s.$$

Although u is constant even up to the second order corrections during the fast transition, p is not constant in the first correction, see (5.9). We also measure the change in p with the slow difference function,

$$\begin{aligned} \Delta_s p &= t_s e^{\Lambda_2 \delta^{-\mu}} \delta^{\beta-\gamma} \Lambda_2 + \tilde{t}_s e^{\Lambda_3 \delta^{-\mu}} \delta^{\beta-\gamma} \Lambda_3 + \tilde{t}_f e^{\Lambda_4 \delta^{-\mu}} \cdot 0 - e^{-\Lambda_2 \delta^{-\mu}} \delta^{\beta-\gamma} \Lambda_2, \\ &= \delta^{\beta-\gamma} (t_s - 1)(\Lambda_2 - \Lambda_3), \end{aligned} \quad (5.65)$$

to leading order. On the other hand, we can measure the change in p over the fast regime, much like section 5.2, equation (5.29). We define the fast difference function Δ_f as,

$$\begin{aligned}
 \Delta_f p &= \int_{I_f} p_\xi(\xi) d\xi, \\
 &= \delta^{\gamma-\beta} \int_{I_f} (v_0^2 u + 2\bar{u}v_0 v + \delta^{2+\beta} au + \delta^{2+2\theta-2\gamma+\beta} b\ell^2 u + \delta^{2-2\gamma+2\beta} b\lambda u \\
 &\quad - (\delta^{1+\frac{1}{2}\beta} c + \delta^{2+\gamma-\beta} s) u_\xi) d\xi,
 \end{aligned} \tag{5.66}$$

We use the fact that, at the boundary of I_f , the two difference functions must be equal; $\Delta_f p = \Delta_s p$. Moreover, as we are interested in zeros (and poles) of the slow transmission function, we set $t_s = 0$, so that

$$\delta^{\beta-\gamma}(\Lambda_3 - \Lambda_2) = \Delta_f p. \tag{5.67}$$

In the evaluation of $\Delta_f p$, we may choose $u = 1$, because it must be a constant and we use the one-parameter freedom of choice in determining an eigenfunction. If **A1–A3** and (5.46) are satisfied, we can always choose a μ as defined in (5.21) such that $\Delta_f p$ is, at leading order, purely associated with the fast variables, that is,

$$\Delta_f p = \delta^{\gamma-\beta} \int_{I_f} 2\bar{u}v_0(\xi)v(\xi) + v_0^2(\xi) d\xi, \tag{5.68}$$

In particular, this implies we must choose

$$0 < \mu < \min\{2 + 2\theta - 2\gamma + \beta, 2 - 2\gamma + 2\beta, \gamma - \beta, 1 + \gamma - \frac{1}{2}\beta\}. \tag{5.69}$$

See Figure 5.2 and take into account assumption (5.46) to verify that in our restricted regime for γ and β , we can always choose μ within this range.

Equation (5.68) does not stand on itself but is directly linked to the stability problem (5.50). Our slow eigenvalue problem thus becomes

$$\begin{cases} \delta^{2(\gamma-\beta)} \int_{I_f} 2\bar{u}v_0(\xi)v_{\text{in}}(\xi) + v_0^2(\xi) d\xi = \Lambda_3 - \Lambda_2, \\ v_{\text{in},\xi\xi} + (2\bar{u}v_0 - b(\lambda + 1))v_{\text{in}} = -v_0^2 \end{cases} \tag{5.70}$$

We can rewrite (5.70) into one equation: the so-called nonlinear eigenvalue problem (NLEP) as is used in [34],

$$v_{\xi\xi} + (2\bar{u}v_0 - b(\lambda + 1))v = \frac{2\delta^{2(\gamma-\beta)}\bar{u}v_0^2}{\delta^{2(\gamma-\beta)} \int_{I_f} v_0^2(\xi) d\xi - \Lambda_3 + \Lambda_2} \int_{I_f} v_0(\xi)v(\xi) d\xi. \tag{5.71}$$

Using (5.19), we derive

$$\int_{I_f} v_0^2(\xi) d\xi = \frac{6b\sqrt{b}}{\bar{u}^2}, \quad (5.72)$$

which simplifies equation (5.71),

$$\begin{aligned} & v_{\text{in},\xi\xi} + \left(\frac{3b}{\cosh^2\left(\frac{\sqrt{b}\xi}{2}\right)} - b(\lambda + 1) \right) v_{\text{in}} \\ &= \frac{\frac{27}{4}\delta^{2(\gamma-\beta)}b^3 \operatorname{sech}^2\left(\frac{\sqrt{b}}{2}\xi\right)}{\delta^{2(\gamma-\beta)}b\sqrt{b} - (\Lambda_3 - \Lambda_2)\bar{u}^2} \int_{I_f} \frac{v_{\text{in}}}{\cosh^2\left(\frac{\sqrt{b}}{2}\xi\right)} d\xi. \end{aligned} \quad (5.73)$$

Following [34], we transform equation (5.71) using the following substitutions,

$$\xi = \frac{2}{\sqrt{b}}t, \quad v_{\text{in}}(\xi) = y(t), \quad \lambda = \frac{1}{4}P^2 - 1. \quad (5.74)$$

We only consider $\operatorname{Re}(P) > 0$, to stay away from the essential spectrum, see (5.54) and Figure 5.13. To convert P into λ , we use the principal square root. Substituting (5.74) into (5.73) yields

$$y_{tt} + \left(\frac{12}{\cosh^2(t)} - P^2 \right) = \frac{K}{\cosh^4(t)} \int_{I_f} \frac{y(t)}{\cosh^2(t)} dt, \quad (5.75)$$

with

$$K = \frac{9\delta^{2(\gamma-\beta)}}{\delta^{2(\gamma-\beta)} + \frac{\bar{u}^2(\Lambda_2 - \Lambda_3)}{6b\sqrt{b}}}. \quad (5.76)$$

Following [34], the differential equation for y can be modified to a hypergeometric differential equation for $G(x)$ with a second substitution,

$$y(t) = G(t)/(\cosh(t))^P, \quad t = \tanh^{-1}(2x - 1).$$

The exact derivation of the solutions of that hypergeometric differential equation is detailed in [34], and an alternative expression for K is derived,

$$K(P) = \frac{P(P-1)(P-2)(P-3)}{16\mathcal{R}(P)}, \quad (5.77)$$

where

$$\mathcal{R}(P) = \frac{-1}{(P+3)(P+2)(P+1)} \int_0^1 \int_0^\xi \xi(1-\xi) \left(\frac{x(1-\xi)}{\xi(1-x)} \right)^{P/2} k(P, 1-x) k(P, \xi) dx d\xi, \quad (5.78)$$

where $k(P, \xi)$ is defined as,

$$k(P, \xi) = (P-3)(P-2)(P-1) + 12(P-3)(P-2)\xi + 60(P-3)\xi^2 + 120\xi^3. \quad (5.79)$$

For consistency in K , we must equate (5.76) and (5.77), and we arrive at the final formulation of the eigenvalue problem.

$$\delta^{-2(\gamma-\beta)} (\Lambda_2 - \Lambda_3) \frac{\bar{u}^2}{6b\sqrt{b}} = \frac{9}{K(P)} - 1, \quad (5.80)$$

with $K(P)$ as in the formulation (5.77). The right hand side of (5.80) has poles of $\mathcal{O}(1)$ for $P = 1$ and $P = 3$, see Figure 5.14 and [34, 35]. They link directly to two of the fast eigenvalues (5.62), $\lambda_f^0 = \frac{5}{4}$ and λ_f^2 and hence the positive eigenvalue λ_f^0 does not necessarily destabilize the pattern. This phenomenon is often referred to as the ‘NLEP-paradox’ see [35].

Periodic solutions

In the previous section, we have derived equation (5.80) which determines the stability properties of a 1-pulse $(U_{\text{hom}}, V_{\text{hom}})$. In this subsection, we briefly comment on how the same equation determines stability of periodic solutions $(U_{\text{p},s}, V_{\text{p},s})$. For homoclinic solutions, which are localized, the eigenfunctions are localized as well. Hence, the full spectrum consists of discrete eigenvalues $\hat{\lambda}$ for given $\hat{\ell}$, united with the essential spectrum corresponding to the background state. Perturbations of periodic solutions are in general represented by both a wave number $\hat{\ell}$ as well as a $\hat{\gamma} \in S^1$, because the eigenfunctions are not localized. This implies that the eigenvalues $\hat{\lambda}$ outside σ_{ess} , see (5.54), are not discrete for a given $\hat{\ell}$. Instead, there exist curves of essential spectrum parametrized by $\hat{\gamma}$, [51].

For periodic solutions with a sufficient length, these $\hat{\gamma}$ -parametrized curves of spectrum may be exponentially approximated by the discrete eigenvalue corresponding to a localized pulse, because the periodic solution is ‘nearly’ localized. The period of the solutions constructed in section 5.3, has a length of $\mathcal{O}(\frac{1}{\delta^{\gamma-\frac{1}{2}\beta+1}})$ in ξ . If we assume that $q(0) = 0$ we can construct a fundamental interval for the periodic solution as

$$I_{\text{per}} = \left(-\frac{l}{\delta^{\gamma-\frac{1}{2}\beta+1}}, \frac{l}{\delta^{\gamma-\frac{1}{2}\beta+1}} \right),$$

with $l > 0$. The eigenfunctions (U, V) of (5.42) corresponding to a periodic solution $(U_{\text{per},s}, V_{\text{per},s})$ may then be called nearly localized if both U and V are exponentially small on the boundaries of I_{per} . For the V -pulse, this is clear, because V decays exponentially fast to zero already within the fast interval I_f , which is smaller than I_{per} . What is left is to verify that the decay rate of U is also fast enough. About this decay rate and the validity of the approximation, we formulate the following lemma.

Lemma 5.4.4. *For periodic solutions of (5.2) as constructed in section 5.3, with wave length of $\mathcal{O}\left(\frac{1}{\delta^{1+\gamma-\frac{1}{2}\beta}}\right)$, we may approximate the spectrum outside σ_{ess} by the discrete values that are solutions to (5.80) in any of the following regimes.*

- (i) $\beta < 2\gamma$;
- (ii) $\beta \geq 2\gamma$ and $\gamma - \frac{1}{2}\beta - 1 < \theta < \gamma$.

Proof. To show this, we will work with the rescaled coordinates and system (5.45). Outside the fast interval I_f , the equation for u decouples because v is exponentially small. We obtain,

$$u_{\xi\xi} = \delta^{2\gamma-2\beta} \left[\delta^{2+\beta} au + (\delta^{2+2\theta+\beta-2\gamma} \ell^2 + \delta^{2+2\beta-2\gamma} \lambda) bu - \left(\delta^{1+\frac{3}{2}\beta-\gamma} c + \delta^2 s \right) u_\xi \right], \quad (5.81)$$

which is a second order ODE for u with constant coefficients. The solution for u is a linear combination of exponentials in variable $\delta^r \xi$, where

$$r = \min\{1, 1 + \gamma - \frac{1}{2}\beta, 1 + \theta - \frac{1}{2}\beta\}, \quad (5.82)$$

is the decay rate of u . If we require u to be exponentially small on the boundaries of I_{per} , which is $\mathcal{O}\left(\frac{1}{\delta^{1+\gamma-\frac{1}{2}\beta}}\right)$, we must satisfy

$$1 + \gamma - \frac{1}{2}\beta > r = \min\{1, 1 + \gamma - \frac{1}{2}\beta, 1 + \theta - \frac{1}{2}\beta\} \quad (5.83)$$

In other words, the length of the fundamental interval I_{per} must be asymptotically strictly larger than the decay of u . If we want to exponentially approximate the spectrum corresponding to periodic solutions by discrete eigenvalues, condition (5.83) must be satisfied. Note that the strict inequality (5.83) can never be satisfied if $r = 1 + \gamma - \frac{1}{2}\beta$, the same parameter combination is stated on the left side of the inequality. This implies that if $\beta \geq 2\gamma$, a restriction must be put on θ so that $r = 1 + \theta - \frac{1}{2}\beta$, in order to satisfy (5.83). Combining this with condition

(5.46), this yields the result stated in (ii). If, on the other hand, $\beta < 2\gamma$, then $r \neq 1 + \gamma - \frac{1}{2}\beta$ and this immediately implies that (5.83) is satisfied, so we arrive at the statement of (i). \square

Since θ is only a dummy parameter restrictions on θ change the function space of perturbations against which we will test the (in)stability of periodic patterns. By condition (5.46), we put an upper bound on the transverse wave number of the perturbation. A consequence of Lemma 5.4.4 is that if $\beta \geq 2\gamma$, the stability statements derived from equation (5.80) for periodic solutions are only valid for a smaller subclass of perturbations. Namely, those perturbations that have a transverse wave number that is not only bounded below by (5.46), but also bounded above by requiring $\theta < \gamma$.

5.4.2 Proof of stability theorems

In this section, we analyze (5.80), to prove Theorems 5.4.1 and 5.4.2. The right-hand side of (5.80) is plotted as a graph over $P \in \mathbb{R}$ in Figure 5.14. Note

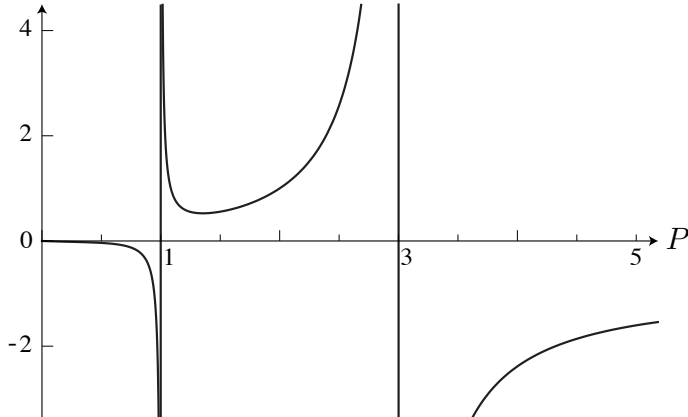


Figure 5.14: Black: Graph of $\frac{9}{K(P)} - 1$ with $P > 0$ and real-valued. Note that there are vertical asymptotes at $P = 1$ and $P = 3$. These are the poles of the slow transmission function, and they cancel two of the zeros of the fast transmission function, λ_f^0 and λ_f^2 , see (5.62).

that, as $\lambda \in \mathbb{C}$, so is P . The representation of Figure 5.14 is therefore not exhaustive. Note that, indeed, the graph is singular at $P = 1$ and $P = 3$, where the function has poles of order 1. In the cases that λ is real, however, the solutions of (5.80) may be visualized as the intersections of the graph in Figure 5.14 and a real-valued curve of the left hand side of (5.80) as a function over P . We clarify

this in the proofs of the Theorems 5.4.1–5.4.3. As was already obvious from their formulations, the magnitude of $\Lambda_{2,3}$ makes a crucial difference. From (5.52) which we derive

$$\Lambda_2 - \Lambda_3 = \delta^{1+\gamma-\frac{1}{2}\beta} \sqrt{c^2 + 4a + 4b(\delta^{2\theta-2\gamma}\ell^2 + \delta^{\beta-2\gamma}\lambda)}. \quad (5.84)$$

Note that

$$\mathcal{O}(\Lambda_2 - \Lambda_3) = \mathcal{O}(\delta^r), \quad (5.85)$$

where r was defined in (5.82).

Proof. (of Theorem 5.4.1).

If the left hand side of equation (5.80) is much larger than $\mathcal{O}(1)$, there are solutions for $P \gtrapprox 1$ and $P \lesssim 3$, because the right hand side has poles for $P = 1$ and $P = 3$. By choosing θ appropriately, namely

$$\theta < 2\gamma - \frac{3}{2}\beta - 1, \quad (5.86)$$

we obtain $r < 2(\gamma - \beta)$, so that the left hand side of (5.80) is asymptotically large. That implies that there is always a $\hat{\ell}$ such that there exists a solution $P \lesssim 3$, which corresponds to $\lambda = \frac{5}{4}$. Note that condition (5.46) is automatically satisfied in this case. Hence, perturbations with a transverse wave number that is small enough grow exponentially, so the patterns are 2D-unstable. This result holds for both the 1-pulse and periodic solutions, because (5.86) implies by assumption **A2** that $\theta < \gamma$, see Lemma 5.4.4. \square

Proof. (of Theorem 5.4.2)

This theorem concerns only patterns in one spatial dimension. Hence, we do not consider transverse perturbations so we may set $\ell = 0$ in equation (5.80) or, more specifically, (5.84). This simplifies equation (5.80) to

$$\delta^{1-\gamma+\frac{3}{2}\beta} \sqrt{c^2 + 4a + 4\delta^{\beta-2\gamma}b\lambda} \frac{\bar{u}^2}{6b\sqrt{b}} = \frac{9}{K(P)} - 1. \quad (5.87)$$

- (i) If $\beta < \gamma - \frac{1}{2}$ and $\beta \geq \frac{2}{3}(\gamma - 1)$, then the left hand side of (5.80) is much larger than $\mathcal{O}(1)$, so the same argument as in the proof of Theorem 5.4.1 applies. There is an eigenvalue $\lambda \lesssim \frac{5}{4}$, so the solution is 1D-unstable.
- (ii) If $\beta > \gamma - \frac{1}{2}$ and $\beta > \frac{2}{3}(\gamma - 1)$, the left hand side of (5.80) is asymptotically small. Thus, we solve

$$0 = \frac{9}{K(P)} - 1.$$

By a numerical evaluation of the analytic expressions (5.76)–(5.79), we find that this occurs for $P \approx 0.56 \pm 0.52i$ or $\lambda \approx -0.99 \pm 0.14i$. Hence, the pattern is 1D-stable.

- (iii) If $\beta = \gamma - \frac{1}{2}$ and $\beta > \frac{2}{3}(\gamma - 1)$, recall the definition of C_1 in (5.47), so that the leading order of equation (5.87) becomes

$$\frac{1}{2}C_1 = \frac{1}{\sqrt{P^2 - 4}} \left(\frac{9}{K(P)} - 1 \right), \quad (5.88)$$

which is equivalent to equation (5.15) of [34]. Thus, there is a Hopf bifurcation when this equation is solved for a purely imaginary set of eigenvalues λ_{\pm} . Using numerical evaluation we can derive immediately that this occurs when

$$\frac{1}{2}C_1 = H^* \approx 0.661,$$

at which $\lambda \approx \pm 0.535i$. This implies that the pattern is 1D-stable for $C_1 < 2H^*$ and 1D-unstable for $C_1 > 2H^*$. Since we know that in this case $\bar{u} = u_0 = \frac{6b\sqrt{b}}{\sqrt{c^2 + 4a}}$ (see 5.30), we can simplify this to

$$\sqrt{\frac{b}{c^2 + 4a}} < 2H^*.$$

This proves this part of the theorem.

- (iv) If $\beta > \gamma - \frac{1}{2}$ and $\beta = \frac{2}{3}(\gamma - 1)$ equation (5.80) reduces to leading order to,

$$C_1 \sqrt{C_2} = \frac{9}{K(P)} - 1. \quad (5.89)$$

The left hand side of this equation does not depend on λ and is always real-valued. The stability of a pattern changes if the real part of an eigenvalue λ passes zero. The special case $\lambda = 0$ corresponds to $P = 2$, and a simple check with [34] yields

$$\lim_{P \rightarrow 2} \frac{9}{K(P)} - 1 = 1. \quad (5.90)$$

Which implies that (5.89) is solved for a zero eigenvalue if

$$C_1 \sqrt{C_2} = 1.$$

Hence, this is where a bifurcation occurs. A straightforward verification yields that the pattern is 1D-stable if $C_1 \sqrt{C_2} < 1$, and 1D-unstable if

$C_1\sqrt{C_2} > 1$. Since this is the case that $\beta = \frac{2}{3}(\gamma - 1)$, we use solutions u_0^\pm of (5.35) for \bar{u} . That implies that

$$C_1^\pm = \frac{\left(1 \pm \sqrt{1 - \frac{24b\sqrt{b}}{\sqrt{c^2+4a}}}\right)^2}{24b},$$

so the pattern is stable if,

$$\frac{\left(1 \pm \sqrt{1 - \frac{24b\sqrt{b}}{\sqrt{c^2+4a}}}\right)^2}{24b\sqrt{b}} \sqrt{c^2 + 4a} < 1,$$

which is always true for u_0^- , and never true for u_0^+ . Hence, the pattern with $\bar{u} = u_0^-$ is in this case always 1D-stable, and the pattern with $\bar{u} = u_0^+$ is always 1D-unstable. This concludes the proof of part (iv) of the theorem.

For cases (v) and (vi) we have $\beta = -1$ and $\gamma = -\frac{1}{2}$, we rewrite the leading order terms of equation (5.87) to

$$C_1 = \frac{1}{\sqrt{P^2 - 4 + C_2}} \left(\frac{9}{K(P)} - 1 \right). \quad (5.91)$$

Recall also the values (5.35) for \bar{u} and the existence requirement (5.34). While C_1 is real-valued, $P \in \mathbb{C}$. We use MATHEMATICA to solve for which values of P the right hand side of (5.91) is real-valued, and plot its values against the real part of these values of P . For several values of C_2 , we have illustrated this in Figure 5.15. The P -values of intersections of the left and right side of (5.91), correspond to eigenvalues λ via (5.74). Regardless of the value of C_2 , there is an asymptote at $P = 3$ ($\lambda = \frac{5}{4}$). Hence, a stability criterion is always an upper limit for C_1 . On the other hand, as C_1 approaches 0, equation (5.91) approaches case (ii) of this theorem and the pattern is stable for every C_2 of $\mathcal{O}(1)$. Hence, there is always a bifurcation, although the nature of it may vary. A transition between a Hopf bifurcation or a zero eigenvalue occurs when the minimum of the right hand side of (5.91) for real-valued P occurs exactly at $P = 2$. That happens for

$$C_2 = C_2^* = -\frac{9}{2K'(2)} \approx 1.333,$$

which separates the cases (v) and (vi).

- (v) This case occurs if $C_2 > C_2^*$ and (5.34) is satisfied. That implies

$$\frac{24b\sqrt{b}}{\sqrt{c^2 + 4a}} < \min \left\{ \frac{24b}{\sqrt{C_2^*}}, -1 \right\}. \quad (5.92)$$

If $C_2 > C_2^*$, the right hand side of (5.91) is real-valued in a neighborhood of $P = 2$. Hence, there is a bifurcation with a zero eigenvalue. We use (5.90) to derive that the pattern is 1D-stable if

$$C_1 < \frac{1}{\sqrt{C_2}},$$

and 1D-unstable if $C_1 > \frac{1}{\sqrt{C_2}}$. A straightforward computation yields that the pattern with $\bar{u} = u_0^+$ never satisfies this case but undergoes a saddle-node bifurcation when it collides with u_0^- , i.e. when (5.34) is equality. The pattern with $\bar{u} = u_0^-$, is always stable, apart from that same bifurcation point.

- (vi) Using both conditions $C_2 \leq C_2^*$ and (5.34), we derive that case (vi) occurs for

$$\frac{24b}{\sqrt{C_2^*}} \leq \frac{24b\sqrt{b}}{\sqrt{c^2 + 4a}} \leq 1,$$

which is only a nonempty range if $b \leq \frac{\sqrt{C_2^*}}{24} \approx 0.048$. In this case, destabilization occurs through a Hopf bifurcation. For $\text{Re}(P) > 0$, P has nonzero imaginary part if and only if λ has nonzero imaginary part. If $\lambda = i\kappa$ with $\kappa \in \mathbb{R}$, i.e. at the bifurcation point, $P = 2\sqrt{i\kappa + 1}$, see (5.74). We substitute $P = 2\sqrt{i\kappa + 1}$ in (5.91) and for every C_2 , we solve for which κ the right hand side of (5.91) has zero imaginary part,

$$\text{Im} \left(\frac{1}{\sqrt{4i\bar{\kappa}(C_2) + C_2}} \left(\frac{9}{K \left(2\sqrt{i\bar{\kappa}(C_2) + 1} \right)} - 1 \right) \right) = 0. \quad (5.93)$$

This yields a curve that assigns to every $C_2 \in (0, C_2^*)$ the value of the right hand side of (5.91) at the Hopf bifurcation, see the right panel of Figure 5.14, which is exactly the function $Z(C_2)$ defined in (5.49). A 1D-stability requirement is then,

$$C_1 < Z(C_2),$$

where equality coincides with the Hopf bifurcation. The value of the eigenvalues as function of C_2 is depicted in Figure 5.16, where we see that $C_2 \downarrow 0$ returns the same result as described in case (iii) of this theorem.

□

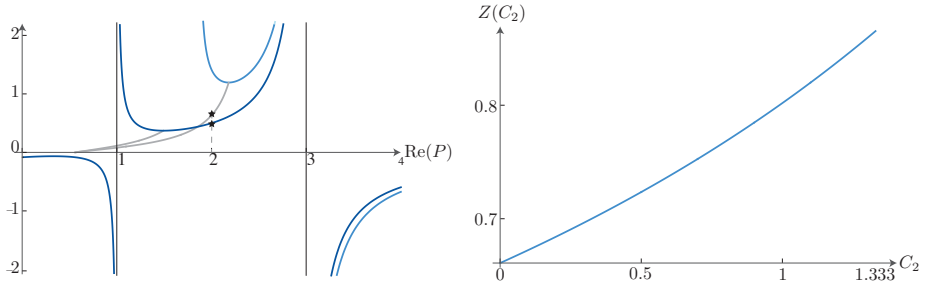


Figure 5.15: Left: Two times the graph of the right hand side of (5.91) for two values of C_2 , for values of $P \in \mathbb{C}$ for which the expression equals a value in \mathbb{R} , plotted against the real part of the corresponding P . When P has nonzero imaginary part, the graph is gray. Dark blue corresponds to $C_2 = 4$, while lighter blue corresponds to $C_2 = 0.5$. The stars indicate where the intersections with $P = 2$ are, i.e. at the bifurcation point. Right: The function $Z(C_2)$ (see (5.49)) for those values of C_2 for which $Z(C_2)$ is real-valued, and with $\bar{\kappa}$ for $C_2 \in (0, C_2^*)$.

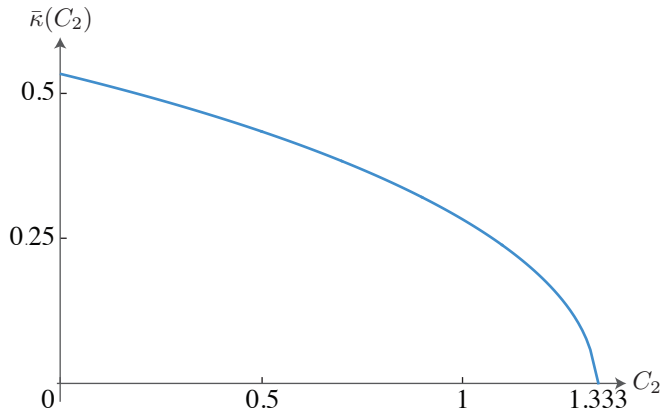


Figure 5.16: The function $\bar{\kappa}$ for $C_2 \in (0, C_2^*)$, which assigns to every C_2 the imaginary part of the eigenvalues at the Hopf bifurcation.

Proof. (of Theorem 5.4.3). In Theorem 5.4.3, the only change compared to Theorem 5.4.2 is that this concerns periodic solutions with long wave lengths. Following Lemma 5.4.4, the results for the 1-pulse may be carried over to this situation exactly if $\beta < 2\gamma$. The case (ii) of that lemma does not apply, because for one spatial dimension there is no parameter θ . Selecting exactly those parameter

regimes that satisfy $\beta < 2\gamma$, yields the results stated in the theorem. \square

The results of the Theorems 5.4.1 is derived from testing the stability of solutions (U_0, V_0) of (5.2) against perturbations in two dimensions. Of these perturbations, the wave number of the transverse perturbation factor may be arbitrarily small, but has an upper bound defined by (5.46). The Theorems 5.4.2 and 5.4.3, however, consider only patterns with one spatial dimension and hence perturbations in only one space variable. If, however, we consider a more restrictive function space for perturbations in two spatial dimensions, we may carry over the results of Theorems 5.4.2 and 5.4.3 to two-dimensional stability.

Corollary 5.4.5. *Let the assumptions **A1** and **A3** be satisfied and let $\beta \geq \frac{2}{3}(\gamma - 1)$. Let (U_0, V_0) be a slow/fast 1-pulse solution of (5.2), trivially extended in the y direction. Let X be the function space spanned by perturbations*

$$e^{i\hat{\ell}} (\hat{u}(\chi), \hat{v}(\chi)),$$

with $\hat{\ell} \ll \delta^{2\gamma - \frac{3}{2}\beta - 1}$. Then, the statements of Theorem 5.4.2 summarize the two-dimensional stability of (U_0, V_0) against functions space X .

Let (U_0, V_0) be a slow/fast periodic solution of (5.2), trivially extended in the y direction. Then, the statements of Theorem 5.4.3 summarize the two-dimensional stability of (U_0, V_0) against functions space X .

Proof. The proof follows immediately from the observation that if $\hat{\ell} \ll \delta^{2\gamma - \frac{3}{2}\beta - 1}$, $\theta \geq 2\gamma - \frac{3}{2}\beta - 1$, which is more restrictive than (5.46). The proof of Theorem 5.4.1 can no longer be applied. In fact, if the wave number is not too large, the leading order equation that determines the stability, (5.80), is (5.87). Hence, the results from Theorems 5.4.2 and 5.4.3 follow. \square

The Theorems 5.4.1–5.4.3 particularize the 2D-instability and 1D-stability results for a range of parameter and scaling regimes. Since the results are concluded from the Evans function that was derived in section 5.4.1 for 1-pulses and where it was explicitly used that the function has a slow/fast splitting, our results are not exhaustive. If wave numbers become too large (i.e. when (5.46) is violated), equation (5.80) does not describe the leading order approximation of the eigenvalues. In fact, it can be shown that the unstable eigenvalue $\lambda(\ell)$ of (the proof of) Theorem 5.4.1 become negative as ℓ increases further, see also [42]. Similarly, if $\beta > 2\gamma$, the constructed periodic solutions cannot be considered ‘nearly’ localized, and therefore the associated spectrum cannot be approximated by discrete values united with σ_{ess} . In that case, the stability problem is similar to that of the periodic solutions of the Gierer-Meinhardt equations, see [157]. A full analysis of this case is, however, not part of the present article.

5.5 Conclusions and ecological implications

The need for a mathematical framework to study vegetation patterns has been acknowledged at least since [88, 133, 58]. So far, in various mathematical models, both analytic and numerical results have been derived, [58, 88, 133, 142, e.g.]. However, the trade-off between manageable analytics and a realistic model is ever apparent. In the original Klausmeier, (5.1), or the Gray-Scott model, the existence of patterns has been thoroughly studied and reported in [88] and [34, 39, e.g.]. With the introduction of the generalized Klausmeier-Gray-Scott model in [159], the combination of water diffusion (Gray-Scott) with the advective term induced by a gentle slope (Klausmeier) came forth to be quite effective. In more recent times, both analytic and numerical results about solutions and pattern formation in the gKGS system have been published, [159, 145, 143]. Apart from the intrinsic value of homoclinic or periodic pulse solutions of the gKGS system, they also form the foundation for complex pattern dynamics as, for example, pulse interactions. Still, rigorous results on the existence and stability of traveling slow/fast solutions of neither homoclinic nor periodic type have been reported in the literature.

In this article, we have explored the existence and stability of traveling stripe patterns of the generalized Klausmeier-Gray-Scott(5.2). They arise as multiscale pulse patterns in one spatial dimension, trivially extended in the other direction. The scaling of parameters and coordinates in this derivation is nontrivial and crucial to our analysis, and we present it in its most general form.

The existence of traveling single pulse solutions is established using geometric singular perturbation theory. Such a traveling homoclinic solution corresponds to a single strip of vegetation in an elsewhere endless desert: a traveling oasis. Perhaps more realistic are the periodic patterns that were constructed in section 5.3. The stripe patterns that correspond to these solutions are widely observed and in the field of ecology also known as tiger bushes [171]. Both types of solutions have a positive speed, indicating that the patterns travel uphill. This phenomenon is confirmed by observations, and can be explained by a surplus of water on the upper side of a vegetation strip. For homoclinic traveling waves, the values (5.30) imply that as the slope c decreases, the speed of the homoclinic traveling wave also decreases. This is in agreement with the Gray-Scott results, see section 5.1.1, where stationary pulses exist on flat terrain ($c = 0$). Note that as the rainfall, parametrized by a , decreases, the speed decreases. Furthermore, the water density value in the vegetation strip is smaller in the case of a traveling oasis (u_0) compared to traveling periodic patterns for the same set of parameters.

There are several destabilization mechanisms described by the Theorems 5.4.1–5.4.3. Theorem 5.4.1 describes that in the validity regime of our analysis,

defined by assumptions **A1–A3**, there is always a range transverse wave number of perturbations that destabilize the pattern. In other words, stripe patterns will cease to exist, as soon as the perturbations along the vegetation strip have a transverse wave number that is within this regime. Since the scaling regime bounds the slope of the terrain, c , this is in agreement with [143], where two-dimensional stripe patterns are numerically found to be stable only above a certain threshold for the slope. Since we only consider patterns that are trivially extended, it is not yet clear if the patterns will in fact collapse to a desert state. Considering the observations of rhombic or spot patterns, one may suggest that a large wave number perturbation could generate nontrivial two-dimensional patterns, as is also confirmed by the numerical simulations in [143]. If we consider a more ‘mild’ definition of stability, with perturbations in a well-chosen function space, we can make more detailed conclusions about the resilience of stripe patterns, formulated in Corollary 5.4.5.

The Theorems 5.4.2 and 5.4.3 describe stability of homoclinic and periodic patterns, with respect to one-dimensional (non-transversal) perturbations, respectively. In absence of transverse perturbations, the patterns may indeed be stable and several destabilization mechanisms take place as parameters vary. In the cases (iii)-(vi) in Theorem 5.4.2 and case (iii) in 5.4.3, destabilization occurs as C_1 (defined in (5.47)) grows. Reversely, the patterns are stable as long as C_1 is small enough. Since C_1 is minimal for the homoclinic 1-pulse, because u_0 is smaller than $u_{p,h}^*$, the homoclinic 1-pulse is the last pattern to destabilize, i.e. ‘the most stable pattern’. This is completely in agreement with Ni’s conjecture, which was formulated for the Gierer-Meinhardt system in [120], see also [42, 157, 40]. This implies that, as either precipitation (a) or slope (c) decreases, periodic solutions with the larger water density in the vegetation strip destabilize first and the traveling oasis is the last observable pattern. Although this also confirms the numerical observations of [143, 145, 159], it should be remarked that the present analysis only holds for the validity regime of our method, which is characterized by the splitting of fast and slow behavior in the system and defined by **A1–A3**. Furthermore, our analysis is only valid for patterns that are ‘nearly localized’, i.e. that the pattern is a homoclinic pattern or that Lemma 5.3.2 holds. Outside this regime, extra measures are necessary to draw conclusions about the stability (and the existence) of stripe patterns.

The value of \bar{u} – the water density within a vegetated area – for periodic patterns is not explicitly determined in section 5.3, which makes the interpretation of the stability results of section 5.4 less straightforward. However, we do have a lower and upper bound for \bar{u} , namely,

$$\bar{u} \in (u_0, \tilde{u}) = \left(\frac{6b\sqrt{b}}{\sqrt{c^2 + 4a}}, \sqrt{\frac{6b\sqrt{b}}{s}} \right), \quad (5.94)$$

see (5.30) and (5.37). The upper bound can be carried over to C_1 to obtain, by Theorem 5.4.2(iii), a sufficient but not necessary condition for the stability of periodic patterns, namely

$$\frac{\sqrt{b}}{s} < 1.322, \quad (5.95)$$

see (5.88). In other words, it implies a lower bound for the migration speed of the periodic patterns. Together with the upper bound for s defined in (5.36), we have a range of s -values for which one-dimensional periodic patterns exist and are stable,

$$s \in \left(0.756\sqrt{b}, \frac{c\sqrt{c^2 + 4a}}{6b\sqrt{b}} \right). \quad (5.96)$$

This range is nonempty if $4.539b^2 \leq c\sqrt{c^2 + 4a}$. We conclude that even if a or c decreases, this does not have to destabilize the pattern, as long as it adapts to a suitable speed s , to satisfy the stability condition.

For all patterns constructed in this manuscript, we conclude that if a or c decreases the parameter regime in which patterns are stable shrinks, making them less resilient. A general conclusion we may draw is that decreasing rainfall or slope may have a serious negative impact on the ecological resilience of both homoclinic and periodic patterns. This is also confirmed by [32], where field observations show that stripe patterns disappear as the slope decreases.

In mathematical terms, we have considered the existence of homoclinic and spatially periodic slow/fast patterns in a reaction-advection-diffusion model. The advection term breaks the reversibility symmetry of the original reaction-diffusion system. Since this symmetry is a key feature of the establishment of especially the existence of these types of patterns in reaction-diffusion equations – Gray-Scott, Gierer-Meinhardt – several novel ideas have been introduced to incorporate the skew effects of the advection term in the geometric singular perturbation approach. We found that the symmetry breaking effect could be incorporated in the Evans function framework for spectral stability of the patterns in a natural way. Our stability results on one-dimensional patterns provide direct generalizations of previous results in the literature on reaction-diffusion models, see [34, 80, 157, 164]. Moreover, our result on the instability of stripes to the

transverse perturbations, Theorem 5.4.1, is similar to the findings in [42, 118, 143], to a class of reaction-advection-diffusion systems.

5.6 Discussion

In any article where mathematical models are used to describe a natural phenomenon, many simplifications need to be done to keep the work manageable. This, in turn, implies the need for a brief discussion of the conclusions drawn according to the simplified model. As mentioned before, our analysis does not extend beyond stripe patterns, and hence does not describe the widely observed gap or labyrinth patterns described in, for example, [61, 60]. Many of the assumptions made in this article cannot be made in the case where the pattern is not trivially extended in one spatial dimension. Perhaps another type of symmetry could resolve this. Furthermore, we did not incorporate nonlinear diffusion, nor did we examine a spatially dependent slope $C(x, y)$ or a nonconstant speed $S(t)$.

A more general, but prudent remark that should be made, is that the comparison of mathematical results with observation from the field remains to be a delicate task. We did not attempt to estimate the magnitude of parameters, let alone the values of the parameters themselves, from field data. The difficulties related to this data validation are also discussed in [144]. Of course, this makes it difficult to distinguish which of our conclusions drawn are relevant to the natural system it applies to, and which are interesting for the mathematical audience. Especially in the case of stability, it is not easily identified whether stability should indeed be tested against perturbations with all possible transverse wave numbers. Moreover, case (vi) of Theorem 5.4.3 is only valid for $b \lesssim 0.048$. It is not clear if this can be regarded as a valid result if b is assumed to be $\mathcal{O}(1)$ with respect to δ . A necessary continuation of this research should therefore analyze data, to confirm or reject the mathematical theory.

Finally, it should be explicitly noted that our analysis relies heavily on the scaling regimes. The clear advantages of this asymptotic approach is that we can explicitly determine the existence and stability regimes. The major drawback is, however, that we were not able to capture all types of stripe patterns. This could also be an explanation for the fact that we do not recover the stability results of [143], in which 2D-stable stripe patterns were reported for (a slightly rescaled version of) system (5.2) with large slopes. These large slopes may be described by parameters outside the triangular regime defined by assumptions **A1–A3**, and therefore cannot be fully understood by our analysis. However, since this [143] is to our awareness the first mathematical result in the literature that states that singular, far-from-equilibrium stripes may be stable, this challenging problem is intriguing, [42, 118]. Solving it requires a new mathematical approach that goes beyond the currently developed method for reaction-advection-diffusion systems.

This is the topic of ongoing research.

5.7 Acknowledgments

We gratefully acknowledge support from NWO through the NDNS+ cluster, and Robbin Bastiaansen for his help in establishing the simulations of Figure 5.1 and 5.7.

References

- [1] J. Alexander, R. Gardner, and C.K.R.T. Jones. A topological invariant arising in the stability analysis of travelling waves. *J. Reine. Angew. Math.*, 410:167–212, 1990.
- [2] W. Allee. *The Social Life of Animals*. Norton, New York, 1938.
- [3] M. B. Amar, C. Chatelain, and P. Ciarletta. Contour instabilities in early tumor growth models. *Phys. Rev. Lett.*, 106:148101, 2011.
- [4] D. Amor and R. Solé. Catastrophic shifts and lethal thresholds in a propagating front model of unstable tumor progression. *Phys. Rev. E*, 90:022710, 2014.
- [5] E. Angulo, E. Roemer, L. Berec, J. Gascoigne, and F. Courchamp. Double Allee effects and extinction in the island fox. *Conserv. Biol.*, 21:1082–1091, 2007.
- [6] R. Axelrod, D. Axelrod, and K. Pienta. Evolution of cooperation among tumor cells. *P. Natl. Acad. Sci. USA*, 103:13474–13479, 2006.
- [7] S. Balasuriya. Invasions with density-dependent ecological parameters. *J. Theor. Biol.*, 266:657–666, 2010.
- [8] S. Balasuriya and G. Gottwald. Wavespeed in reaction–diffusion systems, with applications to chemotaxis and population pressure. *J. Math. Biol.*, 61:377–399, 2010.
- [9] P. W. Bates and C.K.R.T. Jones. Invariant manifolds for semilinear partial differential equations. *Dynamics Reported*, vol 2 (*Series in Dynamical Systems* vol 2), pages 1 – 38, 1989.
- [10] N. Bellomo, A. Bellouquid, J. Nieto, and J. Soler. Multiscale biological tissue models and flux-limited chemotaxis for multicellular growing systems. *Math. Mod. Meth. Appl. S.*, 20:1179–1207, 2010.

- [11] E. Benoit, J. L. Callot, F. Diener, and M. Diener. Chasse au canards. *Collect. Math.*, 31:37–119, 1981.
- [12] J. Berger. Persistence of different-sized populations: an empirical assessment of rapid extinctions in bighorn sheep. *Conserv. Biol.*, 4:91–98, 1990.
- [13] A. Bertuzzi, A. Fasano, A. Gandolfi, and C. Sinigaglia. Necrotic core of EMT6/Ro tumour spheroids: is it caused by an ATP deficit? *J. Theor. Biol.*, 262:142–150, 2010.
- [14] K. Böttger, H. Hatzikirou, A. Voss-Böhme, E. A. Cavalcanti-Adam, M. A. Herrero, and A. Deutsch. An emerging Allee effect is critical for tumor initiation and persistence. *PLoS Comput. Biol.*, 11(9):e1004366, 2015.
- [15] R. Burrell, N. McGranahan, J. Bartek, and C. Swanton. The causes and consequences of genetic heterogeneity in cancer evolution. *Nature*, 501:338–345, 2013.
- [16] F H Busse. Non-linear properties of thermal convection. *Reports on Progress in Physics*, 41(12):1929–1967, 1978.
- [17] K. Böttger, H. Hatzikirou, A. Voss-Böhme, M.A. Cavalcanti-Adam, E.A. Herrero, and A. Deutsch. An emerging Allee effect is critical for tumor initiation and persistence. *PLoS Comput. Biol.*, 11(9):1–14, 09 2015.
- [18] J. Carr. *Applications of Centre Manifold Theory*. Applied Mathematical Sciences **35**. Springer-Verlag, 1981.
- [19] J.A. Castano, J.E. Pearson, W. Horsthemke, and Swinney H.L. Chemical pattern formation with equal diffusion coefficients. *Phys. Lett. A*, 124(6,7):320–324, 1987.
- [20] M. Chaplain, M. Lachowicz, Z. Szymanska, and D. Wrzosek. Mathematical modelling of cancer invasion: the importance of cell-cell adhesion and cell-matrix adhesion. *Math. Mod. Meth. Appl. S.*, 21:719–743, 2011.
- [21] W. Chen and M.J. Ward. Oscillatory instabilities of multispike patterns for the one-dimensional Gray–Scott model. *Eur. J. Appl. Math.*, 20:187 – 214, 2009.
- [22] W. Chen and M.J. Ward. The stability and dynamics of localized spot patterns in the two-dimensional gray-scott model. *SIAM Journal on Applied Dynamical Systems*, 10(2):582–666, 2011.

- [23] S.N. Chow and J.K. Hale. *Methods of Bifurcation Theory*. Grundlehren der Mathematischen Wissenschaften **251**. Springer–Verlag, 1982.
- [24] J. Connolly, S. Schnitt, J. Stuart, H. Wang, A. Dvorak, and H. Dvorak. Principles of cancer pathology. In *Cancer Medicine*, chapter 29, pages 533–555. BC Dekker, Hamilton, ON, 2000.
- [25] F. Courchamp, L. Berec, and J. Gascoigne. *Allee Effects in Ecology and Conservation*. Oxford University Press, 2008.
- [26] F. Courchamp, T. Clutton-Block, and B. Grenfell. Inverse density dependence and the Allee effect. *Trends Ecol. Evol.*, 14:405–410, 1999.
- [27] F. Courchamp and D. MacDonald. Crucial importance of pack size in the African wild dog *lycaon pictus*. *Anim. Conserv.*, 4:169–174, 2001.
- [28] M.G. Crandall and P.H. Rabinowitz. Bifurcation from simple eigenvalues. *J. Funct. Anal.*, 8:321–340, 1971.
- [29] J. Cushing. Backward bifurcations and strong Allee effects in matrix models for the dynamics of structured populations. *J. Biol. Dyn.*, 8:57–73, 2014.
- [30] H. Davis, C. Taylor, J. Civille, and D. Strong. An Allee effect at the front of a plant invasion: spartina in a Pacific estuary. *J. Ecol.*, 91:321–327, 2004.
- [31] B. de Rijk, A. Doelman, and J.D.M. Rademacher. Spectra and stability of spatially periodic pulse patterns: Evans function factorization via Riccati transformation. *SIAM J. Math. Anal.*, 48(1):61–121, 2016.
- [32] V. Deblauwe, P. Couteron, O. Lejeune, J. Bogaert, and N. Barbier. Environmental modulation of self-organized periodic vegetation patterns in sudan. *Ecography*, 34(6):990–1001, 2011.
- [33] A. Dhooge, W. Govaerts, Kuznetsov Yu.A., H.G.E. Meijer, and B. Sautois. New features of the software matcont for bifurcation analysis of dynamical systems. *Math. Comp. Model. Dyn.*, 14(2):147–175, 2008.
- [34] A. Doelman, R.A. Gardner, and T.J. Kaper. Stability analysis of singular patterns in the 1d Gray–Scott model: a matched asymptotics approach. *Physica D*, 122:1–36, 1998.
- [35] A. Doelman, R.A. Gardner, and T.J. Kaper. Large stable pulse solutions in reaction-diffusion equations. *Indiana Univ. Math. J.*, 50:443–507, 2001.

- [36] A. Doelman, R.A. Gardner, and T.J. Kaper. *A stability index analysis of 1-D patterns of the Gray–Scott model*, volume 737. American Mathematical Soc., 2002.
- [37] A. Doelman and P. Holmes. Homoclinic explosions and implosions. *Philos. T. Roy. Soc. A.*, 354(1709):845–893, 1996.
- [38] A. Doelman, T.J. Kaper, and H. van der Ploeg. Spatially periodic and aperiodic multi-pulse patterns in the one-dimensional Gierer-Meinhardt equation. *Meth. Appl. Anal.*, 8(2):387 – 414, 2001.
- [39] A. Doelman, T.J. Kaper, and P.A. Zegeling. Pattern formation in the 1-d Gray–Scott model. *Nonlinearity*, 10:523–563, 1997.
- [40] A. Doelman, J.D.M. Rademacher, and S. van der Stelt. Hopf dances near the tips of busse balloons. *Discr. Cont. Dyn. Syst.*, 5:61–92, 2012.
- [41] A. Doelman, L. Sewalt, and A. Zagaris. The effect of slow spatial processes on emerging spatiotemporal patterns. *Chaos*, 25(3):036408, 2015.
- [42] A. Doelman and H. van der Ploeg. Homoclinic stripe patternsl. *SIAM J. Appl. Dyn. Syst.*, 1(1):65–104, 2002.
- [43] A. Doelman and F. Veerman. An explicit theory for pulses in two component, singularly perturbed, reaction–diffusion equations. *J. Dyn. Differ. Equ.*, 27(3-4):555–595, 2015.
- [44] W. Eckhaus. *Asymptotic Analysis of Singular Perturbations*. Studies in Mathematics and its Applications **9**. North-Holland, 1979.
- [45] S. I. Ei, H. Izhahara, and M. Mimura. Infinite dimensional relaxation oscillation in aggregation-growth systems. *Discrete Contin. Dyn. Syst. Ser. B*, 17:1859 – 1887, 2012.
- [46] C. Engwer, T. Hillen, M. Knappitsch, and C. Surulescu. Glioma follow white matter tracts: a multiscale DTI-based model. *J. Math. Biol.*, 71:551–582, 2015.
- [47] P. G. Falkowski, R.T. Barber, and V. Smetacek. Biogeochemical controls and feedbacks on ocean primary production. *Science*, 281(5374):200–206, 1998.
- [48] N. Fenichel. Persistence and smoothness of invariant manifolds for flows. *Indiana Univ. Math. J.*, 21(193-226):1972, 1971.

- [49] N. Fenichel. Geometric singular perturbation theory for ordinary differential equations. *J. Diff. Equations*, 31:53 – 98, 1979.
- [50] C. Gao, Q. Xie, Y. Su, J. Koeman, S. Khoo, M. Gustafson, B. Knudsen, R. Hay, N. Shinomiya, and G. Van de Woude. Proliferation and invasion: plasticity in tumour cells. *Proc. Nat. Acad. Sci.*, 120:10528–10533, 2005.
- [51] R.A. Gardner. On the structure of the spectra of periodic travelling waves. *J. Math. Pures Appl.*, 72:415–439, 1993.
- [52] R.A. Gardner. Spectral analysis of long wavelength periodic waves and applications. *J. Reine. Angew. Math.*, 491:149–182, 1997.
- [53] R. Gatenby and E. Gawlinski. A reaction–diffusion model of cancer invasion. *Cancer Res.*, 51:5745–5753, 1996.
- [54] F. Gazzola, H. C. Grunau, and G. Sweers. *Polyharmonic Boundary Value Problems*. Springer Lecture Notes Series. Springer, 1991 edition, 2010.
- [55] A. Gerisch and M. Chaplain. Mathematical modelling of cancer cell invasion of tissue: local and non-local models and the effect of adhesion. *J. Theor. Biol.*, 250:684–704, 2008.
- [56] J. D. Gibbon and M. J. McGuinness. The real and complex lorenz equations in rotating fluids and lasers. *Physica D*, 5:108 – 122, 1982.
- [57] E. Gilad, J. von Hardenberg, A. Provenzale, M. Shachak, and E. Meron. Ecosystem engineers: from pattern formation to habitat creation. *Phys. Rev. Lett.*, 93(9):098105, 2004.
- [58] E. Gilad, J. von Hardenberg, A. Provenzale, M. Shachak, and E. Meron. Ecosystem engineers: from pattern formation to habitat creation. *Phys. Rev. Lett.*, 93(9):098105, 2004.
- [59] D. Gilbarg and N.S. Trudinger. *Elliptic Partial Differential Equations of Second Order*. Grundlehren der mathematischen Wissenschaften **224**. Springer–Verlag, 1983.
- [60] K. Gowda, Y. Chen, S. Iams, and M. Silber. Assessing the robustness of spatial pattern sequences in a dryland vegetation model. *Proc. R. Soc. A*, 472(2187):20150893, 2016.
- [61] K. Gowda, H. Riecke, and M. Silber. Transitions between patterned states in vegetation models for semiarid ecosystems. *Physical Rev. E*, 89(2):022701, 2014.

- [62] P. Gray and K. Scott. Autocatalytic reactions in the isothermal continuous stirred tank reactor: oscillations and instabilities in the system $A+2B \rightarrow 3B$; $B \rightarrow C$. *Chem. Eng. Sci.*, 39(6):1087–1097, 1984.
- [63] M. Greaves and C. Maley. Clonal evolution in cancer. *Nature*, 481:306–313, 2012.
- [64] S. Gregory, C. Bradshaw, B. Brook, and F. Courchamp. Limited evidence for the demographic Allee effect from numerous species across taxa. *Ecology*, 91:2151–2161, 2010.
- [65] M. Groom. Allee effects limit population viability of an annual plant. *Am. Nat.*, 151:487–496, 1998.
- [66] J. Guckenheimer and P. Holmes. *Nonlinear Oscillations, Dynamical Systems and Bifurcations of Vector Fields*. Applied Mathematical Sciences. Springer, 42 edition, 1983.
- [67] K. Harley, P. van Heijster, R. Marangell, G. J. Pettet, and M. Wechselberger. Existence of travelling wave solutions for a model of tumour invasion. *SIAM J. Appl. Dyn. Syst.*, 13:366–396, 2014.
- [68] K. Harley, P. van Heijster, R. Marangell, G. J. Pettet, and M. Wechselberger. Novel solutions for a model of wound healing angiogenesis. *Nonlinearity*, 27:2975–3003, 2014.
- [69] K. Harley, P. van Heijster, R. Marangell, G. J. Pettet, and M. Wechselberger. Numerical computation of an Evans function for travelling waves. *Math. Biosci.*, 266:36–51, 2015.
- [70] E. Hart and L. Aviles. Reconstructing local population dynamics in noisy metapopulations—the role of random catastrophes and Allee effects. *PloS One*, 9:e110049, 2014.
- [71] A. Hastings, K. Cuddington, K.F. Davies, C.J. Dugaw, S. Elmendorf, A. Freestone, S. Harrison, M. Holland, J. Lambrinos, U. Malvadkar, B.A. Melbourne, K. Moore, C. Taylor, and D. Thomson. The spatial spread of invasions: new developments in theory and evidence. *Ecol. Lett.*, 8(1):91–101, 2005.
- [72] H. Hatzikirou, D. Basanta, M. Simon, K. Schaller, and A. Deutch. ‘Go and grow’: The key to the emergence of invasion in tumour progression? *Math. Med. Biol.*, 29:49–65, 2012.

- [73] G. Hek. Geometric singular perturbation theory in biological practice. *J. Math. Biol.*, 60:347–386, 2010.
- [74] D. Henry. *Geometric theory of semilinear parabolic equations*, volume 840. Springer-Verlag New York, 1981.
- [75] R. HilleRisLambers, M. Rietkerk, F. van den Bosch, H.H.T. Prins, and H.D. Kroon. Vegetation pattern formation in semi-arid grazing systems. *Ecology*, 82:50–61, 2001.
- [76] M.H. Holmes. *Introduction to Perturbation Methods*. Texts in Applied Mathematics **20**. Springer, 1995.
- [77] M.H. Holmes. *Introduction to Perturbation Methods*. Texts in Applied Mathematics **20**. Springer–Verlag, 2013.
- [78] J. Huisman, N. N. Pham Thi, D. M. Karl, and B. P. Sommeijer. Reduced mixing generates oscillations and chaos in the oceanic deep chlorophyll maximum. *Nature*, 439:322–325, 2006.
- [79] J. Huisman, P. Van Oostveen, and F.J. Weissing. Critical depth and critical turbulence: two different mechanisms for the development of phytoplankton blooms. *Limnology and Oceanography*, 44(7):1781–1787, 1999.
- [80] D. Iron, M.J. Ward, and J. Wei. The stability of spike solutions to the one-dimensional Gierer–Meinhardt model. *Physica D*, 150:25 – 62, 2001.
- [81] D. Johnson, A. Liebhold, P. Tobin, and O. Bjornstad. Allee effects and pulsed invasion by the gypsy moth. *Nature*, 444:361–363, 2006.
- [82] C.K.R.T. Jones. *Dynamical Systems*. Lecture Notes in Mathematics **1609**. Springer–Verlag, 1995.
- [83] C.K.R.T. Jones, T.J. Kaper, and N. Kopell. Tracking invariant manifolds up to exponentially small errors. *SIAM J. Math. Anal.*, 27(2):558–577, 1996.
- [84] T.J. Kaper. An introduction to geometric methods and dynamical systems theory for singular perturbation problems. In *Proceedings of Symposia in Applied Mathematics*, volume 56, pages 85–132. American Mathematical Society, 1999.
- [85] R. Kapral and K. Showalter. *Chemical Waves and Patterns*. Kluwer, 1995.
- [86] T. Keitt, M. Lewis, and R. Holt. Allee effects, invasion pinning, and species’ borders. *Am. Nat.*, 157:203–216, 2001.

- [87] J.K. Kevorkian and J.D. Cole. *Multiple Scale and Singular Perturbation Methods*. Applied Mathematical Sciences**154**. Springer–Verlag, 1996.
- [88] C.A. Klausmeier. Regular and irregular patterns in semiarid vegetation. *Science*, 284(5421):1826–1828, 1999.
- [89] C.A. Klausmeier and E. Litchman. Algal games: The vertical distribution of phytoplankton in poorly mixed water columns. *Limnology and Oceanography*, 46(8):1998–2007, 2001.
- [90] T. Kolokolnikov, M.J. Ward, and J. Wei. The existence and stability of spike equilibria in the one-dimensional gray–scott model: The low feed-rate regime. *Studies in Applied Mathematics*, 115(1):21–71, 2005.
- [91] T. Kolokolnikov, M.J. Ward, and J. Wei. The existence and stability of spike equilibria in the one-dimensional gray–scott model: the pulse-splitting regime. *Physica D: Nonlinear Phenomena*, 202(3):258–293, 2005.
- [92] T. Kolokolnikov, M.J. Ward, and J. Wei. Zigzag and breakup instabilities of stripes and rings in the two-dimensional gray–scott model. *Studies in Applied Mathematics*, 116(1):35–95, 2006.
- [93] T. Kolokolnikov, J. Wei, and Winter. M. Existence and stability analysis of spiky solutions for the Gierer–Meinhardt system with large reaction rates. *Physica D*, 238:1695 – 1710, 2009.
- [94] K. Korolev, J. Xavier, and J. Gore. Turning ecology and evolution against cancer. *Nat. Rev. Cancer*, 14:371–379, 2014.
- [95] A. Kramer, B. Dennis, A. Liebhold, and J. Drake. The evidence for Allee effects. *Popul. Ecol.*, 51:341–354, 2009.
- [96] C. Kribs-Zaleta and C. Mitchell. Modeling colony collapse disorder in honeybees as a contagion. *Math. Biosci. Eng.*, 11:1275–1294, 2014.
- [97] M. Krupa and P. Szmolyan. Extending geometric singular perturbation theory to nonhyperbolic points—fold and canard points in two dimensions. *SIAM J. Math. Anal.*, 33:286–314, 2001.
- [98] Yu.A. Kuznetsov. *Elements of Applied Bifurcation Theory*. Springer, 3rd edition, 2004.
- [99] B. Lamont, P. Klinkhamer, and E. Witkowski. Population fragmentation may reduce fertility to zero in Banksia–Goodii: a demonstration of the Allee effect. *Oecologia*, 94:446–450, 1993.

- [100] C. Lemerle, B. Di Ventura, and L. Serrano. Space as the final frontier in stochastic simulations of biological systems. *FEBS Lett.*, 579(8):1789–1794, 2005.
- [101] S.A. Levin. *The problem of pattern and scale in ecology*. Ecological Time. Springer, 1995.
- [102] M. Lewis and P. Kareiva. Allee dynamics and the spread of invading organisms. *Theor. Popul. Biol.*, 43:141–158, 1993.
- [103] Q.-X. Liu, A. Doelman, V. Rottschäfer, M. de Jager, P.M.J. Herman, M. Rietkerk, and J. van de Koppel. Phase separation explains a new class of self-organized spatial patterns in ecological systems. *P. Natl. Acad. Sci. USA*, 110(29):11905–11910, 2013.
- [104] E.N. Lorenz. Deterministic, non-periodic flow. *J. Atmos. Sci.*, 20:130 – 141, 1963.
- [105] A.J. Lotka. Contribution to the theory of periodic reaction. *J. Phys. Chem.*, 14:271–274, 1910.
- [106] W.A. Macfadyen. Vegetation patterns in the semi-desert plains of british somaliland. *Geogr. J.*, 116(4/6):199–211, 1950.
- [107] A. Machens, H.-J. Holzhausen, and D. Henning. The prognostic value of primary tumor size in papillary and follicular thyroid carcinoma. *Cancer*, 103:2269–2273, 2005.
- [108] B.P. Marchant, J. Norbury, and H.M. Byrne. Biphasic behaviour in malignant invasion. *Math. Med. Biol.*, 23:173–196, 2006.
- [109] B.P. Marchant, J. Norbury, and A.J. Perumpanani. Traveling shock waves arising in a model of malignant invasion. *SIAM J. Appl. Math.*, 60:463–476, 2000.
- [110] A. Martínez-González, G. Calvo, L. Pérez Romasanta, and V. Pérez-Garcia. Hypoxic cell waves around necrotic cores in glioblastoma: a biomathematical model and its therapeutic implications. *Bull. Math. Biol.*, 74:2875–2896, 2012.
- [111] J. McGillen, E. Gaffney, N. Martin, and P. Maini. A general reaction–diffusion model of acidity and cancer invasion. *J. Math. Biol.*, 68:1199–1224, 2014.

- [112] A.B. Medvinsky, S.V. Petrovskii, I.A. Tikhonova, H. Malchow, and B.-L. Li. Spatiotemporal complexity of plankton and fish dynamics. *SIAM Rev.*, 44(3):311–370, 2002.
- [113] L. Merlo, J. Pepper, B. Reid, and C. Maley. Cancer as an evolutionary and ecological process. *Nat. Rev. Cancer*, 6:924–935, 2006.
- [114] E Meron. Modeling dryland landscapes. *Math. Model. Nat. Phenom.*, 6(01):163–187, 2011.
- [115] E. Meron, E. Gilad, J. von Hardenberg, M. Shachak, and Y. Zarmi. Vegetation patterns along a rainfall gradient. *Chaos Soliton Fract.*, 19:367–376, 2004.
- [116] F. Michor, Y. Iwasa, and M. Nowak. Dynamics of cancer progression. *Nat. Rev. Cancer*, 4:197–205, 2004.
- [117] D.S. Morgan, A. Doelman, T.J. Kaper, et al. Stationary periodic patterns in the 1-D Gray-Scott model. *Methods and applications of analysis*, 7(1):105–150, 2000.
- [118] I. Moyles, W.H. Tse, and M.J. Ward. Explicitly solvable nonlocal eigenvalue problems and the stability of localized stripes in reaction-diffusion systems. *Stud. Appl. Math.*, 136(1):89–136, 2016.
- [119] United Nations. Transforming our world: The 2030 agenda for sustainable development. <https://sustainabledevelopment.un.org>, 2015.
- [120] W.-M. Ni. Diffusion, cross-diffusion, and their spike-layer steady states. *Not. Am. Math. Soc.*, 45(1):9–18, 1998.
- [121] Y. Nishiura and D. Ueyama. Spatio-temporal chaos for the Gray–Scott model. *Physica D*, 150:137 – 162, 2001.
- [122] K.J. Painter and T. Hillen. Mathematical modelling of glioma growth: the use of diffusion tensor imaging (DTI) data to predict the anisotropic pathways of cancer invasion. *J. Theor. Biol.*, 323:25–39, 2013.
- [123] J.E. Pearson. Complex patterns in a simple system. *Science*, 261:189–192, 1993.
- [124] J.E. Pearson and W. Horsthemke. Turing instabilities with nearly equal diffusion coefficients. *J. Chem. Phys.*, 90:1588–1599, 1989.

- [125] A.J. Perumpanani and H.M. Byrne. Extracellular matrix concentration exerts selection pressure on invasive cells. *Eur. J. Cancer*, 35:1274–1280, 1999.
- [126] A.J. Perumpanani, J.A. Sherratt, J. Norbury, and H.M. Byrne. A two parameter family of travelling waves with a singular barrier arising from the modelling of extracellular matrix mediated cellular invasion. *Physica D*, 126:145–159, 1999.
- [127] K. Pienta, N. McGregor, R. Axelrod, and D. Axelrod. Ecological therapy for cancer: defining tumors using an ecosystem paradigm suggests new opportunities for novel cancer treatments. *Translational Oncology*, 1:158–164, 2008.
- [128] G.J.M. Pieters and H.M. Schuttelaars. On the nonlinear dynamics of a saline boundary layer formed by throughflow near the surface of a porous medium. *Physica D*, 237:3075 – 3088, 2008.
- [129] H.J. Poincaré. *Les méthodes nouvelles de la mécanique céleste*, volume 3. Gauthiers-Villars, 1899.
- [130] A. Potapov and H. Rajakaruna. Allee threshold and stochasticity in biological invasions: colonization time at low propagule pressure. *J. Theor. Biol.*, 337:1–14, 2013.
- [131] M. Rietkerk, M.C. Boerlijst, F. van Langevelde, R. HilleRisLambers, J. van de Koppel, L. Kumar, H.H.T. Prins, and A.M. de Roos. Self-organization of vegetation in arid ecosystems. *Am. Nat.*, 160(4):524–530, 2002.
- [132] M. Rietkerk, S.C. Dekker, P.C. de Ruiter, and J. van de Koppel. Self-organized patchiness and catastrophic shifts in ecosystems. *Science*, 305:1926–1929, 2004.
- [133] M. Rietkerk and J. van de Koppel. Alternate stable states and threshold effects in semi-arid grazing systems. *Oikos*, pages 69–76, 1997.
- [134] M. Rietkerk and J. van de Koppel. Regular pattern formation in real ecosystems. *Trends Ecol. Evol.*, 23(3):169–175, 2008.
- [135] J.C. Robinson. *Infinite-Dimensional Dynamical Systems*. Cambridge Texts in Applied Mathematics, 2001.

- [136] N. Ruppender, C. Morrisey, P. Lange, and R. Vesella. Dormancy in solid tumors: implications for prostate cancer. *Cancer Metast. Rev.*, 32:501–509, 2013.
- [137] C. Sanderson, S. Jobbins, and K. Alexander. With Allee effects, life for the social carnivore is complicated. *Popul. Ecol.*, 56:417–425, 2014.
- [138] M. Scheffer, J. Bascompte, W.A. Brock, V. Brovkin, S.R. Carpenter, V. Dakos, H. Held, E.H. van Nes, M. Rietkerk, and G. Sugihara. Early-warning signals for critical transitions. *Nature*, 461:53–59, 2009.
- [139] L. Sewalt, A. Doelman, H.G.E. Meijer, V. Rottschäfer, and A. Zagaris. Tracking pattern evolution through extended center manifold reduction and singular perturbations. *Physica D*, 298:48–67, 2015.
- [140] L. Sewalt, K. Harley, P. van Heijster, and S. Balasuriya. Influences of allee effects in the spreading of malignant tumours. *Journal of Theoretical Biology*, 2016.
- [141] J.A. Sherratt, S. Gourley, N. Armstrong, and K. Painter. Boundedness of solutions of a non-local reaction-diffusion model for adhesion in cell aggregation and cancer invasion. *Euro. J. Appl. Math.*, 20:123–144, 2009.
- [142] J.A. Sherratt and G.J. Lord. Nonlinear dynamics and pattern bifurcations in a model for vegetation stripes in semi-arid environments. *Theor. Popul. Biol.*, 71(1):1 – 11, 2007.
- [143] E. Siero, A. Doelman, M.B. Eppinga, J.D.M. Rademacher, M. Rietkerk, and K. Siteur. Striped pattern selection by advective reaction-diffusion systems: Resilience of banded vegetation on slopes. *Chaos*, 25:036411–1–036411–22, 2015.
- [144] K. Siteur. *Off the beaten track: How ecosystems fail to respond to environmental change*. PhD thesis, Universiteit Utrecht, 2016.
- [145] K. Siteur, E. Siero, M.B. Eppinga, J.D.M. Rademacher, A. Doelman, and M. Rietkerk. Beyond turing: The response of patterned ecosystems to environmental change. *Ecol. Complex.*, 20:81–96, 2014.
- [146] R. Smith, C. Tan, J. Srimani, A. Pai, K. Riccione, H. Song, and L. You. Programmed Allee effect in bacteria causes a tradeoff between population spread and survival. *P. Natl. Acad. Sci. USA*, 111:1969–1974, 2014.
- [147] C. Sparrow. *The Lorenz Equations: Bifurcations, Chaos and Strange Attractors*. Applied Mathematical Sciences **41**. Springer, 41 edition, 1982.

- [148] P. Stephens and W. Sutherland. Consequences of the Allee effect for behaviour ecology and conservation. *Trends Ecol. Evol.*, 14:401–405, 1999.
- [149] P. Szmolyan and M. Wechselberger. Canards in \mathbb{R}^3 . *J. Differ. Equations*, 177:419–453, 2001.
- [150] Z. Szymanska, C. Rodrigo, M. Lachowicz, and M. Chaplain. Mathematical modelling of cancer invasion of tissue: the role and effect of nonlocal interactions. *Math. Mod. Meth. Appl. S.*, 19:257–281, 2009.
- [151] X. Tang, L. Meng, A. Kapranos, F. Xu, I. Hardy, and B. Li. Mutually beneficial host exploitation and ultra-biased sex ratios in quasisocial parasitoids. *Nature Communications*, 5:4942, 2014.
- [152] C. Taylor, H. Davis, J. Civille, F. Grevstad, and A. Hasting. Consequences of an Allee effect in the invasion of a Pacific estuary by *spartina alterniflora*. *Ecology*, 85:3254–3266, 2004.
- [153] M. Tektonidis, H. Hatzikirou, A. Chauvière, M. Simon, K. Schaller, and A. Deutch. Identification of intrinsic in vitro cellular mechanisms for glioma invasion. *J. Theor. Biol.*, 287:131–147, 2011.
- [154] R. Temam. *Infinite-Dimensional Dynamical Systems in Mechanics and Physics*. Applied Mathematical Sciences **68**. Springer, 68 edition, 1988.
- [155] J.-Y. Tinevez, U. Schulze, G. Salbreux, J. Roensch, J.-F. Joannu, and E. Paluch. Role of cortical tension in bleb growth. *P. Natl. Acad. Sci. USA*, 106:18581–18586, 2009.
- [156] A.M. Turing. The chemical basis of morphogenesis. *Philos. T. R. Soc. B*, 237(641):37–72, 1952.
- [157] H. van der Ploeg and A. Doelman. Stability of spatially periodic pulse patterns in a class of singularly perturbed reaction-diffusion equations. *Indiana Univ. Math. J.*, 54:1219 – 1301, 2005.
- [158] B. Van der Pol. On relaxation-oscillations. *The London, Edinburgh, and Dublin Philosophical Magazine and Journal of Science*, 2(11):978–992, 1926.
- [159] S. van der Stelt, A. Doelman, G. Hek, and J.D.M. Rademacher. Rise and fall of periodic patterns in a Generalized Klausmeier–Gray–Scott model. *J. Nonlinear. Sci.*, 23:39–95, 2013.
- [160] A. Vanderbauwhede and G. Iooss. *Center manifold theory in infinite dimensions*. Dynamics Reported **1**. Springer–Verlag, 1992.

- [161] F. Veerman and A. Doelman. Pulses in a Gierer–Meinhardt equation with a slow nonlinearity. *SIAM J. Appl. Dyn. Syst.*, 12:28 – 60, 2013.
- [162] V. Volterra. Variazioni e fluttuazioni del numero d’individui in specie animali conviventi. *Mem. Acad. Lincei Roma*, 2:31–113, 1926.
- [163] J. von Hardenberg, E. Meron, M. Shachak, and Y. Zarmi. Diversity of vegetation patterns and desertification. *Phys. Rev. Lett.*, 87:198101–1–198101–4, 2001.
- [164] M.J. Ward and J. Wei. Hopf bifurcations and oscillatory instabilities of spike solutions for the one-dimensional Gierer-Meinhardt model. *J. Nonlinear Sci.*, 13(2):209–264, 2003.
- [165] M. Wechselberger. Existence and bifurcation of canards in \mathbb{R}^3 in the case of a folded node. *SIAM J. Appl. Dyn. Syst.*, 4:101–139, 2005.
- [166] M. Wechselberger. À propos de canards. *T. Am. Math. Soc.*, 304:3289–3309, 2012.
- [167] M. Wechselberger and G. J. Pettet. Folds, canards and shocks in advection-reaction-diffusion models. *Nonlinearity*, 23:1949–1969, 2010.
- [168] J. Wei. Pattern formations in two-dimensional gray–scott model: existence of single-spot solutions and their stability. *Physica D: Nonlinear Phenomena*, 148(1):20–48, 2001.
- [169] J. Wei and M. Winter. Existence and stability of multiple-spot solutions for the gray–scott model in \mathbb{R}^2 . *Physica D: Nonlinear Phenomena*, 176(3):147–180, 2003.
- [170] A. Wells, J. Grahovac, S. Wheeler, B. Ma, and D. Lauffenburger. Targeting tumor cell motility as a strategy against invasion and metastasis. *Trends Pharmacol. Sci.*, 34:283–289, 2013.
- [171] L. P. White. Brousse tigree patterns in southern niger. *J. Ecol.*, 58(2):549–553, 1970.
- [172] M. Wittman, W. Gabriel, and D. Metzler. Genetic diversity in introduced populations with an Allee effect. *Genetics*, 198:299–310, 2014.
- [173] M. Wittman, W. Gabriel, and D. Metzler. Population genetic consequences of the Allee effect and the role of offspring-number variation. *Genetics*, 198:311–320, 2014.

- [174] R. Wong. *Asymptotic approximations of integrals*. SIAM, 2001.
- [175] M. Yamamichi, T. Yoshida, and A. Sasaki. Timing and propagule size of invasion determine its success by a time-varying threshold of demographic regime shift. *Ecology*, 95:2303–2315, 2014.
- [176] A. Zagaris and A. Doelman. Emergence of steady and oscillatory localized structures in a phytoplankton-nutrient model. *Nonlinearity*, 24:3437 – 3486, 2011.
- [177] A. Zagaris, A. Doelman, N. N. Pham Thi, and B. P. Sommeijer. Blooming in a nonlocal, coupled phytoplankton-nutrient model. *SIAM J. Appl. Math.*, 69:1174 – 1204, 2009.
- [178] Y.R. Zelnik, E. Meron, and G. Bel. Gradual regime shifts in fairy circles. *P. Natl. Acad. Sci. USA*, 112(40):12327–12331, 2015.

Samenvatting

Patronen in natuurlijke systemen

Zoals in de Preface van dit proefschrift al werd betoogd, kan de wiskundige een belangrijke rol spelen in het aanpakken van de globale uitdagingen die de groeiende wereldbevolking met zich meebrengt. Door de gestructureerde aanpak van een wiskundige worden vraagstukken namelijk ontdaan van onnodige details, waardoor deze dikwijls beter te beantwoorden zijn. Voor een dergelijke aanpak is interdisciplinaire samenwerking echter cruciaal. In veel projecten in de toegepaste wiskunde wisselen ecologen, biologen, natuurkundigen of scheikundigen ideeën uit, waardoor de wiskunde steeds meer geïntegreerd raakt in andere wetenschappen. Hiermee is eigenlijk de deelwetenschap van de toegepaste wiskunde geboren.

Een veelgebruikte wiskundige vorm om natuurlijke fenomenen mee te beschrijven is de differentiaalvergelijking, die beschrijft hoe een bepaalde groothed verandert met het verstrijken van, bijvoorbeeld, de tijd. Binnen de toegepaste wiskunde richt patrooninformatie zich op oplossingen van stelsels van zulke differentiaalvergelijkingen die een zekere regelmaat vertonen. In een groot deel van de gevallen gaat het hierbij om reactie-diffusiestelsels, waarbij patronen zich tentoonstellen in de vorm van bijvoorbeeld pulsen, fronts of periodieke oplossingen. Dit proefschrift is een bloemlezing van verschillende patroonoplossingen in reactie-diffusiestelsels met een singuliere verstoring, die een natuurlijk fenomeen beschrijven. De singuliere verstoring betekent in dit geval dat er in ieder van deze patronen sprake is van meerdere schalen in tijd of ruimte. In de analyse en studie van de verschillende modellen die besproken worden, worden uiteenlopende methodes uit de verstoringsanalyse gebruikt. In deze Nederlandse samenvatting wordt per hoofdstuk een beknopt overzicht gegeven van de resultaten.

5.8 Uitgebreide centrumvariëteitreductie

Het ontstaan van patronen in reactie-diffusiestelsels is al vaak bestudeerd, bijvoorbeeld als het gevolg van een bifurcatie of middels een studie naar de amplitude

van een patroon. Wat daarna gebeurt, de evolutie van dergelijke patronen, is vaak minder begrepen, omdat de analyse onvermijdelijk gecompliceerder wordt. Één van de klassieke manieren om patrooninformatie te bestuderen is door middel van centrumvariëteitreductie. Door middel van deze techniek kan het gedrag van een differentiaalstelsel bestudeerd worden rondom een bifurcatie, door het stelsel te projecteren op de deelvariëteit die geassocieerd is met de kern van de differentiaaloperator. Deze methode geeft een lokaal resultaat, omdat één van de voorwaarden voor de toepassing ervan is dat er een ‘spectraal gat’ bestaat, wat ervoor zorgt dat de reductie daadwerkelijk lager-dimensionaal is. In Hoofdstuk 2 breiden we centrumvariëteitreductie uit naar het parameterregime waar die voorwaarde op het spectrum net niet meer geldt. Dit creëert ook de gelegenheid om eventuele secundaire bifurcaties van het primair ontspringende patroon te vinden, waardoor we de evolutie van een patroon na diens formatie beter kunnen begrijpen. De achtergrond waartegen we de methode ontvouwen is die van singulier verstoerde reactie-diffusiestelsels op een begrensd gebied met een homogene, stationaire oplossing. Het (niet-essentiële) spectrum behorende bij een dergelijke differentiaaloperator en achtergrondoplossing valt namelijk uiteen in twee verzamelingen van discrete eigenwaarden, met verschillende asymptotische grootte. Deze splitsing geeft precies de grip die nodig is om de klassieke centrumvariëteitreductie uit te breiden. In wezen is deze klassieke reductie een speciaal geval van de Galerkin methode, waarbij het stelsel geprojecteerd wordt op een oneindig aantal Fourierrichtingen. Galerkins methode resulteert in een oneindig aantal *gewone* differentiaalvergelijkingen die de amplitude van het patroon in verschillende richtingen beschrijft. In het geval van een bifurcatie is het inzichtelijk welke van deze amplitudevergelijkingen bepalend is voor het gedrag, namelijk precies die welke geassocieerd worden met de centrum-eigenwaarden. Wanneer er een oneindig aantal eigenwaarden is met dezelfde asymptotische grootte, is het echter niet te verwachten dat het relevante gedrag beschreven kan worden door een laag-dimensionaal stelsel van gewone differentiaalvergelijkingen. Het gedrag van elke afknotting van oneindig veel vergelijkingen kan immers drastisch veranderen wanneer er slechts één vergelijking meer of minder beschouwd wordt. Een bekend voorbeeld van dit fenomeen is de chaotische attractor in het drie-dimensionale Lorenz stelsel.

Door een geschikte projectie te kiezen en de verstoringssparameter explicet in te zetten, laten we in Hoofdstuk 2 zien dat toch ook wanneer er een oneindig aantal eigenwaarden is met vergelijkbare grootte, een laag-dimensionale reductie mogelijk is. We laten zien dat het op deze manier mogelijk is om vanuit de spectraalanalyse van een homogene, stationaire oplossing niet alleen een transkritische bifurcatie te volgen, maar ook de evolutie van de ontspringende, niet-homogene oplossing. Dit komt doordat het overgrote deel van de amplitudevergelijkingen in essentie

exponentieel aantrekend gedrag beschrijft, wat gemakkelijk te analyseren is. In het stelsel dat we in eerste instantie analyseren blijkt die evolutie te vangen in een reductie van twee dimensies, en binnen die reductie leiden we vervolgens voorwaarden af die een Hopf-bifurcatie genereren. Dit betekent dat we door middel van de spectraalanalyse van een triviaal patroon, we het ontstaan van een niet-triviaal patroon kunnen beschouwen, alsmede oscillerend gedrag van het patroon kort na diens ontstaan. Bovendien blijkt uit numerieke simulaties dat deze bifurcaties en het laag-dimensionale gedrag blijven bestaan wanneer de dynamica van het volledige PDV-stelsel beschouwd wordt (en dus alle oneindig veel dimensies in principe gesimuleerd worden). Vervolgens is deze *uitgebreide centrumvariëteitreductie* in Hoofdstuk 2 toegepast op verschillende andere stelsels van reactie-diffusievergelijkingen, om te tonen hoe breed inzetbaar de ontwikkelde methode is. In het bijzonder is hierbij een laag-dimensionale chaotische attractor gevonden, die, anders dan de oorspronkelijke Lorenz attractor, blijft bestaan in simulaties van het volledige PDV-stelsel.

Al met al kunnen we concluderen dat de uitgebreide centrumvariëteitreductie ervoor zorgt dat niet alleen het ontstaan van patronen in een primaire bifurcatie, maar ook diens evolutie volgens secundaire (of tertiaire, etc.) bifurcaties bestudeerd kunnen worden op een laag-dimensionale variëteit. Doordat het grootste deel van de amplitudevergelijkingen tot op leidende orde exponentieel aantrekend gedrag vertoont, is het helder te identificeren welke vergelijkingen bepalend zijn voor de dynamica van het gehele systeem.

5.9 Stabiliteit van een bodemlaag van fytoplankton

De aanleiding voor het onderzoek dat gepresenteerd is in Hoofdstuk 2 was het artikel [176], waarin de methode min of meer ontwikkeld werd voor een specifiek model wat toegepast wordt op de dynamica van fytoplankton. Deze toepassing vereist wat uitleg. Binnen de verschillende planktonsoorten onderscheidt fytoplankton zich doordat het zijn energie verkrijgt via fotosynthese. Het is het soort plankton dat vergelijkbaar is met een plant, tegenover zooplankton, wat meer weg heeft van een beestje. Fytoplankton vormt de basis van de voedselketen in de oceanen, maar is ook een belangrijke schakel in het aanpakken van het broeikaseffect, omdat het op zeer effectieve wijze koolstofdioxide uit de atmosfeer haalt en omzet in zuurstof.

Wiskundig gezien is fytoplankton interessant omdat observaties laten zien dat de koloniën zich concentreren op een zeer specifieke diepte: ze zijn gelokaliseerd. Dit is toe te schrijven aan de balans die zij trachten te vinden tussen de beschikbaarheid van licht en voedingsstoffen, afkomstig van respectievelijk het wateroppervlak en de bodem. Wanneer het water waar het model betrekking op heeft erg diep of troebel is, kan licht niet tot aan de bodem penetreren. Het plankton

zal in dat geval de gunstige diepte zoeken waar zowel licht als voeding optimaal verkrijgbaar zijn, en dat is niet aan de bodem. Dit fenomeen noemen we een *diep chlorofyl maximum*, en is de focus van [176]. Wanneer het water echter niet erg diep is, reikt het zonlicht tot aan de bodem, en aangezien de voedingsvoorziening aan de bodem optimaal is, is de gunstigste diepte voor de planktonkolonie dan wel op de bodem; er vormt zich dan een *bodemlaag*.

In Hoofdstuk 3 staat een reactie-diffusiestelsel centraal dat de interactie tussen fytoplankton en diens voedingsstoffen beschrijft. Dit bewuste model is in wiskundige context eerder geanalyseerd in [177] en [176]. In [177] is de lineaire stabiliteit van de homogene oplossing (geen plankton, constante voedingsstof) bestudeerd, en daar werd al ontwaard welke parameters verantwoordelijk zijn voor het vormen van een diep chlorofyl maximum, dan wel een bodemlaag. Het spectrum van de homogene oplossing verdeelt zich over twee verzamelingen, en afhankelijk van de precieze parameters van het systeem is de eigenwaarde die hoort bij een bodemlaag of een diep chlorofyl maximum het grootst. Dit geeft precies aan welk van beide profielen in de eerste plaats zal ontstaan bij het destabiliseren van de homogene oplossing. Numerieke continuatie van deze bifurcaties heeft in [177] laten zien dat een diep chlorofyl maximum vrijwel direct na ontspringen periodiek gaat trillen. In [176] wordt bewijs geleverd voor deze numerieke conclusie door te laten zien dat de transkritische bifurcatie die hoort bij de oorsprong van de gelokaliseerde oplossing, binnen een klein parametergebied wordt opgevolgd door een (secundaire) Hopf bifurcatie. Eigenlijk wordt in [176] dus een rudimentaire versie van uitgebreide centrumvariëteitreductie uitgevoerd.

Na de ontplooiing van de precieze methodiek die aan de resultaten van [176] ten grondslag ligt, in Hoofdstuk 2, wordt deze reductie in Hoofdstuk 3 toegepast op het fytoplanktonmodel. In eerste instantie wordt de methode nog verder verfijnd. In plaats van een reductie naar twee niet-triviale, en oneindig veel triviale amplitudevergelijkingen (gewone differentiaalvergelijkingen), presenteren we deze reductie in Hoofdstuk 3 in een equivalente vorm waarbij een gewone differentiaalvergelijking aan één lineaire partiële differentiaalvergelijking gekoppeld is. Deze lineaire PDV blijkt oplosbaar, waardoor de reductie helder gepresenteerd en toegepast kan worden. In eerste instantie herontdekken we in Hoofdstuk 3 kort de resultaten uit [176]. Dat wil zeggen, we vinden de transkritische bifurcatie waarbij een diep chlorofyl maximum ontstaat, en de vrijwel direct daaropvolgende Hopf bifurcatie die maakt dat de planktonconcentratie gaat oscilleren.

Vervolgens bekijken we het parameterregime waarin een bodemlaag ontspringt in plaats van een diep chlorofyl maximum en analyseren we de stabiliteit van deze ontstane bodemlaag. Anders dan in het geval van een diep chlorofyl maximum, tonen we met behulp van de uitgebreide centrumvariëteitreductie aan dat een stationaire bodemlaag niet kort na zijn ontstaan kan destabiliseren.

In plaats daarvan blijft het patroon bestaan als stationaire oplossing van het systeem, in elk geval binnen het parameterregime waarin onze reductie toepasbaar is. Dit gedrag is bovendien bevestigd door middel van numerieke simulaties. Toch blijkt de analyse van de bodemlaag significant anders dan die van het diep chlorofyl maximum, omdat er hogere orde termen nodig zijn in de asymptotische analyse.

5.10 Tumorspreiding met een Allee effect

Binnen de ecologie is het Allee effect een bekend fenomeen. Het beschrijft de groeidrempel van een populatie; de populatie kan zich pas voortplanten wanneer er genoeg individuen zijn. Er zijn verschillende verklaringen voor dit Allee effect, zoals de noodzaak voor genetische diversiteit, het niet kunnen vinden van een partner, of te weinig bescherming van elkaar tegen roofdieren. Het Allee effect is al in vele disciplines een bekend begrip, maar dat dit ook aanwezig zou zijn in de groei van sommige tumoren is een vrij recent inzicht. Desalniettemin is het intuïtief heel goed te motiveren, alleen al door het feit dat kleine tumoren minder gevaarlijk worden geacht dan grote.

We richten ons in Hoofdstuk 4 op hoe tumorcellen de omgevende gezonde cellen infiltreren. Het model dat gebruikt wordt neemt aan dat dit gebeurt via haptische of chemotaxis, door de extracellulaire matrix; de voorkeursrichting van de tumorcellen om naartoe te groeien, is die van de gezonde cellen. We simplificeren het model tot één oneindig lange ruimtelijke dimensie en wiskundig gezien is zo'n doordringend front van tumorcellen een lopende golf met verschillende randvoorwaarden aan beide kanten van het domein. Aangezien de tumoren waar we ons op richten een heel duidelijke rand hebben, zou de overgang tussen de twee gebieden scherp moeten zijn. Zo'n snelle transitie is een fenomeen dat je vaak ziet bij singulier verstoerde problemen, dus er is in ons model ook een kleine parameter aanwezig.

Binnen kankeronderzoek is het vrijwel onmogelijk om een modelkeuze te maken die onbetwist blijft. Onze keuze viel op een model dat voorgesteld is in [125] en verder ontwikkeld is in [67] vanwege de relevante ervaring die we hiermee al hadden en de goede vergelijkingsmogelijkheden. Evenwel is het reactie-advectie-diffusiestelsel uit [67] aangepast om het Allee effect te bestuderen, tegenover het oorspronkelijke model waarin de voortplanting van tumorcellen gemodelleerd is door middel van een logistische groeiterm. Dit houdt in dat de populatie groeit via een kwadratisch verband totdat zij zo groot is dat de draagkracht van het ecosysteem bereikt is. Wanneer er sprake is van een groeidrempel, zou de voortplantingsterm van de populatie negatief moeten zijn bij een kleine populatiedichtheid. We modelleren het Allee effect daarom met een kubische term.

In [67] is bewezen dat het model met logistische groei vier types lopende golfoplossingen heeft. De soorten worden van elkaar onderscheiden door de snelheid van de transitie van tumorisch naar gezond gebied, maar ook door de dichtheid van tumorcellen in het gezonde gebied verder weg van deze transitie. Wegens de eerdergenoemde scherpe rand van sommige tumoren, worden niet alle types die geconstrueerd zijn in [67] relevant geacht. Toch blijken drie van de vier soorten oplossingen zichtbaar in numerieke simulaties van het PDV-model, wat een indicatie is voor de stabiliteit van deze lopende golven.

Het toevoegen van het Allee effect in het model heeft een tweevoudig resultaat. Enerzijds laten we zien dat alleen de meest relevante van de verschillende types oplossingen uit [67] blijft bestaan in de aanwezigheid van een groeidrempel, terwijl de andere types niet meer bestaan. Anderzijds, bevestigen we de experimentele resultaten die eerder niet te verklaren waren met een model van deze vorm. Dit betreft de relatie tussen de invasiesnelheid van een tumor en de dichtheid van collageen (het belangrijkste onderdeel van de extracellulaire matrix). Die relatie blijkt niet monotoon te zijn, maar een duidelijk maximum te hebben. Deze *bifasische relatie* is ook aangetoond in het model dat we beschouwen in Hoofdstuk 4, en was geen kenmerk van het logistische groeimodel.

De methoden die we gebruiken in dit hoofdstuk zijn afkomstig uit de geometrische verstoringsanalyse en canard theorie, wat wordt toegelicht in sectie 1.4.

5.11 Vegetatiepatronen met een lange golflengte

De laatste natuurlijke toepassing van wiskundige modellen die beschouwd wordt in dit proefschrift speelt zich af in semi-droge gebieden van de aarde. Het is een breed geaccepteerd feit dat, onderhevig aan klimaatverandering, de woestijnen zich langzaam uitbreiden. Dit is problematisch omdat woestijngrond onvruchtbare is voor de verbouwing van de gewassen die nodig zijn voor het voeden van de continu groeiende maatschappij. Omdat tijdens de overgang van vruchtbare naar kale grond allerlei vegetatiepatronen geobserveerd zijn is dit bij uitstek een natuurfenomeen waar wiskundigen zich over kunnen buigen. De patronen die geobserveerd worden zijn grofweg in te delen in drie groepen: strepen, stippen, en labyrinthpatronen. In het geval dat het grondoppervlak licht glooiend is en er geen sprake is van begrazing, zijn het vooral de streeppatronen die geobserveerd worden. Deze strepen vormen zich parallel aan de hoogtecontouren van de helling, en migreren langzaam omhoog. Deze beweging kan verklaard worden door het feit dat er een wateroverschot bovenaan de helling is, waardoor een gewas zich aan die zijde beter kan voorplanten, terwijl het watertekort onderaan de helling ervoor zorgt dat vegetatie afsterft. Dit specifieke fenomeen bestuderen we in Hoofdstuk 5.

Het model dat geanalyseerd wordt is wederom van het reactie-advectie-diffusietype en modelleert de interactie tussen water- en vegetatiedichtheid op gebieden met een helling. Het model heet het *gegeneraliseerd Klausmeier-Gray-Scott (gKGS) model*, omdat het in een zeker opzicht lijkt op twee voorgangers: het Klausmeier model [88] en het Gray-Scott model [62]. De eerste modelleert water zonder diffusie, en de tweede modelleert een gebied zonder helling. Door beide mechanismen samen te voegen kunnen meer aspecten van dit natuurlijke fenomeen beschreven worden dan in ieder van de individuele modellen doet.

Het ruimtelijke domein waarop de analyse van Hoofdstuk 5 zich afspeelt is twee-dimensionaal. Maar aangezien strepen triviaal uitgebreid zijn in één richting, is het existentieprobleem van streeppoplossingen in het gKGS model in essentie één-dimensionaal. De streeppatronen zoals ze geobserveerd worden in de woestijn zijn daarom wiskundig te beschrijven als een periodieke herhaling van bijna gelokaliseerde pulsen van vegetatie, die met een constante snelheid voortbewegen. Net als in het vorige hoofdstuk, gaat het hier dus om een lopende golfoplossing.

Een studie naar het bestaan van dergelijke oplossingen en diens stabiliteit was in het geval van vlak terrein al gedaan in [34, 39, 36], met het Gray-Scott model. De technieken die gebruikt zijn in Hoofdstuk 5 zijn grotendeels afkomstig van deze referenties, maar dienden in sommige gevallen sterk aangepast te worden. Een cruciaal verschil tussen beide modellen is namelijk het gebrek aan symmetrie in het gKGS model. Hierdoor zijn een groot deel van de argumenten voor de bewijzen ongeldig. In Hoofdstuk 5 hebben we daarom andere technieken ontwikkeld en toegepast om ook zonder symmetrie stellingen te kunnen bewijzen over het bestaan van streeppatronen.

Het moet gezegd worden dat in dit hoofdstuk, waarin de resultaten sterk afhankelijk zijn van asymptotische argumenten, een tamelijk specifieke keuze is gemaakt voor de parameterruimte waarin de patronen zich vormen. Ook deze schalingsafhankelijkheid is gepresenteerd in Hoofdstuk 5.

Nadat eerst de existentie van streeppatronen met een lange golflengte is afgeleid, beschouwen we de stabiliteit van deze patronen. De numerieke resultaten uit [143], die aantonen dat strepen stabiel kunnen zijn tegen verstoringen (zoals je die tegenkomt in de natuur), gaf aanleiding om te verwachten dat de geconstrueerde patronen van Hoofdstuk 5 dat ook zouden zijn. Het feit dat streeppatronen instabiel zijn op vlak terrein (wat volgt uit eerdere resultaten in het Gray-Scott model, [143]) maar stabiel worden wanneer het terrein glooit, is bovendien te motiveren vanuit het feit dat het ene geval niet, en het andere wel geobserveerd wordt. Toch tonen we in Hoofdstuk 5 aan dat, in het schalingsregime waar we ons tot beperkt hebben, verstoringen in de transversale richting van het patroon groeien. Met andere woorden; de streeppatronen uit dat

hoofdstuk zijn, wanneer beschouwd in twee ruimtelijke dimensies, instabiel. De meest aannemelijke verklaring hiervoor is de restrictie die opgelegd wordt door de verstoringsanalyse; de parameters waarmee numerieke simulaties gedaan zijn in [143] vallen wellicht niet in het door ons toegestane parametergebied.

Toch is de kous hiermee nog niet af. Hoewel twee ruimtelijke dimensies overduidelijk een betere beschrijving geven van de realiteit, zijn de patronen in één dimensie (dus zonder de triviale uitbreiding) in wiskundig opzicht zeker ook interessant. Deze patronen blijken wel stabiel te kunnen zijn, en in Hoofdstuk 5 wordt een precies overzicht gegeven van de mogelijke bifurcaties.

De methoden die gebruikt worden in dit hoofdstuk zijn geometrische verstoringsanalyse, alsmede een Evans functie analyse waarbij het meerschalige karakter van dit probleem uitgebuit wordt.

Dankwoord

Arjen, aan wie anders kan ik mijn eerste woorden richten? Hoewel ik na onze eerste kennismaking tijdens een hoorcollege een beetje van mijn stuk gebracht was, ben ik vanaf het eerste moment dat je mijn scriptie ging begeleiden ontzettend op je gesteld geraakt. Ik heb genoten van onze afspraken waarin je me nieuwe wiskunde uitlegde voor het bord, en misschien nog wel meer van de gezellige gesprekken vanuit de luie stoel met een kopje koffie. Je hebt altijd vertrouwen in me gehad, en je open karakter maakte dat ik bij je kon lachen en huilen. Dat je niet bang bent om de student centraal te stellen, of je eigen ideeën over boord te gooien (wat eigenlijk nooit nodig bleek te zijn), maakt je een heel goede begeleider. Dat je daarnaast een virtuoos wiskundige bent met een kritische blik op je eigen vakgebied, maakt je een briljante begeleider. Ik ga onze samenwerking enorm missen.

Dan natuurlijk Peter, die binnen vier maanden zoveel indruk wist te maken dat hij als co-promotor bij mijn promotie betrokken werd. Mijn tijd in Australië is geweldig geweest, niet in de laatste plaats dankzij jouw gastvrijheid. We hebben heel intensief gewerkt, maar door je tomeloze enthousiasme en humor was het altijd leuk. Vooruit, misschien had het ook iets met de zon te maken.

Mijn leuke collega's maakten dat ik met plezier naar mijn werk ben gegaan. Stéphanie, Stefanie, Frits, Eric, Corine, Suzanne, Maja en natuurlijk mijn wiskundebroertje Björn: heel erg bedankt voor een fijne tijd.

Maar harde inspanning moet gecompenseerd worden met hardere ontspanning, en hoewel ze het misschien niet beseffen, hebben ook niet-wiskundigen een bijdrage geleverd aan dit proefschrift. Lieve Ewoud, met jou is het leven leuk en met jouw engelengeduld heb je de afgelopen jaren mijn twijfels en zorgen aangehoord. Dat moet wel echte liefde zijn.

Mam, dit lijkt me de juiste gelegenheid om te zeggen dat je een geweldig voorbeeld bent en dat ik alleen maar kan hopen zo'n mooi mens te worden als jij.

Tenslotte wil ik bedanken voor jarenlange vriendschap en blijvende interesse in een proefschrift dat ver van jullie af staat: Carlos, Carolien, Eefje, Erik, Harrie, Joske, Karin, Kelly, Kim, Kristen, Linda, Marloes, Mike, Sophie, Valerie, en ieder

ander die ooit aan me vroeg: ‘Hoe gaat het met je proefschrift?’.

Curriculum Vitae

Lotte Sewalt was born on the 16th of June, 1990 in Alphen aan den Rijn, The Netherlands. After obtaining an ‘Atheneum’ diploma at the Katholieke Scholengemeenschap Ashram College in 2007 she started her mathematical career at Leiden University in that same year. After three years she obtained a Bachelor’s degree in Mathematics. She started teaching high school students at the school she had attended herself, while proceeding with a Master’s program in Applied Mathematics at Leiden University. In August 2012, she graduated cum laude with a thesis called *Pattern formation in a generalized Klausmeier-Gray-Scott model* which was supervised by prof. dr. Arjen Doelman and dr. Vivi Rottschäfer.

In September 2012, she started a Ph.D. research project labeled *Phytoplankton dynamics, spatio-temporal chaos and destabilization mechanisms*. The project was funded by NWO through an NDNS⁺-cluster grant, awarded to prof. dr. Arjen Doelman and dr. Antonios Zagaris. The results associated with this particular project are presented in Chapters 2 and 3 of this thesis. In 2014, she won a travel grant for Ph.D. students which lead to a semester at Queensland University of Technology in Brisbane, Australia. Under the supervision of dr. Peter van Heijster, her time abroad resulted in a successful project and publication on malignant tumor spread, presented in Chapter 4 of this thesis. Upon returning to Leiden, she recommenced the work of her master’s thesis and the extended results are presented in Chapter 5. She presented her work in many oral and poster presentations at both national and international conferences.

Next to doing research, Lotte organized several symposia and seminars of which the *Study group Mathematics with Industry* in 2013 was the most populous. She was also the initiator of the Ph.D. Colloquium at the Mathematical Institute, which connects Ph.D. students with different backgrounds to each other. Moreover, she was teaching assistant in many courses of the Bachelor and Master programs at the institute, and, since 2013, teacher of *Mathematics for Statisticians*. After obtaining the doctor’s degree associated with this thesis, she will start as a Consultant Sustainability at KPMG Staffing & Facility Services.